

# High-resolution large-eddy simulations of scalar transport in forest-edge flows and implications for the interpretation of in-situ micrometeorological measurements

Von der Fakultät für Mathematik und Physik  
der Gottfried Wilhelm Leibniz Universität Hannover  
zur Erlangung des Grades

Doktorin der Naturwissenschaften  
Dr. rer. nat.  
genehmigte Dissertation  
von

Dipl.-Met. Farah Kanani-Sühring  
geboren am 19. Mai 1985 in Hamm

2015

Referent:  
Korreferent:  
Tag der Promotion:

Prof. Dr. Siegfried Raasch  
Prof. Dr. Günter Groß  
20. Mai 2015

# Abstract

Forests cover about one third of the Earth surface and play an important role in the Earth's weather and climate system by directly affecting the soil-vegetation-atmosphere exchange of momentum and scalars (e.g. energy, water, CO<sub>2</sub>), which is realized by turbulent transports. In weather and climate models, turbulent transports are not resolved, and hence, are parametrized as derived by micrometeorological measurements under the assumption of horizontal homogeneity across a surface patch of specific type. However, in heterogeneous landscapes with frequent transitions between surface patches with different surface characteristics, the flow as well as the turbulent fluxes of momentum and scalars can be spatially highly variable in the region near the surface transition, before adjusting to the changing surface conditions. This is particularly pronounced near forest edges, where especially the scalar transport processes are yet scarcely understood. However, the spatial variability of the exchange processes near forest edges contradicts the general assumption of horizontal homogeneity. This in turn questions the applicability of parametrizations in weather and climate models to correctly represent exchange processes in highly fragmented forested landscapes. However, a proper representation of the exchange processes in fragmented forested landscapes becomes increasingly important, since the relative portion of these landscapes is continuously growing e.g. due to deforestation as highly practised in tropical rainforests. In order to improve parametrizations, micrometeorological measurements in fragmented forested landscapes as well as an improved understanding of the scalar transport processes near forest edges are required.

The main goal of this thesis was to contribute to a better understanding of these transport processes, and to enable a better interpretation and planning of micrometeorological measurements in fragmented forested landscapes. For this purpose, the transport of a surface-emitted passive scalar in neutrally-stratified flows across idealized forest edges was studied under different plant physical and meteorological conditions, by means of turbulence-resolving large-eddy simulations (LES).

At first, the applied LES model was successfully validated for representing flows over infinite homogeneous forests and across forest edges, against field and wind-tunnel data. Further, it was investigated which meteorological and plant-physical conditions affect the features of forest-edge flow. It was demonstrated that the properties of the approaching flow, largely influenced by upstream forest patches and the overall atmospheric conditions, strongly affect forest-edge-flow features, in turn questioning the comparability of "real-world" and modelled flow data if the approaching flow is not well represented in model set-ups.

Following, scalar transport processes near windward and leeward forest edges were studied. Downstream of the windward forest edge, as well as in the lee of the forest, local enhancement of scalar concentration and its flux was found, complicating the interpretation of micrometeorological measurements regarding their spatial representativity. By means of a term-by-term analysis of the scalar balance equation, the responsible transport mechanisms for the local scalar enhancement were identified. Moreover, for both scalar-enhancement regions, it was found that the magnitude of the concentration and flux enhancement increases with increasing forest density, while varying wind speeds were more effective on the concentration rather than the flux, with higher concentrations at lower wind speeds. Near the windward edge above the forest patch, the forest density was further found to remarkably affect the location of the scalar-enhancement region with respect to the distance from the windward edge. Based on these findings, recommendations for estimating the regions of enhanced scalar concentration and flux by on-site measurements were proposed, for enabling a better planning and interpretation of micrometeorological measurements near windward and leeward forest edges.

**Keywords:** Forest-atmosphere exchange, Forest-edge flow, Large-eddy simulation

# Kurzzusammenfassung

Wälder bedecken etwa ein Drittel der Erdoberfläche und spielen daher eine wichtige Rolle im Wetter- und Klimasystem der Erde, indem sie signifikant den Austausch von Impuls und Skalaren (z.B. Energie, Wasser, CO<sub>2</sub>) zwischen der Erdoberfläche und der Atmosphäre in Form von turbulenten Transporten beeinflussen. In Wetter- und Klimamodellen werden turbulente Transporte nicht aufgelöst und müssen daher parametrisiert werden. Diese Parametrisierungen sind aus mikrometeorologischen Messungen abgeleitet und unterliegen der Annahme, dass die turbulenten Austauschprozesse über Landoberflächen gleichen Typs horizontal homogen sind. In heterogenen Landschaften mit häufigen Übergängen zwischen unterschiedlichen Landoberflächentypen kann jedoch der turbulente Austausch von Impuls und Skalaren räumlich sehr stark variieren, insbesondere an den Übergängen zwischen unterschiedlichen Oberflächentypen. Diese räumliche Variabilität ist besonders nahe Waldkanten stark ausgeprägt, wo Austauschprozesse von Skalaren bislang allerdings nur unzureichend verstanden sind. Insgesamt steht diese hohe räumliche Variabilität im Widerspruch zu der Annahme horizontaler Homogenität, welches die Anwendbarkeit von Parametrisierungen in Wetter- und Klimamodellen insbesondere für heterogen bewaldete Landschaften in Frage stellt. Eine geeignete Berücksichtigung der Austauschprozesse in heterogen bewaldeten Landschaften gewinnt jedoch zunehmend an Wichtigkeit, da der relative Anteil dieser Landschaften stetig anwächst, z.B. aufgrund der Abholzung der tropischen Regenwälder. Um diese Parametrisierungen zu verbessern werden mikrometeorologische Messungen in derartigen Landschaften benötigt, und es muss ein generelles Verständnis von Skalartransportprozessen nahe Waldkanten entwickelt werden.

Das Hauptziel dieser Arbeit bestand darin, zu einem besseren Verständnis dieser Transportprozesse beizutragen, und im Weiteren eine verbesserte Interpretation und Planung mikrometeorologischer Messungen in heterogen bewaldeten Landschaften zu ermöglichen. Zu diesem Zweck wurde der Transport von an der Erdoberfläche freigesetztem passiven Skalar untersucht. Dazu wurden turbulenzauflösende Grobstruktursimulationen (*engl.* large-eddy simulation – LES) von idealisierten Waldkantenströmungen unter neutralen atmosphärischen Bedingungen für verschiedene Waldbestandsdichten und Windgeschwindigkeiten durchgeführt.

Zunächst wurde anhand eines umfassenden Vergleichs der LES Daten mit Feldexperiment- und Windkanaldaten die Anwendbarkeit des eingesetzten LES Modells zur Simulation von Strömungen über unendlich ausgedehnten Wäldern sowie über Waldkanten bestätigt. Des Weiteren wurde im Rahmen dieses Vergleichs untersucht inwiefern meteorologische und pflanzenphysikalische Gegebenheiten die Eigenschaften von Waldkantenströmungen beeinflussen. Es wurde gezeigt, dass die Eigenschaften der auf die luvseitige Waldkante treffenden Strömung, welche maßgeblich durch stromauf gelegene Waldstücke sowie durch die atmosphärischen Bedingungen beeinflusst werden kann, einen merklichen Einfluss auf die Strömung stromab der luvseitigen Waldkante hat. Diese Erkenntnis hat wiederum Implikationen für die Vergleichbarkeit von modellierten und gemessenen Daten, insbesondere wenn die Merkmale der herannahenden Strömung nicht entsprechend in den Modellen berücksichtigt werden.

Im Weiteren wurden die Skalartransportprozesse in der Umgebung von luvseitigen und leeseitigen Waldkanten mittels LES untersucht. Sowohl stromab von luvseitigen Waldkanten als auch im Lee von Waldstücken konnten lokal erhöhte Skalkonzentrationen und -flüsse beobachtet werden, was die Interpretation mikrometeorologischer Messungen bezogen auf ihre räumliche Repräsentativität erschwert. Mittels einer Analyse der Skalarbilanzterme konnten die für die lokale Skalaransammlung verantwortlichen Transportmechanismen identifiziert werden. Des Weiteren zeigte sich für beide Gebiete mit den erhöhten Konzentrationen und Flüssen, dass sowohl Konzentration als auch Skalarfluss mit wachsender Bestandsdichte zunehmen, während ein Effekt der Windgeschwindigkeit hauptsächlich für die Skalkonzentration beobachtet wurde, mit höheren Konzentrationen bei geringeren Windgeschwindigkeiten. Außerdem zeigte sich, dass die Bestandsdichte einen merklichen Einfluss auf den Ort der Skalaransammlung im Wald hat, bezogen auf die Entfernung zur luvseitigen Waldkante. Auf Grundlage dieser Erkenntnisse wurden Herangehensweisen entwickelt, mittels derer die Gebiete mit möglich erhöhten Konzentrationen und Flüssen abgeschätzt werden können, welches eine bessere Planung und Interpretation mikrometeorologischer Messungen nahe Waldkanten ermöglichen soll.

**Schlagnworte:** Wald-Atmosphären Austausch, Waldkantenströmung, Grobstruktursimulation

# Contents

<b>1</b>	<b>Introduction</b>	<b>1</b>
1.1	Properties of boundary layers above short- or non-vegetated surfaces . . . . .	2
1.1.1	Atmospheric boundary layers . . . . .	2
1.1.2	Laboratory boundary layers . . . . .	3
1.2	Modification of surface-layer flows under the presence of tall vegetation . . . . .	4
1.3	Numerical simulation of atmospheric flows . . . . .	7
1.4	Current state of research . . . . .	8
1.4.1	Steps towards understanding the dynamics of forest-edge flows . . . . .	8
1.4.2	Scalar transport in fragmented forested landscapes . . . . .	10
1.5	Scope of this thesis . . . . .	11
<b>2</b>	<b>Methods</b>	<b>13</b>
2.1	Parallelized large-eddy simulation model PALM . . . . .	13
2.1.1	Governing model equations . . . . .	13
2.1.2	Parametrization of subgrid scales . . . . .	14
2.1.3	Embedded plant canopy model . . . . .	15
2.1.4	Spatial and temporal discretization of the model equations . . . . .	16
2.1.5	Boundary and initial conditions for the solution of the model equations . . . . .	18
2.2	Analysis methods . . . . .	21
2.2.1	Calculation of turbulence statistics in heterogeneous flows . . . . .	21
2.2.2	Typical quantities for the characterization of canopy flows . . . . .	22
2.2.3	Calculation of individual scalar balance terms . . . . .	23
2.3	Validation of PALM under homogeneous canopy flow conditions . . . . .	24
<b>3</b>	<b>Research articles of this cumulative thesis</b>	<b>29</b>
3.1	Research article A: What determines the differences found in forest edge flow between physical models and atmospheric measurements? – An LES study . . . . .	30
3.1.1	Declaration of my contribution . . . . .	30
3.1.2	Published article . . . . .	30
3.2	Research article B: Spatial variability of scalar concentrations and fluxes downstream of a clearing-to-forest transition: A large-eddy simulation study . . . . .	48
3.2.1	Declaration of my contribution . . . . .	48
3.2.2	Author’s version of revised article . . . . .	48
3.3	Research article C: Enhanced scalar concentrations and fluxes in the lee of forest patches: A large-eddy simulation study . . . . .	81
3.3.1	Declaration of my contribution . . . . .	81
3.3.2	Submitted article . . . . .	81
<b>4</b>	<b>Summary and outlook</b>	<b>103</b>
	<b>Acknowledgements</b>	<b>109</b>
	<b>Bibliography</b>	<b>110</b>
	<b>Curriculum Vitae</b>	<b>116</b>

# 1 Introduction

Forests play an important role for Earth’s weather and climate on global to local scales, such as by affecting energy and water balances at the Earth’s surface or by being a major contributor to the global CO<sub>2</sub> cycle. For instance, the world’s forests cover 30% of the land surface (FAO, 2010) and store approximately 50% of terrestrial biosphere carbon (e.g. Falkowski et al., 2000), while they absorb almost 30% of the annual anthropogenic CO<sub>2</sub> emissions (Pan et al., 2011), making forests a major controlling factor for the climate-relevant greenhouse gas CO<sub>2</sub>. On the local scale, forests affect local weather phenomena in complex ways by steering the turbulent exchange of momentum, energy and mass between the Earth’s surface and the overlying atmospheric boundary layer (ABL). In weather prediction and climate models with a typical numerical grid spacing of order  $\mathcal{O}(1 - 100 \text{ km})$ , the turbulent transport of momentum and scalars (e.g. temperature, humidity, CO<sub>2</sub>) between soil, vegetation and atmosphere is not explicitly resolved, and hence must be parametrized. This is commonly achieved by applying soil-vegetation-atmosphere-transfer (SVAT) models at the lower boundary of numerical weather and climate models. SVAT models account for physical and chemical processes within the soil and vegetation layers, and they provide soil and vegetation-type dependent fluxes, representative for the respective land-surface types present within a numerical grid box of the weather or climate model. This approach comprises the assumption that the soil-vegetation-atmosphere exchange on a land-surface patch of certain type is horizontally homogeneous.

With the growing patchiness of the land-surface texture, mainly owing to land-use, most landscapes are characterized by a heterogeneous distribution of different surface types, where forests are more and more fragmented into confined patches. Each surface patch has specific mechanical, thermal and hydrological surface properties, which might abruptly change from one surface patch to the other, especially pronounced at surface discontinuities between forested and unforested patches. The discontinuities in the land-surface texture induce an ongoing adjustment process, where the mean flow crossing the discontinuity, as well as the turbulent processes, constantly have to adjust to the changing surface conditions. Thereby, internal boundary layers (IBL) typically develop above the new surface patch downstream of the discontinuity, wherein the turbulent fluxes of momentum and scalars can be spatially highly variable due to the adjustment process, even if the surface patch actually has horizontally homogeneous properties. This implies that surface-type specific SVAT-model profiles are not necessarily representative to describe turbulent fluxes in landscapes with frequent surface discontinuities, and as supposed, particularly in fragmented forested landscapes. As the patchiness of forests with its entire impact on forest-atmosphere exchange is to-date scarcely understood (Belcher et al., 2012), this impact is not accounted for in today’s weather prediction and climate models.

In order to improve this understanding, micrometeorologists nowadays explicitly perform flux measurements in the vicinity of abrupt surface transitions like forest edges, as for example within the recent “Exchange processes in mountainous Regions” campaign (EGER; Foken et al., 2012), where single-point and area-averaged micrometeorological measurements were performed near a clearing-forest transition. However, different issues affect the quality of these measurements, such as the energy imbalance problem (summarized in detail by Foken, 2008) or the uncertainties in the determination of the field-of-view (footprint; for details see Leclerc and Foken, 2014) of the measurement. Besides these issues, the high spatial

variability of the measured quantities across abrupt surface transitions adds a yet undefined complexity to interpreting the spatial representativity of in-situ measurements. Therefore it is crucial to understand and quantify the potential of forest edges in affecting the local forest-atmosphere exchange, starting at the basics. For this purpose, suitable tools have to be applied that are able to provide a three-dimensional view of turbulent flows in such disturbed ecosystems, for various kinds of meteorological and land-surface conditions. In the past decades, large-eddy simulation (LES) models have been exposed to be a promising tool to fulfil these tasks, and hence, to contribute to a systematic fundamental research. The major goal of this PhD project is to contribute by means of LES to a basic knowledge about turbulent transport processes near forest edges and the implications for a better planning and interpretation of micrometeorological measurements in such flow regimes. Therefore, high-resolution LES of the flow across windward and leeward forest edges are performed under various meteorological and plant-physical conditions, while thoroughly analyzing the physical mechanisms and the overall behaviour of the transport of scalars in forest-edge flows.

Section 1.1 contains a general overview of the structure of boundary layers over short- or non-vegetated surfaces, while Sect. 1.2 describes modifications of this structure due to the presence of tall vegetation canopies such as forests. Further, an overview of numerical modelling techniques for the simulation of atmospheric flows is given in Sect. 1.3. The current state of research in the field of canopy flow, as well as of scalar transport in such flows is given in Sect. 1.4. The scope of this thesis, as well as the underlying research questions are presented in Sect. 1.5.

## 1.1 Properties of boundary layers above short- or non-vegetated surfaces

In the present thesis, canopy flows are simulated within atmospheric boundary layers, as well as within atmospheric-scale laboratory boundary layers. Hence, the main features of both boundary layer types will be described in the following Sects. 1.1.1 and 1.1.2.

### 1.1.1 Atmospheric boundary layers

The atmospheric boundary layer takes direct notice of the land surface, namely because the ABL flow is affected by the exchange of momentum, energy and mass between the Earth's surface and the overlying atmosphere. In the first few millimetres above the surface, in the viscous sublayer, the mean horizontal wind speed is zero, and molecular diffusion is the dominant transport mechanism. Further above in the surface layer, with a depth of order  $\mathcal{O}(10^1 - 10^2 \text{ m})$ , the horizontal wind increases logarithmically with height. Molecular diffusion becomes negligible, and the vertical transport of momentum, energy and mass is taken over by turbulent eddies of different time and length scales, which are primarily generated by wind shear and buoyancy within the surface layer. Vertical turbulent fluxes of the transported quantities within this layer are approximately constant with height. Above the surface layer, the increase of the wind speed with height becomes weaker, and the wind direction continuously turns with height due to the Coriolis force. The mean horizontal flow in this so-called Ekman layer is in equilibrium between surface frictional drag, Coriolis force and large-scale pressure-gradient force. The Ekman layer extends up to the top of the ABL, reaching heights of  $\mathcal{O}(10^2 - 10^3 \text{ m})$  as a function of e.g. thermal stratification of the ABL and the geostrophic wind. The largest turbulent eddies in ABL flows can extend across the entire ABL depth of  $\mathcal{O}(10^3 \text{ m})$ , while the smallest eddies have sizes of  $\mathcal{O}(10^{-3} \text{ m})$ . Time scales of turbulent eddies span a range of  $\mathcal{O}(10^{-3} - 10^3 \text{ s})$ , while largest eddies have the longest lifetimes. Above the ABL in the free atmosphere, the direct impact of the land

surface vanishes so that the flow is almost laminar and in geostrophic equilibrium. The ABL can appear in three main states, characterized by differences in dynamic and thermodynamic forcing, as outlined in the following.

During day-time conditions, when the solar radiation warms the land surface, the surface layer is unstably stratified. This induces turbulent convection that reaches up to the top of the ABL, causing the bulk of the ABL above the surface layer to be well-mixed. Usually, convective boundary layers (CBL) are capped by a temperature inversion, which prevents thermal plumes from penetrating deeply into the free atmosphere. Due to the well-mixed state of the CBL, the turning of the wind with height due to the Coriolis force is less pronounced. In addition to buoyancy, wind shear can likewise generate turbulence in the CBL, however, turbulence generated by wind shear is typically of smaller size than the large buoyant eddies.

Under cloudy and windy conditions with absent convection, near-neutrally stratified boundary layers can be observed. Neutrally-stratified ABL flows are purely shear-driven, so that a well-defined Ekman layer develops. Turbulence in the neutral ABL is thus purely generated by wind shear, strictly speaking, by velocity shear as well as by directional shear due to the turning of the wind direction. With wind shear being the sole turbulence source, the largest turbulent eddies in the neutrally-stratified ABL are typically much smaller than the largest eddies in the CBL.

During night-time conditions, the radiative cooling of the land surface creates a stable thermal stratification between the cold surface and the relatively warm air above. In stably-stratified boundary layers, turbulence is purely generated by wind shear, while at the same time, this small-scale turbulence is strongly damped due to the thermal stability of the boundary layer. Hence, turbulent transports are rather weak to non-existent.

In the present study, NBL and CBL flows are treated.

### 1.1.2 Laboratory boundary layers

While ABL flows are dynamically driven by an equilibrium between pressure-gradient, Coriolis and surface-frictional forces, flows in laboratory boundary layers as in wind tunnels are purely in equilibrium between pressure-gradient and frictional forces, since the contribution of the Coriolis force cannot adequately be represented in the laboratory. A further technical limitation of most wind-tunnel set-ups is the inability to model thermally stratified flows, hence, wind-tunnel experiments usually treat neutral boundary layers.

The differences in dynamical forcing, as compared to an ABL flow, result in somewhat modified vertical profiles of the horizontal mean wind. Without the contribution of the Coriolis force, a constant wind direction is maintained over the entire laboratory boundary layer, as opposed to the turning of the wind with height in the Ekman layer. Due to the height-constant wind direction in the laboratory, turbulence is solely generated by velocity shear, and not additionally by directional shear as in the ABL. Owing to the absent directional shear in the laboratory, vertical gradients of the horizontal wind are slightly larger than in the typical Ekman layer. Nevertheless, the mean wind profile in the laboratory surface-layer can be fine-tuned to match the logarithmic form of an ABL surface-layer wind profile.

The advantage of such set-ups with a height-constant wind direction, e.g. in numerical simulations of idealized forest-edge flows as performed in the present study, is the straightforward accomplishment of systematic studies of scalar transport processes under different plant physical and flow conditions, while maintaining a constantly perpendicular flow across the forest edge. Further, such set-ups are favourable for the direct comparison of LES and wind-tunnel data under controlled boundary- and environmental conditions.



## 1.2 Modification of surface-layer flows under the presence of tall vegetation

Before it will be discussed how tall vegetation modifies surface-layer flow, it is briefly discussed how surface-layer flows can be described by basic surface-layer theory, in order to emphasize the modifications induced by tall vegetation. In a surface layer with short or absent vegetation, the horizontal mean wind is assumed to increase logarithmically with height, starting with zero wind speed near the surface, as illustrated on the left-hand side of Fig. 1.1 by the orange curve above the grass. Due to the roughness of the surface, the zero-level of the wind speed extends from the surface up to the roughness height  $z_0$ , hence, the logarithmic wind profile originates at  $z_0$ . Commonly,  $z_0$  for vegetation is estimated as being 10% of the vegetation height  $H$  (Monteith, 1973). The logarithmic wind profile involves the assumption that the turbulent vertical momentum flux  $WU$  (orange line) is nearly constant with height within the surface layer, according to Monin-Obukhov similarity theory (MOST; Monin and Obukhov, 1954).

In weather or climate models it is commonly assumed that MOST is also valid under the presence of tall vegetation. By applying MOST for tall vegetation it is assumed that the vegetated layer is highly viscous, resulting in a vanishing mean flow within the vegetation canopy. Thus, the land surface is virtually displaced upward up to the displacement height  $z_d \approx 2/3H$  (Monteith, 1973), so that the characteristic surface-layer profiles originate at  $z_d + z_0$ , while assuming that the general form of the profiles is maintained, as illustrated by the orange curve on the right-hand side of Fig. 1.1.

However, simply displacing the surface-layer profiles does not appropriately describe the flow across tall vegetation, implying uncertainties for weather and climate models regarding the representation of turbulent exchange processes within and above tall vegetation such as forests. A forest acts as a permeable viscous layer that removes momentum from the flow due to pressure and viscous drag forces, leading to flow deceleration rather than a complete disappearance of the mean flow. The strength of the deceleration thereby depends on forest morphology, such as the vertical distribution and local amounts of biomass, i.e. the vertical profile of leaf or plant area per unit volume. Owing to these drag forces, the surface-layer profiles are markedly modified by the canopy, illustrated on the right-hand side of Fig. 1.1 by the black curves of  $U$  and  $WU$ , as observed above forested surfaces. For the most part, the canopy-modified  $U$ -profile (black curve) remarkably deviates from the logarithmic form of a typical surface-layer profile (orange curve). Descending towards the forest top, the vertical gradient of  $U$  in the canopy profile is smaller than in the logarithmic profile. Further, instead of reaching zero wind-speed at  $z = z_d + z_0$ , the canopy-modified  $U$ -profile is inflected near the forest top, accompanied by strong wind shear in this region. The further behaviour of  $U$  within the forest strongly depends on the vertical distribution of the plant biomass. With a homogeneous vertical biomass distribution, the decrease of  $U$  towards the forest floor is close to exponential, same as the decrease of the absolute value of  $WU$  towards zero at the forest floor. In contrast, in forests with dense crown layer and sparse trunk space, a secondary wind maximum might occur in the trunk layer (dashed black curve), termed as sub-canopy jet. This jet causes a reversal of  $WU$  (dashed black curve) so that the flux of momentum is directed from the trunk towards the crown layer, as reviewed for the first time by Shaw (1977), leading to a decoupling of the trunk-layer flow from the crown-layer flow.

The modified surface layer above forested surfaces can be subdivided into three characteristic layers: the canopy sublayer (CSL) spans the forest layer up to the forest top at  $z = H$ ; the roughness sublayer (RSL), where the wind profile strongly deviates from a logarithmic form, extends from the forest top roughly up to  $z \approx 3H$ ; the inertial sublayer (ISL) follows above  $z \approx 3H$ , where the flow is not directly affected by the presence of the tall vegetation,

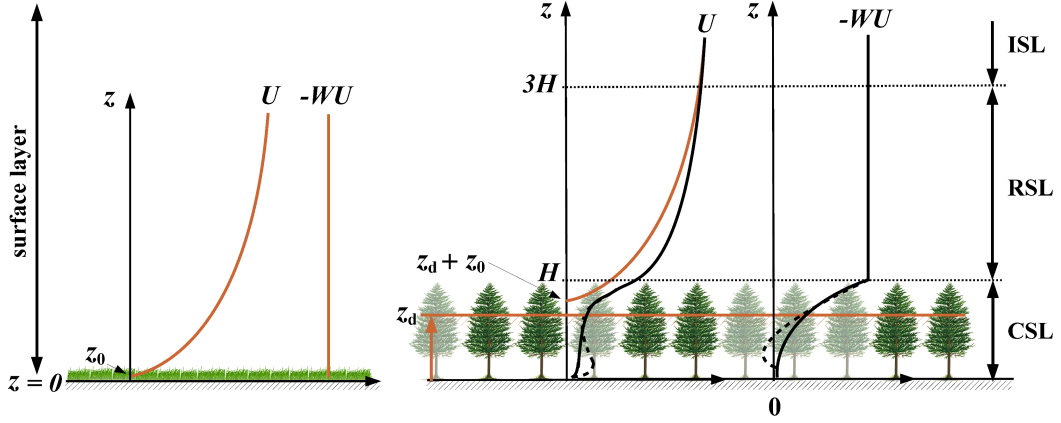


**Figure 1.1:** Vertical profiles of horizontal mean wind  $U$  and vertical momentum flux  $WU$  above short- (left) and tall-vegetated (right) surfaces. The difference between vertically displaced surface-layer profiles and the actual profiles within and above tall vegetation (e.g. forest) shall be highlighted. Orange curves illustrate profiles according to MOST, and black curves visualize the de facto canopy-modified profiles. Solid black curves exemplify profiles for vertically homogeneous forests, while dashed black curves illustrate profiles for forests with open trunk space.  $z_0$  and  $z_d$  are roughness length and displacement height, respectively. The different layers above tall-vegetated surface are separated into the canopy sublayer (CSL), roughness sublayer (RSL) and inertial sublayer (ISL).

and hence, the logarithmic profile according to MOST is retained.

To summarize, the form of the profiles of mean wind and momentum flux on forested surfaces cannot purely be explained by surface-layer theory. Instead, flows above forest canopies show similarities with mixing-layer flows, first formulated by Raupach et al. (1996) as the mixing-layer analogy, which will be explained in the following. The inflected wind profile near the forest top is similar to the wind profile that develops at the horizontal interface between two coflowing streams of different velocities, a typical mixing-layer flow as illustrated by Raupach et al. (1996), c.f. their Fig. 6. The strong wind shear at the interface between the two streams induces inflection-point (Kelvin-Helmholtz) instabilities, leading to the development of mixing-layer vortices with certain length and time scales. The fact that mixing-layer vortices appear rather periodically in space and time distinguishes these vortices from random turbulence, and it introduces a certain coherence to mixing-layer turbulence (Holmes et al., 1996). Thus, mixing-layer vortices are considered to be coherent turbulence structures (CTS) that are highly intermittent.

Above tall-vegetation canopies like forests, mechanisms for the CTS development are quite similar to those in mixing-layer flow. The CTS were found to undergo a stepwise development process, as reviewed in detail by Finnigan (2000), c.f. his Fig. 12, and further by Dupont and Brunet (2009), c.f. their Fig. 1: (1) Initially, Kelvin-Helmholtz waves form at the height where the  $U$ -profile is inflected, triggered or intensified by the appearance of sudden wind gusts; (2) wave-breaking creates transverse rollers; (3) secondary instabilities within the rollers lead to a deformation of the roll-like structures, introducing longitudinal and vertical components to the structures; (4) finally, the deformed rollers transform into complex three-dimensional turbulent structures. This development process takes place within the roughness sublayer, and the developing CTS can be characterized by length scales  $L_s$  and  $\Lambda$ , describing the typical size of the CTS and the streamwise spacing between two neighbouring CTS,

respectively (Raupach et al., 1996):

$$L_s = \frac{U(z=H)}{(\partial U / \partial z)_{z=H}}, \quad (1.1)$$

and

$$\Lambda = m \cdot L_s, \quad (1.2)$$

with  $m = 8.1$  as determined by Raupach et al. (1996) for neutral stratification. Details on the derivation of  $L_s$ ,  $\Lambda$  and  $m$  in canopy flows are given by Raupach et al. (1996). Fully developed CTS scale with  $H$  (e.g. Shaw et al., 1995; Huang et al., 2009), and they can contribute significantly to the vertical turbulent transport of momentum and scalars (e.g. Bergström and Högström, 1989; Gao et al., 1989; Thomas and Foken, 2007).

Summarized, the forest-atmosphere exchange of momentum and scalars can be rather complex, depending e.g. on forest morphology or thermal stratification. The different layers of the forest (or a similar vegetation type) can be decoupled from each other as well as from the overlying atmosphere. For example during daytime, when the solar radiation mainly warms the dense crown layer, a stable stratification develops between the trunk space and the crown layer, while the thermal stratification above the forest top is unstable. The thermal stability within the forest suppresses any kind of turbulent exchange so that the trunk layer can be fully uncoupled from the atmosphere above the forest. However, with the intermittent occurrence of CTS, the different layers can be temporarily coupled, creating turbulent fluxes that are directed against the local vertical gradient of the transported quantity (counter-gradient fluxes; see e.g. Foken, 2006). This complex behaviour of the fluxes highlights once more that surface-layer theory is not applicable in a surface layer covered with tall permeable vegetation. A detailed review of the complexity of forest-atmosphere coupling is given by Thomas and Foken (2007).

Up to this point it was assumed that the vegetation covers the surface quasi-infinitely. In the following, it shall be discussed how a turbulent flow that first streams over an unforested surface (hereafter termed as clearing) reacts to an abrupt change of the surface properties when approaching towards a perpendicularly-oriented clearing-to-forest transition (hereafter termed as windward forest edge). The mean approaching flow is decelerated in front of and entering the forest, owing to dynamic pressure build-up in front of the forest and the aerodynamic drag of the plant elements, respectively, while the flow above the forest is even accelerated for reasons of continuity. At the same time, the mean flow near the windward forest edge is partly deflected upward as a result of the deceleration of the edge-perpendicular mean flow. Further, turbulence is strongly damped when entering the forest, due to pressure and viscous drag forces caused by the trees. The large difference in edge-perpendicular wind speed between the forest interior and the overlying atmosphere creates an inflected wind profile with pronounced shear near the forest top. This and the strong disturbance of the flow at the windward edge induces the stepwise development of the CTS (see above), starting with wave formations at the windward edge. With increasing distance to the windward edge, the CTS subsequently undergo their development stages towards three-dimensional turbulent structures, while continuously growing in size and strength throughout this process (see e.g. Dupont and Brunet, 2009, c.f. Fig. 1), until the flow has adjusted to the abrupt change of the surface roughness. This developing layer of high turbulence intensity forms an internal boundary layer (IBL) above the forest, wherein the flow gradually adjusts to the new surface conditions. The phenomenon of IBLs occurs wherever horizontal flows come across discontinuities in some property of the surface (e.g. roughness, temperature, humidity), as reviewed by Garratt (1990).

At transitions from forest-to-clearing (hereafter termed as leeward forest edge), the flow once more undergoes an adjustment process. During this adjustment, velocity and momentum-

flux profiles adjust back to their surface-layer form, e.g. the horizontal wind speed retains its logarithmic profile. Flows in the lee of forest edges show similarities of backward-facing-step (BFS) flows in the lee of impermeable surface steps like buildings or cliffs, such as flow separation, reattachment and rotor-like circulations (e.g. Chan et al., 2002; Fontan et al., 2013; Markfort et al., 2014). As the flow descends in the lee of the forest, it reattaches back to the clearing surface after a few  $H$  downstream of the leeward edge. As a result, rotor-like recirculations might form in the immediate lee of the forest, owing to pressure redistribution, similar as observed in BFS flows. However, the forest-lee flow cannot purely be described as a BFS flow, since due to the permeability of the forest one part of the flow in the lee originates from the forest interior, denoted as exit flow. Cassiani et al. (2008) found that recirculation and exit-flow passages alternate and occur intermittently in time and along the leeward edge, and further, that the relative occurrence of recirculation events increases with increasing forest density.

Overall, forest edges strongly disturb the mean flow across the edge, as well as the turbulence, indicating a great impact on the forest-atmosphere exchange of momentum and scalars.

### 1.3 Numerical simulation of atmospheric flows

As mentioned in Sect. 1.1, turbulence in atmospheric flows covers a wide range of spatial and temporal scales, which are not resolved in weather prediction or climate models. On the one hand this is due the coarse grid sizes of  $\mathcal{O}(1 - 100 \text{ km})$ , while on the other hand it is owed to the formulation of these models, being based on the Reynolds-averaged Navier-Stokes (RANS) equations. With this technique, all scales of turbulence are filtered from the equations by ensemble-averaging the prognosticated meteorological quantities, so that the entire turbulence spectrum must be parametrized. This applies without exception, even if RANS is applied in studies of local flow phenomena at relatively small grid sizes of  $\mathcal{O}(1 \text{ m})$ , as e.g. applied in canopy flow studies. What remains as an output of RANS models are fields of the resolved mean flow and its scalar constituents, as well as the fully parametrized turbulence statistics. The RANS approach makes flow modelling relatively cost efficient in terms of computational resources. However, the quality of the turbulence statistics totally relies on the applied turbulence parametrizations, which are based on numerous assumptions such as horizontal homogeneity of the flow and isotropy of turbulence. But especially under heterogeneous flow conditions as in flows across forest edges these assumptions are violated, since neither the mean flow is horizontally homogeneous, nor all scales of turbulence are isotropic and might even be strongly intermittent such as CTS, questioning the applicability of RANS for explicitly studying turbulent processes within these flow types.

In order to be entirely independent of the quality of turbulence parametrizations when studying turbulent flows and its scalar constituents, all spatial scales of turbulence must be explicitly resolved, which is known as direct numerical simulation (DNS). The DNS of the entire spectrum of turbulence elements requires the model domain to be sufficiently large for enabling the development of the largest eddies of size  $10^3 \text{ m}$ , and it requires the numerical grid size to be sufficiently small for capturing even the smallest eddies of size  $10^{-3} \text{ m}$  described by the Kolmogorov dissipation length. This means that the DNS of the turbulent flow in a  $1 \text{ km}^3$  domain with a grid-box volume of  $1 \text{ mm}^3$  would require  $10^{18}$  grid points (see e.g. Breuer, 2002). Simulations with such tremendous amounts of grid points are yet unfeasible on state-of-art supercomputers, which are currently equipped for the calculation of up to  $10^{11}$  grid points. Hence, the DNS of atmospheric-scale turbulent flows are to-date not possible.

Consequently, the number of required grid points has to be effectively reduced, whilst maintaining the general framework of the simulation, which is where LES models come into

play. The concept of LES is to explicitly resolve the bulk of the turbulence spectrum containing the bulk of the turbulent kinetic energy (TKE) of the flow, while the smallest eddies contributing marginally to the TKE are parametrized. The cut-off length for separating the smallest eddies from the resolved-scale flow must lie within the inertial subrange of the energy spectrum. This length often corresponds to or is in the range of the numerical grid size. By this means, only the unresolved subgrid scales (SGS) of turbulence must be parametrized, given the assumption that SGS eddies are isotropic and contribute the least to the total turbulent kinetic energy (TKE) of the flow. Consequently, if the LES grid is fine enough, the model results are almost independent on the type of turbulence parametrization. With the currently available computing power, LES models can simulate atmospheric flows with grid sizes down to  $\mathcal{O}(1\text{ m})$ , which is a necessary grid resolution for the explicit simulation of the coherent non-isotropic turbulence typically appearing in canopy flows (see Sect. 2.3).

## 1.4 Current state of research

### 1.4.1 Steps towards understanding the dynamics of forest-edge flows

Our current understanding of the dynamical properties of flows across vegetation canopies is a product of decades of works, roughly since the 1960s, in field campaigns, laboratory studies and numerical simulations. The first overall picture of homogeneous canopy flow was given by Raupach et al. (1996) as the well-known “family portrait” of canopy turbulence, presenting vertical profiles of the mean horizontal flow and a number of turbulence-statistical quantities within and above different vegetation canopies. Several datasets from field and wind-tunnel experiments build the basis for this “family portrait” (see Raupach et al., 1996), measured mostly under (near-) neutral conditions above horizontally quasi-homogeneous vegetation cover of various types (different crops and forests). Further, large efforts have been addressed since the 1970s to build a firm theory of the nature of canopy turbulence. As summarized in detail by Finnigan (2000), we are now able to picture the mechanisms for the CTS development, their characteristic length and time scales, and the way they are dissipated within the canopy while interacting with the foliage. This was achieved by means of different statistical-analysis approaches, e.g. by two-point space-time correlation (applied e.g. by Amiro, 1990; Shaw et al., 1995) and by conditional sampling such as the quadrant-hole technique (applied e.g. by Shaw et al., 1983; Gardiner, 1994) or the more objective empirical orthogonal function analysis (applied e.g. by Finnigan and Shaw, 2000).

Up to that point, most analysis was based on data of horizontally homogeneous canopy flows. In the past decades, attention has moved to more complex canopy flows, specifically addressing the behaviour of turbulent flows across forest edges in fragmented forested landscapes. As mentioned in Sect. 1.2, flows are markedly disturbed when crossing clearing-to-forest or forest-to-clearing transitions. In order to capture the disturbance and the adjustment of the mean flow as well as of the turbulent fluxes of momentum and scalars near forest edges, single-point tower measurements have been performed in the edge regions upstream and downstream of the transitions (e.g. Kruijt et al., 1995; Irvine et al., 1997; Zhu et al., 2004; Thomas and Foken, 2007; Foken et al., 2012; Queck et al., 2014). However, from the technical point-of-view it is difficult to draw a complete picture of the adjustment process based on single-point measurements, since they are way too cost intensive in terms of material and man-power as to build sufficiently large clusters of measurements for capturing the spatial variability of the measured quantities. A further downside of field measurements, even though they are the only way to represent the “real world”, is that they have to deal with issues like the energy-imbalance problem (e.g. Foken, 2008), uncertainties in the footprint determination (e.g. Leclerc and Foken, 2014), and most essentially with the fact that an atmospheric flow is hardly ever stationary. These issues, plus the spatial variability of the

measured quantities near forest edges, highly complicates the interpretation of single-point measurements.

One opportunity to capture a multi-dimensional picture of the turbulent wind field above the forest is to perform wind-tunnel experiments of flows across model forests (e.g. Ruck and Adams, 1991; Marshall et al., 2002; Morse et al., 2002), at relatively lower costs as compared to a set of tower measurements. For the measurement and visualization of the flow, mostly optical measuring systems are employed, e.g. particle image velocimetry or laser doppler anemometry, in order not to disturb the flow. However, both techniques require a free field-of-vision on the area to-be-scanned, restricting the acquisition of flow data within the model forest. Further constraints of wind-tunnel experiments are the general inability of representing certain features of atmospheric flows, such as the Ekman spiral and the thermal stratification of the ABL (see Sect. 1.1.1).

Numerical simulation techniques like RANS and LES have the distinct advantage of being able to simulate these ABL features, as well as to capture not only the above-canopy flow but also the flow field within the vegetation layer (Yang et al., 2006a,b; Cassiani et al., 2008; Sogachev et al., 2008; Bohrer et al., 2009; Schrötte and Dörnbrack, 2013). Further, numerical tools enable comprehensive and systematic studies on how meteorological and plant-physical parameters affect the canopy flow. However, numerical modelling of canopy flows with RANS is somehow constraining since RANS models only provide fully parametrized turbulence statistics assuming isotropy of turbulence, which is not fulfilled for canopy turbulence; whereas, LES models explicitly resolve most scales of turbulence elements (see Sect. 1.3), which is a necessary prerequisite to study turbulent transport processes in canopy flows. With the currently available computing power, LES models can be operated at spatial grid sizes down to  $\mathcal{O}(1\text{ m})$ , enabling the explicit simulation of turbulence down to the scales of canopy turbulence. Despite the small grid sizes, it is still not feasible to simulate a vegetation layer with all its individual plant elements. Hence, since the pioneering work of Shaw and Schumann (1992), vegetation layers are modelled as a porous viscous medium that removes momentum from the flow by means of pressure and viscous drag forces, parametrized as a volume drag force, depending e.g. on the volumetric density of the foliage, the aerodynamic drag and the local wind speed. Thereby it is assumed that turbulence entering the vegetation canopy is rapidly broken down to smaller scales due to pressure and viscous drag of branches and foliage, while these small scales are then again rapidly dissipated (e.g. Shaw and Schumann, 1992; Edburg et al., 2012). This process is termed as the “spectral shortcut” (Shaw and Seginer, 1985; Shaw and Patton, 2003). The volume-drag approach after Shaw and Schumann (1992) has been successfully applied over decades of numerical canopy-flow research (e.g. Kanda and Hino, 1994; Su et al., 1998; Watanabe, 2004; Yang et al., 2006a; Cassiani et al., 2008; Dupont and Brunet, 2009), and despite the constantly improved understanding of canopy flow, this approach is to-date applied in its original form. Recently, this approach was applied in LES of a complex heterogeneous forest site in the Tharandter Wald (Germany Schlegel et al., 2015), based on three-dimensional forest inventory data from terrestrial laser scanning (Schlegel et al., 2012), and compared to on-site tower measurements (Queck et al., 2014). These studies revealed complex flow structures induced by small to midsize forest gaps and local differences in forest density.

Of course, numerical models cannot accurately represent reality, so their ability for simulating a certain flow phenomenon should be tested, favourably against field or wind-tunnel data. Recently, Träumner et al. (2012) have applied Doppler lidar (LIght Detection And Ranging) as a promising tool to capture the three-dimensional wind field above forest edges. Patton et al. (2011) have previously implemented Doppler lidar for CTS detection above an orchard within the CHATS (Canopy Horizontal Array Turbulence Study) experiment. With these possibilities, the lidar technique represents a state-of-the-art method to effectively com-

plement in-situ tower measurements near forest edges, as well as to serve as a data base for the validation of wind-tunnel and numerical studies. However, it should be noted that the application of lidars in forest-edge flows is still in its infancy, hence, appropriate measuring strategies (scan patterns, spatial and temporal resolution) need to be developed and tested in order to collect statistically reliable data of flow phenomena such as CTS. Hence, for the examination of different lidar measuring strategies, LES can in turn be a useful tool. This has been recently demonstrated by Stawiarski et al. (2013), who employed high-resolution LES flow data to investigate how e.g. the limited spatial resolution and the inherent averaging of the lidar, or the limited temporal resolution due to the nature of the scan patterns affect the quality of the lidar measurement. It should be noted that some parts of this section have been adopted in one form or another from article A.

### 1.4.2 Scalar transport in fragmented forested landscapes

Contrary to our quite extensive knowledge of the dynamics of canopy flows, our current understanding of the transport of scalars in forest-edge flows is rather rudimentary (e.g. Belcher et al., 2012). Although it is well known that forest edges markedly disturb the flow field, it is unclear to what extent this disturbance affects the spatial behaviour of scalar concentration and its turbulent flux in the vicinity of forest edges. Only few studies have so far examined scalar transport in forest-edge flows, but their main findings already indicate a certain complexity of the transport processes. Overall, more attention has been paid so far to the scalar transport near windward forest edges, as presented in the following and adopted in some parts from article B.

Based on a field experiment downstream of a moorland-to-forest transition in flat terrain, Klaassen et al. (2002) analyzed the streamwise behaviour of the fluxes of sensible and latent heat above the forest patch, by means of tower measurements above the forest. Klaassen et al. (2002) found that both, sensible and latent heat flux strongly varied above the forest with distance to the windward forest edge. Further, the above-canopy fluxes were locally enhanced at some distance from the edge as compared to further downstream of the forest edge. They argued that the advection of relatively warm and humid air from the moorland into the forest caused the local flux enhancement at distances of up to  $15H$  from the forest edge, with  $H$  being the mean tree height. Klaassen et al. (2002) further determined that the sum of the locally enhanced sensible and latent heat fluxes above the forest overshoot the available energy (sum of net radiation and soil heat flux) on average by 16% of the net radiation.

In a RANS study based on the Klaassen et al. (2002) experiment, Klaassen and Sogachev (2006) further concluded that the magnitude of this overshoot depends on forest density. A larger relative overshoot was found in the simulations with denser forests, whereby the flux enhancement was confined to smaller regions, indicating that the heat fluxes adjust more rapidly above denser forests.

With these findings in mind, Sogachev et al. (2008) studied the transport of  $\text{CO}_2$  in a neutrally-stratified idealized forest-edge flow by means of RANS modelling. They demonstrated that if the  $\text{CO}_2$  sources are located at the surface,  $\text{CO}_2$  fluxes at the canopy top showed a stationary wave-like pattern, which remarkably overshoot/undershot the given near-surface  $\text{CO}_2$  flux, in regions up to  $40H$  from the windward forest edge. The amplitude of the wave-like flux pattern was identified to depend on the overall density of the forest as well as on the vertical distribution of trunks and foliage. Following Klaassen et al. (2002), Sogachev et al. (2008) attributed the streamwise variability of the canopy-top  $\text{CO}_2$  flux to the mean advection of  $\text{CO}_2$  from the clearing into the forest, where a localized  $\text{CO}_2$  accumulation could be observed. They found this advection to be more pronounced in forests where most of the foliage was located in the crown layer. With such forest architectures, a flow can penetrate

more deeply into the relatively sparse trunk layer than in an equally dense but vertically homogeneous forest, forming a so-called sub-canopy jet, as discussed in Sect. 1.2 by means of Fig. 1.1. Sogachev et al. (2008) stated that this jet promotes the streamwise advection of scalar deep into the forest.

However, as RANS is based on fully parametrized turbulence under the assumption of isotropy, it cannot appropriately represent the nature of CTS, which are known to contribute significantly to the forest-atmosphere exchange of momentum and scalars. Hence, despite the findings of Sogachev et al. (2008), it is yet in question to what extent turbulent transport mechanisms contribute to the local scalar accumulation. Here, turbulence-resolving models like LES can provide additional insight concerning this matter.

Even less attention has been addressed to scalar transport in the lee of forests. However, scalar transport has been previously investigated in the lee of hills and surface steps, where flow features are known to be similar to those in the lee of forests, hence, the followingly noted findings of hill and step flows might be transferable to forests. Previous wind-tunnel (e.g. Poggi and Katul, 2007), RANS (e.g. Katul et al., 2006) and LES (e.g. Ross, 2011) studies of the flow across idealized hills demonstrated that scalars accumulate in the lee of the hill, due to the presence of lee-rotor circulations, leading to locally enhanced scalar fluxes. Also in the lee of solid surface steps, local scalar accumulation as a result of lee-rotor formation has been previously reported, detected by means of numerical simulations (e.g. Chan et al., 2002) and flume experiments (e.g. Fontan et al., 2013). As mentioned in Sect. 1.2, similar lee rotors appear in the lee of forests (Bergen, 1975; Cassiani et al., 2008; Detto et al., 2008; Queck et al., 2014), supposing that locally enhanced scalar concentrations and fluxes might also be found near leeward forest edges. The scalar transport in the lee of forests might even be more complex than in the lee of a solid obstacle, since owing to the porosity of the forest, rotor events are strongly intermittent and alternate with exit-flow events, as described in Sect. 1.2. So far only few studies have focused on the flow exiting a forest patch and reattaching to the clearing surface (Cassiani et al., 2008; Detto et al., 2008; Markfort et al., 2014), and even less attention was paid to the scalar transport in such flow regimes.

To summarize, the general knowledge of the complex scalar transport in fragmented forested landscapes is still lacking certain detail, which is albeit a necessary prerequisite for an optimum planning and interpretation of in-situ measurements in such landscapes.

## 1.5 Scope of this thesis

As mentioned in the previous sections, the transport of scalars in flows across forest edges can be highly complex, so that the spatial distribution of scalar concentration and its flux above one and the same surface patch is far from being horizontally homogeneous, whereby horizontal homogeneity is an essential assumption for flux parametrizations in weather and climate models. The entire complexity of the scalar transport and its implications for the spatial representativity of in-situ micrometeorological measurements near forest edges is to-date not sufficiently understood. This condition builds the motivation for the framework of this thesis, wherein by means of LES the disturbance of scalar transport mechanisms at windward and leeward forest edges was studied for the first time in a comprehensive manner, starting at the basics.

Before the scalar transport near forest edges is treated, the overall functionality of the applied LES model with its embedded canopy model for representing canopy flows was verified against field and wind-tunnel data. At first, a case of canopy flow across an infinite horizontally homogeneous forest was simulated, and compared against corresponding canopy-flow profiles derived from tower measurements above different crops and forests, as well as from wind-tunnel experiments (Sect. 2.3). Secondly, in addition to this general validation



of the applied LES model, forest-edge-flow LES were performed and compared to field and wind-tunnel data. This verification profited from the first-time possibility to compare the simulated key features of forest-edge flow downstream of a windward forest edge to multi-dimensional flow data of a lidar field-experiment representing the “real world”, in addition to a corresponding wind-tunnel dataset. This data basis enabled a diverse intercomparison between LES, wind tunnel and “real world”, focusing on three main aspects as discussed in **article A**:

- Are LES models capable of appropriately simulating the key features of disturbed flows above forests downstream of windward forest edges, such as the IBL development?
- To what extent do the key features of the IBL flow downstream of a windward forest edge depend on plant-physical and meteorological conditions, and which implications arise thereof for the comparability of model and field data?
- What are the requirements for capturing statistically reliable flow fields above forest edges in the “real world”, where meteorological conditions are hardly ever stationary?

To answer these questions, systematic parameter studies with different flow forcing, thermal stratification and forest morphology were performed by means of LES, with the purpose of quantifying which parameters cause the most significant modifications of the IBL properties. To assure for comparability of the LES results to the field and wind-tunnel results, ABL flows as well as atmospheric-scale open-channel flows were simulated.

After the validation of the applied LES model for canopy flows, the research proceeded to the next step, namely towards analyzing scalar transport in forest-edge flows, separated into two parts: the windward forest-edge region (**article B**), and the leeward forest-edge region (**article C**). In both parts, the main goal was to examine the reasons and the behaviour of the previously reported local enhancement of scalar concentration and its flux downstream of a forest edge, with the superior goal of enabling a better interpretation and an optimized set-up of in-situ micrometeorological measurements near forest edges. The specific research questions in both parts (**articles B** and **C**) were:

- Which physical mechanisms are responsible for the local enhancement of scalar concentrations and the related turbulent fluxes?
- To what extent is the occurrence and the relative magnitude of the concentration and flux enhancement affected by plant physical and meteorological parameters?
- Which implications arise from the local concentration and flux enhancement for the spatial representativity of micrometeorological measurements?
- How can regions of enhanced scalar concentrations and fluxes be determined in the field, in order to improve the planning and interpretation of these measurements?

In order to contribute to a basic knowledge on this yet-scarcely understood matter, an idealized LES framework was created to study the complexity of the scalar transport from the most basic point of view. Therefore, neutrally-stratified atmospheric open-channel flows across an idealized clearing-forest-clearing configuration in flat terrain were simulated, wherein passive scalar was emitted at the domain surface. This set-up was simulated for a wide range of different forest densities and wind speeds. The transport mechanisms causing the local scalar enhancement were examined by means of a term-wise analysis of the scalar balance equation.

The following part of this thesis is structured as follows: Chapter 2 contains a description of the applied LES and its embedded canopy model, as well as of the applied methods for the data preparation and analysis. In Chapt. 3, the results of this thesis are presented within the research articles A–C. Chapter 4 gives a summary of the main findings of this thesis, and an outlook of future perspectives.

## 2 Methods

For the proposed investigations of forest-edge flows and the transport of passive scalars in such flow regimes, the parallelized LES model PALM (Raasch and Schröter, 2001; Maronga et al., 2015) and its embedded plant canopy model was applied. An overview of the governing equations, the applied physical and numerical methods, as well as the employed plant canopy model is given in Sect. 2.1. The applied methods for the calculation of turbulence statistics in heterogeneous flows, as well as for the analysis of canopy flow features and the scalar-transport mechanisms, are described in Sect. 2.2. Since the embedded canopy model was applied for the first time in an extensive way, the first PALM results of homogeneous canopy flow were validated against data from field and laboratory experiments, as will be presented in Sect. 2.3.

### 2.1 Parallelized large-eddy simulation model PALM

PALM has been developed by the PALM group at the Institute of Meteorology and Climatology (IMUK) at Leibniz Universität Hannover, Germany, based on an existing LES model used at IMUK (Raasch and Etling, 1998). With PALM, atmospheric (e.g. Maronga and Raasch, 2013; Sühling et al., 2014) and oceanic flows (e.g. Noh et al., 2010) can be simulated, with implemented features such as topography (e.g. Letzel et al., 2008) or plant canopy (implemented by Dr. Gerald Steinfeld, former PALM group member). Some general aspects of the herein applied PALM version (release 3.8 revision 874<sup>1</sup>) are described in the following sections. A complete documentation of PALM (4.0) is provided by Maronga et al. (2015).

#### 2.1.1 Governing model equations

PALM was applied to simulate neutral and convective dry boundary layers, with and without Coriolis force, corresponding to ABL and atmospheric-scale open-channel flows as described in Sects. 1.1.1 and 1.1.2, respectively. The model is based on the non-hydrostatic incompressible filtered Boussinesq-approximated momentum equations, with slight modifications of their original form; further governing equations are the first law of thermodynamics, the continuity equation, and a conservation equation for a passive scalar  $S$ :

$$\frac{\partial u_i}{\partial t} = -\frac{\partial u_i u_j}{\partial x_j} - \frac{1}{\rho_0} \frac{\partial p}{\partial x_i} - \frac{1}{\rho_0} \frac{\partial p^*}{\partial x_i} + \frac{\theta - [\theta]}{[\theta]} g \delta_{i3} - \frac{\partial \overline{u_i'' u_j''}}{\partial x_j} + F_{u_i}, \quad (2.1)$$

$$\frac{\partial \theta}{\partial t} = -\frac{\partial u_j \theta}{\partial x_j} - \frac{\partial \overline{u_j'' \theta''}}{\partial x_j} + F_\theta, \quad (2.2)$$

$$\frac{\partial u_j}{\partial x_j} = 0, \quad (2.3)$$

$$\frac{\partial S}{\partial t} = -\frac{\partial u_j S}{\partial x_j} - \frac{\partial \overline{u_j'' S''}}{\partial x_j}, \quad (2.4)$$

respectively. Indices  $i, j, k \in \{1, 2, 3\}$  numerate horizontal velocity components  $u_1 = u$ ,  $u_2 = v$ , and vertical velocity component  $u_3 = w$ , as well as horizontal coordinates  $x_1 = x$ ,

<sup>1</sup>The PALM code is available under <http://palm.muk.uni-hannover.de/browser?rev=874>.

$x_2 = y$ , and vertical coordinate  $x_3 = z$ . Remaining quantities are time  $t$ , constant air density  $\rho_0 = 1 \text{ kg m}^{-3}$ , potential temperature  $\theta$  and its horizontal average  $[\theta]$ , Kronecker delta  $\delta_{ij}$ , and  $g$  is the acceleration due to gravity. Further,  $p$  is a thermodynamic pressure and  $p^*$  a kinematic pressure that results from the Boussinesq approximation and ensures incompressibility of the flow. Terms  $F_{u_i}$  in Eq. 2.1 and  $F_\theta$  in Eq. 2.2 account for mechanic and thermal effects of the plant canopy on the turbulent flow, as will be explained in Sect. 2.1.3.

As mentioned above, the model equations (2.1-2.4) are subject to an implicit filtering, i.e. each quantity is averaged over discrete grid volumes (Schumann, 1975), in order to filter out the SGS turbulence. For reasons of clarity, volume-averaged quantities are not specially labelled, except for the SGS fluxes, where an overbar marks the volume averaging and double primes describe the deviations from the volume average. The SGS fluxes will be further treated in Sect. 2.1.2. A detailed description of the filtering approach used in PALM can be found in Gryschka (2010).

Simulations of ABL and open-channel flows are characterized by different dynamical forcings, described by  $\frac{\partial p}{\partial x_i}$  (see Eq. 2.1):

$$\frac{\partial p}{\partial x_i} = \begin{cases} +\varepsilon_{ijk} f_j u_k - \varepsilon_{i3k} f_3 u_{gk}, & \text{ABL flow,} \\ \frac{\partial p}{\partial x_i}, & \text{open-channel flow,} \end{cases} \quad (2.5)$$

with the Levi-Civita tensor  $\varepsilon_{ijk}$ . For the ABL simulations, the horizontal pressure gradients  $\frac{\partial p}{\partial x_i}$  are expressed via the geostrophic wind  $u_g$  and the Coriolis parameter  $f_i = (0, 2\Omega \cos(\varphi), 2\Omega \sin(\varphi))$ , with the Earth's angular velocity  $\Omega = 2\pi/86400\text{s}$  and the geographical latitude  $\varphi$ . In the open-channel cases, where the Coriolis force is neglected ( $\Omega = 0$ ), the flow is forced by directly prescribing a pressure gradient in the desired direction. This forcing maintains a constant mean wind direction at all heights, which is an advantageous condition for the proposed idealized studies of scalar transport in forest-edge flow.

Incompressibility of the wind field is obtained by means of a Poisson equation for perturbation pressure, which is derived by a predictor-corrector method (Patrinos and Kistler, 1977) and solved by means of fast Fourier transformation (Schumann and Sweet, 1988). Details on the solution of the Poisson equation are given by Raasch and Schröter (2001).

### 2.1.2 Parametrization of subgrid scales

With the filtering of the model equations (2.1-2.4), some unknowns are introduced, namely the SGS turbulent fluxes of momentum, sensible heat and passive scalar, which need to be parametrized. For the determination of the SGS fluxes, a 1.5-order closure approach after Deardorff (1980) is applied, which was formed on the basis of Smagorinsky (1963). This approach connects the SGS flux of a quantity to resolved-scale spatial gradients of this quantity by employing  $K$ -theory:

$$\overline{u_i'' u_j''} = -K_m \left( \frac{\partial u_i}{\partial x_j} + \frac{\partial u_j}{\partial x_i} \right), \quad (2.6)$$

$$\overline{u_i'' \theta''} = -K_h \frac{\partial \theta}{\partial x_i}, \quad (2.7)$$

$$\overline{u_i'' S''} = -K_s \frac{\partial S}{\partial x_i}. \quad (2.8)$$

$K_m$ ,  $K_h$  and  $K_s$  are the SGS eddy diffusivities of momentum, heat and passive scalar, respectively. Following Deardorff (1980),  $K_m$  and  $K_h$  are parametrized as:

$$K_m = 0.1 l \sqrt{e}, \quad (2.9)$$

$$K_h = \left( 1 + \frac{2l}{\Delta} \right) K_m, \quad (2.10)$$

Further,  $K_s$  is assumed to equal  $K_h$ . The SGS mixing length  $l$ ,

$$l = \begin{cases} \min(\Delta, 1.8d) & \text{for } \frac{\partial\theta}{\partial z} \leq 0, \\ \min\left(\Delta, 1.8d, 0.76\sqrt{e}\left(\frac{g}{\theta}\frac{\partial\theta}{\partial z}\right)^{-\frac{1}{2}}\right) & \text{for } \frac{\partial\theta}{\partial z} > 0, \end{cases} \quad (2.11)$$

is an integral measure for the eddy size on the subgrid scale, depending on the characteristic numerical grid length  $\Delta = \sqrt[3]{\Delta x \Delta y \Delta z}$ , with  $\Delta x$ ,  $\Delta y$ ,  $\Delta z$  being the grid lengths in the  $x$ -,  $y$ -,  $z$ -direction, respectively. Further,  $l$  depends on the distance  $d$  to the surface, and on atmospheric stability. For the SGS-TKE  $e$ , an additional prognostic equation is solved:

$$\frac{\partial e}{\partial t} = -\frac{\partial u_j e}{\partial x_j} - \overline{u_i'' u_j''} \frac{\partial u_i}{\partial x_j} + \frac{g}{\theta} \overline{u_3'' \theta''} - \frac{\partial}{\partial x_j} \left\{ \overline{u_j'' \left( e + \frac{p''}{\rho_0} \right)} \right\} - \epsilon + F_e, \quad (2.12)$$

introducing another canopy-related tendency term  $F_e$ , which will be described in Sect. 2.1.3. The sum of the SGS fluxes of turbulent energy  $\overline{u_j'' e}$  and pressure fluctuations  $\overline{u_j'' p''}$ , as well as the SGS dissipation rate  $\epsilon$  are respectively parametrized as:

$$\overline{u_j'' \left( e + \frac{p''}{\rho_0} \right)} = -2 K_m \frac{\partial e}{\partial x_j}, \quad (2.13)$$

$$\epsilon = \left( 0.19 + 0.74 \frac{l}{\Delta} \right) \frac{e^{\frac{3}{2}}}{l}. \quad (2.14)$$

Finally, by means of  $K$ -theory and the additional prognostic equation for the SGS-TKE, the set of governing model equations (Eqs. 2.1-2.4) can be closed.

### 2.1.3 Embedded plant canopy model

The effects that a vegetation canopy exerts on a turbulent flow are modelled in PALM by an embedded canopy model (following Shaw and Schumann, 1992; Watanabe, 2004). It should be noted that PALM is not able to simulate single leafs or branches, rather, the canopy is modelled as a continuous porous medium, i.e. each grid box containing canopy is attributed a volume-averaged drag force. By exerting form (pressure) and viscous drag forces on the flow, the canopy acts as a sink for momentum, which is accounted for by the term

$$F_{u_i} = -c_d a U u_i \quad (2.15)$$

in Eq. 2.1, with the drag coefficient  $c_d$ , leaf/plant area density  $a$  (leaf/plant area per unit volume), absolute velocity  $U = (u^2 + v^2 + w^2)^{1/2}$ , and the respective velocity component  $u_i$ . This approach considers that larger-scale turbulence is rapidly broken down to smaller eddies due to the presence of the plant elements, which is known as the spectral shortcut (Shaw and Seginer, 1985; Shaw and Patton, 2003). The small eddies are then further dissipated due to the roughness of the plant elements (Shaw and Schumann, 1992; Edburg et al., 2012), which is accounted for by the additional term

$$F_e = -2 c_d a U e \quad (2.16)$$

in the prognostic equation for the SGS-TKE  $e$  (Eq. 2.12). Several LES studies exist, which have successfully modelled canopy flows by means of terms  $F_{u_i}$  (Eq. 2.15) and  $F_e$  (Eq. 2.16) to study dynamical properties of homogeneous canopy flows (e.g. Shaw and Schumann, 1992; Kanda and Hino, 1994; Su et al., 1998, 2000; Watanabe, 2004) as well as of forest-edge flows (Yang et al., 2006a,b; Cassiani et al., 2008; Dupont and Brunet, 2008, 2009).

In a heated ABL, the plant canopy might serve as a source for heat, namely when the solar radiation penetrates the forest and warms the foliage, while this in turn warms the surrounding air. Following Shaw and Schumann (1992), this process is included in the first law of thermodynamics (Eq. 2.2) by the additional term

$$F_\theta = -\frac{\partial Q_\theta}{\partial z}, \quad (2.17)$$

being the negative vertical derivative of the vertical kinematic heat flux, defined after the Beer's law relationship

$$Q_\theta(z) = Q_\theta(H) \exp(-\alpha P), \quad \text{with } P = \int_z^H a \, dz, \quad (2.18)$$

with  $Q_\theta(H)$  as the prescribed heat flux at the forest top ( $z = H$ ). Based on  $Q_\theta(H)$ , the heat flux at different heights inside the forest is calculated by this decaying exponential function of the downward cumulative leaf area index  $P$ , with an extinction coefficient  $\alpha = 0.6$ . Eq. 2.18 is derived according to the distribution of net radiation inside vegetation canopies as suggested by Brown and Covey (1966), assuming that the absorption of solar radiation by the foliage is an integral function of the penetrated foliage along the solar-radiation path. This heat flux parametrization has been applied in canopy-flow LES by Shaw and Schumann (1992) and by Bohrer et al. (2009), and the functionality of this approach was validated by Schrötte and Dörnbrack (2013) in high resolution LES with resolved tree structures.

In the present study, the passive scalar is exclusively released at the domain surface, i.e. leaf-air interactions are not considered, hence, no additional canopy-related tendency term is added to the prognostic equation for  $S$  (see Eq. 2.4).

#### 2.1.4 Spatial and temporal discretization of the model equations

In order to solve the model equations in PALM numerically, the equations have to be discretized in space and time, i.e. differentials in the model equations are approximated by finite differences.

The numerical grid in PALM is a staggered Arakawa-C grid (Arakawa and Lamb, 1977), as illustrated in Fig. 2.1. Indices  $i, j, k$  consecutively number the grid points of the numerical grid in the  $x$ -,  $y$ -,  $z$ -direction, respectively. Therein, all scalar variables  $\psi \in \{e, \theta, K_h, K_m, K_S, p, p^*, S\}$  are defined at the centre of a grid box. Velocity components  $u, v, w$  are shifted by half a grid length from the centre, so that they are defined on the walls of a grid box. The staggered grid structure allows that second-order approximations of spatial derivatives can be calculated directly over one grid length without additional interpolation, since the centred derivatives of the velocity components are by this means already defined at the same location as the scalars, and vice versa. In comparison to non-staggered grids, the effective spatial resolution increases by a factor of two in staggered grids (Pielke, 2002).

In PALM, the horizontal grid spacings  $\Delta x$  and  $\Delta y$  are equidistant. In order to save computational resources, the vertical grid spacing  $\Delta z$  can optionally be stretched by a constant factor  $f_{st}$  ( $= 1.08$  in the present study), starting above  $z(k_{st})$ :

$$\Delta z_{k+1} = \begin{cases} \Delta z_k, & k \leq k_{st}, \\ f_{st} \Delta z_k, & k > k_{st}. \end{cases} \quad (2.19)$$

For the discretization of the advection terms in Eqs. 2.1- 2.4 and 2.12, a fifth-order scheme after Wicker and Skamarock (2002) is applied.

The temporal discretization is realized using a third-order Runge-Kutta scheme after Williamson (1980), which is based on dividing the timestep  $\Delta t$  into three sub-timesteps. This

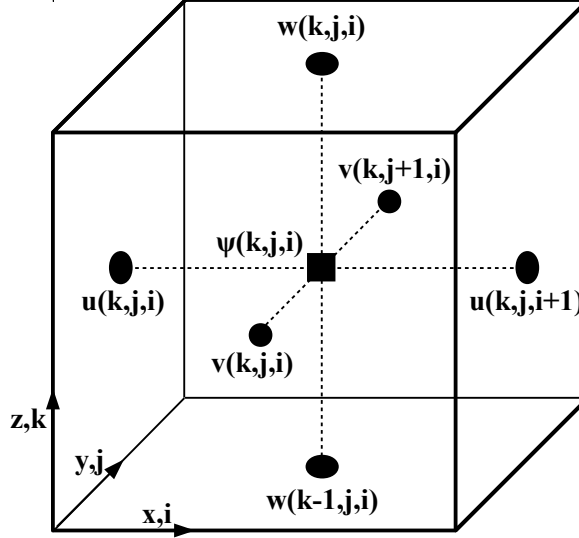


**Figure 2.1:** Arakawa-C grid used in PALM. Indices  $i, j, k$  correspond to the spatial directions  $x, y, z$ , respectively. Scalar quantities  $\psi \in \{e, \theta, K_h, K_m, K_S, p, p^*, S\}$  are defined in the centre of a grid box. Velocity components  $u, v, w$  are shifted from the centre by half a grid length in negative  $x$ -,  $y$ -, and positive  $z$ -direction, respectively.

means the prognostic equations are calculated at three points in time within  $\Delta t$ , namely at  $t + 1/3 \Delta t$ ,  $t + 3/4 \Delta t$  and  $t + \Delta t$ . In order to assure numerical stability of the solution,  $\Delta t$  cannot be arbitrarily large and must be limited sufficiently. This is achieved by applying different timestep criteria for an automatic determination of an appropriate timestep. For one, the CFL criterion (Courant-Friedrichs-Lewy; Courant et al., 1928),

$$\Delta t_{\text{CFL}} \leq \min \left( \frac{\Delta x}{u(k, j, i)}, \frac{\Delta y}{v(k, j, i)}, \frac{\Delta z(k)}{w(k, j, i)} \mid \forall i, j, k \right), \quad (2.20)$$

as well as the diffusion criterion (Roache, 1985),

$$\Delta t_{\text{Diff}} \leq 0.125 \min \left( \frac{\min(\Delta x^2, \Delta y^2, \Delta z^2(k))}{\max(K_m(k, j, i), K_h(k, j, i))} \mid \forall i, j, k \right), \quad (2.21)$$

must be fulfilled. In case of a canopy-flow simulation, an additional plant-canopy criterion is enabled,

$$\Delta t_{\text{PC}} \leq \min \left( \frac{u(k, j, i)}{F_u(k, j, i)}, \frac{v(k, j, i)}{F_v(k, j, i)}, \frac{w(k, j, i)}{F_w(k, j, i)} \mid \forall i, j, k \right), \quad (2.22)$$

with  $F_u, F_v, F_w$  being the components of the canopy drag term  $F_{u_i}$  (Eq. 2.15). Applying this criterion considers that the canopy drag itself cannot deduct more than the available momentum from the flow during one timestep. Generally, canopy-flow LES should employ relatively small grid spacings of  $\mathcal{O}(1 \text{ m})$ , hence, in most cases the CFL or diffusion criteria will determine the maximum timestep. Finally,  $\Delta t$  results from

$$\Delta t = c_{\Delta t} \min(\Delta t_{\text{CFL}}, \Delta t_{\text{Diff}}, \Delta t_{\text{PC}}), \quad (2.23)$$

with  $c_{\Delta t} = 0.9$  as a security factor.

### 2.1.5 Boundary and initial conditions for the solution of the model equations

The bottom boundary of the numerical grid is physical as it mimics the land surface. Lateral boundaries and the top boundary of the numerical grid are unphysical, and they appear because of the vertical and horizontal limitations of the domain size owing to computational constraints. All boundaries have to be applied with appropriate boundary conditions in order to enable the numerical solution of the discretized model equations. Further, the model needs to be initialized with a set of meteorological parameters which describe the meteorological situation to be simulated as closely as possible.

#### Boundary conditions

At the lateral boundaries, cyclic conditions are assigned to simulate the flow across clearing-forest-clearing transitions, corresponding to a periodic repetition of alternating forested and unforested surface patches in the direction of the mean flow. At the domain top ( $z = z_t$ ), Neumann boundary conditions were applied for the horizontal velocity components,  $u(x, y, z_t) = u(x, y, z_t - \Delta z)$  and  $v(x, y, z_t) = v(x, y, z_t - \Delta z)$ , together with a Neumann condition for perturbation pressure,  $\left. \frac{\partial p^*}{\partial z} \right|_{z_t} = 0$ , which ensures for  $w(x, y, z_t) = 0$ . For the SGS-TKE a Neumann boundary condition is assumed,  $\left. \frac{\partial e}{\partial z} \right|_{z_t} = 0$ , as well as for  $\theta$  and  $S$  by means of initial vertical gradients of the respective quantity:

$$\psi(x, y, z_t, t) = \psi(x, y, z_t - \Delta z, t) + \left. \frac{\partial \psi(z, t = 0)}{\partial z} \right|_{z_t} \Delta z|_{z_t}, \quad \psi \in \{\theta, S\}, \quad (2.24)$$

with  $\psi(z, t = 0)$  as the prescribed initial vertical profile of the respective quantity.

The bottom wall of the model domain at  $z = 0$  represents the Earth's surface, treated as a rough impermeable wall. In order to fulfil the no-slip condition of the rough surface, Dirichlet boundary conditions  $u(x, y, z = 0) = 0$  and  $v(x, y, z = 0) = 0$  apply for the horizontal velocity components. Further,  $w(x, y, z = 0) = 0$ , since the surface is impermeable for the flow. To maintain  $w(x, y, z = 0) = 0$  even after the application of the pressure solver, a Neumann condition is assumed for the perturbation pressure:  $\left. \frac{\partial p^*}{\partial z} \right|_{z=0} = 0$ . The prognostic scalar quantities  $\psi \in \{e, \theta, S\}$  are provided with a Neumann boundary condition  $\left. \frac{\partial \psi}{\partial z} \right|_{z=0} = 0$  at the domain surface, in order to ensure that in the case of prescribed near-surface fluxes of  $\psi$ , the resolved scales do not contribute to the prescribed flux.

As mentioned in Sect. 1.1.1, the ABL is affected by the vertical exchange of momentum, heat and mass between the Earth's surface and the overlying atmosphere. Near the surface, this vertical exchange is taken over by small-scale turbulence, which cannot be resolved by the numerical grid in the LES. In the present study, SGS near-surface fluxes of sensible heat and passive scalar,  $\overline{w''\theta''}_0$  and  $\overline{w''S''}_0$ , are directly prescribed. SGS momentum fluxes,  $\overline{w''u''}_0$  and  $\overline{w''v''}_0$ , are determined by applying MOST between the surface and the first vertical staggered-grid level above the surface ( $z_p = 0.5 \Delta z$ ). By this means, the momentum fluxes are related to the friction velocity  $u_*$ ,

$$u_* = \left( (\overline{w''u''}_0)^2 + (\overline{w''v''}_0)^2 \right)^{1/4}, \quad (2.25)$$

which can in turn be extracted from the following relation,

$$\frac{\partial |v_h|}{\partial z} = \frac{u_*}{\kappa z} \phi_m, \quad (2.26)$$

for the vertical gradient of the absolute horizontal velocity  $|v_h|$  at height  $z_p$ , with the von Kármán constant  $\kappa = 0.4$ . Given the Businger-Dyer function for momentum (Businger et al.,

1971; Dyer, 1974),

$$\phi_m = \begin{cases} 1 + 5\text{Rif}, & \text{for Rif} \geq 0, \\ (1 - 16\text{Rif})^{-1/4}, & \text{for Rif} < 0, \end{cases} \quad (2.27)$$

with the dimensionless Richardson number,

$$\text{Rif} = \frac{z_p \kappa g \theta_*}{\theta(z_p) u_*^2}, \quad (2.28)$$

for a dry atmosphere, and the characteristic potential temperature

$$\theta_* = -\frac{\overline{w''\theta''}_0}{u_*}, \quad (2.29)$$

where  $\overline{w''\theta''}_0$  is directly prescribed. With all the above information,  $u_*$  can be determined by vertical integration of Eq. 2.26 between  $z_0$  (prescribed roughness length) and  $z_p$ . Subsequent transposition gives:

$$u_* = \begin{cases} \frac{\kappa |v_h|}{\ln\left(\frac{z_p}{z_0}\right) + 5\text{Rif}\left(\frac{z_p - z_0}{z_p}\right)}, & \text{for Rif} \geq 0, \\ \frac{\kappa |v_h|}{\ln\left(\frac{z_p}{z_0}\right) - \ln\left(\frac{(1+A)^2(1+A^2)}{(1+B)^2(1+B^2)}\right) + 2(\arctan(A) - \arctan(B))}, & \text{for Rif} < 0, \end{cases} \quad (2.30)$$

with coefficients

$$A = (1 - 16\text{Rif})^{1/4}, \quad B = \left(1 - 16\text{Rif} \frac{z_0}{z_p}\right)^{1/4}. \quad (2.31)$$

Based on Eq. 2.25, the following formulation can be derived for the near-surface momentum fluxes:

$$\overline{w''u''}_0 = -u_*^2 \cos(\alpha_0), \quad (2.32)$$

$$\overline{w''v''}_0 = -u_*^2 \sin(\alpha_0), \quad \text{with } \alpha_0 = \arctan\left(\frac{v(z_p)}{u(z_p)}\right). \quad (2.33)$$

Substituting these relations back into Eq. 2.26 connects the momentum fluxes to the vertical gradients of the resolved-scale horizontal velocity components:

$$\frac{\partial u}{\partial z} = \frac{-\overline{w''u''}_0}{u_* \kappa z} \phi_m, \quad (2.34)$$

$$\frac{\partial v}{\partial z} = \frac{-\overline{w''v''}_0}{u_* \kappa z} \phi_m. \quad (2.35)$$

Finally, vertical integration of Eqs. 2.34 and 2.35 from  $z_0$  to  $z_p$  yields the PALM formulations for the near-surface SGS momentum fluxes,

$$\overline{w''u''}_0 = \begin{cases} \frac{-u_* \kappa u(z_p)}{\ln\left(\frac{z_p}{z_0}\right) + 5\text{Rif}\left(\frac{z_p - z_0}{z_p}\right)}, & \text{for Rif} \geq 0, \\ \frac{-u_* \kappa u(z_p)}{\ln\left(\frac{z_p}{z_0}\right) - \ln\left(\frac{(1+A)^2(1+A^2)}{(1+B)^2(1+B^2)}\right) + 2(\arctan(A) - \arctan(B))}, & \text{for Rif} < 0, \end{cases} \quad (2.36)$$

$$\overline{w''v''}_0 = \begin{cases} \frac{-u_* \kappa v(z_p)}{\ln\left(\frac{z_p}{z_0}\right) + 5\text{Rif}\left(\frac{z_p - z_0}{z_p}\right)}, & \text{for Rif} \geq 0, \\ \frac{-u_* \kappa v(z_p)}{\ln\left(\frac{z_p}{z_0}\right) - \ln\left(\frac{(1+A)^2(1+A^2)}{(1+B)^2(1+B^2)}\right) + 2(\arctan(A) - \arctan(B))}, & \text{for Rif} < 0. \end{cases} \quad (2.37)$$



It should be noted that the calculation of  $u_*$  (Eq. 2.30), the momentum fluxes (Eqs. 2.36 and 2.37) and all related quantities is an iterative process, since some of the formulations are implicit, i.e. there are direct interrelations between some of the quantities. A more detailed discussion of the surface-layer treatment in PALM can be found in Steinfeld (2009).

Using surface-layer theory as a lower boundary condition considers that the surface-atmosphere exchange of momentum is steered by the prevailing wind speed and atmospheric stratification, as well as by the roughness of the surface. In most LES studies, the surface roughness is simply described by the roughness length  $z_0$ . As mentioned in Sect. 1.2,  $z_0$  is commonly estimated to equal 10% of the vegetation height (Monteith, 1973), e.g.  $z_0 = 0.1$  m for 1-m tall grass and  $z_0 = 3.0$  m for a 30-m tall forest. As the important momentum sink on the forest patch is the vegetation layer itself and not the surface roughness (Cassiani et al., 2008), the role of  $z_0$  for the calculation of the surface momentum fluxes using MOST can be neglected on the forest patch. Hence, for simplicity, a constant  $z_0 = 0.1$  m was used everywhere in the model domain.

### Initialization

The prescribed initial conditions are somewhat different for atmospheric and open-channel simulations. Atmospheric flows are initialized with mean horizontally homogeneous vertical profiles of  $u$ ,  $v$  and  $e$ , derived from a one-dimensional version of the prognostic equations with fully-parametrized turbulence. The one-dimensional model is based on the prescribed geostrophic wind and the mixing length approach of Blackadar (1997). Resulting initial profiles of  $u$  and  $v$  describe an equilibrium state of the mean flow between the frictional forces of the Earth's surface and the selected geostrophic wind for a fixed prescribed temperature profile. By using the equilibrium  $u$ - and  $v$ -profiles as initial state in the three-dimensional simulation, the spin-up time for the three-dimensional flow to reach a dynamically steady state is significantly reduced as compared to simply initializing with vertically constant profiles. Further, the one-dimensional model provides initial values for  $\overline{w''u''}_0$ ,  $\overline{w''v''}_0$  and  $u_*$ , as well as profile data of  $K_m$  and  $K_h$ .

Open-channel simulations are initialized with analytical profiles for the streamwise velocity component  $u$ , originally derived for Poiseuille flows (flow between two parallel plates) and slightly modified to meet the open-channel conditions. The form of the open-channel profile is thereby equal to the form of the lower half of the Poiseuille-flow profile (see Etling, 2002, p. 265f).

For both, ABL and open-channel simulations, the initial vertical profiles of  $\theta$  and  $S$  are directly prescribed, same as for the one-dimensional model. In the initial stage of a simulation, turbulence is triggered by regularly imposing uncorrelated Gaussian-distributed random perturbations to the horizontal velocity fields, up to the point where the resolved-scale TKE exceeds a prescribed threshold value.

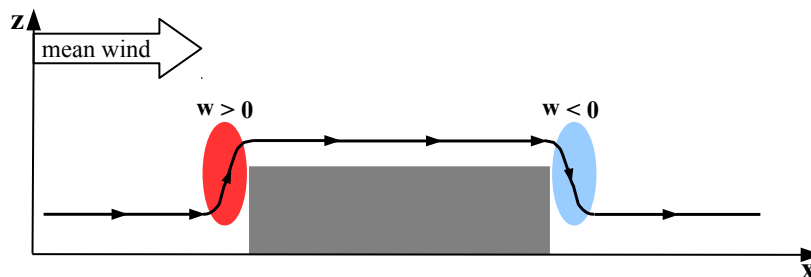


**Figure 2.2:** Sketch of a streamline forming around a solid obstacle. Red and blue ovals mark regions with positive and negative vertical velocities  $w$ , respectively.

## 2.2 Analysis methods

For the investigations presented in articles A–C (see Chap. 3), different analysis methods are applied, which shall be described in the following. At this point, it should be noted that the overbar is no longer used to mark filtered quantities as e.g. in Eq. 2.1; throughout the entire data analysis, the overbar refers to a temporal average. Further, some notations used in this section might differ from the notations used in the articles A–C.

### 2.2.1 Calculation of turbulence statistics in heterogeneous flows

In general, a quantity  $\psi \in \{\theta, S, u, v, w\}$  can be split into a mean part  $[\psi]$  and a deviation  $\psi'$  from this mean, according to Reynolds decomposition:

$$\psi = [\psi] + \psi'. \quad (2.38)$$

In horizontally homogeneous flows,  $[\psi]$  can be equivalent to a horizontal average, making  $\psi'$  the turbulent fluctuation from the horizontal mean. In horizontally heterogeneous flows, e.g. with the presence of forest edge, the definition of a turbulent fluctuation is not as intuitive as for horizontally homogeneous flows. With the presence of surface discontinuities, the horizontal mean is not appropriate to derive the actual turbulence statistics because there is no representative horizontal mean state. This shall be illustrated by means of a two-dimensional example of the flow across a solid rectangular obstacle, presented in Fig. 2.2. Let us simply assume that the flow across the obstacle, visualized by the streamline, is laminar. Due to the presence of the obstacle, the flow is forced upward at the windward obstacle wall (red shading), and it descends at the leeward wall (blue shading). Hence, the vertical velocity  $w$  can locally take positive or negative values, while the horizontal mean  $[w]$  equals zero. Following Eq. 2.38 this would yield  $w' \neq 0$  in the coloured regions, which indicates that there is turbulence, even though the flow is laminar. Also in a turbulent flow this method would yield wrong turbulence statistics, since the local mean flow likewise deviates from the horizontal mean.

One appropriate option for determining turbulence statistics in horizontally heterogeneous flows is to apply temporal averaging, indicated by an overbar ( $\overline{\psi}$ ). This method is typically applied in the field of micrometeorology for the calculation of turbulent fluxes of momentum, energy or other scalars, based on timeseries of the respective quantities, and it is known as the temporal eddy-covariance (EC) method (for details see e.g. Foken, 2006). However, the temporal EC method demands the respective quantities to be temporally stationary, which typically contradicts with the daily cycle of meteorological quantities. Consequently, averaging intervals must be limited, but at the same time long enough to capture all relevant turbulence scales. Another option, e.g. in the case of idealized one-dimensional surface heterogeneities is to apply line averaging along the homogeneous direction, indicated by

angled brackets ( $\langle \psi \rangle$ ), as it is usually applied in idealized forest-edge-flow applications. The calculation of turbulent fluctuations based on  $\langle \psi \rangle$  would refer to a one-dimensional spatial EC method.

Returning to Fig. 2.2, the streamline now represents a time- or line-average (imagining a spanwise elongated obstacle) of a turbulent flow across the obstacle. This means, the local time- or line-average at a position  $(x, z)$  accounts for the mean upward and downward motion of the flow near the obstacle walls. Of course, the temporal or spatial averaging interval has to be sufficiently long to create a statistically steady average. By this means, temporal or spatial fluctuations  $\psi'$  from  $\bar{\psi}$  or  $\langle \psi \rangle$  can purely be considered as turbulence.

Both EC methods are based on Reynolds decomposition as in Eq. 2.38, where  $[\psi]$  is replaced by  $\bar{\psi}$  or  $\langle \psi \rangle$ . Under the assumption of Reynolds postulates (see e.g. Foken, 2006), variances and covariances of turbulent quantities  $\psi', \phi' \in \{\theta', S', u', v', w'\}$  can be calculated by:

$$\overline{\psi' \phi'} = \overline{\psi \phi} - \bar{\psi} \bar{\phi}, \quad (2.39)$$

$$\langle \psi' \phi' \rangle = \langle \psi \phi \rangle - \langle \psi \rangle \langle \phi \rangle. \quad (2.40)$$

$$[\psi' \phi'] = [\psi \phi] - [\psi] [\phi]. \quad (2.41)$$

Under stationary conditions the fluxes derived by Eqs. 2.39 and 2.40 should be equal, given that statistics are sufficient.

In the present study, the forest edge is always oriented along the  $y$ -direction, and the mean flow is perpendicular to the forest edge, i.e. the line average in the following always refers to an average in the homogeneous  $y$ -direction, parallel to the orientation of the forest edge. Both EC methods are applied within the framework of this study.

### 2.2.2 Typical quantities for the characterization of canopy flows

For the proposed comparison (see Sect. 1.5) of LES data with lidar data of a field experiment and laser anemometry data of a wind-tunnel model, typical quantities characterizing canopy flows were analyzed. The definition of these quantities is illustrated in Fig. 2.3, presenting the formation of an IBL above a forest of height  $H$ . The streamwise and vertical axis are normalized with  $H$ . As a comparative quantity, the standard deviation  $\sigma_u$  of the edge-perpendicular velocity component  $u$ ,

$$\sigma_u = \sqrt{\overline{u' u'}}, \quad (2.42)$$

was selected as a measure for the turbulence intensity of the streamwise flow within the IBL above the forest.  $\sigma_u$  was found to be an adequate measure to retrieve the structure of the IBL, as previously used by Träumner et al. (2012) for the comparison of the field and wind-tunnel data. The variance  $\overline{u' u'}$  was calculated in all LES, field and wind-tunnel datasets by means of the temporal EC method (see Eq. 2.39), employing a 15-min time average. Additionally, several 15-min variances (ensemble members) of situations with similar meteorological conditions were averaged to form an ensemble average. In the LES, statistically independent ensemble members were collected in time and along the homogeneous  $y$ -direction. Field and wind-tunnel ensemble member were purely collected in time. In order to make the measurement data comparable to the LES data,  $\sigma_u$  was normalized with a reference velocity  $u_{\text{ref}}$ , which is defined as the mean velocity  $\bar{u}$  at the forest edge at  $z/H = 2$ , same as used by Träumner et al. (2012).

The IBL top as marked by the solid black line in Fig. 2.3 is defined at the height above which  $\sigma_u \leq 1.01\sigma_{u_0}$ , where  $\sigma_{u_0}$  is a measure for the mean turbulence intensity of the approaching background flow. As outlined by the dashed red lines,  $\sigma_{u_0}$  was defined as the vertical average of  $\sigma_u$  between  $z/H = 2$  and  $z/H = 3$ , at  $x/H = -1$ . This specific layer average of  $\sigma_u$

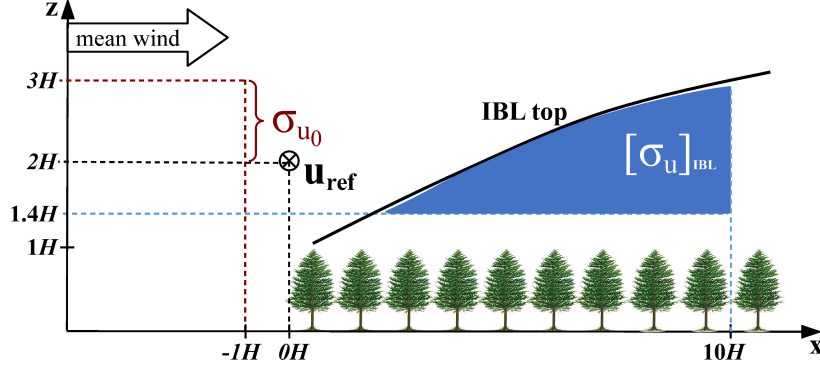


**Figure 2.3:** Sketch of an IBL above a forest patch (based on original sketch by B.Sc. Katrin Scharf, member of the PALM group, 2014). The definition of different quantities used for the characterization of the IBL properties are illustrated: standard deviation  $\sigma_u$  of the streamwise velocity component  $u$ ,  $\sigma_{u_0}$  as a measure for the mean turbulence intensity in the approaching background flow,  $u_{\text{ref}}$  as a reference velocity used for normalization, and  $[\sigma_u]_{\text{IBL}}$  as the IBL average of  $\sigma_u$ , calculated within the blue-shaded region.  $H$  is the forest height.

was chosen as the smallest intersecting set between all datasets, since datasets from the field and wind-tunnel experiments were partially incomplete. By this definition of  $\sigma_{u_0}$ , the IBL turbulence level is set into direct relation with the properties of the background flow, which accounts for the impact of the upstream forest. Namely, in the case of short clearings and due to the cyclic lateral boundary conditions in the LES, a certain amount of turbulence generated above the forest is transported with the flow towards the windward forest edge.

As a further comparative quantity,  $[\sigma_u]_{\text{IBL}}$  was calculated as an IBL average of  $\sigma_{u_0}$  over the blue-shaded area. The IBL-average area reaches vertically from  $z/H = 1.4$  up to the IBL top, and it extends horizontally to  $x/H = 10$ , which was the maximum data coverage of the wind-tunnel data.

Concerning the LES, all analysis data were output after the flow had reached a (quasi-) stationary state, approximately after 2 hr of simulated time. The term “quasi” refers to the CBL simulations, where due to constant surface heating the CBL depth permanently grows, and hence, the CBL properties never become truly stationary. Rather, a quasi-stationary state is reached at some point of the simulation, whereafter the mean temperature profiles maintain their general form. Simulation and measurement set-ups are described in article A.

### 2.2.3 Calculation of individual scalar balance terms

In articles B and C, the LES investigation of scalar transport processes near forest edges is based on the transport equation for a passive scalar  $S$  (Eq. 2.4) as solved in PALM. The first term on the right-hand side of Eq. 2.4 is the advection term, which describes all resolved-scale transport processes, while the second term describes the SGS scalar transport.

In order to determine which physical mechanisms are of importance for the scalar transport near forest edges, the advection term as solved by PALM is split into its mean and turbulent contribution. This is done by assuming the applicability of Reynolds averaging (see Sect. 2.2.1) and Eq. 2.40. Further, by substituting Eq. 2.8 into Eq. 2.4 (see Sect. 2.1.2), and by consistently adopting the line average “ $\langle \rangle$ ” to all terms, Eq. 2.4 is modified to:

$$\frac{\partial \langle S \rangle}{\partial t} = - \frac{\partial \langle u_i \rangle \langle S \rangle}{\partial x_i} - \frac{\partial \langle u'_i S' \rangle}{\partial x_i} + \frac{\partial}{\partial x_i} \langle K_s \frac{\partial S}{\partial x_i} \rangle. \quad (2.43)$$

All transport terms can be further split into their contribution in the three spatial directions

$x$ ,  $y$  and  $z$ :

$$\underbrace{\frac{\partial \langle S \rangle}{\partial t}}_I = \underbrace{-\frac{\partial \langle u \rangle \langle S \rangle}{\partial x}}_{IIa} - \underbrace{\frac{\partial \langle u' S' \rangle}{\partial x}}_{IIIa} + \underbrace{\frac{\partial}{\partial x} \langle K_s \frac{\partial S}{\partial x} \rangle}_{IVa} \\
 \underbrace{-\frac{\partial \langle v \rangle \langle S \rangle}{\partial y}}_{IIb} - \underbrace{\frac{\partial \langle v' S' \rangle}{\partial y}}_{IIIb} + \underbrace{\frac{\partial}{\partial y} \langle K_s \frac{\partial S}{\partial y} \rangle}_{IVb} \\
 \underbrace{-\frac{\partial \langle w \rangle \langle S \rangle}{\partial z}}_{IIc} - \underbrace{\frac{\partial \langle w' S' \rangle}{\partial z}}_{IIIc} + \underbrace{\frac{\partial}{\partial z} \langle K_s \frac{\partial S}{\partial z} \rangle}_{IVc}, \quad (2.44)$$

and are individually calculated as output quantities during the simulations.

Each term on the right-hand side of Eq. 2.44 describes a net-transport of  $S$  through a grid volume, contributing to the local temporal change of  $S$  (term I) within this grid volume. The scalar  $S$  can be transported either by the mean flow (II), by resolved-scale turbulence (III) or by SGS turbulence (IV), in the edge-perpendicular ( $x$ ), edge-parallel ( $y$ ) or vertical ( $z$ ) direction, respectively marked by a,b,c. A positive net transport by a single term, including the dedicated sign in Eq. 2.44, implies an increase of  $S$  with time, and vice versa.

Given that the model domain is sufficiently elongated in the homogeneous (edge-parallel) direction  $y$ , the flow can be assumed to be statistically homogeneous in this direction. Hence, the line-averaged net-transport of  $S$  in the  $y$ -direction should be vanishingly small, and consequently, it should not have any effect on the streamwise (edge-perpendicular) distribution of  $S$ . This was proven to be valid, by verifying that the prognosticated temporal change of  $S$  in Eq. 2.4 equals the sum of the individually calculated remaining terms (II-IVa,c) on the right-hand side of Eq. 2.44.

## 2.3 Validation of PALM under homogeneous canopy flow conditions

Within the framework of this thesis, PALM together with its embedded canopy model was used for the first time in an extensive way. Before PALM was employed to study the scalar transport in canopy flows, the ability of PALM for adequately representing the typical features of canopy flows had to be verified. This verification was performed on the basis of a PALM set-up of the flow across an infinite horizontally homogeneous vegetation canopy, which will be described further below. PALM data were compared against datasets of various field and wind-tunnel experiments of near-neutral flows across different horizontally homogeneous cereal-crop or forest canopies. A summary of the experiments and the datasets is given by Raupach et al. (1996) in the well-known “family portrait” of canopy turbulence, as presented in Fig. 2.4 by the various black curves, showing vertical profiles of the mean streamwise wind speed  $u$  (a), the turbulent vertical momentum flux  $\overline{w'u'}$  (b), and some other second-order moments (c-e), as well as the vertical distribution of leaf area density  $a$  (f). The vertical coordinate is scaled with canopy height  $H$ ;  $u$  is normalized to its value at the canopy top,  $u_H$ ; second order moments are normalized to friction velocity  $u_*$  taken as a vertical average over the constant-flux layer above  $z = H$ .

The PALM set-up was created analogous to a previous canopy-flow LES performed by Watanabe (2004), their case III, describing a pressure-driven neutral open-channel flow across a horizontally and vertically homogeneous canopy of height  $H = 15$  m. Lateral boundaries are cyclic, no-slip conditions hold at the surface, and free-slip conditions at the top of the model domain. The grid size is equidistant in each spatial direction with  $\Delta x_i = 1.5 \text{ m} \hat{=} 0.1H$ , i.e.

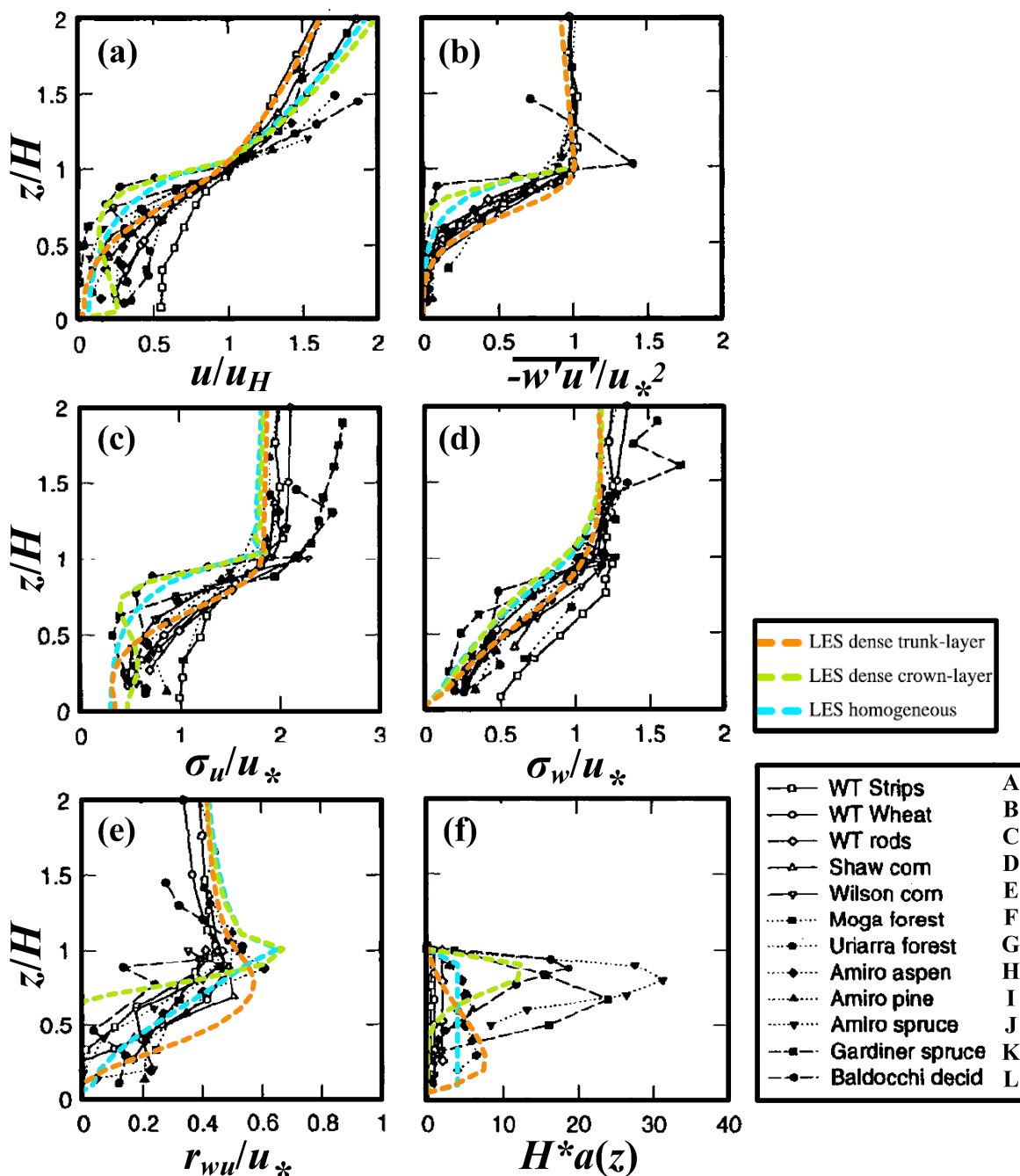


**Figure 2.4:** “Family portrait” of canopy turbulence, adapted after Raupach et al. (1996) c.f. Fig. 1a-e,j with permission of Springer Science+Business Media; showing vertical profiles of mean horizontal wind speed  $u$  (a), turbulent vertical momentum flux  $\overline{w'u'}$  (b), standard deviations  $\sigma_u$  (c) and  $\sigma_w$  (d) of horizontal and vertical velocity components  $u$  and  $w$ , respectively, correlation coefficient  $r_{wu} = \overline{w'u'}/\sigma_u\sigma_w$  (e), and leaf area density  $a$  multiplied with canopy height (f). The vertical coordinate is normalized with  $H$ ;  $u$  is normalized to its canopy-top value  $u_H$ ; second moments are normalized friction velocity  $u_*$  taken from the constant-flux layer above  $z = H$ . Black curves illustrate profiles of the different experiments A–L, as originally plotted by Raupach et al. (1996). Coloured curves present horizontally averaged PALM profiles of simulations with three different vertical leaf-area distributions (f): vertically homogeneous (blue), dense crown layer (green), dense trunk layer (orange).

the canopy is resolved by ten grid points in the vertical direction. A direct pressure gradient  $\frac{\partial p}{\partial x} = 0.01 \text{ Pa m}^{-1}$  (see Eq. 2.5) drives the flow in the  $x$ -direction, resulting in a streamwise wind speed at the canopy top of  $u_H \approx 3 \text{ m s}^{-1}$ . For further details on the set-up, such as the domain size and the flow initialization, see Watanabe (2004).

Three forest morphologies with different profiles of leaf area density  $a(z)$  were simulated, spanning a wide range of canopy types, as illustrated by the coloured curves in Fig. 2.4f: a vertically homogeneous canopy (blue), a canopy with dense crown layer (green), and a canopy with dense trunk layer (orange). In all three cases, the leaf area index ( $LAI$ : vertical integral over  $a(z)$ ) was identical at a value of  $LAI = 2$ , which is in the range of the experiment canopies (see Raupach et al., 1996). PALM data analysis began after the flow had reached a stationary state (after 2 hr of simulated time), and horizontally averaged vertical profiles of the “family-portrait” quantities were time averaged over 5 hr of simulated time, which are presented by means of the coloured curves in Fig. 2.4a–e.

Comparing the profiles of the PALM runs (coloured curves) and the experiments (black curves) shows a fairly good agreement, both the shape of the profiles and the data range of the dynamical quantities in the experiments are well reproduced by PALM. To be specific, the inflected wind profile being the most famous feature of canopy flows, as theoretically discussed in Sect. 1.2, is well represented in the different PALM simulations (see Fig. 2.4a). As expected, the inflection point is more pronounced for canopies where the foliage is concentrated near the canopy top. The secondary wind maximum that forms in the trunk space of a canopy with dense crown layer (e.g. experiment canopy L) is likewise well represented in the corresponding PALM profile (green curve). Moreover, the momentum-flux profiles in PALM predict fairly well the exponential decay with decreasing height between the canopy top and the surface, as well as the nearly height-constant flux within the roughness sublayer above the canopy. Also for the other second-order moments (c–e), a fairly good agreement between PALM and experiment data can be observed. Overall, this qualitative and quantitative agreement between PALM and experiment data indicates that PALM is able to adequately represent the characteristic dynamical features of canopy flow.

In previous LES studies of canopy flow (e.g. Shaw and Schumann, 1992; Watanabe, 2004; Yang et al., 2006a; Ross, 2011), spatial grid sizes were typically chosen in a way that the vegetation canopy is resolved by at least ten grid points in the vertical direction. The above comparison of PALM data against several sets of field and wind-tunnel data of homogeneous canopy flows has indicated an overall qualitative and quantitative agreement between PALM and experiment data, suggesting that the vertical resolution of the canopy with ten grid points is sufficient for adequately representing mean and turbulent features of canopy flow. Nevertheless, PALM was further validated, and the sensitivity of the results on grid size was evaluated. Therefore, based on the simulation with a vertically homogeneous canopy (see blue curves in Fig. 2.4) with a grid size  $\Delta x_i = 1.5 \text{ m} \hat{=} 0.1H$  (hereafter simulation S10), two additional simulations of the same set-up were performed with different grid sizes,  $\Delta x_i = 0.75 \text{ m} \hat{=} 0.05H$  (simulation S20) and  $\Delta x_i = 3.0 \text{ m} \hat{=} 0.2H$  (simulation S05), corresponding to a vertical resolution of the canopy with 5 (S05), 10 (S10) and 20 (S20) grid points. As comparative quantities for the grid-size sensitivity study, the characteristic length scales of CTS were analyzed in the PALM data, and compared to corresponding results of the same field and wind-tunnel experiments A–L as mentioned above. It should be noted that this part of the validation has been treated within the framework of a Bachelor project by student Hannes Schulz, under my supervision. As mentioned in Sect. 1.2, CTS above vegetation canopies are characterized by the shear length scale  $L_S$  (see Eq. 1.1) and the separation length  $\Lambda$  between two neighbouring CTS. The streamwise separation  $\Lambda_x$  can be calculated by means of different statistical approaches such as two-point correlation or wavelet analysis, as discussed by Raupach et al. (1996). Here,  $\Lambda_x$  was calculated at  $z = H$  according to

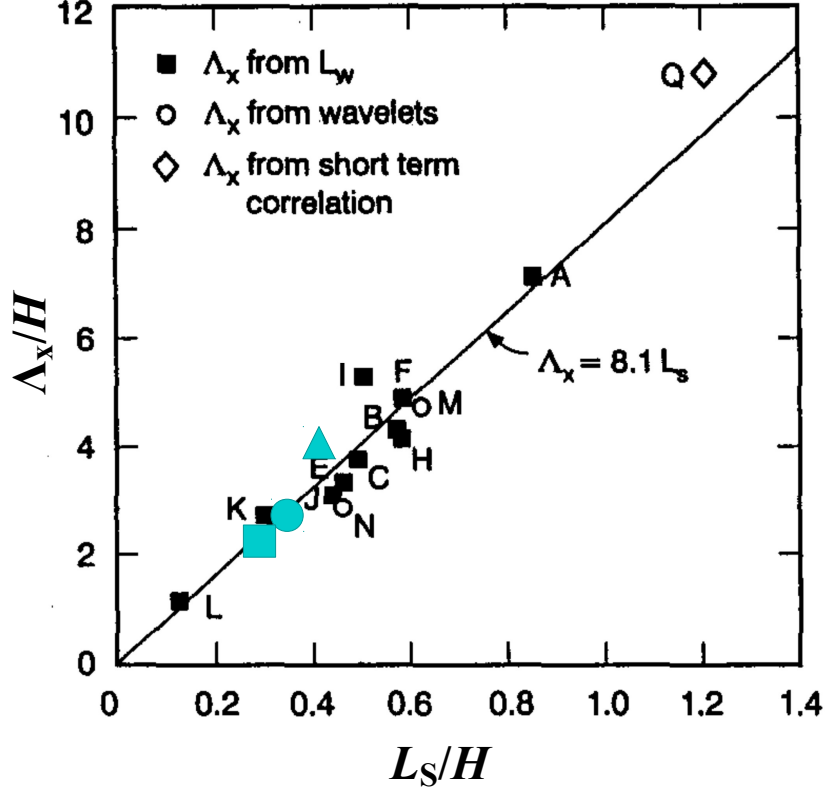


**Figure 2.5:** Streamwise separation  $\Lambda_x$  of coherent turbulence at  $z = H$ , plotted against the shear length scale  $L_S$ , both normalized with  $H$  (adapted after Raupach et al. (1996) c.f. Fig. 8 with permission of Springer Science+Business Media). Data of the experiment canopies (black symbols) is calculated based on different statistical analysis approaches like two-point correlation and wavelet analysis (for details see Raupach et al., 1996). Blue symbols mark data of our simulations S05 (triangle), S10 (circle) and S20 (square), calculated by means of streamwise two-point correlation of the vertical velocity component  $w$  at  $z = H$ .

Watanabe (2004) via the streamwise integral length scale  $L_w$  as follows:

$$\Lambda_x(z = H) = 2\pi L_w(z = H) = 2\pi \int_0^\infty r_{ww}(dx, z = H) dx, \quad (2.45)$$

with  $r_{ww}$  as the streamwise two-point autocorrelation function for vertical velocities:

$$r_{ww}(dx, z = H, t) = \frac{[w'(x + dx, y, z = H, t) w'(x, y, z = H, t)]}{[\sigma_w^2](z = H, t)}. \quad (2.46)$$

Thereby, the local  $w'$  is defined as the fluctuation from the horizontal average  $[w]$ , as marked by the square brackets.  $dx$  is the spatial lag in the streamwise direction, and  $[\sigma_w^2]$  is the horizontally averaged variance of  $w$ . For statistical reasons,  $r_{ww}$  was additionally time averaged over 5 hr of simulated time, same as the profile data presented above.

Raupach et al. (1996) proposed a linear relation between  $\Lambda_x$  and  $L_S$ , namely  $\Lambda_x = 8.1 \cdot L_S$ , based on the length scales derived from the field and wind-tunnel datasets A–L, which is shown in Fig. 2.5 (adopted from Raupach et al., 1996), where  $\Lambda_x$  values of all experiments are plotted against the respective  $L_S$  values (black symbols), both normalized with  $H$ .  $\Lambda_x$  and  $L_S$  values of the simulations S05, S10, and S20 are visualized by the blue symbols. Overall, the length scales simulated with PALM agree well with the relation between  $\Lambda_x$  and  $L_S$  as found by Raupach et al. (1996). However, it strikes that for case S05 with the largest grid



size, both  $\Lambda_x$  and  $L_S$  are about 50% larger than for cases S10 and S20, where the calculated length scales are in fact rather similar, indicating that the representation of CTS does not significantly change from S10 to S20. This similarity suggests that a vertical resolution of ten grid points for the canopy layer is sufficient to resolve the relevant turbulence scales from an LES point-of-view, and hence, to adequately represent the features of canopy flow.

An additional validation of PALM under more complex flow conditions such as the flow across a windward forest edge is presented as a part of article A.

### 3 Research articles of this cumulative thesis

This chapter contains two peer-reviewed research articles (A, B) and one research article to-be-submitted for peer-review soon (C), all of which are a result of this PhD project. It should be noted that there might be slight deviations in the notations of variables and parameters among the three articles, as well as between the articles and the introductory words in Chapt. 1 and 2.

**Research article A** deals with the question how plant-physical and meteorological conditions affect the development and properties of internal boundary layers above forest patches downstream of clearing-to-forest transitions. The investigations are performed on the basis of an intercomparison between two-dimensional flow data from a lidar measuring campaign at a forest-edge site in Germany, a corresponding wind-tunnel experiment of forest-edge flow, and a set of idealized forest-edge-flow LES with different meteorological and plant-physical conditions. By means of LES, we determine which physical parameters - such as mean wind profiles, thermal stratification, forest density and forest-gap size - are critical for the comparability of atmospheric and wind-tunnel measurements of flows across forest edges. Two main objectives are pursued in the course of this investigation: (1) Verification of the applied LES model PALM with its embedded canopy model for the simulation of forest-edge flows; and (2) Verification of the applicability of lidar as a state-of-art tool to provide multi-dimensional information of forest-edge flow in nature.

In **research article B**, we investigate the spatial variability of scalar transport above a forested surface patch downstream of a clearing-to-forest transition. Investigations are based on several idealized LES runs, simulating neutral flow across a windward forest edge in flat terrain, for a wide range of forest densities and wind speeds. One objective of this study is to evaluate the important scalar transport mechanisms that lead to observed local enhancements of scalar concentration and its turbulent flux above the forest patch downstream of the windward forest edge. This is done by means of a separate analysis of every single scalar-balance term. It is further analyzed to what extent the behaviour of the local scalar enhancement depends on parameters like forest density and wind speed. An improved understanding of the scalar transport near forest edges has direct implications for the interpretation of in-situ micrometeorological measurements in such flow regimes. We therefore develop approaches for estimating the regions of enhanced scalar concentration and flux, leading towards an optimized planning and interpretation of the in-situ measurements.

**Research article C** treats the behaviour of the scalar transport near forest-to-clearing transitions, being a follow-up study to the work presented in article B. Above the clearing in the lee of the forest patch, local enhancement of scalar concentration and its turbulent flux likewise occurs, similar as presented in article B for the windward forest-edge region. By means of LES data of the same simulations, we again analyze the scalar-balance terms in order to identify the important transport mechanisms leading to the local scalar enhancement in the lee of the forest. We further examine how the magnitude of the concentration and flux enhancement is affected by forest density and wind speed. Finally, we state implications for the set-up and interpretation of micrometeorological measurements, and we propose a new method for localizing regions of disturbed scalar transport based on on-site measurements.

## 3.1 Research article A: What determines the differences found in forest edge flow between physical models and atmospheric measurements? – An LES study

### 3.1.1 Declaration of my contribution

The idea for the article was developed in collaboration with all authors of the article. I performed all LES runs and the related data analysis, as well as the qualitative and quantitative comparison of LES, lidar and wind tunnel data. The set-up and the implementation of the lidar field experiment, as well as the corresponding data analysis was performed by Dr. Katja Träumner and her working group at Karlsruhe Institute of Technology (KIT) in Karlsruhe, Germany. The wind-tunnel experiment was planned and conducted by Prof. Dr. Bodo Ruck and his group at KIT in Karlsruhe, Germany. They also provided preprocessed data sets of their experiments. Animated visualizations linked to the article were created by Dr. Björn Maronga with the help of Helge Knoop, Prof. Dr. Siegfried Raasch and myself, on the basis of my simulation data. Discussions and reviews of the original manuscript by Dr. Katja Träumner, Prof. Dr. Bodo Ruck, Prof. Dr. Siegfried Raasch and Dr. Matthias Sühling helped to improve the content and structure of the article. The quality of the article was further increased by the valuable remarks of the two anonymous reviewers of the article.

### 3.1.2 Published article

This article has been published with open access in *Meteorologische Zeitschrift*.  
Submitted: 28 October 2013. Accepted: 11 February 2014. Published online first: 4 April 2014. Online issue: Volume 23(1), 33–49, June 2014.

**Kanani, F., K. Träumner, B. Ruck and S. Raasch, 2014:** What determines the differences found in forest edge flow between physical models and atmospheric measurements? – An LES study. *Meteorol. Z.*, **23(1)**, 33–49, doi: 10.1127/0941-2948/2014/0542.



# What determines the differences found in forest edge flow between physical models and atmospheric measurements? – An LES study

FARAH KANANI<sup>1\*</sup>, KATJA TRÄUMNER<sup>2</sup>, BODO RUCK<sup>3</sup> and SIEGFRIED RAASCH<sup>1</sup>

<sup>1</sup>Institute for Meteorology and Climatology, Gottfried-Wilhelm-Leibniz Universität Hannover, Germany

<sup>2</sup>Institute for Meteorology and Climate Research, Karlsruhe Institute of Technology, Germany

<sup>3</sup>Institute for Hydrodynamics, Karlsruhe Institute of Technology, Germany

(Manuscript received October 28, 2013; in revised form February 4, 2014; accepted February 11, 2014)

## Abstract

A recent study has shown that Doppler lidar is a state-of-the-art method to obtain spatially and temporally resolved flow fields in forest edge flow regimes. In that study, the general flow features observed by lidar were found to be similar to those detected above a physical tree model in a wind tunnel. But in pivotal details, for example regarding the absolute height and the inner structure of the internal boundary layer (IBL), significant differences were detected. The main objectives of this Large-Eddy Simulation (LES) study are to analyze these differences and to associate them to the meteorological and physical differences between the set-ups of the wind tunnel and the atmospheric measurement. This enables on the one hand a model evaluation for the LES and the physical model respectively, and on the other hand a better understanding of the results from the lidar measurements. Results from an LES with neutral stratification and without Coriolis force show a similar IBL structure as in the wind tunnel and represent well-known characteristics of forest edge flow. A variation of the forest density only marginally affects the IBL structure. The presence of a finite forest clearing as observed at the lidar site increases the turbulence level of the IBL, compared to a set-up with a quasi-infinite clearing like in the wind tunnel. Including Coriolis force further enhances the turbulence levels to values observed by lidar. An increasing thermal instability results in even higher turbulence levels. Hence, differences between wind tunnel and atmospheric measurements are mainly traced back to differences in the flow forcing and in the onflow conditions upstream of the forest edge. Furthermore, a statistical analysis reveals that insufficient averaging of the lidar data also contributes to the observed deviations from the wind tunnel results. Based on this analysis, we suggest that at least two and a half hours of measurements during equivalent atmospheric conditions are necessary to obtain a statistically representative mean IBL structure.

**Keywords:** large-eddy simulation, forest edge flow, wind tunnel, doppler lidar, internal boundary layer

## 1 Introduction

Forest edges represent one of the most distinct discontinuities in natural surface conditions, leading to the development of complex turbulent flow structures. Due to form and viscous drag from trunks, branches and leaves the turbulent flow is significantly disturbed downstream of a forest edge. The mean flow is decelerated in front of and inside the forest, while a flow acceleration can be observed above the forest (e.g. DUPONT and BRUNET, 2009; MORSE et al., 2002; YANG et al., 2006a), resulting from the narrowing of the flow cross-section. This produces a pronounced shear layer near the forest top with an inflection point in the vertical profile of mean streamwise velocity (e.g. FINNIGAN, 2000). As a result, Kelvin-Helmholtz instabilities are introduced to the flow and lead to the development of complex coherent turbulence structures (CTS) downstream of the forest edge (DUPONT and BRUNET, 2009).

Starting from the edge, these CTS continuously grow in size and strength, until the flow properties have fully adjusted to the change in surface conditions (BELCHER et al., 2012; DUPONT and BRUNET, 2009). Fully developed CTS scale with forest height (e.g. FINNIGAN, 2000; FINNIGAN et al., 2009; RAUPACH et al., 1996). They are strong enough to penetrate deep into the forest and therefore effectively contribute to the forest-atmosphere exchange of energy, momentum and trace gases such as CO<sub>2</sub> (e.g. BERGSTRÖM and HÖGSTRÖM, 1989; FINNIGAN, 1979; KATUL et al., 1997; RAUPACH, 1981; WALLACE et al., 1972). The layer above the forest, in which the flow adjustment takes place, is termed internal boundary layer (IBL). The IBL has been first studied in the context of abrupt changes in surface roughness (e.g. GARRATT, 1990; JEGEDE and FOKEN, 1999). Above the IBL, the abruptly changing surface conditions have no effect on the turbulent flow.

Our present knowledge about forest edge flow has been drawn from a combination of field measurements, laboratory studies and numerical simulations. *In situ* tower measurements have been performed upstream

\*Corresponding author: Farah Kanani, Institute for Meteorology and Climatology, Gottfried-Wilhelm-Leibniz Universität Hannover, Herrenhäuser Straße 2, Hannover 30419, Germany, e-mail: kanani@muk.uni-hannover.de

and downstream of, within and above forests (e.g. IRVINE et al., 1997; KRUIJT et al., 1995; RAYNOR, 1971; THOMAS et al., 2006; ZHU et al., 2004) to determine characteristic wind and momentum flux profiles for these regions and to understand the flow adjustment in transition flows. However, even though these tower measurements of e.g. turbulent CO<sub>2</sub> or heat fluxes are performed in the real world and therefore should truly represent the local atmospheric properties, the interpretation of these flux measurements is difficult. This is because the turbulent transport is highly variable within a forest-edge flow regime, spatially due to the surface transition and temporally due to variations of atmospheric conditions (e.g. SHAW et al., 1988). With wind tunnel (WT) studies of forest flow (e.g. MARSHALL et al., 2002; MORSE et al., 2002; RUCK and ADAMS, 1991), multi-dimensional information on the turbulent wind field above the forest can be captured at lower costs compared to a set of tower measurements. However, due to the constraints of a WT, it is difficult to account for thermal stratification and to reproduce a typical atmospheric-boundary-layer wind profile. Moreover, it is rather difficult to measure the wind field inside the model forest with the available measuring techniques like e.g. particle image velocimetry.

Numerical simulation techniques like Large-Eddy Simulation (LES) have the advantage of being able to mimic atmospheric-boundary-layer features like the Ekman spiral and thermal stratification (e.g. RAASCH and FRANKE, 2011; STEINFELD et al., 2007; SÜHRING and RAASCH, 2013). Furthermore, LES can provide highly resolved information on the turbulent wind field in a forest-edge flow regime, even inside the forest (e.g. BOHRER et al., 2009; CASSIANI et al., 2008; DUPONT and BRUNET, 2009; SCHRÖTTLE and DÖRNBRACK, 2013; YANG et al., 2006a; YANG et al., 2006b). Atmospheric and plant physical conditions like wind speed, forest density and especially the thermal stability can be varied stepwise, at a much lower effort compared to a WT study. This way, the effect of each factor on e.g. the IBL structure can be systematically investigated.

But before LES can be reliably used for these applications, LES model results have to be validated against field measurements. Previous LES studies of forest edge flow (e.g. YANG et al., 2006a) have been tested against WT models and results from tower measurements, where the former cannot fully represent the atmospheric conditions and the latter cannot provide a complete multi-dimensional picture of the IBL structure. Thus, a validation of LES set-ups against field measurements that can provide a multi-dimensional view of the IBL structure above a forest is urgently needed. Recent studies by TRÄUMNER et al. (2012) revealed that Doppler lidar is a promising tool for this challenge. The lidar technique presents a state-of-the-art method to effectively complement *in situ* tower measurements near forest edges. Also PATTON et al. (2011) have previously implemented Doppler lidar for coherent structure de-

tection above an orchard within the CHATS (Canopy Horizontal Array Turbulence Study) experiment.

Once validated, LES is besides a useful tool for virtually testing different lidar measuring strategies prior to an atmospheric measurement. LES data can be employed to investigate how e.g. the limited spatial resolution and the inherent averaging of the lidar or the limited temporal resolution due to the nature of the scan patterns affect the quality of the lidar measurement. With this approach lidar scan patterns can be optimized for appropriately capturing atmospheric flow phenomena like e.g. wind gusts or CTS above a forest. STAWIARSKI et al. (2013) showed first applications of this straight-forward approach.

In order to study the applicability of the lidar system for capturing turbulence structures above a forest, TRÄUMNER et al. (2012) compared streamwise velocity and corresponding standard deviation fields from atmospheric lidar measurements (AM) with those from laser Doppler anemometry measurements in the WT. The WT model was built to adequately represent the lidar measuring site (for details see TRÄUMNER et al., 2012). Lidar data were available for a number of stable and unstable cases, whereas the WT was operated under neutral conditions. TRÄUMNER et al. (2012) found a qualitative agreement between AM and WT data. The IBL height and the range of standard deviation above the WT forest were in between the observed values of the stable and the unstable cases of the AM. Too few neutral situations were detected in the AM data for a direct comparison with the neutral situation in the WT. Despite this general agreement, no quantitative agreement regarding a visually estimated IBL height and concerning the values of the normalized standard deviation could be found. The unstable cases in the AM showed a faster IBL growth and higher standard deviations. This deviation from the WT data might be explained by the differences in atmospheric stability and flow forcing, being a distinct difference between AM and WT. Another difference lies in the characteristics of the approaching flow. At the lidar site, a forest patch and houses were present approximately 1.5 km upstream of the examined clearing-to-forest transition, while the approaching WT flow was not disturbed by any upstream forest patch. This might create different onflow conditions, because the flow reaching the lidar forest edge can still be affected by the upstream located obstacles when the clearing length turns out to be insufficient. Moreover, there might have been deviations in forest structure and density between the real and the modeled forest, since exact information about these quantities were not available for the lidar site. The efficiency of the flow distortion by a forest increases with increasing forest density (e.g. CASSIANI et al., 2008). These mentioned uncertainties concern the ability of remodeling the AM conditions in the WT. Regarding the AM dataset, insufficient statistics might have also caused a deviation from the WT data.

Using LES, one objective of the present study is to identify which of the above mentioned uncertain-

ties can explain the observed differences between AM and WT. For this purpose different LES set-ups are simulated to investigate the effect of forest density, clearing length, Coriolis force and atmospheric stability on the IBL structure. LES especially enables to examine the effect of atmospheric stability, which is one of the main differences between the WT set-up and the AM conditions. Furthermore, it is investigated if the available lidar statistics allow to identify the mean IBL structure, which would be representative for the conditions during the sampling periods of the AM data. Another objective of this LES study is to reproduce the distinct IBL deformation that was observed in the AM data. This step provides the opportunity of testing our LES model and the used set-ups against multi-dimensional data from the field. It shall be noted that the present investigation focuses on situations with moderately strong wind speeds and does not refer to the simulation of individual severe wind gusts, which have been investigated e.g. in a recent wind tunnel study by [TISCHMACHER and RUCK \(2013\)](#).

Prior to the discussion of the results, a brief description of the field experiment, wind tunnel model and LES set-ups is given in the following chapter. As a first step of the systematic parameter study, the LES data of an idealized WT-like set-up with neutral stratification are compared to the WT data. The discussion of these results is presented together with the results of the parameter studies in the third chapter of this article, followed by a summary of the conclusions.

## 2 Measurement and model set-up

### 2.1 Doppler Lidar experiment

Doppler lidars use pulses of infrared light to remotely determine the line-of-sight velocity of aerosol particles in the atmosphere, which move with the wind. Depending on the used pulse width, the pulse repetition frequency and the sampling frequency, the line-of-sight wind can be measured with a spatial resolution of 10 to 100 m and a precision of approximately  $0.15 \text{ m s}^{-1}$ .

In a field study in winter 2009/2010 two Doppler lidars, a passive temperature and humidity profiler as well as an energy balance station were set-up near a forest edge in Hatzenbühl (Germany) to investigate the wind field in front of and above the forest ([TRÄUMNER et al., 2012](#)). The used lidar data for the present study were obtained by the Doppler lidar “WindTracer” (from Lockheed Martin Coherent Technologies Inc.) in a scanning mode, moving the laser beam in vertical slices perpendicular to the forest edge from  $0$  to  $10^\circ$  elevation. Details of the instrument can be found in [TRÄUMNER et al. \(2011\)](#).

The lidar data were divided by the cosine of the elevation angle to estimate the horizontal wind velocity, projected on a Cartesian grid with a horizontal resolution of 50 m, and a vertical resolution of 15 m and averaged over 15 min. For the following discussion of

the results, a 15-min average is defined as one ensemble member (EM). For a wind direction nearly perpendicular to the edge, 28 EM with stable and nine EM with unstable atmospheric conditions were available. This resulted in one ensemble average over the stable cases and one ensemble average over the unstable cases. Since heat flux data were not available for all of the selected EM, the classification into stable and unstable EM was based on vertical temperature gradients (stable:  $\frac{\partial\theta}{\partial z} > 0.001 \text{ K m}^{-1}$ , unstable:  $\frac{\partial\theta}{\partial z} < -0.001 \text{ K m}^{-1}$ ), derived from vertical profiles of the potential temperature in the lowest 300 m. Overall, heat fluxes covered a range of  $-0.03 \text{ K m s}^{-1}$  to  $0.05 \text{ K m s}^{-1}$  during this measuring campaign.

Differently to the WT and the LES, the flow direction cannot be kept constant and perpendicular during the AM and might show natural variations. However, the EM from the lidar measurements were chosen in a way that it is reasonable to assume that the mean velocity component perpendicular to the line-of-sight is zero.

The used set-up and analysis technique enables a two-dimensional vertical view of the wind field from about 850 m in front of the forest edge to 1000 m behind the edge, with a vertical extension of 75 m closest to the lidar and up to 850 m downstream of the edge. Upstream of the forest edge, another forest patch and a residential area were present, starting at a distance of  $\sim 1.5 \text{ km}$  from the edge.

### 2.2 Wind tunnel model

A tree model of the forest at the Hatzenbühl site was constructed with a scale of 1:200 and positioned in a closed 29-m long atmospheric boundary layer wind tunnel. An initial wind profile following a power law with a profile exponent of 0.26 was applied. The wind velocity in front of and above the model forest was measured with a two-dimensional laser Doppler anemometer along sixteen vertical profiles at heights of 0 to 0.4 m (0 to 80 m) at locations from 0.1 m (20 m) in front of the edge to 1.3 m (260 m) in the tree stand. A detailed description of this technique can be found in ([RUCK, 1987](#)). For more information on the WT set-up see also [TRÄUMNER et al. \(2012\)](#).

### 2.3 Large-Eddy Simulation

#### 2.3.1 Model basics

For the presented study, the **PAR**allelized **LES** Model **PALM**<sup>1</sup> ([RAASCH and ETLING, 1998](#); [RAASCH and SCHRÖTER, 2001](#)) was used for a dry atmosphere. PALM is based on the non-hydrostatic incompressible Boussinesq equations and the conservation equations of energy and mass. Advection terms were solved according to the fifth-order scheme after [WICKER and SKAMAROCK \(2002\)](#). A third-order Runge-Kutta scheme was

<sup>1</sup>At revision 874, <http://palm.muk.uni-hannover.de/browser?rev=874>

applied for the time integration (WILLIAMSON, 1980). The Poisson equation for pressure that ensures incompressibility, was solved by the means of Fast Fourier Transformation. To model the effect of turbulence scales smaller than the numerical grid size on the large-scale flow (DEARDORFF, 1980), an additional prognostic equation is solved for the subgrid-scale (SGS) turbulent kinetic energy (TKE). Random perturbations were initially imposed on the horizontal velocity field to trigger turbulence. Lateral domain boundaries were cyclic. No-slip conditions were prescribed at the domain surface and the surface momentum fluxes were parametrized using Monin-Obukhov Similarity Theory (MONIN and OBUKHOV, 1954). At the upper domain boundary, free-slip conditions were applied.

PALM has been successfully used to simulate various atmospheric and laboratory scenarios under neutrally (e.g. LETZEL et al., 2008) and weakly stably stratified conditions (STEINFELD et al., 2007), as well as under convective conditions (e.g. RAASCH and FRANKE, 2011). Flow phenomena have not only been investigated above homogeneous surfaces, but also within heterogeneously heated convective boundary layers (e.g. LETZEL and RAASCH, 2003; STEINFELD et al., 2008; SÜHRING and RAASCH, 2013) and in neutrally stratified flows around obstacles (INAGAKI et al., 2012).

The effect of the forest on the turbulent flow was modeled by a canopy model, which is implemented in PALM according to SHAW and SCHUMANN (1992) and WATANABE (2004). Due to form (pressure) and viscous drag, the forest acts as a sink for momentum. This behavior is described at each numerical grid point as a grid-box-averaged effect on the resolved-scale turbulent flow by adding the term  $F_{u_i} = c_d a U \bar{u}_i$  to the momentum equations:

$$\begin{aligned} \frac{\partial \bar{u}_i}{\partial t} = & -\frac{\partial (\bar{u}_k \bar{u}_i)}{\partial x_k} - \frac{\partial \bar{p}}{\partial x_i} - \frac{\partial \bar{p}^*}{\partial x_i} \\ & + \frac{\bar{\theta}^*}{\theta_0} g \delta_{i3} - \frac{\partial \tau_{ki}}{\partial x_k} - F_{u_i}. \end{aligned} \quad (2.1)$$

An overbar denotes the spatial filtering of the subgrid scales, which corresponds to a volume (grid box) average. Indices  $i, k \in \{1, 2, 3\}$  describe edge-perpendicular, edge-parallel and vertical velocity components  $u_1 = u$ ,  $u_2 = v$ ,  $u_3 = w$  and spatial coordinates  $x_1 = x$ ,  $x_2 = y$  and  $x_3 = z$ , respectively. Remaining quantities are time  $t$ , kinematic pressure  $p$ , perturbation pressure  $p^*$ , potential temperature fluctuation  $\theta^*$  from the horizontal mean, reference state  $\theta_0$ , gravitational acceleration  $g$ , and the Kronecker delta  $\delta$ . Implying K-theory, the SGS stress tensor  $\tau_{ki} = -K_m \left( \frac{\partial \bar{u}_i}{\partial x_k} + \frac{\partial \bar{u}_k}{\partial x_i} \right)$ , with  $K_m = c_m l \sqrt{e}$  being the turbulent diffusion coefficient for momentum. The Smagorinsky coefficient  $c_m$  is set to 0.1 and  $e$  is the SGS TKE, which is calculated by an additional prognostic equation as described further below. The mixing length  $l$  under neutral and unstable conditions equals either the numerical grid length  $\Delta$  or 1.8 times the distance

to the surface, whichever is the smaller value. The efficiency of momentum reduction by the forest canopy as described in term  $F_{u_i}$  depends on drag coefficient  $c_d$ , leaf area density  $a$ , absolute velocity  $U = (\bar{u}^2 + \bar{v}^2 + \bar{w}^2)^{1/2}$  and the respective velocity component  $\bar{u}_i$ . Furthermore, the forest also has an effect on the unresolved small-scale turbulence, which is considered by the additional term  $F_e = 2c_d a U e$  in the prognostic equation for the SGS TKE  $e$ :

$$\begin{aligned} \frac{\partial e}{\partial t} = & -\frac{\partial (\bar{u}_k e)}{\partial x_k} - \tau_{ki} \frac{\partial \bar{u}_i}{\partial x_k} + \frac{g}{\theta_0} W_3 \\ & + \frac{\partial}{\partial x_k} \left( 2K_m \frac{\partial e}{\partial x_k} \right) - \epsilon - F_e, \end{aligned} \quad (2.2)$$

with  $W_3$  being the vertical component of the SGS sensible heatflux  $W_k = -K_h \frac{\partial \bar{\theta}}{\partial x_k}$ , where  $\theta$  is the potential temperature and  $K_h = K_m \left( 1 + \frac{2l}{\Delta} \right)$  is the turbulent diffusion coefficient for heat. The dissipation rate  $\epsilon$  is parametrized by  $\epsilon = (0.19 + 0.74 \frac{l}{\Delta}) \frac{e^{3/2}}{T}$ .

With the widely used approach for  $F_e$ , proposed by SHAW and SCHUMANN (1992), it is assumed that plant elements rapidly break down turbulence structures to smaller scales. It is further assumed that this small-scale turbulence, generated as wake turbulence in the lee of plant elements, is smaller than the energy-containing scales of SGS TKE and therefore rapidly dissipated (EDBURG et al., 2012). This type of canopy model has been successfully applied in LES studies of homogeneous canopy flow (e.g. KANDA and HINO, 1994; SHAW and SCHUMANN, 1992; SU et al., 1998; SU et al., 2000; WATANABE, 2004) as well as forest edge flow (e.g. CASIANI et al., 2008; DUPONT and BRUNET, 2008, 2009; YANG et al., 2006a; YANG et al., 2006b).

When simulating a heated atmospheric boundary layer, the forest additionally acts as a source  $F_\theta = \frac{\partial Q_\theta}{\partial z}$  for heat (SHAW and SCHUMANN, 1992) in the first law of thermodynamics:

$$\frac{\partial \bar{\theta}}{\partial t} = -\frac{\partial (\bar{u}_k \bar{\theta})}{\partial x_k} - \frac{\partial W_k}{\partial x_k} - F_\theta, \quad (2.3)$$

$F_\theta$  is described as the vertical derivative of the upward vertical kinematic heat flux

$$Q_\theta(z) = Q_\theta(H) \exp(-\alpha P), \quad P = \int_z^H a dz. \quad (2.4)$$

$Q_\theta(H)$  is the prescribed heat flux at the forest top ( $z = H$ ), starting of which the heat fluxes at the different levels inside the forest are calculated by this decaying exponential function of the downward cumulative plant area index  $P$ . The extinction coefficient  $\alpha$  is set to 0.6. With this approach it is assumed that the foliage inside the forest is heated by the solar radiation penetrating into the forest, according to the distribution of net radiation as suggested by BROWN and COVEY (1966). This parametrization has been applied in LES of canopy flow by SHAW and SCHUMANN (1992) as well as BOHRER

et al. (2009), and found independently in high resolution LES with resolved tree canopy structures by SCHRÖTTLE and DÖRNBRACK (2013).

The set of model equations is completed by the continuity equation for an incompressible flow:  $\frac{\partial \bar{u}_k}{\partial x_k} = 0$ .

### 2.3.2 Simulation set-ups

Prior to the comparison between lidar and LES data, PALM and the applied canopy model were tested against the WT data. The flow across an idealized forest edge was simulated under neutral conditions, representing the situation in the WT as closely as possible. The model domain extended over  $154H \times 38H \times 13H$  in stream-wise ( $x$ ), spanwise ( $y$ ) and vertical ( $z$ ) direction, with  $H = 30\text{m}$  being the forest height (Fig. 1). A grid resolution of 3 m was used in each direction, resolving the forest with 10 grid points in the vertical. In a sensitivity study with different grid sizes (not shown), this resolution has been tested to be sufficient to resolve the canopy-scale turbulence structures. The forest covered  $33H$  (= forest length  $L_{F0}$ ) of the domain length  $L_x$  and extended over the total domain width  $L_y$ . With the cyclic boundary conditions, this resulted in a total clearing length of  $L_{Cl} = L_x - L_{F0} = 121H$ . The domain height was chosen in a way that developing CTS are not affected by the free-slip rigid domain top. With the chosen domain width, being a multiple of the separation scale of CTS (e.g. FINNIGAN et al., 2009), it was assured that the CTS are properly captured. The forest was assumed to be horizontally homogeneous. This is in slight contradiction to the real forest and the WT set-up, where the individual tree heights and species (broad-leafed trees, conifers) were considered. However, the vertical structure was inhomogeneous as described by the vertical profile of plant area density  $a$  in Fig. 2, where the vertical axis has been normalized with forest height  $H$ . The plant area index  $\text{PAI} = \int_0^H a(z) dz$  was set to 8 for this first simulation, hereafter named **PAI8**, and varied to 2 and 4 in the following studies. The value of  $\text{PAI} = 8$  lies within the typical range of forest densities observed in coniferous and broad-leafed forests, as present at the lidar site. A constant canopy drag coefficient of  $c_d = 0.2$  was assumed, which is a typical value for trees and has been applied in other forest-edge-flow studies (e.g. CASIANI et al., 2008; DUPONT and BRUNET, 2008; KATUL and ALBERTSON, 1998). In accordance to the WT conditions, the Coriolis force was neglected. The flow forcing was accomplished by a constant direct pressure gradient of  $\frac{\partial \bar{p}}{\partial x} = -0.0017\text{Pa m}^{-1}$  (see third term of Eq. 2.1) in the  $x$ -direction, assuring for a purely edge-perpendicular flow at all heights. This value was determined by tuning the pressure gradient in order to match the mean wind profiles of LES and WT (Fig. 3). For normalization, the values  $u_{\text{ref}} = 8.3\text{m s}^{-1}$  in the LES and  $u_{\text{ref}} = 7.6\text{m s}^{-1}$  in the WT were taken at the forest edge at  $2H$  above the ground. A constant roughness length of  $z_0 = 0.1\text{m}$  was set for the forested as well as for the non-forested area. Since the forest acts as the main momentum sink, this

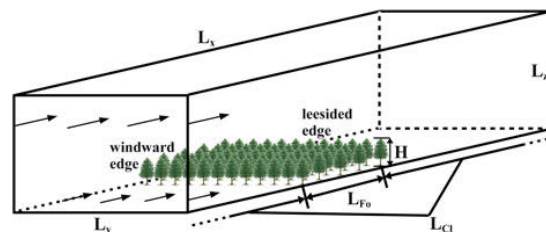


**Figure 1:** Sketch of the LES model domain.  $L_x$ ,  $L_y$ ,  $L_z$  are domain length, width and height, respectively. The forest extends over a length of  $L_{F0}$  in  $x$ -direction and over the total domain width  $L_y$ . The forest height is  $H = 30\text{m}$ . The clearing length  $L_{Cl} = L_x - L_{F0}$  describes the total length of the unforested part of the domain. The forest edge is oriented perpendicular to the mean flow (marked by arrows).

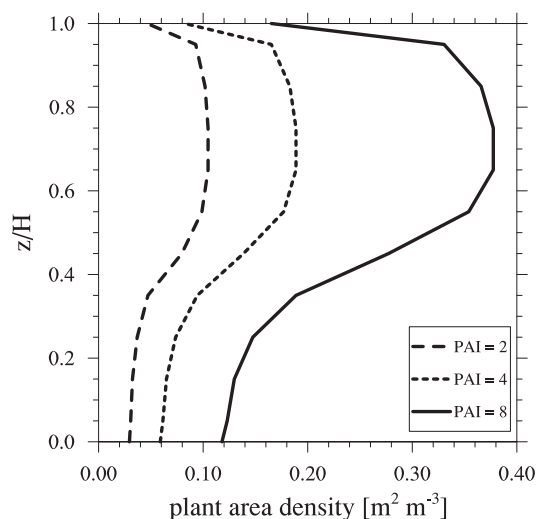


**Figure 2:** Vertical profiles of different plant area densities. The ordinate is normalized with forest height  $H$ . Plant area indices (PAI) of 2, 4 and 8 are used, each with the same vertical plant distribution.

value does not really come into effect for the forested surface and is just prescribed for completeness.

In the following, the set-ups of the parameter studies are described and summarized in Tab. 1. As information on forest density of the real and the model forest was not available, **PAI8** was repeated with  $\text{PAI} = 2$  (**PAI2**) and  $\text{PAI} = 4$  (**PAI4**) to quantify the effect of forest density on the IBL structure, c.f. Fig. 2 in DUPONT and BRUNET (2009). Thereby the vertical distribution of plant area was maintained (Fig. 2). One difference between the lidar experiment and the WT set-up were the different onflow conditions. While a forest patch and houses were present 1.5 km upstream of the examined forest edge at the lidar site, the flow across the WT forest was not disturbed by any upstream forest edge. In order to study the effect of an upstream located forest on the IBL development downstream of a clearing-to-forest transition, LES with different clearing lengths  $L_{Cl}$  were conducted. The existence of an upstream located forest



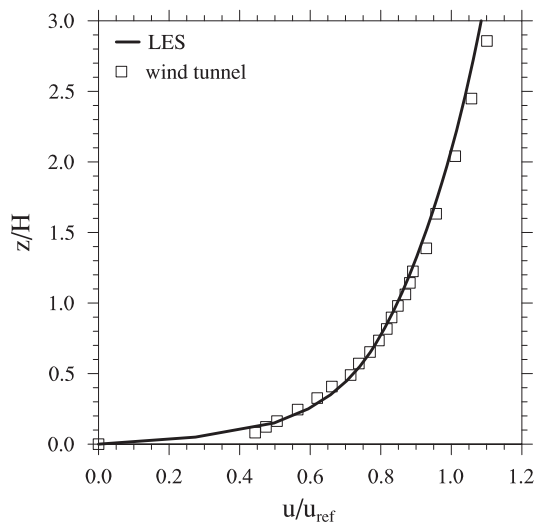


**Figure 3:** Vertical profiles of  $u$ -velocity (edge-perpendicular component) from wind tunnel (squares) and LES (solid line). Profiles are taken at  $x = -1H$  ( $1H$  upstream of the windward edge) and are normalized with reference speed  $u_{\text{ref}} = u(x = 0H, z = 2H)$ . The ordinate is normalized with forest height  $H$ . Velocities are time averaged and LES data are additionally averaged along the edge-parallel direction.

**Table 1:** Overview of the used LES set-ups (N: neutral, U: unstable, Q: prescribed kinematic heat flux at clearing surface and forest top).

LES run	PAI	$L_{cl}$	Coriolis force	stratification	$u_{\text{ref}}$ ( $\text{ms}^{-1}$ )
PAI8	8	121 $H$	no	N	8.3
PAI2	2	121 $H$	no	N	8.5
PAI4	4	121 $H$	no	N	8.3
LCL5	8	51 $H$	no	N	8.4
LCL10	8	102 $H$	no	N	9.6
LCL20	8	204 $H$	no	N	10.7
GEO-N	8	51 $H$	yes	N	5.3
GEO-U1	8	51 $H$	yes	U	6.4
				( $Q = 0.05 \text{ K ms}^{-1}$ )	
GEO-U2	8	51 $H$	yes	U	7.0
				( $Q = 0.1 \text{ K ms}^{-1}$ )	

edge in the LES results from the cyclic lateral boundary conditions. Based on the set-up of **PAI8**, clearing lengths of  $L_{Cl} = 51H$ ,  $L_{Cl} = 102H$  and  $L_{Cl} = 204H$  (**LCL5**, **LCL10** and **LCL20**) were simulated. The aspect ratio  $r = L_{Fo}/L_{Cl}$  was held constant at 0.5 among the three simulations to keep the averaged surface friction in the model domain constant. This setting is necessary to maintain the shape of the vertical profile of the mean wind, so that the flow conditions of the three simulations are as similar as possible.

Another difference between lidar experiment and WT set-up was that Coriolis force and thermal stratification could not be considered in the latter. In order to quantify the effect of these differences in atmospheric conditions on the IBL structure, LES with geostrophic

forcing were conducted under Neutral (**GEO-N**) and Unstable (**GEO-U**) conditions, based on the set-up of **LCL5** where the clearing length matches the one at the lidar site. Under atmospheric conditions, the pressure term in Eq. 2.1 is described by  $\frac{\partial p}{\partial x_i} = \varepsilon_{ijk} f_j \bar{u}_k + \varepsilon_{ijk} f_3 \bar{u}_{k_g}$ . Index  $g$  denotes the geostrophic wind components  $u_g$  and  $v_g$ , which were set to  $10.0 \text{ ms}^{-1}$  and  $-4.5 \text{ ms}^{-1}$  respectively. The Coriolis parameter  $f_i = (0, 2\Omega \cos(\varphi), 2\Omega \sin(\varphi))$  is described by the Earth's rotation  $\Omega = 2\pi/24 \text{ hr}$  and the chosen latitude  $\varphi = 55^\circ$ . With the wind shift with height due to the Coriolis force, this forcing produces a near-surface flow direction approximately perpendicular to the forest edge. The domain height was increased to 2700 m, in order to allow the Ekman-layer wind profile to develop appropriately. To save computational resources, the vertical grid spacing was gradually stretched to 25 m above  $z = 450 \text{ m}$ , which is well above the levels affected by the forest edge. The simulations with unstable stratification (**GEO-U**) were additionally driven by a constant sensible heat flux, with the same value at the clearing surface and the forest top. By keeping the heat input homogeneous, the IBL development can be studied purely as a result of roughness changes, with additional effects of buoyancy. Two simulations were conducted with heat fluxes of  $0.05 \text{ K ms}^{-1}$  (**GEO-U1**) and  $0.1 \text{ K ms}^{-1}$  (**GEO-U2**). These values were chosen to provide a general estimate about the behavior of the IBL development for moderately and strongly heated atmospheric boundary layers. There was no attempt to simulate the real heat fluxes, because flux values were not available for the sampling period of the unstable lidar EM. Both simulations were initialized with a constant  $\theta = 300 \text{ K}$  up to  $z = 500 \text{ m}$ , followed by a strong inversion of  $0.01 \text{ K m}^{-1}$  up to the domain top. For a better comparability of these atmospheric LES with results from field measurements or other LES, some background information is presented. Figure 4 presents Hovmöller diagrams of the horizontally and half-hourly averaged  $\theta(z/H, t)$  for the LES cases **GEO-U1** (a) and **GEO-U2** (b). In both cases, the well-mixed convective boundary layer warms due to the prescribed surface heating, which leads to an increase of the boundary-layer depth  $z_i$  in the temporal evolution. Thereby  $z_i$  is defined as the height at which the vertical temperature gradient reaches its maximum value (following SULLIVAN et al., 1998). As expected,  $\theta$  and in turn  $z_i$  increase faster when a stronger surface heating is present (**GEO-U2**). The average  $z_i$  (over last three hours) equals  $34H$  ( $\hat{=} 1020 \text{ m}$ ) for **GEO-U1** and  $40H$  ( $\hat{=} 1200 \text{ m}$ ) for **GEO-U2**. We calculated vertical profiles of the Richardson number  $Ri = \frac{g/\theta_0 \partial \theta / \partial z}{(\partial u_h / \partial z)^2}$ , derived from the horizontally and temporally averaged vertical profiles of  $\theta$  and  $u_h = \sqrt{u^2 + v^2}$ . For the two convective regimes **GEO-U1** and **GEO-U2**, maximum  $Ri$  values of  $-1.5$  and  $-4.0$  were found respectively within the convective boundary layer.

The overbar in Eq. 2.1–2.3 is not carried along after this point.

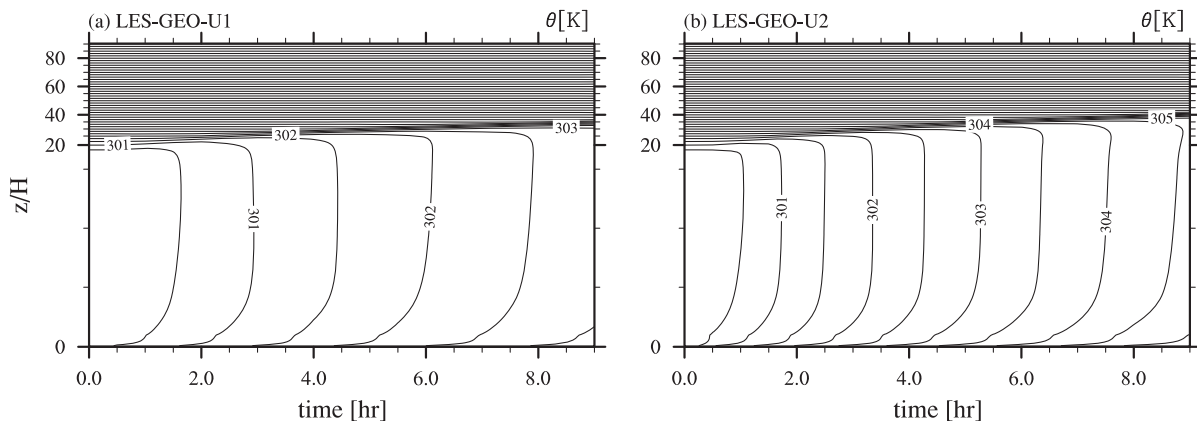


**Figure 4:** Hovmöller diagrams of the horizontally and half-hourly averaged potential temperature  $\theta$  for the LES cases (a) **GEO-U1** and (b) **GEO-U2**.

### 2.3.3 Analysis Methods

The comparison between LES, AM and WT data was based on streamwise vertical slices of standard deviation  $\sigma_u$  of streamwise velocity  $u$ . This quantity was used exclusively, as it was also used as a basis for the comparison between the AM and WT data in TRÄUMNER et al. (2012), and it provides information about the turbulence level and is therefore adequate to retrieve information about the IBL structure.  $\sigma_u$  was calculated in the same way as for AM and WT datasets, using the temporal eddy-covariance method (e.g. FOKEN, 2008).

The vertical slices of  $\sigma_u$  were output after the flow had reached a (quasi-) stationary state. To exclude the effect of different mean background wind speeds between AM, WT and the different LES, resulting from the different atmospheric conditions, all presented data were normalized with an individual reference velocity  $u_{\text{ref}}$  of the respective AM, WT and LES cases. In the LES data, the calculation of  $\sigma_u$  was based on a three-hour time average of the  $u$ -velocity, and for better statistics, the calculated  $\sigma_u$  was hereafter averaged along the edge-parallel direction, if not mentioned otherwise.

To evaluate the effect of the parameters on the IBL structure, the IBL heights were calculated for each presented dataset. Several approaches exist to estimate the IBL depth, summarized by GARRATT (1990). The IBL top in the present study is defined at the height above which  $\sigma_u \leq 1.01\sigma_{u_0}$  (following SHIR, 1972). According to SHIR (1972), who used the surface stress to estimate the IBL depth related to a pure roughness change,  $\sigma_{u_0}$  is the near-surface value of  $\sigma_u$  upstream of the forest edge, where flow characteristics should be representative for the underlying surface conditions. However, with  $\sigma_{u_0}$  values taken from certain distances upstream of the forest edge, calculated IBL heights deviated up to  $1H$  from visually identified IBL heights. The reason for this difference is that with a relatively short clearing length of  $51H$ , used in several simulations to match lidar site conditions, the flow above the clearing has not fully adjusted

to the surface conditions after having been disturbed at the leesided forest edge. Thus, the flow reaching the windward forest edge still carries the turbulence that has been produced above the forest upstream of the clearing. Therefore, these  $\sigma_{u_0}$  values are not representative for the surface conditions of the clearing. To take into account that the advected turbulence increases the turbulence level in front of and above the forest, a modified  $\sigma_{u_0}$  was calculated by averaging  $\sigma_u$  values at  $x = -1H$  within a layer between  $z = 2H$  and  $z = 3H$ . This specific layer average of  $\sigma_{u_0}$  was used because it represented the only overlap between AM, WT and LES data at this specific  $x$ -position.

To quantify which fraction of the observed difference in turbulence level between AM and WT can be attributed to each parameter, an IBL-averaged  $\sigma_u$  ( $\langle\sigma_u\rangle_{\text{IBL}}$ ) was calculated. For comparison reasons,  $\langle\sigma_u\rangle_{\text{IBL}}$  was defined in all datasets as the average over the IBL region from  $z = 1.4H$  to the IBL top and up to a distance of  $10H$  downstream of the forest edge, because this was the maximum coverage of the WT data.

Furthermore, the shear length scale  $L_s = \frac{u(H)}{(\partial u / \partial z)_{z=H}}$  (RAUPACH et al., 1996) that defines the depth of the shear layer at the canopy top, was calculated for a better comparability of our results with results from previous LES studies and field experiments.

## 3 Results and discussion

To illustrate the IBL development behind a forest edge, a snapshot<sup>2</sup> of the absolute value of the three-dimensional rotation  $|\zeta| = |\varepsilon_{ijk} \partial_{x_j} u_k|$  is presented in Fig. 5. The snapshot is taken after three hours of simulation time from LES PA18. This quantity has been chosen for this

<sup>2</sup>The corresponding animation is available under <http://palm.muk.uni-hannover.de/wiki/gallery/movies/forest>. It was created with VAPOR, a product of the Computational Information Systems Laboratory at the National Center for Atmospheric Research, [www.vapor.ucar.edu](http://www.vapor.ucar.edu)

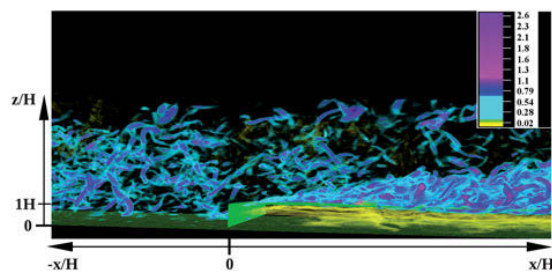


**Figure 5:** Three-dimensional snapshot of the absolute value of the three-dimensional rotation  $|\zeta| = |\varepsilon_{ijk} \partial_{x_j} u_k|$  [ $\text{s}^{-1}$ ] after three hours of simulation time from PAI8. High values in pink illustrate strong turbulence, lower values in yellow mark areas with weak turbulence. The mean flow is directed from left to right and the forest edge is oriented perpendicular to the streamwise direction. The forest edge is at  $x = 0H$  and is marked by the light green isosurface.

illustration as it is a measure for the flows turbulence intensity. The mean flow direction is from left to right and the forest edge is at  $x = 0H$ , marked by the green isosurface. High rotation values are drawn in pink, low values in yellow and intermediate values in blue.

Figure 5 illustrates to what extent a turbulent flow is modified when coming up against a forest edge. In front of the forest, the approaching flow is rather turbulent, with different scales of turbulence being quite unorganized. Entering the forest, the turbulence is damped due to pressure and viscous drag forces. Meanwhile above the forest, turbulence is effectively generated due to the strong velocity shear near the forest top. With increasing distance from the forest edge, the developing turbulence structures grow in size and strength, forming a layer of high turbulence activity, within the flow adjusts to the new surface conditions. This layer represents the IBL.

### 3.1 Comparison between LES and wind tunnel data

As a first step, the LES data of PAI8 are compared to the WT data. This step is taken to demonstrate the capability of PALM, with the implemented canopy model, to adequately reproduce the IBL properties downstream of a forest edge. Figure 6 presents normalized standard deviation  $\sigma_u/u_{\text{ref}}$  from WT (a) and LES (b). Axes are normalized with forest height  $H$  and the forest edge is located at  $x = 0H$ . White space in the plots masks areas where WT or AM data are not available due to technical constraints. LES data are available inside the forest, but to keep the focus on the area of interest above the forest, this area is masked in the LES data as well. The dashed black lines represent the IBL tops, calculated as described in Sect. 2.3.3.

Data of WT and LES generally show a qualitative and quantitative agreement regarding the shape of the IBL and the turbulence intensity. As expected, the IBL grows with distance to the forest edge, resulting from the nature of the CTS evolution of e.g. horse shoe vortices as simulated for forest canopy flow by FINNIGAN

et al. (2009). The maximum values of  $\sigma_u$  do not occur directly behind the edge but further downstream. This behavior corresponds to previous findings (e.g. DUPONT and BRUNET, 2008; MORSE et al., 2002) and can also be explained by the stepwise development process of CTS behind forest edges. As previously explained, the developing CTS grow in size and strength with increasing distance to the edge and thus, the strongest CTS occur further downstream from the edge. Additionally, the turbulence production is suppressed in the region near the forest edge, where the mean upward-directed flow, as a result from horizontal flow deceleration, transports relatively slow and less turbulent air out of the forest (e.g. DUPONT and BRUNET, 2008; MORSE et al., 2002). Regarding the observed turbulence level from WT and LES, similar  $\sigma_u$  values have been reported by YANG et al. (2006a), derived from field, WT and numerical experiments. The overall agreement between WT and LES data allows the conclusion that our simulations adequately account for the drag effect of the forest on the turbulent flow. Our LES model can therefore be used to expose the reasons for the differences found between real-world lidar measurement and wind tunnel study.

### 3.2 Comparison between LES and field data

On the right-hand side of Fig. 6, the corresponding AM data are presented for the unstable (c) and the stable (d) ensemble averaged cases. The dashed black lines again mark the IBL tops. For the stable case (d), the 1%  $\sigma_u$ -criterion had to be changed to 35% to determine a reasonable IBL top, because under stable conditions the relatively small upstream  $\sigma_u$  values are not retained anywhere above the forest (as can be seen in Fig. 7 (b)). The relatively small  $\sigma_u$  values below  $z = 3H$  in front of the forest edge can be attributed to the fact that the stable thermal stratification is most pronounced near the surface. Hence, turbulence suppression is much stronger there than in larger heights or above the forest.

Comparing Fig. 6 (c) and (d) with the neutral LES case (b), it is evident that IBL height and range of  $\sigma_u$  values of the neutral LES lie in between the lidar observations under unstable and stable conditions, as also observed by TRÄUMNER et al. (2012) for the comparison between AM and WT data. In the unstable case, the IBL grows faster and higher than under neutral or stable conditions, probably caused by the additional turbulence generation by buoyancy, what will be discussed in Sect. 3.3.3. In turn, the suppression of turbulence under stable conditions leads to the observed lower IBL height and  $\sigma_u$  values. Now the question arises, whether the differences between AM and WT data can be purely explained by the effect of different stratification. Comparing e.g. the  $\langle \sigma_u \rangle_{\text{IBL}}$  values of the unstable lidar case (c) and the WT (a) with  $0.23 u_{\text{ref}}$  and  $0.19 u_{\text{ref}}$ , respectively, results in a deviation of nearly 20%. Besides the stratification, the effect of Coriolis force or differences in plant physical conditions such as forest density and clearing length might also be relevant and are therefore investigated in the following.

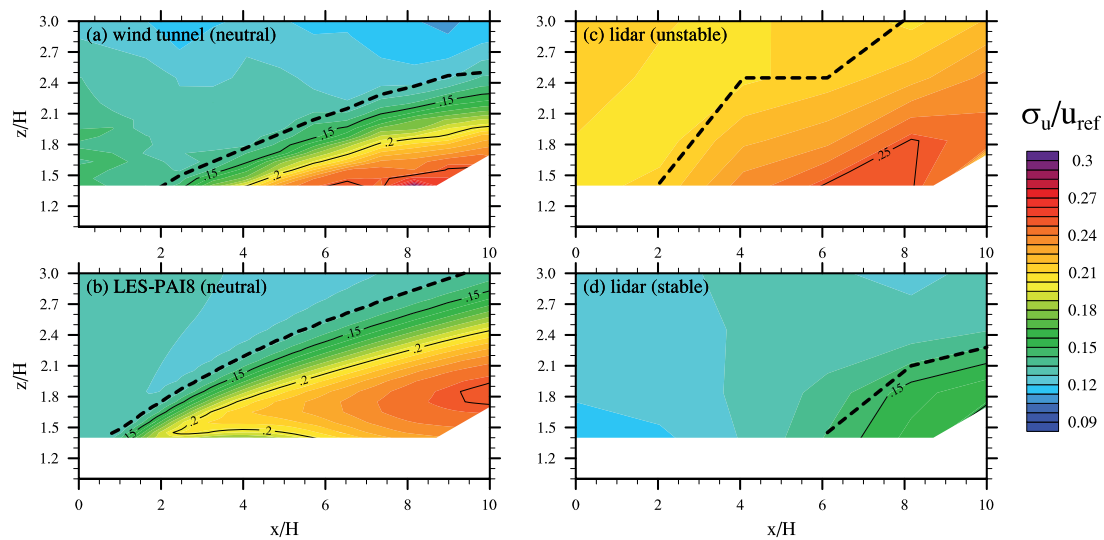


**Figure 6:** Streamwise vertical slices of mean normalized standard deviation  $\sigma_u/u_{\text{ref}}$  from (a) wind tunnel and (b) LES PAI8 under neutral conditions and from the lidar measurements under (c) unstable and (d) stable conditions. The dashed black lines mark the IBL tops. Isolines are plotted at steps of 0.05. Axes are normalized with forest height  $H$  and the forest edge is at  $x = 0H$ . White space masks areas where wind tunnel and lidar data are not available. For a better comparison, this area is also masked in the LES plot, even though LES data are available within the forest.

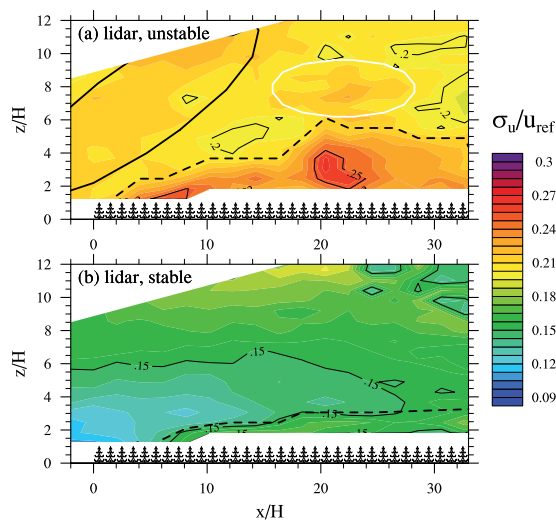


**Figure 7:** Lidar observations for (a) unstable and (b) stable conditions, as in Fig. 6 (c,d), but for an extended region. Trees mark the canopy layer. The white circle highlights an area with relatively high  $\sigma_u$  values, which might or might not be attributed to the IBL. The occurrence of such large structures in the  $\sigma_u$  field makes a clear identification of the IBL height difficult.

Since the lidar observations are the starting point for this investigation, the  $\sigma_u$ -slices of Fig. 6 (c) and (d) are presented for a horizontally and vertically extended region in Fig. 7 (a) and (b), respectively. Providing two-dimensional flow information for such an elongated area in the field is a unique feature of the Doppler lidar measurements. Looking at the extended  $\sigma_u$ -field in Fig. 7 (a)

first of all reveals that a clear identification of the IBL height is difficult. The IBL as bounded by the dashed black line has no smooth boundary. Moreover, it is not clear whether or not the large region of enhanced turbulence (white circle) is to be attributed to the IBL, which would significantly modify the IBL structure. According to the applied IBL criterion, the white-circled area does not belong to the IBL. However, the same high  $\sigma_u$  values that are observed within the IBL also occur within the circled area, which somehow connects this area to the IBL. The most probable reason for this indefinite IBL structure in the unstable lidar case is that the ensemble average over the available nine EM is insufficient to average out larger-scale turbulence structures, which occur in the form of convection or strong wind gusts. In order to try to reproduce the occurrence of such larger structures in the LES data, a statistical analysis was additionally carried out. This analysis will be presented subsequent to the discussion of the parameter study.

### 3.3 Effects of plant physical and atmospheric parameters on IBL development

#### 3.3.1 Forest density

As forest density information of the real forest was not available, the effect of an incorrectly modeled forest density on the IBL structure was investigated. Results for plant area indices of 2, 4 and 8 (PAI2, PAI4, PAI8) are presented in Fig. 8 (a–c), showing mean normalized standard deviation  $\sigma_u/u_{\text{ref}}$  for the same region as in Fig. 7. The dashed black lines mark the calculated IBL tops. In contrast to AM and WT data, LES data are

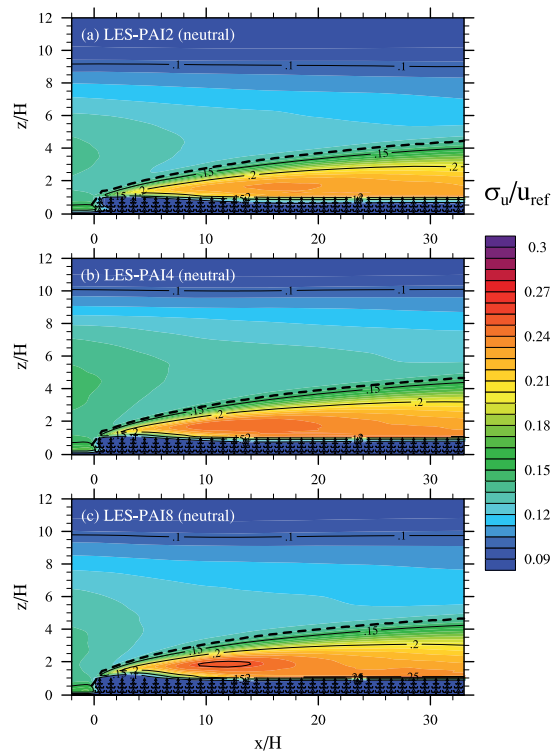


**Figure 8:** Streamwise vertical slices of mean normalized standard deviation  $\sigma_u/u_{\text{ref}}$  from LES under neutral stratification with different forest densities: (a) **PAI2**, (b) **PAI4** and (c) **PAI8**. The same region as in Fig. 7 is plotted. Trees mark the canopy layer. Dashed black lines mark the IBL tops. For comparison reasons, isolines are additionally plotted at steps of 0.05.

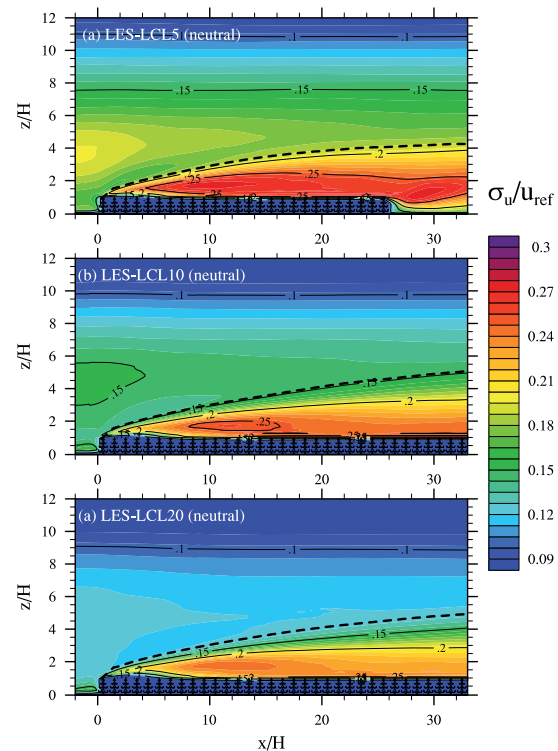


**Figure 9:** Same as Fig. 8 (c) with  $\text{PAI} = 8$ , but with different clearing lengths: (a)  $L_{\text{Cl}} = 51H$  (**LCL5**), (b)  $L_{\text{Cl}} = 102H$  (**LCL10**) and (c)  $L_{\text{Cl}} = 204H$  (**LCL20**). The forest lengths  $L_{\text{F0}}$  differ between the three cases, because the aspect ratio  $r = L_{\text{F0}}L_{\text{Cl}}^{-1}$  was held constant at 0.5. For that reason, the forest in (a) already ends at  $x \approx 26H$ .

also available inside and right above the forest, but these regions are not subject of the present investigation.

The comparison of **PAI2** (a), **PAI4** (b) and **PAI8** (c) shows no significant effect of forest density on IBL height. However, with a denser canopy, higher values of  $\sigma_u$  occur within the IBL, indicating that stronger CTS develop above denser forests. For example, the maximum  $\sigma_u$  value of  $0.25 u_{\text{ref}}$  for **PAI8** is 5% higher than the value for **PAI2**. At the same time, the maximum  $\sigma_u$  values can be found closer to the forest edge. These findings for  $\sigma_u$  can also be detected for the vertical momentum fluxes (not shown; calculated analogous to  $\sigma_u$  respective the variance of  $u$ ). One exception is that the IBL height is slightly lower for all **PAI** cases by about  $0.4H$  compared to the IBL heights derived from  $\sigma_u$ . And overall, the IBL momentum fluxes (absolute values) are smaller than  $\sigma_u^2$  by a factor of four, which agrees well with findings by **FINNIGAN (2000)** and **YANG et al. (2006a)**.

Regarding the adjustment of the momentum fluxes for different **PAI**, similar findings were reported by **DUPONT and BRUNET (2009)**, i.e. that momentum fluxes are higher above denser forests and the maximum fluxes occur closer to the forest edge. They attributed this behavior to the development of the different CTS stages,

which they found to be faster above denser canopies. This results from the stronger wind shear above denser forests (not shown), which forms due to the stronger flow deceleration within and acceleration above the canopy, caused by the higher drag. The stronger shear in turn leads to stronger turbulence generation and hence to a faster flow adjustment. The adjusted shear lengths of  $L_s/H = 0.37$  (**PAI2**),  $L_s/H = 0.25$  (**PAI4**) and  $L_s/H = 0.17$  (**PAI8**) also agree well with those determined by **DUPONT and BRUNET (2009)** as presented in their Fig. 4. Our  $L_s$  values further blend in nicely with data from wind tunnel and field experiments, as summarized by **RAUPACH et al. (1996)** and later also discussed by **FINNIGAN (2000)**, lending further confidence to our results.

However, since different forest densities produce only slight differences in the IBL structure, an incorrectly modeled forest density is probably not responsible for the observed large differences between AM and WT data.

### 3.3.2 Clearing length

In order to study the effect of upstream located obstacles on the forest edge flow with respect to the difference between AM and WT conditions, simulations with

clearing lengths of  $L_{Cl} = 51H$  (**LCL5**),  $L_{Cl} = 102H$  (**LCL10**) and  $L_{Cl} = 204H$  (**LCL20**) were carried out (Fig. 9 (a–c)), based on the set-up of **PAI8**. As mentioned earlier, the forest lengths  $L_{Fo}$  differ here, because the aspect ratio  $r$  was held constant to assure for a constant averaged surface friction.

Just like for the forest density, a variation in  $L_{Cl}$  exhibits no significant effect on the IBL height (marked by dashed black lines). It should be noted that the IBL heights are only similar up to  $x \approx 20H$ , because the forest in **LCL5** does not extend beyond  $x = 26H$ , in contrast to the other cases. In contrast to the similar IBL heights, the general level of  $\sigma_u$  values is found to increase with decreasing clearing length. For instance,  $\langle \sigma_u \rangle_{IBL}$  is with a value of  $0.24u_{ref}$  for **LCL5** 20% higher than for **LCL20**. The maximum  $\sigma_u$  value of  $0.29u_{ref}$  for **LCL5** is 12% higher compared to the value for **LCL20**. These higher values result from the fact that for shorter clearings the level of the advected turbulence from the leesided edge is still higher when reaching the windward forest edge, which contributes to the total IBL turbulence level. For example the background turbulence level, quantified by  $\sigma_{u_0}$  (Sect. 2.3.3) increases from  $0.16u_{ref}$  (**LCL20**) to  $0.19u_{ref}$  (**LCL5**), i.e. by 16%. The advection of a higher turbulence level, compared to the background turbulence above the IBL, can also be observed in the AM data (Fig. 7 (a): region between solid black lines). The higher turbulence level is advected from the upstream located houses and trees (not shown). Despite the increase in turbulence intensity from **LCL20** to **LCL5**, the adjusted shear lengths are equal for all **LCL** cases, with  $L_s/H = 0.17$  near the far end of each forest. This indicates that  $L_s$ , i.e. the depth of the shear layer, seems to depend mainly on forest density (see Sect. 3.3.1) and not on the effect of upstream obstacles. And this further confirms that the modification of the IBL structure from **LCL20** to **LCL5** is mainly a result of the modified background turbulence rather than of a modified shear layer.

Overall, higher  $\sigma_u$  values should be expected with shorter clearings. Hence, the presence of the upstream located forest patch and houses at the lidar site, which were not considered in the WT, can produce significantly higher turbulence levels. However,  $\sigma_{u_0} = 0.19u_{ref}$  in **LCL5** is still 10% lower than  $\sigma_{u_0} = 0.21u_{ref}$  in the unstable lidar case. The large differences in IBL height between AM and WT data cannot be explained by the effect of the clearing length.

### 3.3.3 Atmospheric stability

Contrary to the WT and the so far discussed LES setups, the lidar experiment took place in a real atmospheric boundary layer, where the atmospheric stability is usually never strictly neutral and where depending on the stability a more or less pronounced Ekman layer describes the boundary-layer wind profile. To estimate the effect of the background wind profile and the atmospheric stability on the IBL structure, additional LES

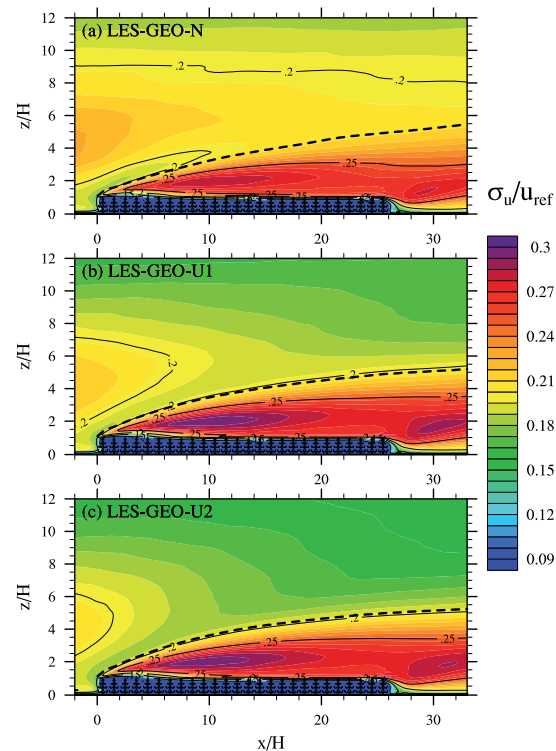


**Figure 10:** Same as Fig. 9 (a), but with a geostrophic flow forcing under (a) neutral conditions (**GEO-N**) and unstable conditions with kinematic heat fluxes of (b)  $0.05 \text{ K m s}^{-1}$  (**GEO-U1**) and (c)  $0.1 \text{ K m s}^{-1}$  (**GEO-U2**), prescribed homogeneously at the clearing surface and the forest top.

with geostrophic forcing under neutral and unstable conditions were conducted. These simulations were based on **LCL5**, as the clearing length of this case matches the one at the lidar site and the IBL turbulence level agreed already well with the level in the unstable lidar case.

Switching from direct pressure gradient forcing (**LCL5** in Fig. 9 (a)) to geostrophic forcing (**GEO-N** in Fig. 10 (a)) slightly modifies the IBL height. The IBL in the latter case grows slightly faster so that at  $x = 20H$  it is about  $1H$  higher than in the former case. This can be attributed to the stronger shear in **GEO-N**, due to the additional directional shear, that allows the developing CTS to propagate further upward than in **LCL5**. Another difference to **LCL5** is the overall higher IBL turbulence level in **GEO-N**, which is with  $\langle \sigma_u \rangle_{IBL} = 0.25u_{ref}$  an increase of 4%. The higher  $\sigma_u$  values are directly connected to the higher turbulence level of the background flow, which is advected from the leesided forest edge, as already reported in the previous section. Although the same clearing length is used in both cases, the advected turbulence level ( $\sigma_{u_0}$ ) that reaches the windward edge is higher in **GEO-N** by 10%. The reason for this is again the stronger shear, which helps to maintain the higher turbulence level over a longer distance from the lee edge.

Now with a characteristic atmospheric background wind profile (with Coriolis force), not only the IBL properties but also the background turbulence levels closely match those observed by lidar under unstable stratification (Fig. 7 (a)). While  $\sigma_{u_0}$  deviates by 35 % between the WT and the unstable lidar case, the  $\sigma_{u_0}$  values of the latter case and **GEO-N** are nearly equal with both being approximately  $0.21 u_{\text{ref}}$ . This finding allows the conclusion that the effect of a freely developing atmospheric wind profile versus a WT profile can additionally cause significant quantitative discrepancies regarding the level of turbulence, as observed by TRÄUMNER et al. (2012) between AM and WT data.

Under unstable conditions (**GEO-U1**), controlled in the LES by homogeneous surface and forest-top heating, the turbulence level in the lower part of the IBL slightly increases (Fig. 10 (b)) compared to the neutral case **GEO-N** (a). The maximum  $\sigma_u$  values of  $0.28 u_{\text{ref}}$  for **GEO-N** and  $0.29 u_{\text{ref}}$  for **GEO-U1** deviate by about 3 %. This can be associated with the effect of buoyancy that supports the CTS development due to the additional thermal instability. A similar finding was reported by BOHRER et al. (2009), who determined based on field and LES data that buoyancy contributes to or takes over part of the TKE production above the forest. They further stated that the TKE production by convection is characterized by a larger integral length scale, which might explain the slightly faster growth of the IBL from **GEO-N** to **GEO-U1**. But nevertheless, the IBL reaches the same height of  $z = 4.75 H$  at  $x = 20 H$  in both cases. Figure 10 (b) further reveals that the effect of the leesided edge is less pronounced under unstable conditions, i.e. lower turbulence levels are advected than in **GEO-N**. This results from the fact that the flow from the forest-to-clearing transition adjusts faster to the conditions above the clearing (not shown), what can be attributed to the large scale vertical mixing above the clearing due to the effect of buoyancy. Despite the homogeneous heating, the relative effect of buoyancy is much more pronounced above the clearing because the effect of shearing is relatively weak here. Above the forest, this relation is reversed, as most of the turbulence is generated by the strong wind shear. Now as can be seen in the upper part of the IBL, the  $\sigma_u$  values are smaller than in **GEO-N**, caused by the overall weaker background turbulence. This effect does not hold for the lower IBL part, where the buoyancy effect is more present. Overall, the mean IBL turbulence level increases by 4 % from **GEO-N** to **GEO-U1**. Increasing the heating from  $0.05 \text{ K m s}^{-1}$  (**GEO-U1**) to  $0.1 \text{ K m s}^{-1}$  (**GEO-U2**; Fig. 10 (c)) does not significantly modify the IBL properties. The effect of the leesided forest edge further decreases due to the further enhanced vertical mixing above the clearing, decreasing the turbulence level in the approaching flow. The IBL  $\sigma_u$  values remain nearly constant because the effect of the even weaker background turbulence compensates the effect of the stronger heating. We assume that the contribution of the shear-induced CTS to the IBL turbulence level

is invariant here, as THOMAS et al. (2006) found from tower measurements under varying atmospheric conditions that these CTS showed no dependency on atmospheric stability.

The above mentioned findings hold for the applied moderately strong wind speeds. At low wind speeds, the effect of buoyancy is suspected to dominate the effects of wind shear and therefore might prevent the development of an IBL, but this is yet to be investigated in detail. The highest  $\sigma_u$  values of **GEO-U1** and **GEO-U2** with nearly  $0.3 u_{\text{ref}}$  were not observed in the AM data (Fig. 7 (a)), although, with vertical temperature gradients in the range of  $-0.001$  to  $-0.004 \text{ K m}^{-1}$ , the thermal instability of the unstable lidar EM seemed to be similar to the one in **GEO-U1** ( $\frac{\partial \theta}{\partial z} = -0.002 \text{ K m}^{-1}$ ) and **GEO-U2** ( $\frac{\partial \theta}{\partial z} = -0.004 \text{ K m}^{-1}$ ). But since more concrete information on the thermal instability, e.g. based on measured heatfluxes, are not available for these lidar cases, we cannot make a definite statement at this point. Due to this incomplete information, our aim was not to reproduce the unstable lidar-experiment conditions, but rather to demonstrate possible effects of an unstable stratification on the IBL development for moderately and relatively strong heated atmospheric boundary layers.

The so far presented results show that variations of the parameters clearing length (i.e. upstream obstacles), Coriolis force and thermal instability (positive buoyancy) can cause deviations in the IBL turbulence level, which are of the same magnitude as the difference between the WT and the unstable lidar case. We can estimate that under (nearly) neutral conditions, an incorrect consideration of the clearing length or the total neglect of upstream obstacles has the major effect. Compared to the Coriolis-force effect on  $\langle \sigma_u \rangle_{\text{IBL}}$  with 4 %, the consideration of a finite clearing as present at the lidar site produced a 20 % higher  $\langle \sigma_u \rangle_{\text{IBL}}$ . Hence, the latter has a five-fold stronger effect. Under unstable conditions, it is complicated to separately distinguish the relative importance of each parameter based on the available LES data. This is connected with the fact that e.g. in a convective boundary layer, the effect of the Coriolis force is less pronounced due to the well-mixed state of the boundary layer. Furthermore, it was found that the advection of turbulence from the upstream forest decreases from neutral to unstable conditions. But in order to explicitly quantify the remaining importance of the clearing length relative to the buoyancy effect, further LES studies under unstable conditions need to be conducted. The understanding of forest edge flow in such conditions is still rather limited. We assume though that especially for short clearings with  $L_{\text{Cl}} < 50 H$  and relatively weak thermal instabilities, the neglect of an upstream forest in the WT probably leads to significantly larger errors than the assumption of neutral conditions.

Up to this point, the investigated parameters are all related to the possibility on how far the conditions from the field can be reproduced in the WT. But as previously mentioned, a clear identification of the IBL char-

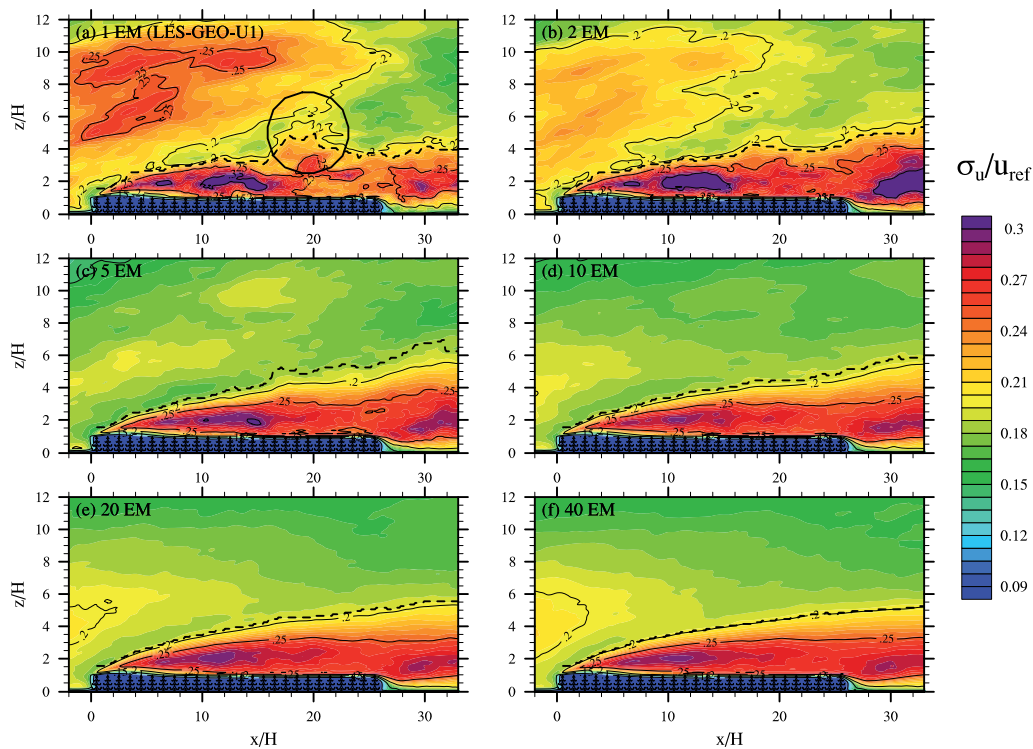


**Figure 11:** Same as Fig. 10 (b), but instead of the edge-parallel average an ensemble average over (a) one, (b) two, (c) five, (d) ten, (e) 20 and (f) 40 ensemble members was applied. Analogous to the lidar EM, one LES EM corresponds to a 15-min-average of a single vertical slice.

acteristics could not be drawn for the unstable lidar case (Fig. 7 (a)), as the occurrence of a large turbulence structure (white circle) substantially deformed the IBL. This deformation is possibly caused by a thermal vortex, as e.g. discussed by THOMAS et al. (2006) for field measurements and by SCHRÖTTE and DÖRNBRACK (2013) for LES, but it might also be caused by strong intermittent wind gusts that are known to occur near forest edges (e.g. DUPONT and BRUNET, 2008, 2009; YANG et al., 2006a). In both cases, the IBL deformation indicates that statistics are insufficient to average out the effect of such individual flow structures on a statistically reliable mean IBL. Therefore, results of a statistical analysis are discussed in the following section.

### 3.4 Effect of insufficient statistics on the detection of the IBL structure

If the number of EM is not large enough to average out eventually occurring larger turbulence structures, turbulence statistics are insufficient to produce a well-defined mean state of the IBL, regarding the IBL height and the inner structure. This problem arises especially under unstable conditions, where generally larger structures occur than under stable conditions. For the former case, only nine lidar EM were available.

The following investigation of the statistics was therefore based on the unstable LES case **GEO-U1**. It

shall be exemplarily demonstrated how far the mean IBL structure deviates, in case of insufficient averaging of e.g. thermal vortices, from the results of the 3-hr time- and line-averaged reference **GEO-U1** in Figure 10 (b), which is assumed to be the virtual reality. For this purpose, Fig. 11 presents ensemble averages over different numbers of EM: (a) 1 EM, (b) 2 EM, (c) 5 EM, (d) 10 EM, (e) 20 EM, (f) 40 EM. Analogous to one lidar EM, one LES EM thereby comprises a 15-min average of one individual (not line averaged) streamwise vertical slice of  $\sigma_u/u_{ref}$ . The individual LES EM are sampled from the last three hours of the simulation **GEO-U1**, spatially and temporally independent in a statistical sense. The spread in the flow conditions between the EM, e.g. in the quantity  $u_{ref}$ , is less than 5% with an average  $u_{ref} \approx 6.5 \text{ m s}^{-1}$ .

It is evident from Fig. 11 (a) that in case of only one EM (**GEO-U1-1EM**), the whole picture strongly deviates from the reference **GEO-U1** (10 (b)). For instance, the IBL boundary exhibits a distinct deformation (Fig. 11 (a), black circle), similar to the lidar observations (Fig. 7 (a), white circle), whereas the reference **GEO-U1** shows a smooth and continuous growth of the IBL. In addition, the maximum  $\sigma_u$  value for **GEO-U1-1EM** is nearly 13% higher than for reference **GEO-U1**, and it occurs almost  $5H$  further downstream. The relatively chaotic structure of the IBL in Fig. 11 (a) complicates e.g. an estimation of the different stages of the flow adjustment, which can be a valuable information



for the interpretation of tower measurements. A further large difference between **GEO-U1-1EM** and **GEO-U1** can be detected in the appearance of the advected background flow. The advected turbulence level within the high-turbulence plume bounded by the 0.2-isoline in **GEO-U1-1EM** takes maximum  $\sigma_u$  values of  $0.26u_{\text{ref}}$ , which is 20% higher than the advected maximum values for **GEO-U1**. Moreover, this large-scale plume in **GEO-U1-1EM** reaches significantly larger heights and distances downstream of the windward forest edge as the advected turbulence in the reference **GEO-U1**. And this plume even partly connects with the IBL. Such a plume of relatively high  $\sigma_u$  values can also be observed in the lidar data (Fig. 7 (a)), in the area between the solid black lines.

The fact that this pronounced upward-directed plume vanishes in the LES with an increasing EM number (Fig. 11 (a–f)) indicates that the plume in the lidar data might indeed be an artifact of insufficient averaging. Also the IBL deformation in **GEO-U1-1EM** is smoothed out with an increasing number of EM, which is an additional indication that the IBL deformation in the lidar data might also be a result of an insufficient EM number. Overall, the different LES ensemble averages demonstrate that an increasing EM number has a smoothing effect on the IBL boundary and the inner IBL structure. Thereby, the IBL  $\sigma_u$  values converge towards the values of the reference **GEO-U1**. Looking e.g. at the relative difference between the  $\sigma_u(x/H, z/H)$  in the IBL of **GEO-U1** and the  $\sigma_u(x/H, z/H)$  in the corresponding region of each **GEO-U1-#EM** reveals that maximum differences decrease from 21% (**GEO-U1-1EM**) to 10% (**GEO-U1-10EM**) and finally reach 5% for **GEO-U1-40EM**. The IBL averages of the differences decrease from 8% (**GEO-U1-1EM**) to 5% (**GEO-U1-10EM**) and take values of 2% for both **GEO-U1-20EM** and **GEO-U1-40EM**. Thus, if the margin of the error by insufficient averaging is e.g. desired to be less than 5%, we suggest to average over more than 10 EM with equal atmospheric conditions.

We are aware that atmospheric conditions are highly non-stationary, not only from day to day, but also or especially in the course of a day. Consequently, we propose that much more than 10 EM from a confined range of atmospheric conditions are necessary, to obtain a statistically relevant picture of the mean flow structure above a forest, which can be representative for this specific range of conditions (e.g. regarding wind speed and direction, atmospheric stability). Based on these findings we can conclude that the 9 lidar EM forming the unstable case, which were obtained from four different days with variations in  $u_{\text{ref}}$  between  $2.7$  and  $7.0\text{ m s}^{-1}$ , variations in  $\frac{\partial\theta}{\partial z}$  (in the lowest 300m) between  $0.001$  and  $0.004\text{ K m}^{-1}$  and  $Ri$  from  $-2$  to  $-7$ , were not sufficient to fulfill this purpose. We further assume that in windy (nearly) neutral conditions, where buoyancy effects might be neglected, the number of required EM with equal atmospheric conditions can be less than ten.

This assumption is based on the smaller integral time scale of now dominating shear-induced CTS with 20–30 s, compared to the time scale of attached thermal eddies with 190–210 s (e.g. THOMAS et al., 2006). And according to LENSCHOW et al. (1994), flows with smaller integral time or length scales require smaller averaging periods for obtaining a certain measuring accuracy, as opposed to flows with larger length scales.

## 4 Summary

A recent study by TRÄUMNER et al. (2012) has identified Doppler lidar to be a state-of-the-art technique to obtain two-dimensional information of the turbulent flow field in forest edge flow regimes. While general flow features were found to be similar in comparison with laser Doppler anemometry data from a dedicated wind tunnel study, quantitative differences were detected regarding the absolute height and the inner structure of the IBL. Compared to the data from the neutrally stratified wind tunnel, IBL height and turbulence strength was found to be higher for the unstable lidar cases and lower for the stable lidar cases. This comparison by TRÄUMNER et al. (2012) was based on the standard deviation  $\sigma_u$  of streamwise velocity.

One main objective of this LES study was to analyze these differences and to associate them to the meteorological and physical differences between the set-ups of the wind tunnel and the atmospheric measurement. In the present investigation, several differences were identified between the set-ups, regarding thermal stratification, flow forcing, presence of obstacles upstream of the forest edge and forest density. In order to determine which of these parameters might be responsible for the detected deviations in the IBL properties, different LES parameter studies were conducted. As a first step, the IBL properties as observed in the wind tunnel data could be reproduced using a wind-tunnel-like LES set-up. Based on the parameter studies, the observed deviations between the atmospheric lidar measurement and the wind tunnel could mainly be traced back to differences in the onflow and the background flow conditions. The forest density showed only minor effects on IBL height and the detected turbulence levels.

The presence of upstream located obstacles (forest patch and houses upstream of the clearing-to-forest transition at the lidar site), which were not considered in the wind tunnel, was found to have the major effect on the IBL turbulence level. With decreasing clearing length (unforested region) in the LES, the IBL turbulence level increases to values found in the lidar data, which can be ascribed to the enhanced advection of turbulence produced above the upstream located forest patch. Hence, with the presence of upstream obstacles, turbulence levels are expected to be higher than with a quasi-infinite clearing like in the wind tunnel, especially for clearings shorter than 50 forest heights. The effect of the upstream forest patch was determined to be most pronounced under neutral conditions. Under unstable conditions, this

effect decreases with increasing instability due to the large scale vertical mixing by thermal plumes, which promotes the adjustment of the flow to the surface conditions of the clearing. Although not investigated within the scope of this study, it is presumed that the advection of turbulence from the leesided edge will also be less pronounced under conditions with a stable thermal stratification, where turbulence is damped due to the negative buoyancy.

Accounting for the effect of the Coriolis force and the thermal stratification on an atmospheric measurement, both of which cannot be reproduced in most wind tunnels, exposed to have a major effect on the background turbulence level. The Coriolis force increases the mean vertical shear of the flow in the neutral LES, which enhances the overall turbulence level compared to the LES without Coriolis force. But this increase is much more pronounced for the background turbulence than for the IBL turbulence, and it is in the same range as the increase in the background turbulence level when considering a finite rather than a quasi-infinite clearing. Regarding the IBL turbulence level, the clearing length was found to have a five-fold stronger effect than the Coriolis force. Under unstable conditions, the additional effect of positive buoyancy leads to a slight increase of the IBL turbulence level, which is of the same magnitude as the increase after consideration of the Coriolis force. These findings hold for the applied moderately strong wind speeds, where the above-canopy turbulence production by wind shear dominates the production by positive buoyancy. Situations where buoyancy significantly dominates over shear, e.g. with weak winds and strong convection, might not even at all permit the development of an IBL. A thorough investigation of the IBL structure downstream of a forest edge under various atmospheric stability and wind speed regimes is subject to further study. Of special interest should thereby be the interplay of the buoyancy effect on the relative effect of the clearing length, since our first results have indicated that the effect of the latter might be less pronounced under unstable than under neutral conditions.

The other objective of this LES study was to try to reproduce the distinct IBL deformation, which occurred in the data of the unstable lidar case and thus prevented a clear identification of the IBL. By using an atmospheric LES set-up with unstable thermal stratification, a likewise deformed IBL could be detected when statistics were insufficient to average out larger-scale turbulence structures like thermal eddies. On the one hand, this agreement with two-dimensional field data confirmed that our LES model is capable of appropriately modeling the turbulent flow above a forest canopy. On the other hand, the statistical analysis revealed that the available nine 15-min-averages from the lidar, where atmospheric conditions (wind speed, thermal instability) differed to some extent, were not sufficient to produce a mean state of the IBL, which can be representative for this range of observed conditions. It was shown with the LES that at least ten 15-min-averages, i.e. two and a half

hours worth of data from equal atmospheric conditions are necessary to reduce the error in the IBL structure due to insufficient averaging to 5 %. Hence, much more than two and a half hours of data should be available for an atmospheric measurement, since the atmosphere is usually never strictly stationary, i.e. atmospheric conditions change on different time scales. The number of required 15-min-averages thereby depends on the covered range of atmospheric conditions and should be increased with increasing range. To summarize, with the help of LES we were able to identify reasons for the distinct differences observed by TRÄUMNER et al. (2012) between data from atmospheric measurements and from the wind tunnel.

Overall, Doppler lidar is a state-of-the-art tool to capture turbulence structures above forests as volume averages and, given that statistics are sufficient, to provide two-dimensional information of mean IBL characteristics. While lidar is the only way of providing these multi-dimensional information in the field, LES can be used for systematic parameter studies under realistic atmospheric conditions at a relatively low effort. To make use of these possibilities, LES results have to be validated against multi-dimensional field data, which can be supplied by lidar. In turn, LES is a helpful tool to a priori test the suitability of different Doppler lidar measuring strategies. We want to emphasize that a combined application of lidar and LES is essential to thoroughly investigate the IBL structure behind forest edges and the turbulent transport by CTS for various atmospheric regimes.

## 5 Acknowledgments

This work was supported by the German Research Foundation (DFG) under grant number [RA 617/23-1]. Special thanks to Andreas WIESER, who designed and implemented the measuring set-up and contributed valuable ideas to this project. All simulations were performed on the SGI Altix ICE at The North-German Supercomputing Alliance (HLRN) in Hannover and Berlin. NCL<sup>3</sup> and VAPOR<sup>4</sup> have been used for data analysis and visualization. We appreciate the two anonymous reviewers for their constructive and valuable comments that helped to improve this manuscript.

## References

- BELCHER, S., I. HARMAN, J. FINNIGAN, 2012: The wind in the willows: flows in forest canopies in complex terrain. – *Ann. Rev. Fluid Mech.* **44**, 479–504.
- BERGSTRÖM, H., U. HÖGSTRÖM, 1989: Turbulent exchange above a pine forest ii. organized structures. – *Bound.-Layer Meteor.* **49**, 231–263.

<sup>3</sup>The NCAR Command Language (Version 6.1.2) [Software]. (2013). Boulder, Colorado: UCAR/NCAR/CISL/VETS. <http://dx.doi.org/10.5065/D6WD3XH5>

<sup>4</sup>A product of the Computational Information Systems Laboratory at the National Center for Atmospheric Research, [www.vapor.ucar.edu](http://www.vapor.ucar.edu)

- BOHRER, G., G. KATUL, R. WALKO, R. AVISSAR, 2009: Exploring the effects of microscale structural heterogeneity of forest canopies using large-eddy simulations. – *Bound.-Layer Meteor.* **132**, 351–382.
- BROWN, K., W. COVEY, 1966: The energy-budget evaluation of the micro-meteorological transfer process within a cornfield. – *Agric. Meteorol.* **3**, 73–96.
- CASSIANI, M., G. KATUL, J. ALBERTSON, 2008: The effects of canopy leaf area index on airflow across forest edges: large-eddy simulation and analytical results. – *Bound.-Layer Meteor.* **126**, 433–460.
- DEARDORFF, J., 1980: Stratocumulus-capped mixed layers derived from a three-dimensional model. – *Bound.-Layer Meteor.* **18**, 495–527.
- DUPONT, S., Y. BRUNET, 2008: Edge flow and canopy structure: a large-eddy simulation study. – *Bound.-Layer Meteor.* **126**, 51–71.
- DUPONT, S., Y. BRUNET, 2009: Coherent structures in canopy edge flow: a large-eddy simulation study. – *J. Fluid Mech.* **630**, 93–128.
- EDBURG, S., D. STOCK, B. LAMB, E. PATTON, 2012: The effect of the vertical source distribution on scalar statistics within and above a forest canopy. – *Bound.-Layer Meteor.* **142**, 365–382.
- FINNIGAN, J., 1979: Turbulence in waving wheat. ii. structure of momentum transfer. – *Bound.-Layer Meteor.* **16**, 213–236.
- FINNIGAN, J., 2000: Turbulence in plant canopies. – *Annu. Rev. Fluid Mech.* **32**, 519–571.
- FINNIGAN, J., R. SHAW, E. PATTON, 2009: Turbulence structure above a vegetation canopy. – *J. Fluid Mech.* **637**, 387–424.
- FOKEN, T., 2008: *Micrometeorology* – Springer Berlin Heidelberg, pp. 306.
- GARRATT, J., 1990: The internal boundary layer - a review. – *Bound.-Layer Meteor.* **50**, 171–203.
- INAGAKI, A., M. CASTILLO, Y. YAMASHITA, M. KANDA, H. TAKIMOTO, 2012: Large-eddy simulation of coherent flow structures within a cubical canopy. – *Bound.-Layer Meteor.* **142**, 207–222.
- IRVINE, M., B. GARDINER, M. HILL, 1997: The evolution of turbulence across a forest edge. – *Bound.-Layer Meteor.* **84**, 467–496.
- JEGEDE, O., T. FOKEN, 1999: A study of the internal boundary layer due to a roughness change in neutral conditions observed during the linex field campaigns. – *Theor. Appl. Climatol.* **62**, 31–41.
- KANDA, M., M. HINO, 1994: Organized structures in developing turbulent flow within and above a plant canopy, using a large-eddy simulation. – *Boundary-Layer Meteorol.* **68**, 237–257.
- KATUL, G., J. ALBERTSON, 1998: An investigation of higher-order closure models for a forested canopy. – *Bound.-Layer Meteor.* **89**, 47–74.
- KATUL, G., G. KUHN, J. SCHIEDGE, C. HSIEH, 1997: The ejection-sweep character of scalar fluxes in the unstable surface layer. – *Bound.-Layer Meteor.* **83**, 1–26.
- KRUIJT, B., W. KLAASSEN, R. HUTJES, 1995: Edge effects on diffusivity in the roughness layer over a forest. – In: COUTTS, M., J. GRACE (Eds.): *Wind and Trees*. – Cambridge University Press, Cambridge, 60–70.
- LENSCHOW, D., J. MANN, L. KRISTENSEN, 1994: How long is long enough when measuring fluxes and other turbulence statistics. – *J. Atmos. Oceanic Technol.* **11**, 661–673.
- LETZEL, M., S. RAASCH, 2003: Large-eddy simulation of thermally induced oscillations in the convective boundary layer. – *J. Atmos. Sci.* **60**, 2328–2341.
- LETZEL, M., M. KRANE, S. RAASCH, 2008: High resolution urban large-eddy simulation studies from street canyon to neighbourhood scale. – *Atmos. Env.* **42**, 8770–8784.
- MARSHALL, B., C. WOOD, B. GARDINER, S. BELCHER, 2002: Conditional sampling of forest canopy gusts. – *Bound.-Layer Meteor.* **102**, 225–251.
- MONIN, A., A. OBUKHOV, 1954: Osnovnye zakonmernosti turbulentnogo peremeshivaniya v prizemnom sloe atmosfery (basic laws of turbulent mixing in the atmosphere near the ground). – *Tr. Akad. Nauk SSSR Geophys. Inst.* **24**, 163–187.
- MORSE, A., B. GARDINER, B. MARSHALL, 2002: Mechanisms controlling turbulence development across a forest edge. – *Bound.-Layer Meteor.* **103**, 227–251.
- PATTON, E., T. HORST, P. SULLIVAN, D. LENSCHOW, S. ONCLEY, W. BROWN, S. BURNS, A. GUENTHER, A. HELD, T. KARL, S. MAYOR, L. RIZZO, S. SPULER, J. SUN, A. TURNIPSEED, E. ALLWINE, S. EDBURG, B. LAMB, R. AVISSAR, R. CALHOUN, J. KLEISSL, W. MASSMAN, K. T. PAW U, J. WEIL, 2011: The canopy horizontal array turbulence study. – *Bull. Amer. Meteor. Soc.* **92**, 593–611.
- RAASCH, S., D. ETTLING, 1998: Modeling deep ocean convection: large-eddy simulation in comparison with laboratory experiments. – *J. Phys. Ocean.* **28**, 1786–1802.
- RAASCH, S., T. FRANKE, 2011: Structure and formation of dust-devil-like vortices in the atmospheric boundary layer - a high resolution numerical study. – *J. Geophys. Res.* **116**, D16120.
- RAASCH, S., M. SCHRÖTER, 2001: Palm - a large-eddy simulation model performing on massively parallel computer. – *Meteorol. Z.* **10**, 363–372.
- RAUPACH, M., 1981: Conditional statistics of Reynolds stress in rough-wall and smooth-wall turbulent boundary layers. – *J. Fluid Mech.* **108**, 363–382.
- RAUPACH, M., J. FINNIGAN, Y. BRUNET, 1996: Coherent eddies and turbulence in vegetation canopies: the mixing-layer analogy. – *Bound.-Layer Meteor.* **78**, 351–382.
- RAYNOR, G., 1971: Wind and temperature structure in a coniferous forest and a contiguous field. – *Forest Sci.* **17**, 351–363.
- RUCK, B., 1987: Laser doppler anemometry - a non-intrusive optical measuring technique for fluid velocity. – *Part. Part. Syst. Charact.* **4**, 26–37.
- RUCK, B., E. ADAMS, 1991: Fluid mechanical aspects in the pollutants transport to coniferous trees. – *Bound.-Layer Meteor.* **56**, 163–195.
- SCHRÖTTLE, J., A. DÖRNBRACK, 2013: Turbulence structure in a diabatically heated forest canopy composed of fractal pythagoras trees. – *Theor. Comput. Fluid Dynam.* **27**, 337–359.
- SHAW, R., U. SCHUMANN, 1992: Large-eddy simulation of turbulent flow above and within a forest. – *Bound.-Layer Meteor.* **61**, 47–64.
- SHAW, R., G. D. HARTOG, H. NEUMANN, 1988: Influence of foliar density and thermal stability on profiles of reynolds stress and turbulence intensity in a deciduous forest. – *Bound.-Layer Meteor.* **45**, 391–409.
- SHIR, C., 1972: A numerical computation of airflow over a sudden change of surface roughness. – *J. Atmos. Sci.* **29**, 304–310.
- STAWIARSKI, C., K. TRÄUMNER, C. KNIGGE, R. CALHOUN, 2013: Scopes and challenges of dual-doppler lidar wind measurements - an error analysis. – *J. Atmos. Ocean. Tech.* **30**, 2044–2061.
- STEINFELD, G., M. LETZEL, S. RAASCH, M. KANDA, A. INAGAKI, 2007: Spatial representativeness of single tower measurements and the imbalance problem with eddy-covariance fluxes: results of a large-eddy simulation study. – *Bound.-Layer Meteor.* **123**, 78–98.
- STEINFELD, G., S. RAASCH, T. MARKKANEN, 2008: Footprints in homogeneously and heterogeneously driven boundary layers derived from a lagrangian stochastic particle model embed-

- ded into large-eddy simulation. – *Bound.-Layer Meteor.* **129**, 225–248.
- SU, H., R. SHAW, K. T. PAW U, C. MOENG, P. SULLIVAN, 1998: Turbulent statistics of neutrally stratified flow within and above a sparse forest from large-eddy simulation and field observations. – *Bound.-Layer Meteor.* **88**, 363–397.
- SU, H., R. SHAW, K. T. PAW U, 2000: Two-point correlation analysis of neutrally stratified flow within and above forest from large-eddy simulation. – *Bound.-Layer Meteor.* **49**, 423–460.
- SÜHRING, M., S. RAASCH, 2013: Heterogeneity-induced heat-flux patterns in the convective boundary layer: can they be detected from observations and is there a blending height? – a large-eddy simulation study for the litfass-2003 experiment. – *Bound.-Layer Meteor.* **148**, 309–338.
- SULLIVAN, P., C. MOENG, B. STEVENS, D. LENSCHOW, S. MAYOR, 1998: Structure of the entrainment zone capping the convective atmospheric boundary layer. – *J. Atmos. Sci.* **55**, 3042–3064.
- THOMAS, C., J. MAYER, F. MEIXNER, T. FOKEN, 2006: Analysis of low-frequency turbulence above tall vegetation using doppler sodar. – *Bound.-Layer Meteor.* **119**, 563–587.
- TISCHMACHER, M., B. RUCK, 2013: Interaction of gusts and forest edges - an experimental wind-tunnel study. – *Forestry* **86**, 523–532.
- TRÄUMNER, K., C. KOTTMEIER, U. CORSMEIER, A. WIESER, 2011: Convective boundary-layer entrainment: Short review and progress using doppler lidar. – *Bound.-Layer Meteor.* **141**, 369–391.
- TRÄUMNER, K., A. WIESER, B. RUCK, C. FRANK, L. RÖHNER, C. KOTTMEIER, 2012: The suitability of doppler lidar for characterizing the wind field above forest edges. – *Forestry* **85**, 399–412.
- WALLACE, J., H. ECKELMANN, R. BRODKEY, 1972: The wall region in turbulent flow. – *J. Fluid Mech.* **54**, 39–48.
- WATANABE, T., 2004: Large-eddy simulation of coherent turbulence structures associated with scalar ramps over plant canopies. – *Bound.-Layer Meteor.* **112**, 307–341.
- WICKER, L., W. SKAMAROCK, 2002: Time-splitting methods for elastic models using forward time schemes. – *Mon. Wea. Rev.* **130**, 2088–2097.
- WILLIAMSON, J., 1980: Low-storage runge-kutta schemes. – *J. Comp. Phys.* **35**, 48–56.
- YANG, B., M. RAUPACH, R. SHAW, K. T. PAW U, A. MORSE, 2006a: Large-eddy simulation of turbulent flow across a forest edge. part i: flow statistics. – *Bound.-Layer Meteor.* **120**, 377–412.
- YANG, B., A. MORSE, R. SHAW, K. T. PAW U, 2006b: Large-eddy simulation of turbulent flow across a forest edge. part ii: momentum and turbulent kinetic energy budgets. – *Bound.-Layer Meteor.* **121**, 433–457.
- ZHU, J., X. LI, Y. GONDA, T. MATSUZAKI, 2004: Wind profiles in and over trees. – *J. Forestry Res.* **15**, 305–312.

## 3.2 Research article B: Spatial variability of scalar concentrations and fluxes downstream of a clearing-to-forest transition: A large-eddy simulation study

### 3.2.1 Declaration of my contribution

I conducted all simulations and data analysis for the preparation of the article, which was written by myself. Animated visualizations linked to the article were created by Dr. Björn Maronga with the help of Helge Knoop, Prof. Dr. Siegfried Raasch and myself, on the basis of my simulation data. Internal reviews of the original manuscript by Prof. Dr. Siegfried Raasch, Dr. Matthias Sühling and Dr. Micha Gryschka provided valuable comments for the improvement of the article. Additionally, the remarks of the two anonymous reviewers of the article brought further improvements.

### 3.2.2 Author's version of revised article

This article has been published in *Boundary-Layer Meteorology*. With permission of Springer Science+Business Media, the author's final version of this article is deposited here. Permission was not granted by Springer Science+Business Media to deposit the published article version.

Submitted: 25 April 2014. Accepted: 18 November 2014. Published online: 24 December 2014. Online issue: Volume 155, 1–27, April 2015.

**Kanani-Sühling, F. and S. Raasch, 2015:** Spatial variability of scalar concentrations and fluxes downstream of a clearing-to-forest transition: A large-eddy simulation study. *Boundary-Layer Meteorol.*, **155**, 1–27, doi: 10.1007/s10546-014-9986-3.

Boundary-Layer Meteorology manuscript No.  
(will be inserted by the editor)

---

## Spatial variability of scalar concentrations and fluxes downstream of a clearing-to-forest transition: A large-eddy simulation study.

Farah Kanani-Sühring · Siegfried Raasch

Received: date / Accepted: date

**Abstract** The aim of this large-eddy simulation (LES) study is to improve the yet scarce understanding of the scalar (e.g. CO<sub>2</sub>) transport in forest-edge flows. In order to contribute to a basic knowledge on the scalar transport, we focus on idealized neutral flows across a clearing-to-forest transition, with a passive scalar released from a horizontally homogeneous source at the clearing and at the forest floor. Corresponding to previous studies, we found pronounced peaks in scalar concentration and flux downstream of the forest edge, where the flux peak significantly exceeded the given surface flux. We investigated for the first time those transport mechanisms that steer the scalar accumulation, by analyzing the terms in the scalar transport equation. The analysis reveals that the accumulation is accomplished by the streamwise convergence of the mean and turbulent transport. In order to investigate how the concentration and flux enhancement behaves under different conditions, we performed a series of simulations with varying forest density and wind speed. We demonstrate a strong dependence of the peak location and magnitude on forest density. With increasing density, concentration and flux peaks were found closer to the forest edge and peak values increased significantly. Decreasing the wind speed caused an increase of the concentration peak, while the flux peak remained unaffected. For an adequate interpretation and design of micrometeorological measurements near forest edges, it is necessary to identify the regions (fetches) with enhanced concentrations and fluxes. We therefore analyzed different approaches for a proper fetch estimation.

**Keywords** Enhanced scalar fluxes · Fetch determination · Forest-edge flow · Large-eddy simulation · Micrometeorological measurements · Scalar concentration peak

---

Farah Kanani-Sühring · Siegfried Raasch  
Institut für Meteorologie und Klimatologie, Leibniz Universität Hannover  
Herrenhäuser Str. 2, 30419 Hannover, Germany  
E-mail: kanani@muk.uni-hannover.de

## 1 Introduction

Forest edges are well known to have a complex effect on the mean and the turbulent components of a flow (e.g. Yang et al., 2006a,b; Dupont and Brunet, 2008, 2009), and consequently on the transport of momentum, energy and mass (e.g. Klaassen et al., 2002; Klaassen and Sogachev, 2006; Sogachev et al., 2008). This complicates the interpretation of micrometeorological measurements in landscapes with frequent transitions from unforested to forested surface patches, e.g. as performed within the worldwide FLUXNET program (e.g. Baldocchi et al., 2001) or the recent ExchanGE processes in mountainous Regions (EGER; Foken et al., 2012) campaign.

A forest-edge flow, e.g. a flow that crosses a clearing-to-forest transition, undergoes an adjustment process due to the change in surface conditions. Towards and into the forest, the mean flow is decelerated and partly deflected upward as a response to the form and viscous drag of the forest. For the same reason, turbulence is damped when the flow enters the forest. Above the forest, the streamwise flow is partly accelerated for reasons of continuity, which creates, together with the decelerated in-canopy flow, a strong shear layer near the forest top. Resulting Kelvin-Helmholtz instabilities and the prevailing strong perturbations of the flow at the transition lead to the development of coherent turbulence structures (CTS; for details see e.g. Dupont and Brunet, 2009; Finnigan, 2009; Huang et al., 2011). These CTS grow in size and strength with increasing distance to the forest edge, whereby fully developed CTS scale with forest height (e.g. Finnigan, 2000; Poggi et al., 2004; Huang et al., 2009), and, in the form of sweeps and ejections, significantly contribute to the forest-atmosphere exchange of momentum, energy and mass (e.g. Bergström and Högström, 1989; Gao et al., 1989; Lu and Fitzjarrald, 1994; Brunet and Irvine, 2000; Steiner et al., 2008). The layer of developing CTS forms an internal boundary layer (IBL; e.g. Garratt, 1990), and as the consequence of the flow adjustment downstream of the forest edge, other quantities such as scalar concentrations (e.g. CO<sub>2</sub>, temperature, humidity) and their corresponding turbulent fluxes likewise undergo a spatial adjustment.

However, in contrast to our knowledge of the dynamical complexity of forest-edge flows, our understanding of the scalar transport in such flows is rather rudimentary (e.g. Belcher et al., 2012). Only a few studies (e.g. Klaassen et al., 2002; Klaassen and Sogachev, 2006; Sogachev et al., 2008; Ross and Baker, 2013) exist that have investigated the scalar concentration and flux distribution in forest-edge flow regimes. These studies already indicated that in- and above-canopy scalar fluxes as well as concentrations are highly variable downstream of a forest edge. And if a patchwise forested terrain is hilly rather than flat, this variability can be even more pronounced (e.g. Ross and Baker, 2013). Even the existence of a hill in fully forested terrain (without forest-edge effects) produces a horizontal variability in scalar concentrations and fluxes, due to the horizontal and vertical advection induced by the hill (e.g. Katul et al., 2006; Ross, 2011). A thorough understanding of the complex scalar transport near forest edges is yet to be developed, in order to estimate

the regions where concentrations and fluxes strongly deviate from their (adjusted) equilibrium values. With the growing patchiness of European forests and landscapes in general, this knowledge is crucial to interpreting the spatial representativity of micrometeorological measurements. In turn, the quality of such measurements determines how well we can estimate the forest-atmosphere exchange of energy, momentum and mass.

Klaassen et al. (2002) analyzed the heat-flux adjustment in a field experiment downstream of a moorland-to-forest transition in flat terrain. They found that the sum of sensible and latent heat fluxes above the forest overshoots the available energy (sum of net radiation and soil heat flux), on average by 16 % of the net radiation, up to distances of  $15H$  from the forest edge,  $H$  being the mean tree height. Klaassen et al. (2002) attributed the enhanced fluxes to the advection of relatively warm and humid air from the moorland into the forest.

Klaassen and Sogachev (2006) further concluded that the deviation of above-canopy fluxes from given surface fluxes depends on forest density. For denser forests, deviations were found to be larger and confined to smaller regions, hence, fluxes adjusted more rapidly above denser canopies.

Using a two-equation model, Sogachev et al. (2008) found a streamwise variation of  $\text{CO}_2$  fluxes downstream of a clearing-to-forest transition. Canopy-top fluxes showed a wave-like pattern, which overshoot and undershot the net ecosystem exchange (NEE) of  $\text{CO}_2$  at distances up to  $40H$  from the forest edge. The wave amplitude was shown to depend on the density and the vertical structure of the forest. As in Klaassen et al. (2002), Sogachev et al. (2008) attributed this flux variability to the effect of streamwise advection of  $\text{CO}_2$  into the trunk space and a localized  $\text{CO}_2$  accumulation. They found this advection to be more pronounced in forests with sparse trunk and dense crown space, where the flow penetrates deeper into the lower part of the forest (sub-canopy) than in an equally dense but vertically homogeneous forest. In the former case, the streamwise in-canopy wind speed takes maximum values in the trunk space, forming a so-called sub-canopy jet (e.g. Cassiani et al., 2008; Dupont and Brunet, 2008). The resulting positive momentum flux in this region leads to a decoupling of the lower and upper part of the in-forest flow, promoting the horizontal scalar advection deep into the forest. The localized  $\text{CO}_2$  accumulation directly leads to the detected  $\text{CO}_2$  flux enhancement in this region.

Ross and Baker (2013) found, by means of numerical simulation, a tracer accumulation inside the forest downstream of the transition, not only in flat, but also in hilly, terrain. Their results show that the magnitude of the tracer accumulation strongly depends on the positioning of the forest patch with respect to the hill summit, i.e. the hill can intensify or weaken the tracer accumulation in comparison to a case with a forest patch in flat terrain.

The scope of our large-eddy simulation (LES) study is to contribute to a basic understanding of the complex scalar transport processes near forest edges. Owing to the complexity of this problem, we take an idealized approach for the investigation of the in-canopy and above-canopy scalar transport, simulating the flow across an idealized clearing-to-forest transition in flat terrain



under neutral conditions. We emit a passive scalar at a constant rate from a horizontally homogeneous source at the clearing and at the forest floor. These conditions mimic the case of pure soil respiration of e.g. CO<sub>2</sub> (without chemical reactions), where according to Sogachev et al. (2008) the most pronounced scalar concentration and flux patterns develop. We place special focus on the scalar transport and the scalar accumulation inside the forest, to our best knowledge for the first time in such detail. First of all, we analyze the transport mechanisms inside the forest in order to identify the cause of the local scalar accumulation as a function of distance from the forest edge. As mentioned above, this question has been briefly discussed by Sogachev et al. (2008) by means of Reynolds-averaged Navier Stokes (RANS) modelling, and thus is reanalyzed herein by a corresponding analysis of the terms in the scalar transport equation. In contrast to RANS, the LES model is capable of explicitly resolving the turbulent flow down to the scales of the CTS, as they have typical length scales in the order of  $H$ , with the streamwise length scales being larger than the vertical length scales (e.g. Shaw et al., 1995; Huang et al., 2009). This enables a thorough study of the turbulent scalar transport, at a sufficient spatial resolution even inside the forest. We further investigate to what extent plant physical and atmospheric parameters affect the streamwise variability of scalar concentrations and fluxes, by performing a series of LES with different leaf area indices (LAI) and wind speeds. Finally, we analyze and propose different approaches for the estimation of fetch requirements for the adjustment of scalar fluxes, and we provide recommendations for required fetches.

The article is organized as follows: Sect. 2 deals with the description of the applied LES model, the embedded canopy model, simulation set-ups and analysis techniques. Results and discussions of the proposed investigation are presented in Sect. 3, which provides a presentation of the phenomenon of the scalar accumulation in Sect. 3.1, followed by the analysis of the scalar transport mechanisms in Sect. 3.2. Subsequently, Sect. 3.3 and Sect. 3.4 discuss the effect of forest density and wind speed on the concentration and flux distribution, respectively, followed by fetch estimations in Sect. 3.5. Section 4 gives a summary of the main conclusions. In the following, the term forest edge always refers to the transition from clearing to forest.

## 2 Methods

### 2.1 LES and embedded canopy model

We use the **PA**rallelized **LES** **M**odel **P**ALM (Raasch and Schröter, 2001), revision 874<sup>1</sup>, which is based on the non-hydrostatic incompressible Boussinesq equations and the conservation equations of energy and mass. Incompressibility of the flow is obtained by solving a Poisson equation for pressure by means of fast Fourier transformation (Schumann and Sweet, 1988).

---

<sup>1</sup> The code can be accessed under <http://palm.muk.uni-hannover.de/browser?rev=874>.

The advection terms are discretized by a fifth-order scheme (Wicker and Skamarock, 2002), and for the time integration, a third-order Runge-Kutta scheme is used (Williamson, 1980). To account for the effect of the smallest turbulence scales on the larger scales (Deardorff, 1980), an additional prognostic equation is solved for the subgrid-scale (SGS) turbulent kinetic energy (TKE). In the initial phase of the simulation, turbulence is triggered by imposing random perturbations to the horizontal velocity fields. At the domain surface, no-slip conditions and zero vertical velocity are applied, and surface momentum fluxes are parametrized using Monin-Obukhov similarity theory (Monin and Obukhov, 1954). Lateral boundary conditions are cyclic, and free-slip conditions are prescribed at the upper domain boundary.

The effect of the forest on the turbulent flow is modelled by an embedded canopy model (following Shaw and Schumann, 1992; Watanabe, 2004). Due to form (pressure) and viscous drag, the forest acts as a sink for momentum. This behaviour is described at each numerical grid point as a grid-box-averaged effect on the resolved-scale turbulent flow by adding the term  $F_{u_i} = c_d a U \tilde{u}_i$  to the momentum equations,

$$\frac{\partial \tilde{u}_i}{\partial t} = -\frac{\partial (\tilde{u}_k \tilde{u}_i)}{\partial x_k} - \frac{1}{\rho_0} \frac{\partial \tilde{p}}{\partial x_i} - \frac{1}{\rho_0} \frac{\partial \tilde{p}^*}{\partial x_i} - \frac{\partial \tau_{ki}}{\partial x_k} - F_{u_i}, \quad (1)$$

where the tilde denotes a volume average over a grid box, according to the filtering concept of LES. With the indices  $i, k \in \{1, 2, 3\}$ ,  $u_i$  describes edge-perpendicular, edge-parallel and vertical velocity components  $u$ ,  $v$ ,  $w$ , and  $x_i$  describes spatial coordinates  $x$ ,  $y$  and  $z$ , respectively. Remaining quantities are time  $t$ , basic-state air density  $\rho_0 = 1.0 \text{ kg m}^{-3}$ , large-scale pressure distribution  $p$ , perturbation pressure  $p^*$  and SGS stress tensor  $\tau_{ki} = -K_m (\partial \tilde{u}_i / \partial x_k + \partial \tilde{u}_k / \partial x_i)$ , implying K-theory with  $K_m = 0.1 l \sqrt{e}$  being the turbulent diffusion coefficient for momentum. Also,  $e$  is the SGS TKE for which an additional prognostic equation is solved (see below). Under neutral conditions, the mixing length  $l$  equals either the numerical grid length  $\Delta$  or  $1.8 z$ ,  $z$  being the distance to the surface, whichever is the smaller value. Term  $F_{u_i}$  depends on drag coefficient  $c_d$ , leaf area density  $a$ , absolute velocity  $U = (\tilde{u}^2 + \tilde{v}^2 + \tilde{w}^2)^{1/2}$  and the respective velocity component  $\tilde{u}_i$ .

The effect of the forest on the SGS turbulence is considered by the additional term  $F_e = 2 c_d a U e$  in the prognostic equation for the SGS TKE  $e$ ,

$$\frac{\partial e}{\partial t} = -\frac{\partial (\tilde{u}_k e)}{\partial x_k} - \tau_{ki} \frac{\partial \tilde{u}_i}{\partial x_k} + \frac{\partial}{\partial x_k} \left( 2 K_m \frac{\partial e}{\partial x_k} \right) - \epsilon - F_e, \quad (2)$$

with  $\epsilon = (0.19 + 0.74 l / \Delta) e^{3/2} / l$  being the dissipation rate. By applying this widely-used approach (Shaw and Schumann, 1992), it is assumed that the larger-scale turbulence is rapidly broken down to smaller scales while interacting with the plant elements. The small scales are then rapidly dissipated (e.g. Shaw and Schumann, 1992; Edburg et al., 2012). This process is known as the spectral shortcut (e.g. Shaw and Seginer, 1985; Shaw and Patton, 2003). Several LES studies exist, wherein the modelling of flow-forest interactions

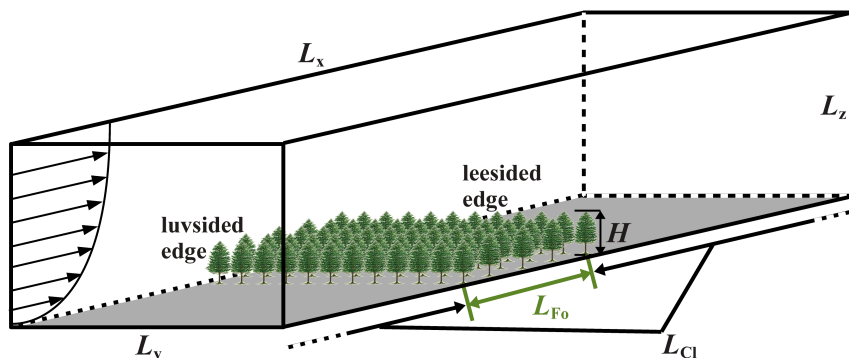


**Fig. 1** Sketch of the LES model domain.  $L_x$ ,  $L_y$ ,  $L_z$  are domain length, width and height, respectively. The forest extends over a length of  $L_{Fo} = 33H$  in the  $x$ -direction and over the total domain width  $L_y$ . The forest height is  $H = 30$  m. The clearing length  $L_{Cl} = 44H$  describes the total length of the unforested part of the domain. The flow (arrows) is directed perpendicular to the forest edge. The grey surface illustrates the homogeneous scalar source.

with terms  $F_{u_i}$  and  $F_e$  has been successfully applied in studies of the dynamical features of homogeneous canopy flows (e.g. Shaw and Schumann, 1992; Kanda and Hino, 1994; Su et al., 1998, 2000; Watanabe, 2004) as well as of forest-edge flows (e.g. Yang et al., 2006a,b; Cassiani et al., 2008; Dupont and Brunet, 2008, 2009).

The transport of a passive scalar  $S$  is calculated from,

$$\frac{\partial \tilde{S}}{\partial t} = -\frac{\partial(\tilde{u}_i \tilde{S})}{\partial x_i} + \frac{\partial}{\partial x_i} \left( K_s \frac{\partial \tilde{S}}{\partial x_i} \right), \quad (3)$$

with  $K_s = K_h = (1+2l/\Delta) K_m$  (Deardorff, 1980) being the turbulent diffusion coefficient for a passive scalar, assumed to be equal to the diffusion coefficient for heat  $K_h$ .

The continuity equation for an incompressible flow,  $\partial \tilde{u}_k / \partial x_k = 0$ , completes the set of model equations for the simulation of a neutrally-stratified flow. For reasons of clarity, the tilde denoting the volume average, e.g. as in Eq. 1, is omitted in the following.

## 2.2 Simulation set-up and case studies

We simulate a neutral flow across an idealized forest edge, accounting purely for the dynamical effects on the scalar transport. As illustrated in Fig. 1, the dimensions of the model domain are  $L_x \times L_y \times L_z = 77H \times 38H \times 13H$  in streamwise, spanwise and vertical direction, respectively, with a forest height of  $H = 30$  m.

With a uniform grid length of 3 m in all directions, the forest volume is resolved by ten grid points in the vertical direction. In a sensitivity study (not

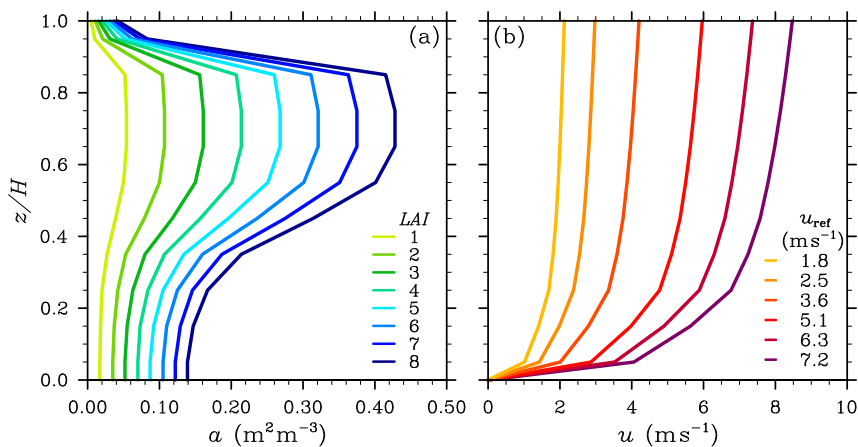


**Fig. 2** Vertical profiles of the different **a** leaf area densities and **b** steady-state velocity profiles of the approaching flow ( $u$ -component), used in the present study.

shown), this vertical resolution was found to be sufficient for explicitly resolving the energy-containing turbulence structures down to the typical scales of the CTS. In addition, the detected length and separation scales of these structures were in the same range as those observed in various field and wind-tunnel studies of canopy flow (e.g. Raupach et al., 1996). Also the flow statistics were found to fit well into the *Family Portrait* described in Raupach et al. (1996). Furthermore, the flow dynamics derived from a forest-edge-flow LES were in good agreement with wind-tunnel and Doppler lidar results (Kanani et al., 2014).

In the streamwise direction, the domain is partly forested with a patch length  $L_{F_0} = 33H$ , whereas the spanwise direction is fully forested. With the periodic lateral boundaries, the total clearing patch length  $L_{C1}$  in the streamwise direction adds up to  $44H$ . To ensure that CTS are properly captured, a domain width of  $L_y = 38H$  is chosen, being multiple times larger than the separation scale of the fully developed CTS (e.g. Finnigan, 2009). The chosen domain height of  $L_z = 13H$  is sufficient to minimize the effect of the free-slip rigid domain top on the developing CTS. While the forest is homogeneous in the horizontal directions, the vertical leaf area distribution is heterogeneous, with a sparse trunk and a dense crown space. A constant value of  $c_d = 0.2$  is set, which is a typical value for trees as applied previously (e.g. Cassiani et al., 2008; Dupont and Brunet, 2008).

In order to force the flow uniformly in the edge-perpendicular direction at all heights (as marked by the arrows in Fig. 1), the Coriolis force is neglected, and instead a longitudinal pressure gradient  $\partial p/\partial x$  (see Eq. 1) is prescribed (see below). The flow is initialized with suitable analytical profiles derived from a priori information, and a horizontally homogeneous (aerodynamic) roughness length of  $z_0 = 0.1$  m is assumed. The same roughness length is simply used everywhere in the domain, since the role of the surface roughness for the

**Table 1** Overview of the different  $LAI$ , longitudinal pressure gradients  $\partial p/\partial x$  and reference velocities  $u_{\text{ref}}$  used in the present study.

LES run	$LAI$	$\partial p/\partial x$ (Pa m <sup>-1</sup> )	$u_{\text{ref}}$ (m s <sup>-1</sup> )
LAI1	1	-0.0017	4.6
LAI2	2	-0.0017	4.6
LAI3	3	-0.0017	4.6
LAI4	4	-0.0017	4.6
LAI5	5	-0.0017	4.6
LAI6	6	-0.0017	4.6
LAI7	7	-0.0017	4.6
LAI8	8	-0.0017	4.6
UREF1	4	-0.00025	1.8
UREF2	4	-0.0005	2.5
UREF3	4	-0.001	3.6
UREF5	4	-0.002	5.1
UREF6	4	-0.003	6.3
UREF7	4	-0.004	7.2

calculation of the surface momentum fluxes using Monin-Obukhov similarity theory can be neglected on the forest patch. This is because the canopy layer is the important sink for momentum, which is explicitly resolved by the drag force (Cassiani et al., 2008).

A passive scalar  $S$  is released both at the clearing and at the forest floor (illustrated by grey surface colouring in Fig. 1), at a temporally and spatially constant rate of  $Q_{S_0} = 0.2 \mu\text{g m}^{-2} \text{s}^{-1}$ . The surface source strength  $Q_{S_0}$  is included in the SGS parametrization as a flux boundary condition in Eq. 3. At the domain top, a Neumann boundary condition is applied for the scalar  $S$ , i.e.  $S$  is set to the same value as the concentration at the height level below, meaning that top-boundary sinks are neglected, in order to focus purely on the scalar transport from the surface source. Of course, such a source configuration causes a constant increase in scalar concentration during the simulation, but this is regarded in the interpretation of the results (see Sect. 3.1). Sinks or sources in the canopy volume (leaf-air interactions) are likewise neglected. To eliminate effects of the dynamical spin-up phase of the simulation on the scalar concentration field, the scalar emission is first initiated after the mean flow has reached a steady state (after 2 h of simulated time). For the same reason, the initial scalar concentration is set to zero in the entire model domain.

In order to investigate how the concentration and the flux distribution depend on plant physical and atmospheric conditions, sensitivity studies with varying forest density and wind speed are carried out (see Table 1). Forest densities with typical values for the  $LAI = 1$  to 8 (Asner et al., 2003) are assumed, while retaining the vertical distribution of leaf area. The  $LAI$  is defined as the vertical integral of the leaf area density  $a$ . Vertical profiles of  $a$  are shown in Fig. 2a, with the vertical axis normalized with  $H$ . For the  $LAI$  study, the wind speed  $u_{ref} = 4.6 \text{ m s}^{-1}$ , where  $u_{ref}$  is defined at  $x_{ref} = -10H$  ( $10H$  upstream of the examined forest edge) and  $z_{ref} = 0.35H$ . In the wind-speed study (UREF#),  $\partial p/\partial x$  is stepwise increased (see Table 1) at a constant

$LAI = 4$ , resulting in  $u_{ref}$  between 1.8 and 7.2 m s<sup>-1</sup>, covering a range of low to moderate wind speeds. Corresponding steady-state velocity profiles of the streamwise flow upstream of the forest edge ( $u$ -component at  $x_{ref}$ ) are presented in Fig. 2b.

### 2.3 Analyzing methods

In order to study the processes that are responsible for the scalar transport inside the forest, the terms in the scalar transport equation (Eq. 3) are examined. The two terms on the right-hand side of Eq. 3 describe the net transport of  $S$  by resolved and subgrid scales, respectively. Since all transport mechanisms are analyzed separately, the total resolved-scale net transport (first term on the right-hand side of Eq. 3) is split into the net transports by the mean flow and by the resolved-scale turbulence. With a quantity  $\psi \in \{u_i, S\}$  split into its mean value  $\langle \psi \rangle$  and the fluctuation  $\psi'$  from this mean, and applying Reynolds averaging conditions, the averaged total resolved-scale flux can be written as,

$$\langle u_i S \rangle = \langle u_i \rangle \langle S \rangle + \langle u_i' S' \rangle. \quad (4)$$

The mean as marked by the angled brackets corresponds to a line average along the edge-parallel homogeneous ( $y$ -) direction, which is used here as the appropriate averaging operation, since the mean and turbulent wind field is only in this direction statistically homogeneous. Substituting Eq. 4 into Eq. 3, and consistently applying the line average to all terms, yields the following formulation of Eq. 3,

$$\begin{aligned} \underbrace{\frac{\partial \langle S \rangle}{\partial t}}_I &= - \frac{\partial \langle u_i \rangle \langle S \rangle}{\partial x_i} - \frac{\partial \langle u_i' S' \rangle}{\partial x_i} + \frac{\partial}{\partial x_i} \langle K_s \frac{\partial S}{\partial x_i} \rangle \\ &= \underbrace{- \frac{\partial \langle u \rangle \langle S \rangle}{\partial x}}_{IIa} \quad \underbrace{- \frac{\partial \langle u' S' \rangle}{\partial x}}_{IIIa} \quad \underbrace{+ \frac{\partial}{\partial x} \langle K_s \frac{\partial S}{\partial x} \rangle}_{IVa} \\ &\quad \underbrace{- \frac{\partial \langle v \rangle \langle S \rangle}{\partial y}}_{IIb} \quad \underbrace{- \frac{\partial \langle v' S' \rangle}{\partial y}}_{IIIb} \quad \underbrace{+ \frac{\partial}{\partial y} \langle K_s \frac{\partial S}{\partial y} \rangle}_{IVb} \\ &\quad \underbrace{- \frac{\partial \langle w \rangle \langle S \rangle}{\partial z}}_{IIc} \quad \underbrace{- \frac{\partial \langle w' S' \rangle}{\partial z}}_{IIIc} \quad \underbrace{+ \frac{\partial}{\partial z} \langle K_s \frac{\partial S}{\partial z} \rangle}_{IVc}. \end{aligned} \quad (5)$$

Term I quantifies the local temporal change of  $S$ ; terms II(a-c) describe the net transport of  $S$  by the mean flow in edge-perpendicular ( $x$ -), edge-parallel ( $y$ -) and vertical ( $z$ -) directions, respectively; terms III(a-c) quantify the net transport of  $S$  by the resolved-scale turbulence in each direction; terms IV(a-c) describe the net transport of  $S$  by the SGS turbulence in each direction. A positive net transport by a certain term (including the dedicated sign in

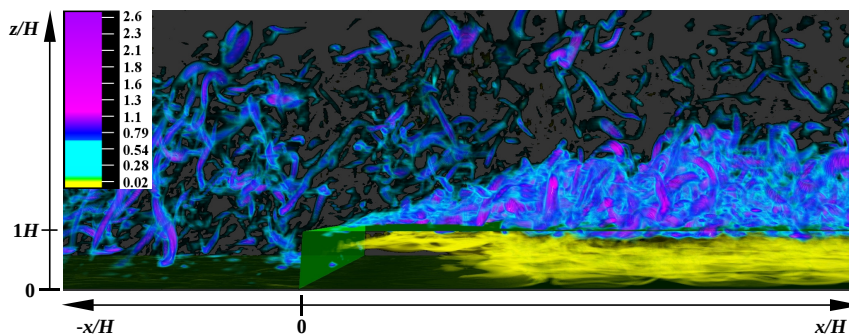


**Fig. 3** Three-dimensional snapshot of the absolute value of the vorticity  $\zeta = |\varepsilon_{ijk} \partial_{x_j} u_k|$  ( $\text{s}^{-1}$ ) after 3 h of simulation time from LAI8 (Video animation available at <http://dx.doi.org/10.5446/14297>). High values in pink illustrate strong turbulence, lower values in yellow mark areas with weak turbulence. The mean flow is directed from left to right and the forest edge is oriented perpendicular to the streamwise direction. The forest edge is at  $x/H = 0$ , marked by the light-green vertical isosurface (Kanani et al., 2014).

Eq. 5) implies that this term leads to a concentration accumulation and vice versa. Assuming that the model domain is sufficiently large in the  $y$ -direction, terms (II-IV)b can be neglected, because the wind field is statistically homogeneous in this direction. This was confirmed by the fact that the residual of the remaining terms on the right-hand side of Eq. 5 equal term I.

An overbar “ $\bar{\phantom{x}}$ ” is used in the following to mark quantities that are, in addition to the line average “ $\langle \phantom{x} \rangle$ ”, time-averaged over 3 h of simulation time, where the scalar transport is stationary. For clarification, the line-averaged fluxes and flux divergences (see Eq. 5) reach a steady state in the temporal evolution, after an adjustment phase of approximately 30 min from the first scalar emission.

### 3 Results and discussion

The complexity of the flow dynamics in forest-edge flow regimes directly imprints complexity on the distribution of scalar concentrations and fluxes. The disturbance and adjustment of a turbulent flow at a clearing-to-forest transition is illustrated by means of a three-dimensional snapshot<sup>2</sup> of the absolute value of the vorticity  $\zeta = |\varepsilon_{ijk} \partial_{x_j} u_k|$  (Fig. 3), taken from simulation LAI8 after 3 h of simulation time. This quantity is presented as a measure for the flow’s turbulence intensity, with high values drawn in pink and low values in yellow. The mean flow direction is from left to right and the forest edge is at  $x/H = 0$ , as marked by the green isosurface.

Upstream of the forest edge, the turbulent flow is composed of randomly distributed turbulence elements of different size. As this turbulent flow pene-

<sup>2</sup> The corresponding animation is available under <http://dx.doi.org/10.5446/14297>. It was created with VAPOR, a product of the Computational Information Systems Laboratory at the National Center for Atmospheric Research, [www.vapor.ucar.edu](http://www.vapor.ucar.edu).

trates the forest, the turbulence is strongly damped, due to the existing drag forces. As mentioned in Sect. 1, a strong shear layer is present near the forest top, resulting from the weak in-canopy wind and the relatively strong above-canopy flow velocity. This vertical shear leads together with the massive flow disturbance at the forest edge to the development of CTS, which grow in size and strength in the streamwise direction, until the flow has adjusted to the new surface conditions. The developing CTS form a growing IBL, characterized by enhanced turbulence activity, as compared to the flow above the IBL that is undisturbed by the surface transition. Fully developed CTS are strong enough to penetrate deep into the forest, and thus can effectively contribute to the mixing of in-canopy and above-canopy air and its properties.

### 3.1 The phenomenon of in-canopy scalar accumulation

As a starting point for the following investigations, Fig. 4 presents  $x$ - $z$  slices of the mean flow quantities  $\langle \bar{u} \rangle$  (a) and  $\langle \bar{w} \rangle$  (b), the mean turbulent vertical momentum flux  $\langle \overline{w'u'} \rangle$  (c), as well as the mean scalar concentration  $\langle \bar{S} \rangle$  (d), exemplarily for a sparse (left: LAI2) and a dense (right: LAI8) forest.  $\langle \overline{w'u'} \rangle$  is calculated using a version of Eq. 4, with  $u_i$  and  $S$  being replaced by  $w$  and  $u$ , respectively. Dynamical quantities are normalized with  $u_{\text{ref}}$ , while  $\langle \bar{S} \rangle$  is normalized with the reference concentration  $S_{\text{ref}}$ , taken at the same  $x$ - $z$  position  $(x_{\text{ref}}, z_{\text{ref}})$  as  $u_{\text{ref}}$  (as marked in Fig. 4a,d). By this means, in-canopy concentrations are set into relation with a concentration value, which is undisturbed by the presence of the forest. And further, this normalized concentration approaches a steady level in the temporal evolution, after a certain adjustment phase. So, each applied time average spans over a period of time where  $\langle S \rangle(t)/S_{\text{ref}}(t)$  shows nearly no trend. Only the domain part of greater interest is presented, with a stretched vertical axis for better visualization. Axes are normalized with  $H$ , the forest edge is at  $x/H = 0$  and the forest volume is surrounded by the dashed black lines.

Comparing the dynamics (Fig. 4a-c) of simulations LAI2 and LAI8 exhibits a very similar behaviour upstream and a few  $H$  downstream of  $x_{\text{ref}}$ . Towards and into the forest, the flow is decelerated in streamwise direction and deflected upward, as a response to the form and viscous drag by the forest (e.g. Belcher et al., 2003; Dupont and Brunet, 2008). In simulation LAI8, this flow modification starts further upstream and is more pronounced than for LAI2, since the magnitude of the drag increases proportionally with increasing  $LAI$ . This is in agreement with previous LES results reported e.g. by Cassiani et al. (2008) and Dupont and Brunet (2009), who simulated forest densities in the same range as in the present study. At the forest edge, a small region of mean downward motion can be detected (e.g. Cassiani et al., 2008), but the overall relevance of this region is rather small. Furthermore,  $\langle \overline{w'u'} \rangle$  shows (Fig. 4c) that an IBL develops above the forest (c.f. Fig. 3), as a result of the flow adjustment to the new surface conditions. Maximum absolute values of  $\langle \overline{w'u'} \rangle$  (marked by red asterisks in Fig. 4c) are higher and occur closer to the for-



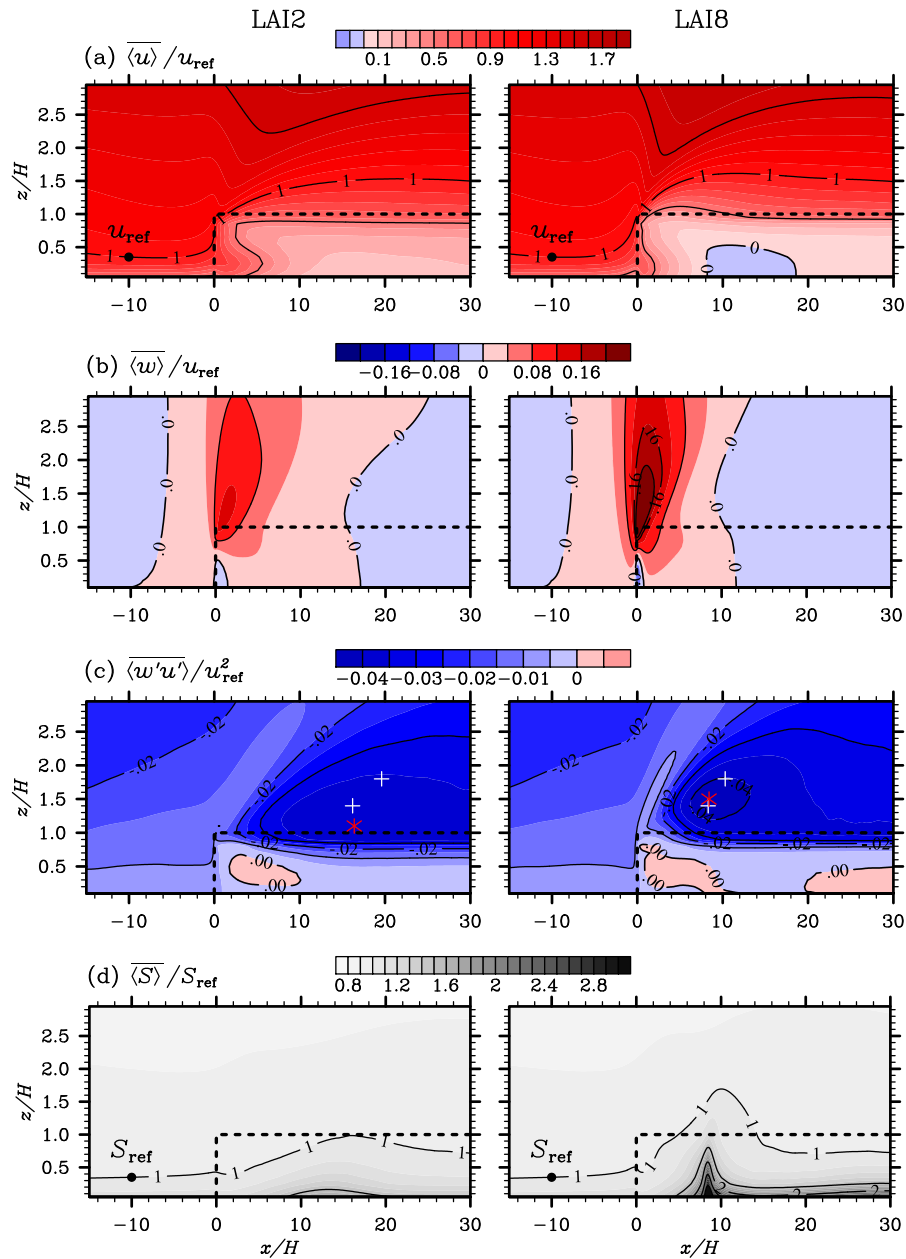


**Fig. 4** Streamwise vertical slices of: mean streamwise and vertical velocity components, **a**  $\overline{\langle u \rangle}$  and **b**  $\overline{\langle w \rangle}$ , respectively, **c** mean vertical turbulent momentum flux  $\overline{\langle w'u' \rangle}$  and **d** mean scalar concentration  $\overline{\langle S \rangle}$ , from simulation LAI2 (left) and LAI8 (right). The mean corresponds to a spatial average in the spanwise (edge-parallel) direction and a 3-h time average, denoted by angled brackets and overbar, respectively. Reference velocity and concentration for normalization,  $u_{\text{ref}}$  and  $S_{\text{ref}}$ , are defined upstream of the forest edge as marked in the plots. The forest volume is marked by the dashed black lines. Red asterisks in **c** mark positions of the maximum absolute values of  $\overline{\langle w'u' \rangle}$ ; white crosses mark the respective maximum in the  $x$ -direction at the specific height.

est edge for LAI8, again in agreement with findings of Dupont and Brunet (2009). The white crosses in Fig. 4c mark the positions of the maximum absolute values of  $\langle w'u' \rangle$  in the  $x$ -direction at two different heights, as needed for the discussion in Sect. 3.5.

One pronounced feature of forest-edge flow in a regime with a sparse trunk and dense crown space, is the presence of a sub-canopy jet (Fig. 4a,  $0 \leq x/H \lesssim 10$ ). This means that in the front part of the forest, the vertical profile of  $\langle u \rangle$  peaks within the trunk space, because this region opposes less drag against the flow than the denser crown space. Hence, the flow deceleration proceeds less rapidly in the trunk space. The sub-canopy jet extends further into the forest and reaches higher velocities for LAI2 than for LAI8, owing to the overall weaker drag in the sparser forest. In simulation LAI2, the jet reaches distances of  $10H$  into the forest, while the jet extends to  $x/H \approx 7.5$  in LAI8. The presence of a sub-canopy jet has been reported in previous LES studies, where e.g. in Dupont and Brunet (2009) the jet also reached distances of about  $10H$  into the forest for  $LAI = 2$ . Cassiani et al. (2008) detected sub-canopy jets with penetration distances of  $13H$  ( $LAI = 2$ ) and  $7H$  ( $LAI = 8$ ). In the RANS study of Sogachev et al. (2008), the jet was present up to  $x/H = 18$  for  $LAI = 2$ . Also in field experiments sub-canopy jets were found, as e.g. reported by Dupont et al. (2012), with penetration distances of up to  $15H$  at  $LAI \approx 2$ . The shorter penetration distances found in the present study, as compared to those reported by Sogachev et al. (2008) and Dupont et al. (2012), can be attributed to the higher trunk-space density in the present set-up, which prevents the jet from reaching too far into the forest. The presence of a sub-canopy jet causes decoupling of the lower and upper part of the in-forest flow (e.g. Sogachev et al., 2008), as illustrated by the positive momentum flux in this region (red areas in Fig. 4c), promoting the horizontal transport of surface-emitted scalars deep into the forest.

Another interesting feature in the mean streamwise flow (Fig. 4a) is the presence of an in-canopy recirculation zone (ICR) in simulation LAI8, roughly extending from  $8H$  to  $19H$  in the  $x$ -direction. The occurrence of an ICR can be attributed to the presence of a low-pressure zone (not shown) in this region, which develops due to the vertical mass transport out of the forest (e.g. Cassiani et al., 2008). This transport is more efficient for LAI8 than for LAI2, because the maximum vertical velocities are higher for LAI8 (see Fig. 4b), hence, an ICR in the mean streamwise flow only forms in the dense forest. Cassiani et al. (2008) reported ICR in canopies with  $LAI \geq 6$ , occurring at similar distances from the leading forest edge as detected in the present study for LAI8. They further found the ICR zones to be located deeper into the forest for larger  $LAI$ . In the RANS of Sogachev et al. (2008), ICR were found for  $LAI \geq 3$  in regions between  $x/H = 22$  and  $30$ . In the present LES study, an ICR was detected for  $LAI \geq 5$ , with mean streamwise extents and maximum reversed velocities as listed in Table 2.

The phenomenon of the scalar accumulation is visualized in Fig. 4d. While  $\langle \bar{S} \rangle / S_{\text{ref}}$  upstream of  $x/H = 0$  is nearly equal for both  $LAI$  values and fairly homogeneous in the streamwise direction, the concentration distribution inside

**Table 2** Occurrence of an in-canopy recirculation in the mean streamwise flow for different *LAI*. The respective maximum reversed *u*-velocity is listed, as well as the vertically-averaged left ( $X_{\text{ICR,l}}$ ) and right ( $X_{\text{ICR,r}}$ ) boundary of the in-canopy recirculation.

LES run	largest negative $u$ [ $\text{m s}^{-1}$ ]	$X_{\text{ICR,l}}$ [ $H$ ]	$X_{\text{ICR,r}}$ [ $H$ ]
LAI1-LAI4	–	–	–
LAI5	-0.1	11.7	16.0
LAI6	-0.18	10.2	17.0
LAI7	-0.3	9.1	17.4
LAI8	-0.36	8.3	18.5

the forest shows strong horizontal gradients, despite the horizontally homogeneous scalar emission. Both *LAI* cases exhibit a concentration increase with depth into the forest, until the concentrations reach their peak value at a certain distance from the forest edge. This was previously observed by Sogachev et al. (2008) for a similar set-up, and by Ross and Baker (2013) for forest patches on flat as well as on hilly terrain, with similarly located scalar peaks as in the present study, even though the scalar boundary conditions were different (surface source versus canopy source) between the present and the Ross and Baker (2013) study. Moreover, Fig. 4d further reveals that the peak properties, such as position and magnitude, are rather different between both *LAI* values. Peak values are significantly larger and are located closer to the forest edge for LAI8 than for LAI2, as will be discussed in detail in Sect. 3.3.1. The presence of a concentration peak and the different behaviour between the *LAI* cases highlights the need for a thorough understanding of the scalar transport in forest-edge-flow regimes.

In the following section, the information on the flow features is combined together with the analysis of the scalar balance terms (see Sect. 2.3), in order to explain the mechanisms for the in-canopy scalar accumulation.

### 3.2 Mechanisms for the in-canopy scalar transport

Figure 5 presents the scalar balance terms, calculated after Eq. 5, as a function of the distance  $x/H$  to the forest edge, for LAI2 (a) and LAI8 (b). The quantity  $\mathcal{Y} = \int_0^H (I, \dots, IV) dz$ , i.e. each term (I-IV) is vertically integrated from the surface to the forest top, similar as in Sogachev et al. (2008), and averaged over 3 h as marked by the overbar. Positive values (positive net transport) of  $\mathcal{Y}$  indicate a scalar accumulation, and negative values (negative net transport) a scalar depletion. The grey shading marks the region where the peak concentrations occur between  $z/H = 0$  and 1. As illustrated in Fig. 4d (left), this region is wider for LAI2, because the concentration peaks at the different heights are located at different  $x/H$ . In simulation LAI8 (Fig. 4d, right), peak positions are nearly constant with height. This different behaviour between the *LAI* cases can be explained by the absence/presence of the ICR (Fig. 4a). With an ICR (LAI8), the flow convergence is stronger and spatially more confined than without ICR (LAI2), hence, the scalar is lifted straight upward along

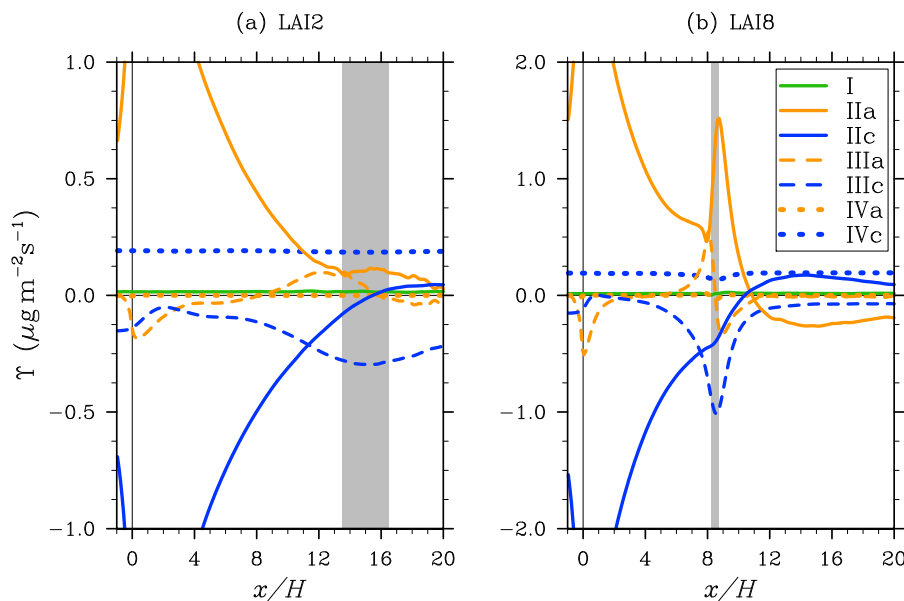


**Fig. 5** Vertically-integrated (from surface to forest top) time-averaged scalar balance terms, plotted as a function of distance  $x/H$  to the forest edge ( $x/H = 0$ ), for **a** LAI2 and **b** LAI8. The grey-shaded areas mark the regions where concentration peaks occur between  $z/H = 0$  and 1. This region is wider for LAI2, because the peaks are located at different  $x/H$  at the different heights.

the convergence line for cases with an ICR. Without an ICR, the streamwise flow has a considerable component into the forest in the concentration-peak region (Fig. 4a, left), with a larger vertical gradient of  $\langle \bar{u} \rangle$  than with an ICR. Consequently, the lifted scalar is displaced in the streamwise direction.

From Fig. 5 it is evident that the temporal change of  $S$ , term I (green solid line), takes spatially homogeneous small positive values for both LAI cases, i.e. the scalar concentration increases with time since no scalar sinks were considered. The overall spatial evolution of terms II-IV is similar for LAI2 and LAI8, whereby the values are generally larger for LAI8 (note the different ordinates), and the peaks are more pronounced and confined to a smaller region. This can be attributed to the larger drag in the denser canopy, and additionally, to the presence of an ICR in the peak region (grey shading). It should be noted that the horizontal net transport by subgrid scales (IVa) is negligible.

The net transport by individual terms is largest immediately downstream of the forest edge, as also found by Sogachev et al. (2008) (c.f. their Fig. 3a), since the surface transition is where the sudden flow disturbance by the forest is most pronounced. In this region, the net transport by the horizontal and vertical mean flow, terms IIa,c (orange, blue solid lines), are the main contributors to term I, with absolute values of more than 13-fold (LAI2) and 20-fold (LAI8) larger than the respective resolved-scale (IIIa,c: long-dashed) and SGS

(IVa,c: short-dashed) turbulent transport. Thereby, the streamwise convergence of the mean flow leads to a scalar enhancement (IIa), together with the vertical transport by subgrid scales (IVc). This enhancement is compensated mainly by the mean vertical transport (IIc), due to the strong upward motion in this region, and partly by the resolved-scale turbulent transport (IIIa,c). At this point, it should be noted that term IVc does in some regions contribute significantly to the scalar enhancement, which can be attributed to the large contribution of the SGS vertical transport at the first grid points above the surface. However, this contribution is nearly constant in the streamwise direction, hence, it cannot explain the localized scalar accumulation and is therefore not further treated.

With increasing distance from the forest edge, the net transport by the mean flow (IIa,c) decreases, before a secondary peak occurs for term IIa, at  $x/H \approx 15$  for LAI2 and at  $x/H \approx 8.5$  for LAI8. As mentioned above, this peak is much more developed for LAI8, owing to the stronger flow convergence due to the higher drag and the presence of the ICR. In contrast to terms IIa,c, the net transport by the resolved-scale turbulence (IIIa,c) increases towards the respective peak regions (grey shading), which is due to the growing efficiency of the developing CTS farther away from the forest edge, and due to the high concentration fluctuations (not shown). In the grey-shaded region, terms IIIa,c are of similar or even larger magnitude than terms IIa,c, which indicates that the net transport here is taken over to a considerable amount by turbulent transport processes. Especially for LAI2, the negative net transport (concentration depletion) in the grey-shaded region is almost entirely realized by the vertical resolved-scale turbulent transport (IIIc). In simulation LAI8, term IIIc also makes the largest negative contribution, but the sum of the net transport by the mean vertical flow (IIc) and by the resolved-scale horizontal turbulence (IIIa) makes a similar contribution to the total negative net transport. This partitioned contribution in LAI8 can again be attributed to the presence of the ICR, which causes the formation of a distinct convergence line (see Fig. 4a, LAI8) in the grey-shaded region of Fig. 5b, and thus promotes the vertical transport by the mean flow. Also the resolved-scale streamwise turbulent net-transport (IIIa) is not to be neglected in the peak regions of both LAI cases. Term IIIa is positive upstream of its zero-crossing in the centre of the grey shading, and the values of IIIa are, at their peak, of the same magnitude as the net transport by the streamwise mean flow (IIa). Downstream of the zero-crossing of term IIIa, values are negative, and the negative peaks take similar values as the respective positive peaks of term IIIa. This significant contribution of the streamwise resolved-scale turbulent transport in our LES was not detected in the RANS study of Sogachev et al. (2008), where the turbulent transport is fully parametrized.

To summarize, the scalar accumulation in the peak regions of both LAI cases is steered by the locally-enhanced mean streamwise net-transport (IIa), due to the streamwise flow convergence - as previously stated by Sogachev et al. (2008) - but also in equal parts by the streamwise resolved-scale turbulent net-transport (IIIa), which was identified for the first time in the present

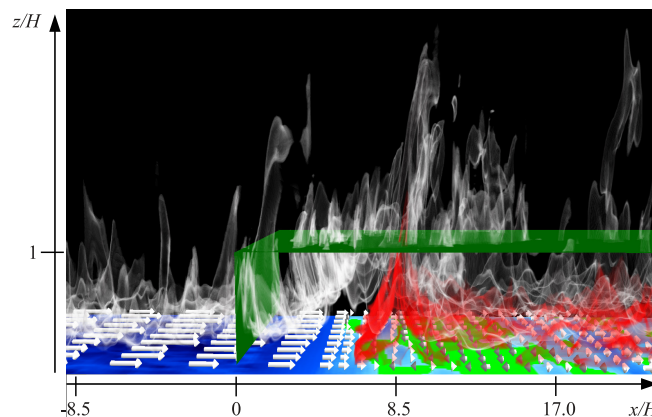


**Fig. 6** Three-dimensional snapshot of scalar concentration and streamwise flow for LAI8 (video animation available at <http://dx.doi.org/10.5446/14311>). Shades of red and white illustrate concentrations of  $18 \pm 2 \mu\text{g m}^{-3}$  and  $6.2 \pm 0.2 \mu\text{g m}^{-3}$ , respectively. The forest volume is surrounded by the green iso-surface. Blue surface colouring marks a near-surface flow from left to right and green colouring marks the opposite flow direction. Arrows additionally illustrate direction and strength of the flow. Only part of the model domain is shown and the vertical direction is stretched by a factor of 6 for better visualization.

investigation. Thereby, the relative contribution of term IIIa with respect to term IIa is larger in the sparser forest. The scalar depletion in the peak regions of both LAI cases is accomplished to a large portion by the vertical resolved-scale turbulent net-transport (IIIc), and in the dense forest to a similar portion also by the sum of the mean vertical net-transport (IIc) and the streamwise resolved-scale turbulent net-transport (IIIa), which is another discovery of this LES study.

The transport mechanisms are visualized by a three-dimensional snapshot<sup>3</sup> of the instantaneous streamwise flow and scalar distribution (Fig. 6), taken from simulation LAI8. Shades of red and white illustrate concentrations of  $18 \pm 2 \mu\text{g m}^{-3}$  and  $6.2 \pm 0.2 \mu\text{g m}^{-3}$ , respectively. The surface colouring visualizes the near-surface streamwise flow, with blue for a flow from left to right and green for the opposite flow direction. Arrows additionally illustrate direction and strength of the flow. Only a part of the total model domain is presented here, and for better visualization, the vertical direction is stretched by a factor of 6. It should be noted that this instantaneous view of the scalar distribution does not allow a one-to-one comparison with the spatial distribution of the vertically-integrated and time-averaged scalar balance terms in Fig. 5, which describe a net-transport of the scalar and not an instantaneous distribution.

Upstream of the forest edge, the scalar is uniformly distributed, apart from the random turbulent fluctuations. Inside the forest, with distance to the edge, the scalar starts to accumulate due to the streamwise flow convergence (see arrows). The highest concentrations occur at about  $x/H \approx 8.5$  (see red shades),

<sup>3</sup> The related VAPOR animation is available at <http://dx.doi.org/10.5446/14311>.

where the opposing flows meet, i.e. where the presence of the ICR (green surface colouring) creates a confined convergence line. Furthermore, a general upward scalar transport is visible in the region between the forest edge and the scalar peak (see contiguous white shades inside and above the forest), resulting from the upward flow deflection. The relatively high concentrations above the forest around  $x/H \approx 8.5$ , and the frayed appearance of the white shades, indicate an efficient turbulent mixing of scalar plumes out of the forest, even up to heights of  $z/H \approx 2$ . Downstream of the peak, concentrations are again more homogeneously distributed in the horizontal, with strong random fluctuations, which result from the turbulent mixing of the scalar by the fully developed CTS. It should be noted that concentrations are generally higher downstream of the peak than upstream. This can be attributed to the overall weaker advection and turbulent mixing deep inside the forest, despite the contribution of the CTS, as compared to the more efficient scalar transport above the clearing. The high streamwise variability of the scalar distribution, which will be discussed in the following sections, once again highlights the complexity of the scalar transport in forest-edge flows. This in turn demonstrates how complicated the interpretation of concentration and flux measurements can be in fragmented forested landscapes.

### 3.3 Effect of forest density and wind speed on scalar distribution

Previous numerical studies (e.g. Cassiani et al., 2008; Sogachev et al., 2008) have reported a dependence of the behaviour of the mean flow and the turbulent fluxes on LAI. The LAI is therefore presumed to have an effect on the scalar distribution within a forest. This effect is discussed in the following section by analyzing the scalar-peak characteristics for  $LAI$  ranging from 1 to 8. A corresponding analysis of the wind-speed effect follows subsequently to this discussion.

#### 3.3.1 Effect of forest density

Figure 7 presents mean scalar concentration  $\overline{\langle S \rangle}$  at  $z/H = 0.35$  as a function of distance  $x/H$  to the forest edge, for different  $LAI$  and normalized with  $S_{\text{ref}}$ .

All presented LAI cases expose a concentration peak downstream of the forest edge. While concentrations for  $LAI < 5$  approach a constant value downstream of the respective peak, as a result of the adjustment of the scalar transport and distribution to the surface conditions of the forest patch, concentrations for  $LAI \geq 5$  do not reach constant values within this length of the forest and even exhibit a secondary peak. Further LES with  $L_{\text{Fo}} = 20H$  and  $50H$  (based on the set-up of simulation LAI8) revealed no secondary peak, suggesting that this peak might be a result of the interplay between the final scalar adjustment and the effect of the lee-sided forest edge, where another recirculation zone sets up (e.g. Cassiani et al., 2008). These features are sub-

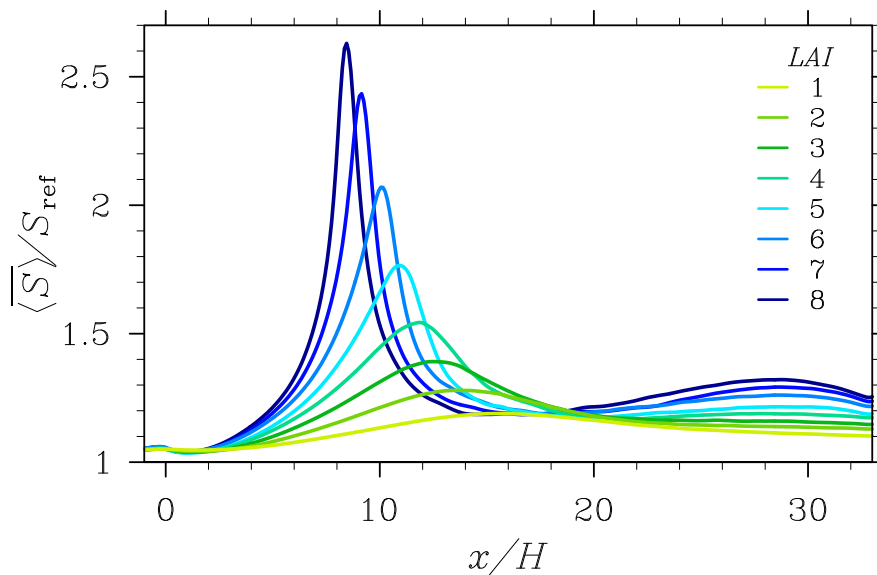


**Fig. 7** Mean scalar concentration  $\overline{\langle S \rangle}$  at  $z/H = 0.35$  as a function of distance  $x/H$  to the forest edge, for different  $LAI$  and normalized with  $S_{\text{ref}}$ . Different line colours mark the concentration distributions of the simulated  $LAI$  cases.

ject to ongoing studies. The (primary) peak however, being the subject of the following discussion, is not affected by the variation of  $L_{F0}$ .

With increasing  $LAI$ , the in-canopy concentrations start to increase closer to the forest edge. Thereby, the scalar-peak position  $X_{S_p}$  ( $= X(\overline{\langle S \rangle}_{\text{max}})/H$ ) is shifted towards the edge, ranging from  $x/H = 8$  for  $LAI8$  to  $x/H = 16$  for  $LAI1$  at  $z/H = 0.35$ . This behaviour can be attributed to the higher drag at larger  $LAI$ , which causes the region of streamwise flow convergence to be located closer by the forest edge, and with it the region of enhanced scalar concentration.

Not only  $X_{S_p}$  shows a dependence on  $LAI$ , but also the peak magnitude  $S_p$  ( $= \overline{\langle S(X_{S_p}) \rangle} / S_{\text{ref}}$ ). It varies from 1.2 ( $LAI1$ ) to nearly 2.7 ( $LAI8$ ). The higher peak values at larger  $LAI$  can again be attributed to the stronger flow convergence. Additionally, the larger drag leads to a stronger suppression of the turbulent mixing, and thus to overall higher concentrations.

Figure 8 shows  $X_{S_p}$  (a) and  $S_p$  (b) of the respective peaks, plotted against  $LAI$ . Different line patterns and colours mark different heights within the forest.

Figure 8a,b reflects the general findings from Fig. 7, namely that with increasing  $LAI$ ,  $X_{S_p}$  moves closer to the forest edge and  $S_p$  increases. Figure 8a further reveals that the relation between  $X_{S_p}$  and  $LAI$  strongly depends on the examined height level. Close to the ground, a nearly linear relation can be detected between  $X_{S_p}$  and  $LAI$ , whereas at higher  $z/H$ -levels the relation shows a more exponential shape. As mentioned in Sect. 3.2,  $X_{S_p}$  shifts away



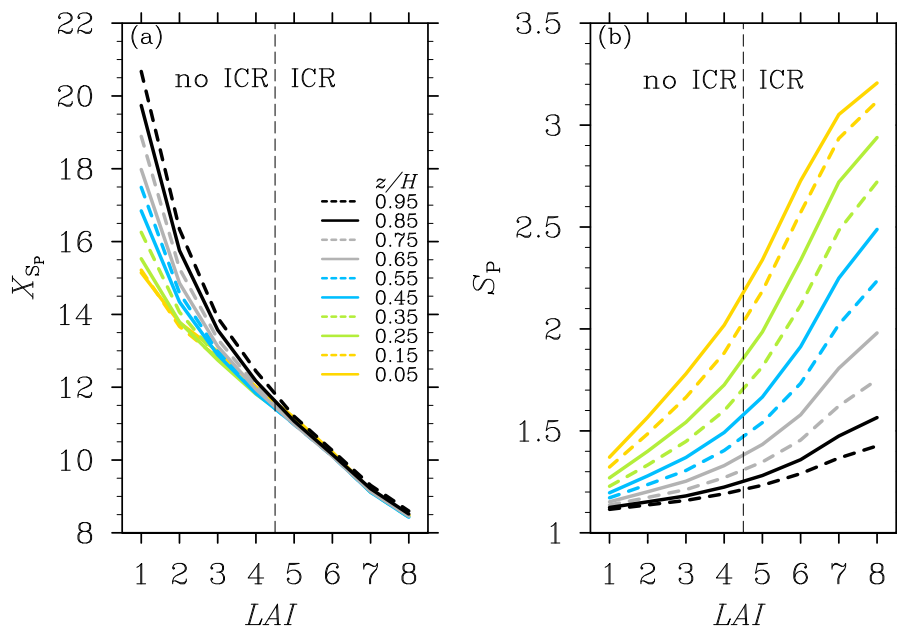


**Fig. 8** **a** Position  $X_{S_p}$  and **b** magnitude  $S_p$  of the concentration peak, plotted against  $LAI$ . Different line colours and patterns mark the examined in-canopy heights. The dashed black line separates the  $LAI$  cases with occurrence of an ICR from the cases without an ICR.

from the forest edge with increasing height in cases without ICR ( $LAI < 5$ ), and  $X_{S_p}$  remains constant with height in cases with ICR ( $LAI \geq 5$ ). The vertical black line separates these two groups, and it clarifies that exactly to the left of this line the curves diverge, leading to the alternate relations between  $X_{S_p}$  and  $LAI$  at the different heights.

The increase of  $S_p$  with increasing  $LAI$  (Fig. 8b) shows, just like  $X_{S_p}(LAI)$  (Fig. 8a), a strong dependence on the examined height level. The steepest slopes of  $S_p(LAI)$  can be found near the surface (yellow and green lines), with 2.4-times higher peak values for  $LAI_8$  than for  $LAI_1$  at  $z/H = 0.05$ . Towards the forest top,  $S_p$  deviates less between the different  $LAI$ , e.g. at  $z/H = 0.95$  by a factor of 1.3 between  $LAI_1$  and  $LAI_8$ .

Also for the relation between  $S_p$  and  $LAI$  (Fig. 8b) an effect of the presence of an ICR can be detected, namely that the slope of the curves is steeper with ICR than without. This implies that in forests with ICR the increase of the peak magnitude with increasing  $LAI$  proceeds at a higher rate, since the flow convergence is stronger in the presence of an ICR.

Compared to the concentration  $S_{ref}$  within the undisturbed flow upstream of the forest, peak concentrations can be higher by factors of up to 2.5 (Fig. 7), keeping in mind that the scalar was homogeneously released from the clearing and at the forest floor. Also with respect to the concentrations in the rear part of the forest,  $S_p$  can be up to twice as high, with highest deviations at the largest  $LAI$ . Thus, if measurements happen to be located within the scalar-

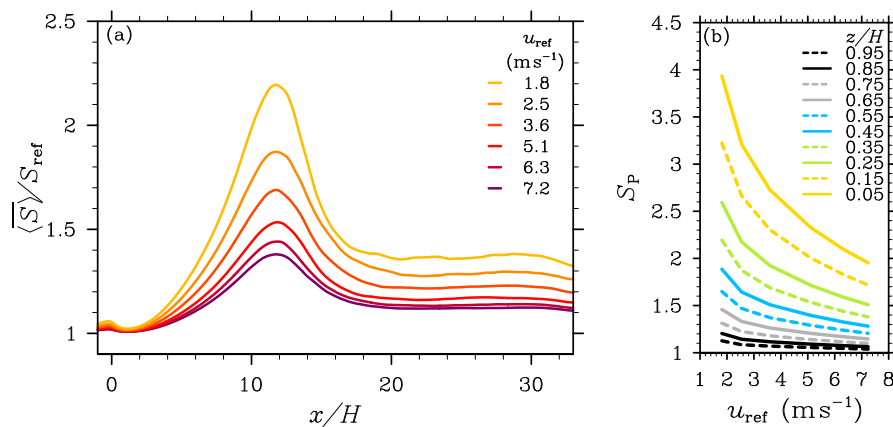


**Fig. 9** **a** Mean scalar concentration  $\langle S \rangle$  at  $z/H = 0.35$  as a function of distance  $x/H$  to the forest edge, normalized with  $S_{\text{ref}}$ . Different line colours mark the concentration distributions of the simulated UREF cases, at  $LAI = 4$ . **b** Peak magnitude  $S_{\text{P}}$  against  $u_{\text{ref}}$  at different heights. Different line colours and dash patterns mark the examined in-canopy heights.

peak region, it is rather difficult to draw general conclusions for in-canopy concentrations from such disturbed measurements.

### 3.3.2 Effect of wind speed

As described in Sect. 2.2, LES with different  $u_{\text{ref}}$  ranging from 1.8 to 7.2 m s<sup>-1</sup> were carried out. Figure 9a shows the mean scalar concentration  $\langle S \rangle$  for different  $u_{\text{ref}}$  at  $z/H = 0.35$  as a function of distance  $x/H$  to the forest edge, normalized with  $S_{\text{ref}}$ .

While  $S_{\text{P}}$  as well as the overall concentration level increase with decreasing  $u_{\text{ref}}$ , the peak position  $X_{S_{\text{P}}}$  remains invariant. The latter can be attributed to the fact that the flow deceleration due to the forest drag acts proportional to the square of the wind speed, i.e. the flow deceleration  $F_{u_i}$  (see Eq. 1) is, by definition, steered in such a way that the flow at a given  $LAI$  is always stopped within the same distance, independently of wind speed. Consequently, the region of strongest flow convergence, which is where the scalar accumulates, remains at a fixed location. The increase of the scalar concentration with decreasing  $u_{\text{ref}}$  follows, on the one hand, from the weaker turbulent mixing due to the overall weaker shear at smaller flow velocities, and on the other hand, from the weaker transport by the mean flow. Downstream of the respective scalar peaks, roughly beyond  $x/H = 20$ , concentrations reach their equilibrium values, which are overshoot in the peak regions by up to 60 % (UREF1). The deviations between the peak and the equilibrium concentrations are largest at the smallest  $u_{\text{ref}}$ . This means that especially under weak-wind conditions, large deviations from the equilibrium concentrations must be expected when measurements are located in the peak region.

Figure 9b illustrates the relation between  $S_P$  and  $u_{\text{ref}}$  at different heights within the forest. As already seen in Fig. 9a for  $z/H = 0.35$ , peak concentrations increase with decreasing wind speed. For the smallest  $u_{\text{ref}}$ , the near-surface  $S_P$  is up to a factor of 4 higher than the respective  $S_{\text{ref}}$  (above the clearing at the same height), again keeping in mind that the scalar was homogeneously released at the clearing and at the forest floor. Towards the highest  $u_{\text{ref}}$ , this factor decreases to 2, i.e. near-surface concentrations are about twice as high for UREF1 than for UREF7. This difference between the  $u_{\text{ref}}$  cases decreases to a factor of 1.1 towards the forest top.

### 3.4 Effect of forest density and wind speed on scalar fluxes

As shown above, mean scalar concentrations exhibit a high streamwise variability, despite the horizontally homogeneous surface source. A clear dependence of the concentration distribution on forest density and wind speed was found. In the following, we discuss how the corresponding scalar fluxes respond to the flow disturbance at the forest edge under the different conditions.

#### 3.4.1 Effect of forest density

Figure 10 presents mean resolved-scale turbulent scalar fluxes  $\overline{\langle w's' \rangle}$  for different  $LAI$  as a function of distance  $x/H$  to the forest edge, at  $z/H = 1.4$  (a) and  $z/H = 1.8$  (b). These positions correspond to heights of 12 and 24 m above the forest, respectively, which are typical heights for micrometeorological measurements above forests (e.g. Foken et al., 2012). The height  $z/H = 1.4$  is specifically chosen for a later comparison with the field measurements of Klaassen et al. (2002). At the presented heights, SGS contributions to the total turbulent fluxes are smaller than 1 %. Fluxes inside and just above the forest are not discussed, because SGS contributions are not negligible here. The net ecosystem exchange  $NEE$ , which in the present study equals the surface source strength  $Q_{S_0}$ , is used to normalize the scalar fluxes. It should be noted that  $\overline{\langle w's' \rangle}/NEE$  does not equal unity upstream of the forest, since the scalar flux decreases linearly with height (similar to the typical vertical profile of the sensible heat flux in a convective boundary layer), due to the given scalar-source configuration.

As detected for the concentration distributions (Fig. 7), the respective fluxes (Fig. 10) also show pronounced peaks at certain distances  $x/H$  from the forest edge, with likewise differing peak characteristics between the  $LAI$  cases. Similar to  $X_{S_P}$ , the flux-peak position  $X_{F_P}$  is located closer to the forest edge for larger  $LAI$ . At  $z/H = 1.4$  (a),  $X_{F_P}$  varies between 21 and 8 for  $LAI = 1$  to 8, respectively. A similar range of  $X_{F_P}$  values is detected at  $z/H = 1.8$  (b), but only slightly shifted downstream with the mean wind. The flux-peak magnitude  $F_P$  remarkably increases with increasing  $LAI$ , as detected in Sect. 3.3.1 for the behaviour of  $S_P(LAI)$ . This can be attributed

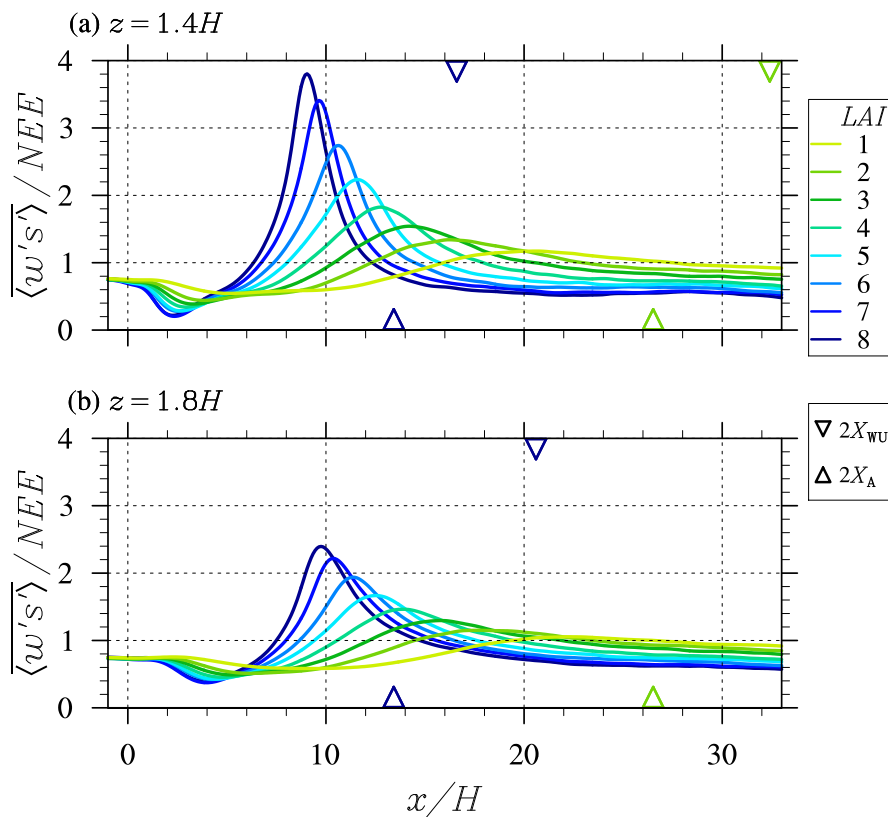


**Fig. 10** Mean resolved-scale turbulent scalar flux  $\overline{\langle w's' \rangle}$  as a function of distance  $x/H$  to the forest edge, at **a**  $z/H = 1.4$  and **b**  $z/H = 1.8$ , normalized with  $NEE$ . Different line colours mark the fluxes for different  $LAI$ .  $NEE$  equals the surface source strength  $Q_{S_0} = 0.2 \mu\text{g m}^{-2} \text{s}^{-1}$ . Upward and downward pointing triangles mark the positions of  $2X_A$  and  $2X_{WU}$ , respectively, exemplarily for  $LAI2$  and  $LAI8$ . In **b**,  $2X_{WU}$  for  $LAI2$  is not visible as it lies outside of the plotted area.

to the stronger wind gusts at larger  $LAI$  (not shown), efficiently transporting the scalar out of the forest, and further attributed to the larger vertical concentration gradients (see Fig. 4). At  $z/H = 1.4$  (a),  $F_P$  takes values from 1.2 ( $LAI1$ ) to 3.8 ( $LAI8$ ), which highlights that the streamwise flux-variability and the deviation of the fluxes from the  $NEE$  strongly depends on  $LAI$ . These values imply that the fluxes within the respective peak regions can overshoot the  $NEE$  by as much as 280 % for  $LAI8$  and by at least 20 % for  $LAI1$ . This outcome clearly questions the spatial representativity of in situ measurements above forests, performed too close to a clearing-forest transition. Of course, these quantitative conclusions depend on the behaviour of the vertical flux profile, and hence, on the distribution of scalar sinks and sources throughout the boundary layer. If e.g. a sink is present at the boundary-layer top, representing the mixing of scalar-poor air from the free atmosphere into the

boundary layer, the scalar flux would be rather constant with height or might even increase, which could yield even more enhanced overshoots than those observed with a linearly decreasing flux profile.

Nevertheless, we found the overshoot in simulation LAI1 to be similar to observations of Klaassen et al. (2002) from micrometeorological measurements at  $z/H = 1.4$ , above a 24-m tall forest with  $LAI = 1.8$ . Klaassen et al. (2002) detected a positive energy imbalance, caused by locally enhanced sensible and latent heat fluxes, corresponding to 16 % of the net radiation. Thus, the overshooting of the  $NEE$  with 20 % (LAI1) to 35 % (LAI2) in the present study exhibits the same magnitude as the observations from the field experiment of Klaassen et al. (2002). Furthermore, also the distances at which the overshooting is found in the present study, namely between  $x/H = 17$  (LAI2) and  $x/H = 21$  (LAI1), agree well with the fetches of  $20H$  determined by Klaassen et al. (2002). Even though the scalar fluxes of the present study are not directly comparable to the heat fluxes in Klaassen et al. (2002), owing to the different sink-source distribution, the detected similarity of the fetches and the relative flux overshoots lend confidence to our results.

The span of  $F_P$  values between the LAI cases decreases towards larger heights, but it still covers values between 1.1 (LAI1) and 2.4 (LAI8) at  $z/H = 1.8$  (Fig. 10b). At the same time, the deviation of each  $F_P$  from its respective equilibrium flux decreases with increasing distance to the forest top. Both findings can be attributed to the vanishing impact of the flow disturbance at the forest edge towards larger heights above the forest. As expected, scalar fluxes above the IBL top ( $z/H \approx 3-4$ ) are nearly homogeneous in the streamwise direction (not shown). Ross (2011) also reported a decreasing spatial flux-variability with increasing height above a fully forested hill. In hilly terrain, the flow separation in the lee of the hill leads to the local scalar accumulation, and hence, to the horizontal variability of concentrations and fluxes as a function of the hill scale. A comparison with the results from Ross (2011) shows that the effect of the hill morphology on the magnitude of the flux variability can be of the same order as the above-presented effect of the forest density.

#### 3.4.2 Effect of wind speed

Results of Sect. 3.3.2 indicate that the scalar concentration distribution near forest edges not only depends on forest density, but also on wind speed. In contrast, a variation of the wind speed from  $u_{\text{ref}} = 1.8$  to  $7.2 \text{ m s}^{-1}$  does not exhibit to have any effect on the detected flux patterns (not shown), as also reported by Sogachev et al. (2008). Although in-canopy concentrations increase with decreasing wind speed, the  $\langle w'S' \rangle$  distributions remain the same. This is because turbulent fluctuations  $w'$  and  $S'$  (from  $\langle w \rangle$  and  $\langle S \rangle$ , respectively) are inversely proportional to each other with changing wind speed. For example, at higher wind speeds, intermittent wind gusts are stronger, and hence,  $w'$  is larger than at lower wind speed. But at the same time,  $S'$  is generally smaller at larger  $u_{\text{ref}}$ , because the stronger shear, and consequently the stronger tur-

bulent mixing, lead to overall lower concentrations and reduced concentration gradients.

To summarize, the wind speed does not introduce additional complexity to the behaviour of flux patterns downstream of the leading forest edge. But the effect of wind speed on in-canopy concentrations should not be neglected, e.g. when it comes to the estimation of chemical reaction rates based on concentration measurements.

### 3.5 How to interpret and design micrometeorological measurements

Micrometeorological measurements are mostly set up at heights affected by the forest, where according to the presented results and to previous findings (e.g. Klaassen et al., 2002; Sogachev et al., 2008), mean scalar fluxes are spatially highly variable. For the interpretation of these measurements, it is therefore crucial to understand and quantify this spatial variability, in order to give recommendations on how to select spatially representative measuring positions. The term “representative” comprises that the measured mean fluxes characterize the mean turbulent exchange between forest and overlying atmosphere of a quasi-infinite forest. Consequently, “representative” micrometeorological measurements must be designed to capture fluxes that are adjusted to the modified surface conditions, i.e. they are no longer disturbed by the presence of the surface transition. Therefore, general fetch requirements should be proposed for appropriate sensor positioning. Belcher et al. (2012) suggested, based on the numerical simulations of Sogachev et al. (2008), that the scalar-flux adjustment should be completed at distances of  $2 X_A$  downstream of the forest edge, with

$$X_A = c_A L_c \ln \left( H \frac{U_B(H)}{L_c u_*} \right) \quad (6)$$

being the length of the flow-adjustment region within the canopy (Belcher et al., 2003, 2012). Coceal and Belcher (2004) suggested a value of 3 for the scaling coefficient  $c_A$ , based on numerical simulations of urban canopy flows. The canopy drag length  $L_c = 1/c_d a$  (e.g. Finnigan and Brunet, 1995; Belcher et al., 2003).  $U_B$  is the wind speed of the approaching flow, and  $u_*$  is the friction velocity in the above-canopy boundary layer.

$X_A$  was calculated for the presented LAI study, using a vertically averaged value of  $a$  for each LAI case. The upward-pointing triangles in Fig. 10a,b mark the corresponding positions of  $2 X_A$ , for reasons of clarity only for LAI2 (green) and LAI8 (dark blue). It should be noted that  $X_A$  takes the same value (at a specific  $LAI$ ) for both heights, since it is calculated as an average over the forest volume. Values of  $2 X_A$  decrease with increasing  $LAI$ , which follows directly from Eq. 6, and it was also previously stated e.g. by Dupont and Brunet (2009) that a flow adjusts more rapidly in denser forests.

In simulation LAI2, fetches of  $2 X_A$  are sufficient to allow the fluxes to be fairly adjusted (with deviations of less than 10 %) to the respective near-constant flux at  $x/H = 33$ , assumed to represent the adjusted flux. This is

visible for both presented heights (Fig. 10a,b). However, for LAI8 it is obvious that fetches of  $2 X_A$  are insufficient for a likewise flow adjustment. Fluxes at  $2 X_A$  still overshoot the adjusted fluxes by 70 % at  $z/H = 1.4$  (a) and by 100 % at  $z/H = 1.8$  (b). This indicates a strong LAI-dependence of the applicability of the  $2 X_A$ -fetch for the determination of the length of the flux-adjustment region.

To further visualize this dependence, the flux-adjustment position  $X_{FA}$  was calculated for each LAI case and at each height between  $z/H = 1.4$  and  $z/H = 2.0$ .  $X_{FA}$  describes the position  $x/H$ , where the scalar flux downstream of the flux peak first deviates by less than 10 % from the adjusted flux. Figure 11 presents  $X_{FA}$  (blue dots) as a vertical average between  $z/H = 1.4$  and  $z/H = 2.0$ , normalized with  $X_A$  and plotted against  $LAI$ . Vertical blue lines (error bars) illustrate the standard deviation of the respective height-averaged  $X_{FA}$  value. The dashed black line marks the  $2 X_A$ -fetch. It is evident that the factor, which has to be multiplied to the respective LAI-dependent  $X_A$  for an appropriate estimation of  $X_{FA}$ , increases linearly with increasing  $LAI$ , from about 2 for the smallest  $LAI$  to almost 4 for the largest  $LAI$ . According to the linear regression as marked by the solid blue line in Fig. 11, the required fetch  $X_{FA}$  for the flux adjustment can be determined by applying a correction factor  $c_f$  as follows:

$$X_{FA} = c_f X_A = (0.28 LAI + 1.58) X_A. \quad (7)$$

The linearity between  $X_{FA}/X_A$  and  $LAI$  is directly connected to the quality of  $X_A$  in quantifying the length of the flow-adjustment region inside the canopy for this range of  $LAI$ . We found that particularly for LAI cases with ICR occurrence, the respective  $X_A$  value is far from correctly marking the adjustment region. For example in simulation LAI8,  $X_A = 6.7H$ , yet, the streamwise flow (see Fig. 4a, right) is not adjusted at this location, but it rather shows a flow reversion extending downstream to  $x/H = 18.5 = X_{ICR,r}$  (see also Table 2). Assuming that  $X_{ICR,r}$  roughly marks the downstream distance where the in-canopy flow is adjusted,  $X_A$  significantly underestimates the length of the adjustment region. The relation between  $X_{ICR,r}/X_A$  and  $LAI$  is presented in Fig. 11 (brown dots, with error bars and regression line as drawn for  $X_{FA}/X_A(LAI)$ ) for each  $LAI$  with an ICR. The more  $X_{ICR,r}/X_A$  deviates from 1.0, the lower the ability of  $X_A$  to correctly mark the adjustment region. It is evident that the quality of  $X_A$  decreases with increasing  $LAI$ , as the deviation between  $X_A$  and  $X_{ICR,r}$  increases. Interestingly,  $X_{ICR,r}/X_A(LAI)$  follows a very similar slope as  $X_{FA}/X_A(LAI)$ , which suggests that the linear relation between  $X_{FA}/X_A$  and  $LAI$  results directly from the behaviour of the quality of  $X_A$ .

The relation in Eq. 7 should be generally applicable for forest sites with sparse trunk and dense crown space, for the simulated wide range of  $LAI$  under conditions where surface sources of a scalar dominate over canopy sources/sinks. How this relation might have to be modified under conditions with different source-sink distributions, vertically homogeneous forests or non-neutral atmospheric stratification, is subject to further studies.

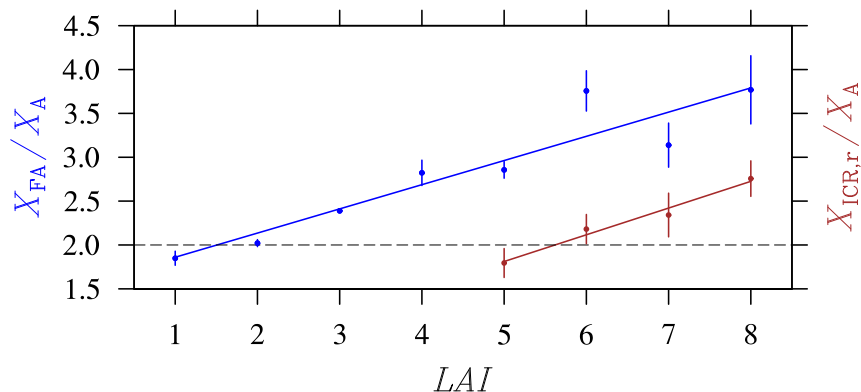


**Fig. 11** Height-averaged (between  $z/H = 1.4$  and  $z/H = 2.0$ ) flux-adjustment position  $X_{FA}$  (blue dots), normalized with  $X_A$  and plotted against  $LAI$ . The dashed black line marks the relation  $X_{FA}/X_A = 2.0$ . Brown dots illustrate the relation between  $X_{ICR,r}/X_A$  and  $LAI$ , with  $X_{ICR,r}$  (height-averaged) being the downstream boundary of the ICR for  $LAI$  with an ICR. Blue and brown vertical lines (error bars) illustrate the standard deviations of the respective height-averaged  $X_{FA}$  and  $X_{ICR,r}$  values, respectively. Solid lines describe the respective regressions of the two functions.

In the following, an additional fetch-approach is presented, which can be applied under the simulated conditions without involving an empirical function. The present investigations revealed that the peak positions of scalar fluxes at a specific height above the forest (Fig. 10) agree fairly well with the  $x/H$ -position  $X_{WU}$  of the momentum-flux peak (absolute value) at that height (Fig. 4c, white crosses), i.e. momentum and scalar adjustment proceed in the same manner. This spatial agreement is valid for flux boundary conditions (e.g. Belcher et al., 2012), i.e. in situations where the scalar source strength is independent of spatial concentration gradients (e.g. in case of soil respiration of  $CO_2$ ). Hence, under the conditions analyzed in the present study,  $X_{WU}$  can be used to identify  $X_{Fp}$ , and to quantify the necessary fetch for the fluxes to be adjusted. This is illustrated in Fig. 10a,b by the downward-pointing triangles, representing  $2 X_{WU}$  exemplarily for LAI2 (green) and LAI8 (dark blue). At  $z/H = 1.8$  (b),  $2 X_{WU} = 38.4$  for LAI2 and therefore lies outside of the plotted area. It can be seen for both presented heights in Fig. 10 that a distance of  $2 X_{WU}$  is sufficient to allow the scalar fluxes to adjust to an equilibrium value. In practice, this implies that solely the location of the largest absolute value of the momentum flux has to be determined at the desired measuring height, in order to define the required fetch. For this purpose, Doppler lidars could be applied. Träumner et al. (2012) and Kanani et al. (2014) have shown in a combined application of lidar, wind tunnel and LES that the utilized Doppler lidar was able to adequately measure the forest-edge-flow features. We are certainly aware that this cost-intensive tool is mostly not an option for the set-up of short-term measuring campaigns, but it might be useful for the preparation of long-term micrometeorological measurements near forest edges.



#### 4 Summary

Our aim was to improve the understanding of the scalar transport near forest edges, in order to enable a better interpretation and design of in situ micrometeorological measurements in such locations. Because of the yet scarce understanding in this field of study, we simulated idealized neutral flows across a clearing-to-forest transition (forest edge) in flat terrain. In order to keep the scalar sources simple, a passive scalar was released from a horizontally homogeneous source at the clearing and at the forest floor. Despite the homogeneous source strength, we found a high streamwise variability in the scalar concentrations and fluxes, similar to the results of previous observational and numerical experiments (Klaassen et al., 2002; Klaassen and Sogachev, 2006; Sogachev et al., 2008; Ross and Baker, 2013). Concentrations and fluxes formed a pronounced peak inside and above the forest downstream of the forest edge.

We discussed for the first time (to our best knowledge) in detail the main scalar transport mechanisms and the cause of the local scalar accumulation (concentration peak). By calculating the terms in the scalar transport equation, we found that the scalar accumulation is partly accomplished by the streamwise mean-flow convergence, in agreement with Sogachev et al. (2008). With the ability of LES to resolve the bulk of the turbulence, in contrast to the RANS results in Sogachev et al. (2008), we additionally found that the scalar accumulation is realized in equal parts also by the convergence of the streamwise turbulent transport. The scalar depletion in the peak region is mainly accomplished by the divergence of the vertical turbulent transport. In dense forests, the depletion is also in equal parts realized by the divergence of the transport by the vertical mean flow and by the turbulent flow in the streamwise direction. We found this to be directly connected to the occurrence of a streamwise flow reversion in this region, which only develops in dense forests with  $LAI > 4$  (see also Cassiani et al., 2008).

We further investigated in detail to what extent plant physical and atmospheric parameters affect the scalar accumulation. We revealed from a series of LES with varying forest densities ( $LAI = 1$  to  $8$ ) that the concentration peak is found closer to the forest edge with increasing  $LAI$ , due to the higher drag. Peak locations were found at distances between  $8$  ( $LAI = 8$ ) and  $20$  ( $LAI = 1$ ) forest heights downstream of the edge. Peak concentrations increased with increasing  $LAI$ , with values for  $LAI = 8$  being twice as high as for  $LAI = 1$ . Increasing the 10-m wind speed in a range from  $1$  to  $7 \text{ m s}^{-1}$  showed no change in the peak location. However, peak concentrations increased by a factor of two from the highest to the lowest wind speed. This behaviour can be attributed to the weaker vertical shear at lower wind speeds, and hence to the less efficient turbulent mixing. This strong dependence of in-canopy concentrations on forest density and wind speed has to be considered, e.g. when estimating chemical-reaction rates based on concentration measurements. Based on Ross and Baker (2013), who numerically studied the scalar transport above a partially forested hill, we can assume that the existence of a hill additionally affects the magnitude of the concentration variability. Depending on the po-

sitioning of the forest patch with respect to the hill summit, Ross and Baker (2013) found decreased as well as increased concentration peaks, in comparison with a case of a partially forested flat terrain as simulated herein.

We also analyzed how the scalar fluxes behave under the different conditions. In agreement with Sogachev et al. (2008), scalar fluxes show a pronounced peak downstream of the forest edge. Similar to the behaviour of the concentration peak, we found the scalar flux peak to be located closer to the forest edge with increasing  $LAI$ , and peak fluxes increased significantly, keeping in mind that the given surface fluxes were equal for all  $LAI$  values. Peak fluxes above the forest were found to exceed the underlying surface fluxes by factors of up to four for the largest  $LAI$ . For the sparsest forest, the deviations from the surface fluxes were of the same magnitude as found in a field experiment of Klaassen et al. (2002) for a similarly sparse forest. A variation of the wind speed in our LES revealed no effect on the scalar-flux behaviour, in agreement with Sogachev et al. (2008). Ross (2011) suggests that the presence of a hilly terrain, even if fully forested, can have a noticeable effect on the scalar-flux variability. This effect is of the same order of magnitude as the effect of forest density discussed in the present study. In summary, the large deviations from the surface fluxes, the high streamwise variability of the scalar flux and its strong dependence on  $LAI$  highlight the large uncertainty that is introduced to the interpretation of in situ micrometeorological measurements in forest-edge flow regimes.

If the intention of a micrometeorological experiment is to measure “undisturbed” fluxes, i.e. fluxes that have adjusted to the new surface conditions downstream of the transition, these measurements have to be made at a location far downstream of the forest edge. In order to determine such a location, general fetch estimations must be provided. We analyzed whether the dynamical adjustment length  $X_A$  proposed by Belcher et al. (2003, 2012), being a function of e.g. canopy drag, wind speed and friction velocity, is applicable for this purpose. Based on the results of Sogachev et al. (2008), it was assumed by Belcher et al. (2012) that a distance of  $2 X_A$  from the forest edge is sufficient for the scalar fluxes to be adjusted. However, our results revealed that the prefactor of 2 holds only for the sparsest forests, and it increases linearly up to 4 for the largest  $LAI$ . Based on these findings, we proposed an empirical function for the determination of this prefactor. We further presented an alternative approach, which allows estimation of the required fetch for the scalar flux adjustment based on the location of the momentum-flux peak. In cases where surface sources dominate over canopy (leaf surface) sources, and where the source strength does not depend too much on local gradients, the scalar-flux peak location coincides with the momentum-flux peak location. We propose that twice the distance from the forest edge to the momentum-flux peak location should be sufficient for the scalar-flux adjustment under such scalar boundary conditions. The location of the momentum-flux peak can e.g. be identified by using Doppler lidar (Träumner et al., 2012; Kanani et al., 2014). While this state-of-the-art tool is mostly not an option for short-term measuring campaigns, it might be useful for the preparation of long-term micromete-

orographical measurements. It should be noted that this holds for relatively flat terrain, i.e. where forest-edge effects are assumed to be more dominant than orographical effects.

It is well known from previous studies (e.g. Klaassen et al., 2002; Sogachev et al., 2008) that, under conditions where canopy sources dominate or where the source strength depends on local gradients, scalar fluxes adjust less rapidly than momentum fluxes. However, so far no concrete relation was found between the adjustment processes. This highlights that further thorough investigations are necessary under various atmospheric (thermal stability), plant physical (forest structure, clearing and forest length), orographical and scalar-source-sink conditions. This is crucial for the detailed understanding of the scalar transport and adjustment processes in forest-edge regimes, and this is the prerequisite for proper fetch estimations. Reliable fetch estimations are in turn essential to improve the spatial representativity and thus the quality of micrometeorological measurements, which in the wider sense will improve the estimation of the forest-atmosphere exchange of energy and mass as an input for weather prediction and climate models. The presented LES study has provided, e.g. with the detailed analysis of the in-canopy scalar transport processes, a starting point for future investigations in this field of study.

**Acknowledgements** This study was supported by the German Research Foundation (DFG) under grant RA 617/23-1. All simulations were performed on the SGI Altix ICE at The North-German Supercomputing Alliance (HLRN) in Hannover and Berlin. NCL<sup>4</sup> and VAPOR have been used for data analysis and visualization. We thank the two anonymous reviewers for their detailed comments that helped to improve this manuscript.

## References

- Asner GP, Scurlock JMO, Hicke JA (2003) Global synthesis of leaf area index observations: implications for ecological and remote sensing studies. *Global Ecol Biogeogr* 12(3): 191–205.
- Baldocchi D, Falge E, Gu L, Olson R, Hollinger D, et al. (2001) FLUXNET: A new tool to study the temporal and spatial variability of ecosystem-scale carbon dioxide, water vapor, and energy flux densities. *Bull Am Meteorol Soc* 82: 2415–2434.
- Belcher SE, Harman IN, Finnigan JJ (2012) The wind in the willows: flows in forest canopies in complex terrain. *Annu Rev Fluid Mech* 44: 479–504.
- Belcher SE, Jerram N, Hunt JCR (2003) Adjustment of a turbulent boundary layer to a canopy of roughness elements. *J Fluid Mech* 488: 369–398.
- Bergström H, Högström U (1989) Turbulent exchange above a pine forest ii. organized structures. *Boundary-Layer Meteorol* 49: 231–263.
- Brunet Y, Irvine MR (2000) The control of coherent eddies in vegetation canopies: streamwise structure spacing, canopy shear scale and atmospheric stability. *Boundary-Layer Meteorol* 94(1): 139–163.
- Cassiani M, Katul GG, Albertson JD (2008) The effects of canopy leaf area index on air-flow across forest edges: large-eddy simulation and analytical results. *Boundary-Layer Meteorol* 126: 433–460.
- Coceal O, Belcher SE (2004) A canopy model of mean winds through urban areas. *Q J R Meteorol Soc* 130: 1349–1372.

<sup>4</sup> The NCAR Command Language (Version 6.1.2) [Software]. (2013). Boulder, Colorado: UCAR/NCAR/CISL/VETS. <http://dx.doi.org/10.5065/D6WD3XH5>.

- Deardorff JW (1980) Stratocumulus-capped mixed layers derived from a three-dimensional model. *Boundary-Layer Meteorol* 18: 495–527.
- Dupont S, Brunet Y (2008) Edge flow and canopy structure: a large-eddy simulation study. *Boundary-Layer Meteorol* 126: 51–71.
- Dupont S, Brunet Y (2009) Coherent structures in canopy edge flow: a large-eddy simulation study. *J Fluid Mech* 630: 93–128.
- Dupont S, Irvine MR, Bonnefond JM, Lamaud E, Brunet Y (2012) Turbulent structures in a pine forest with a deep and sparse trunk space: stand and edge regions. *Boundary-Layer Meteorol* 143: 309–336.
- Edburg SL, Stock D, Lamb BK, Patton EG (2012) The effect of the vertical source distribution on scalar statistics within and above a Forest Canopy. *Boundary-Layer Meteorol* 142: 365–382.
- Finnigan JJ (2000) Turbulence in plant canopies. *Annu Rev Fluid Mech* 32: 519–571.
- Finnigan JJ, Brunet Y (1995) Turbulent airflow in forests on flat and hilly terrain. In: Coutts MP, Grace J (eds) *Wind and trees*. Cambridge University Press, Cambridge, pp 340
- Finnigan JJ, Shaw RH, Patton EG (2009) Turbulence structure above a vegetation canopy. *J Fluid Mech* 637: 387–424.
- Foken T, Meixner FX, Falge E, Zetzsch C, Serafimovich A, Bargsten A, Behrendt T, Biermann T, Breuninger C, Dix S, Gerken T, Hunner M, Lehmann-Pape L, Hens K, Jocher G, Kesselmeier J, Lers J, Mayer JC, Moravek A, Plake D, Riederer M, Rtz F, Scheibe M, Siebicke L, Srgel M, Staudt K, Trebs I, Tsokankunku A, Welling M, Wolff V, Zhu Z (2012) Coupling processes and exchange of energy and reactive and non-reactive trace gases at a forest site results of the EGER experiment. *Atmos Chem Phys* 12: 1923–1950.
- Gao W, Shaw RH, Paw U KT (1989) Observation of organized structures in turbulent flow within and above a forest canopy. *Boundary-Layer Meteorol* 47: 349–377.
- Garratt J (1990) The internal boundary layer - a review. *Boundary-Layer Meteorol* 50: 171–203.
- Huang J, Cassiani M, Albertson JD (2009) The effects of vegetation density on coherent turbulent structures within the canopy sublayer: a large-eddy simulation study. *Boundary-Layer Meteorol* 133: 253–275.
- Huang J, Cassiani M, Albertson JD (2011) Coherent turbulent structures across a vegetation discontinuity. *Boundary-Layer Meteorol* 140: 1–22.
- Kanani F, Träumner K, Ruck B, Raasch S (2014) What determines the differences found in forest edge flow between physical models and atmospheric measurements? – An LES study. *Meteorol Z Pre-Pub DOI: 10.1127/0941-2948/2014/0542*.
- Kanda M, Hino M (1994) Organized structures in developing turbulent flow within and above a plant canopy, using a large-eddy simulation. *Boundary-Layer Meteorol* 68: 237–257.
- Katul GG, Finnigan JJ, Poggi D, Leuning R, Belcher SE (2006) The influence of hilly terrain on canopy-atmosphere carbon dioxide exchange. *Boundary-Layer Meteorol* 118: 189–216.
- Klaassen W, Sogachev A (2006) Flux footprint simulation downwind of a forest edge. *Boundary-Layer Meteorol* 121: 459–473.
- Klaassen W, Van Breugel PB, Moors EJ, Nieveen JP (2002) Increased heat fluxes near a forest edge. *Theor Appl Climatol* 72: 231–243.
- Lu CH, Fitzjarrald DR (1994) Seasonal and diurnal variations of coherent structures over a deciduous forest. *Boundary-Layer Meteorol* 69: 43–69
- Monin AS, Obukhov AM (1954) Osnovnye zakonomernosti turbulentnogo peremeshivaniya v prizemnom sloe atmosfery (Basic laws of turbulent mixing in the atmosphere near the ground). *Tr Akad Nauk SSSR Geophys Inst* 24: 163–187.
- Poggi D, Porporato A, Ridolfi L, Albertson JD, Katul GG (2004) The effect of vegetation density on canopy sub-layer turbulence. *Boundary-Layer Meteorol* 111: 565–587.
- Raasch S, Schröter M (2001) Palm - a large-eddy simulation model performing on massively parallel computers. *Meteorol Z* 10: 363–372
- Raupach MR, Finnigan JJ, Brunet Y (1996) Coherent eddies and turbulence in vegetation canopies: the mixing-layer analogy. *Boundary-Layer Meteorol* 78: 351–382.
- Ross AN (2011) Scalar transport over forested hills. *Boundary-Layer Meteorol* 141: 179–199.
- Ross AN, Baker TP (2013) Flow over partially forested ridges. *Boundary-Layer Meteorol* 146: 375–392.

- Schumann U, Sweet RA (1988) Fast Fourier transforms for direct solution of Poissons equation with staggered boundary conditions. *J Comput Sci* 75: 123–137.
- Shaw RH, Patton EG (2003) Canopy element influences on resolved- and subgrid-scale energy within a large-eddy simulation. *Agric For Meteorol* 115: 5–17.
- Shaw RH, Schumann U (1992) Large-eddy simulation of turbulent flow above and within a forest. *Boundary-Layer Meteorol* 61: 47–64.
- Shaw RH, Seginer I (1985) The dissipation of turbulence in plant canopies. In: *Proceedings of the 7th Symposium of the American Meteorological Society on Turbulence and Diffusion*. Boulder, Colorado, pp. 200–203.
- Shaw RH, Brunet Y, Finnigan JJ, Raupach MR (1995) A wind tunnel study of air flow in waving wheat: two-point velocity statistics. *Boundary-Layer Meteorol* 76: 349–376.
- Sogachev A, Leclerc MY, Zhang G, Rannik Ü, Vesala T (2008) CO<sub>2</sub> fluxes near a forest edge: a numerical study. *Ecol Appl* 18(6): 1454–1469.
- Steiner AL, Pressley SN, Botros A, Jones E, Chung SH, Edburg SL (2011) Analysis of coherent structures and atmosphere-canopy coupling strength during the CABINEX field campaign. *Atmos Chem Phys* 11: 11921–11936
- Su HB, Shaw RH, Paw U KT (2000) Two-point correlation analysis of neutrally stratified flow within and above a forest from large-eddy simulation. *Boundary-Layer Meteorol* 49: 423–460.
- Su HB, Shaw RH, Paw U KT, Moeng CH, Sullivan PP (1998) Turbulent statistics of neutrally stratified flow within and above a sparse forest from large-eddy simulation and field observations. *Boundary-Layer Meteorol* 88: 363–397.
- Träumner K, Wieser A, Ruck B, Frank C, Röhner L, Kottmeier C (2012) The suitability of Doppler lidar for characterizing the wind field above forest edges. *Forestry* 85: 399–412.
- Watanabe T (2004) Large-eddy simulation of coherent turbulence structures associated with scalar ramps over plant canopies. *Boundary-Layer Meteorol* 112: 307–341.
- Wicker L, Skamarock W (2002) Time-splitting methods for elastic models using forward time schemes. *Mon Weather Rev* 130: 2088–2097
- Williamson JH (1980) Low-storage Runge-Kutta schemes. *J Comput Phys* 35: 48–56
- Yang B, Raupach MR, Shaw RH, Paw U KT, Morse AP (2006) Large-eddy simulation of turbulent flow across a forest edge. Part I: flow statistics. *Boundary-Layer Meteorol* 120: 377–412.
- Yang B, Morse AP, Shaw RH and Paw U KT (2006) Large-eddy simulation of turbulent flow across a forest edge. Part II: momentum and turbulent kinetic energy budgets. *Boundary-Layer Meteorol* 121: 433–457.

### 3.3 Research article C: Enhanced scalar concentrations and fluxes in the lee of forest patches: A large-eddy simulation study

#### 3.3.1 Declaration of my contribution

The article was written by myself, and I performed the associated simulations and the data analysis. Internal discussions within the PALM group as well as comments on the original manuscript by Prof. Dr. Siegfried Raasch and Dr. Matthias Sühling improved the quality of the article.

#### 3.3.2 Submitted article

This article was submitted to *Boundary-Layer Meteorology* and is currently in the review process. The general business terms of the journal *Boundary-Layer Meteorology* (publisher Springer Science + Business Media) allow the use of the submitted article as a part of a dissertation.

**Kanani-Sühling, F. and S. Raasch, 2015:** Enhanced scalar concentrations and fluxes in the lee of forest patches: A large-eddy simulation study. Submitted to *Boundary-Layer Meteorol.*, under review.

<b>Boundary-Layer Meteorology manuscript No.</b> (will be inserted by the editor)
--

---

## Enhanced scalar concentrations and fluxes in the lee of forest patches: A large-eddy simulation study

Farah Kanani-Sühring · Siegfried Raasch

Received: date / Accepted: date

**Abstract** By means of large-eddy simulation, we investigated the transport of surface-emitted passive scalar in the lee of forest patches under neutral atmospheric conditions in flat terrain, for different forest densities and wind speeds, as a follow-up study to similar investigations near windward forest edges. The goal of this study was to improve the scarce understanding of the transport mechanisms, in order to enable a better interpretation and an optimized set-up of micrometeorological measurements near leeward forest edges. We found a pronounced local enhancement of scalar concentration and its flux in the lee zone of the forest, while further downstream above the unforested surface, the scalar transport adjusted to an equilibrium with the underlying surface conditions. By means of a term-by-term analysis of the scalar transport equation, we determined the local accumulation of scalar to be caused by the convergence of (1) mean and turbulent streamwise transport and (2) mean vertical transport. However, the relative importance of each transport mechanism for the accumulation process was found to depend strongly on forest density. Based on systematic parameter studies, we found concentrations to remarkably increase with increasing forest density and with decreasing wind speed, while fluxes were invariant of wind speed and showed a similar relation to forest density as the concentrations. We finally propose an approach in order to localize and estimate enhanced concentrations and fluxes at micrometeorological sites, based on along-the-way measured high-frequency flow data.

**Keywords** Enhanced scalar fluxes · Forest-edge flow · Large-eddy simulation · Lee recirculation · Scalar accumulation

---

Farah Kanani-Sühring · Siegfried Raasch  
Institut für Meteorologie und Klimatologie, Leibniz Universität Hannover  
Herrenhäuser Str. 2, 30419 Hannover, Germany  
E-mail: kanani@muk.uni-hannover.de

## 1 Introduction

The transport of scalars like temperature, humidity and trace gases (e.g. CO<sub>2</sub>) is highly complex in fragmented forested landscapes. Previous studies (Klaassen et al., 2002; Sogachev et al., 2008; Ross and Baker, 2013; Kanani-Sühring and Raasch, 2014) have shown that the mean and the turbulent transport processes are markedly modified near clearing-to-forest transitions (windward forest edge), as compared to further upstream or downstream. This is due to the abrupt change of mechanic and thermodynamic surface properties at the transition. Scalar concentrations and their turbulent vertical fluxes inside and above a finite forest patch were found to be locally enhanced with respect to their adjusted equilibrium value further downstream of the windward forest edge, due to flow-convergence effects. This certainly complicates the interpretation of micrometeorological measurements concerning their spatial representativeness in such fragmented forested landscapes. The mentioned studies focused on flows over windward forest edges. Up to date it is still an open question, how the transport of scalars behaves in the lee of forest patches, where the flow gradually adjusts to the properties of the relatively smoother clearing surface.

We know that flows in the lee of permeable obstacles, such as forest patches (Bergen, 1975; Miller et al., 1991; Cassiani et al., 2008; Detto et al., 2008; Frank and Ruck, 2013; Belcher et al., 2012; Queck et al., 2014), can exhibit distinct flow patterns like flow separation, recirculation and reattachment. Similar patterns are observed in the lee of hills (Raupach et al., 1992; Finnigan and Belcher, 2004; Katul et al., 2006; Poggi and Katul, 2007; Ross, 2008, 2011), single buildings (e.g. Letzel et al., 2008, 2012) or simple steps (e.g. Armaly et al., 1983; Kostas et al., 2002; Markfort et al., 2014), and within street canyons (e.g. Chan et al., 2002; Cai et al., 2008; Fontan et al., 2013). For example, in the lee of crosswind-elongated hills or sharp steps, flows tend to recirculate due to pressure redistribution, before they reattach back to the surface behind the obstacle. This was found mostly from laboratory studies (e.g. Chan et al., 2002; Poggi and Katul, 2007; Fontan et al., 2013; Markfort et al., 2014) or numerical simulations (e.g. Raupach et al., 1992; Katul et al., 2006; Frank and Ruck, 2013; Ross, 2008, 2011). In the past decades, special attention has been addressed to flows across abrupt solid surface steps, termed backward-facing-step (BFS) flows, extensively studied in wind tunnels and with numerical simulation tools such as Reynolds-averaged Navier-Stokes (RANS) or large-eddy simulation (LES) models. The purpose of those BFS-flow studies was mostly directed towards urban applications, e.g. with respect to the investigation of street-canyon ventilation or pollutant dispersion.

Flows in the lee of permeable steps like forest patches also show features of BFS flow (Cassiani et al., 2008; Detto et al., 2008). However, these flows cannot purely be described as a BFS flow, since due to the porosity of the forest, a certain amount of the flow originates from the forest interior, termed exit flow (Cassiani et al., 2008; Detto et al., 2008). By means of LES, Cassiani et al. (2008) revealed that both flow types, BFS and exit flow, form an intermittent



composition at transitions from forested to unforested land surfaces. Same was reported by Detto et al. (2008) from field measurements near a leeward forest edge, where they identified intermittent rotor formation in sonic-anemometer data. Such alternating rotor- and through-flow periods were already identified decades ago by Bergen (1975), performing a smoke-release experiment in a forest gap. Cassiani et al. (2008) further revealed that the relative contributions of BFS and exit flow strongly depend on forest density, with a more frequent occurrence of BFS events in the lee of denser forests.

In heterogeneous flow regimes, not only the flow dynamics are locally perturbed, but also the transport of scalars between land surface, vegetation and atmosphere. In a wind-tunnel experiment about the flow across a forested hill, Poggi and Katul (2007) detected a local accumulation of fluorescent dye within the rotor region on the lee side of the hill. Analogue findings were drawn by Katul et al. (2006) and Ross (2011) from RANS and LES with similar set-ups, reporting large streamwise variations of the tracer concentration across the hill with maximum concentrations near the separation point on the lee side, accompanied with enhanced tracer fluxes. Also in the lee of abrupt steps, local tracer accumulation has been previously reported, by means of numerical simulations (e.g. Chan et al., 2002) and flume experiments (e.g. Fontan et al., 2013). So far, only few studies have focused on the flow exiting a forest patch and reattaching to the clearing surface (Cassiani et al., 2008; Detto et al., 2008; Markfort et al., 2014), and even less attention was paid to the scalar transport in such flow regimes. Since forest-lee flows show similarities with flows behind solid obstacles, supposedly, the scalar transport and the spatial scalar distribution likewise share some features. However, due to the intermittence of BFS and exit-flow events in a forest edge flow (permeable step), as compared to a pure BFS flow (solid step), the scalar transport might strongly depend on the forest morphology.

The scope of this LES study, is to examine for the first time in detail the transport and the spatial distribution of a passive scalar in the lee of a span-wise elongated forest patch. Due to the yet scarce understanding, an idealized set-up is explicitly selected, simulating neutral flows in flat terrain across periodic forest-clearing-forest configurations. By varying the forest density and the mean wind speed, we analyze how scalar concentrations and fluxes react under different plant-physical and meteorological conditions. One of the main questions behind this is, to what extent the background conditions and the permeability of an obstacle might modify the scalar transport in the obstacle's lee. Further, this study aims at identifying the resulting implications for planning and interpreting micrometeorological measurements close to leeward forest edges, as well as at proposing a method for the estimation of the regions with enhanced scalar concentrations and fluxes.

Section 2 briefly describes the applied LES model and the used simulation set-ups. Simulation results are discussed in Sect. 3, starting with the general flow features in the lee of the forest patch (Sect. 3.1), followed by a demonstration of the scalar accumulation and an analysis of the scalar-transport mechanisms (Sect. 3.2). Section 3.3 examines the spatial distribution of the

scalar concentration and its flux under different plant-physical and meteorological conditions. In Sect. 3.4, we finally discuss options for planning and interpreting micrometeorological measurements in the lee of forest patches. The main results are summarized in Sect. 4.

## 2 Methods

The investigation of the scalar transport in the lee of forests, being a follow-up to the LES study by Kanani-Sühring and Raasch (2014) about the scalar transport processes inside and above a forest patch, is based on LES data of the same idealized simulations. The present study also utilized the parallelized LES model PALM (Raasch and Schröter, 2001) with its embedded canopy model (at revision 874<sup>1</sup>. A documentation of the most recent PALM release 4.0, with a detailed description of PALMs canopy model is given by Maronga et al. (2015).), to resolve the turbulent flow down to the scales of forest-canopy turbulence, in order to analyze the effect of the flow disturbance at a forest edge on the transport of a passive scalar. Fundamental equations for the simulation of an atmospheric flow in PALM, the formulation of the embedded canopy model, applied numerics and boundary conditions, as well as a detailed description and justification of the simulation set-up and the case studies can be found in Kanani-Sühring and Raasch (2014). Nevertheless, some set-up information are briefly given in the following.

The LES model domain as illustrated in Fig. 1 had a streamwise ( $x$ ), spanwise ( $y$ ) and vertical ( $z$ ) extent of  $L_x \times L_y \times L_z = 77 H \times 38 H \times 13 H$ , respectively, with the forest height  $H = 30$  m. A uniform grid spacing of 3 m was used in each spatial direction. The forest patch covered a length  $L_{Fo} = 33H$  of the domain surface in the  $x$ -direction and the entire  $y$ -direction. The total length of the clearing (unforested part of the domain) adds up to  $L_{Cl} = L_x - L_{Fo} = 44H$ . In the horizontal directions, the forest density was homogeneous, whereas the vertical distribution of the leaf area density  $a$  was heterogeneous, with the bulk of the leaf area concentrated in the crown space. Vertical profiles of  $a$  are presented in Fig. 2a for different leaf area indexes ( $LAI$ : Vertical integral of  $a$ ). The canopy drag coefficient  $c_d$ , which appears as a constant in PALMs canopy model (see Kanani et al., 2014; Kanani-Sühring and Raasch, 2014), was set to a typical value for trees of 0.2 as in previous studies (e.g. Cassiani et al., 2008; Dupont and Brunet, 2008). A purely shear-driven neutrally-stratified flow with omitted Coriolis force was simulated in the  $x$ -direction ( $u$ -velocity component), by prescribing a longitudinal pressure gradient  $\partial p/\partial x$  (see Table 1) oriented perpendicular to the forest edge. After the flow had reached a steady state, passive scalar  $S$  was released from a continuous horizontally homogeneous surface source (see grey-shaded surface in Fig. 1) at a constant rate of  $0.2 \mu\text{g m}^{-3} \text{s}^{-1}$ , both on the clearing and the forest patch. No further sinks or sources of the scalar were considered.

---

<sup>1</sup> The code can be accessed under <http://palm.muk.uni-hannover.de/browser?rev=874>

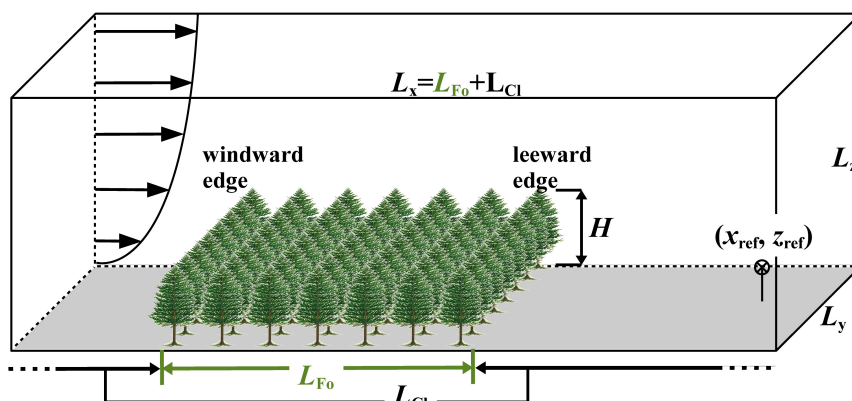


**Fig. 1** Sketch of the LES model domain.  $L_x$ ,  $L_y$ ,  $L_z$  are domain length, width and height, respectively. The forest extends over a length of  $L_{Fo} = 33H$  in the  $x$ -direction and over the total domain width  $L_y$ . The forest height is  $H = 30$  m. The clearing length  $L_{Cl} = 44H$  describes the total length of the unforested part of the domain. The flow (arrows) is directed perpendicular to the forest edge. The grey surface illustrates the homogeneous scalar source.  $(x_{ref}, z_{ref})$  describe coordinates of the reference position, where e.g. reference wind speed  $u_{ref}$  is defined.

**Table 1** Overview of the  $LAI$  values, longitudinal pressure gradients  $\partial p/\partial x$  and reference velocities  $u_{ref}$  used in the present LES study.

LES run	$LAI$	$\partial p/\partial x$ (Pa m <sup>-1</sup> )	$u_{ref}$ (m s <sup>-1</sup> )
LAI1	1	-0.0017	4.6
LAI2	2	-0.0017	4.6
LAI3	3	-0.0017	4.6
LAI4	4	-0.0017	4.6
LAI5	5	-0.0017	4.6
LAI6	6	-0.0017	4.6
LAI7	7	-0.0017	4.6
LAI8	8	-0.0017	4.6
UREF1	4	-0.00025	1.8
UREF2	4	-0.0005	2.5
UREF3	4	-0.001	3.6
UREF5	4	-0.002	5.1
UREF6	4	-0.003	6.3
UREF7	4	-0.004	7.2

As listed in Table 1, eight simulations with different  $LAI$  values were performed (see Fig. 2a), at a given reference wind speed of  $u_{ref} = 4.6$  m s<sup>-1</sup>, as well as six simulations with different wind speeds (see Fig. 2b) at a constant  $LAI = 4$ . Reference wind speed  $u_{ref}$  equals the time- and  $y$ -averaged stream-wise velocity component  $u$  at  $(x_{ref} = 33H, z_{ref} = 0.35H)$  above the clearing downstream of the leeward forest edge.

The scalar transport is analyzed by means of the terms of the scalar transport equation, as previously described and applied by Kanani-Sühring and

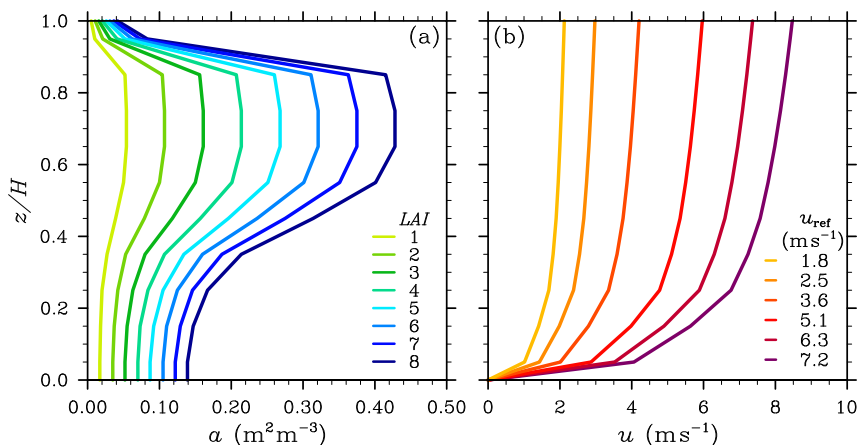


**Fig. 2** Vertical profiles of the different **a** leaf area densities and **b** steady-state wind profiles of the mean flow ( $u$ -component) at position  $x_{\text{ref}}$ , used in the present study (Kanani-Sühring and Raasch, 2014).

Raasch (2014), briefly summarized here:

$$\begin{aligned}
 \underbrace{\frac{\partial \langle S \rangle}{\partial t}}_I &= - \frac{\partial \langle u_i \rangle \langle S \rangle}{\partial x_i} - \frac{\partial \langle u'_i S' \rangle}{\partial x_i} + \frac{\partial}{\partial x_i} \langle K_s \frac{\partial S}{\partial x_i} \rangle \\
 &= \underbrace{- \frac{\partial \langle u \rangle \langle S \rangle}{\partial x}}_{IIa} - \underbrace{\frac{\partial \langle u' S' \rangle}{\partial x}}_{IIIa} + \underbrace{\frac{\partial}{\partial x} \langle K_s \frac{\partial S}{\partial x} \rangle}_{IVa} \\
 &\quad \underbrace{- \frac{\partial \langle v \rangle \langle S \rangle}{\partial y}}_{IIb} - \underbrace{\frac{\partial \langle v' S' \rangle}{\partial y}}_{IIIb} + \underbrace{\frac{\partial}{\partial y} \langle K_s \frac{\partial S}{\partial y} \rangle}_{IVb} \\
 &\quad \underbrace{- \frac{\partial \langle w \rangle \langle S \rangle}{\partial z}}_{IIc} - \underbrace{\frac{\partial \langle w' S' \rangle}{\partial z}}_{IIIc} + \underbrace{\frac{\partial}{\partial z} \langle K_s \frac{\partial S}{\partial z} \rangle}_{IVc}, \quad (1)
 \end{aligned}$$

with velocity components  $u_i \in \{u_1=u, u_2=v, u_3=w\}$  and time  $t$ ;  $K_S$  is the subgrid-scale diffusion coefficient of scalar  $S$ . Angled brackets denote a line average parallel to the forest edge ( $y$ -direction), and a prime describes a fluctuation from this line average. Term I quantifies the local temporal change of  $S$ , which results from the net transport of  $S$  by: mean flow (II), resolved-scale turbulence (III) and subgrid-scale turbulence (IV) in the edge-perpendicular (a), edge-parallel (b) and vertical (c) direction, respectively. A positive net transport by a certain term (including the respective dedicated sign in Eq. 1) implies that this term leads to a concentration accumulation and vice versa.

Wherever mean quantities are presented in the following, e.g. the mean flow or the mean scalar concentration, these quantities are averaged along the  $y$ -direction (marked by angled brackets), and over 3 h of simulated time (marked

by overbar). The data analysis starts 0.5 h after the first scalar emission, where a quasi-stationary state is reached for the scalar concentration.

### 3 Results and discussion

The purpose of this study is to improve the understanding of scalar transport mechanisms and the spatial distribution of scalar concentrations and their turbulent fluxes in the lee of forests, with the overall goal of being able to give recommendations for planning and interpreting micrometeorological measurements in fragmented forested landscapes. Before we will present and discuss the scalar transport and distribution, we will first describe the mean flow field in the lee of a forest.

#### 3.1 Flow properties in the lee of a forest

Figure 3 shows  $x$ - $z$  slices of the mean streamwise and vertical velocity components,  $\overline{\langle u \rangle}$  (a) and  $\overline{\langle w \rangle}$  (b) respectively, of simulations LAI2 and LAI8. Quantities  $\overline{\langle u \rangle}$  and  $\overline{\langle w \rangle}$  are normalized with  $u_{\text{ref}}$ , and plot axes are scaled with  $H$ . The forest is marked by the dashed black lines, with the leeward forest edge at  $x/H = 0$ .

For both  $LAI$ , isolines of  $\overline{\langle u \rangle}/u_{\text{ref}}$  (Fig. 3a) diverge downstream of the forest, and attach back to the clearing surface. This means the streamwise flow from the forest patch, which has a prominent vertical profile with an inflection point near the forest top (not shown, see e.g. Finnigan, 2000; Belcher et al., 2003; Queck et al., 2014), gradually adjusts to the surface conditions of the relatively smooth clearing, i.e. back to a logarithmic rough-wall velocity profile. Consistent with the downward directed isolines of  $\overline{\langle u \rangle}/u_{\text{ref}}$ ,  $\overline{\langle w \rangle}/u_{\text{ref}}$  shows a large region of mean downward motion in the lee of the forest (Fig. 3b, dark-blue area). For both  $LAI$ , the general behaviour of the isolines of  $\overline{\langle u \rangle}$  and  $\overline{\langle w \rangle}$ , as well as the reattachment distance ( $\sim 10H$ , defined as the distance from the leeward edge where the canopy-top  $\overline{\langle u \rangle}$ -isoline attaches back to the clearing surface), agree well with the results of Cassiani et al. (2008) (c.f. their Figs. 6 and 9), who successfully validated their LES results against data of various field experiments with different tree species.

Comparing the mean flow in our Fig. 3 for a sparse (LAI2) and a dense (LAI8) forest indicates some differences in the flow fields. A streamwise flow reversion is present in the lee of the dense forest (Fig. 3a), coinciding with the small region of positive  $\overline{\langle w \rangle}/u_{\text{ref}}$  right behind the lee edge (Fig. 3b, red colours). The flow reversion is a result of an adverse pressure gradient setting up a few  $H$  downstream of the edge, acting against the streamwise flow and forcing it to separate from the surface and to recirculate (Cassiani et al., 2008; Markfort et al., 2014). Such lee recirculations at the outflow edge of forests have been previously detected not only in LES (Yang et al., 2006a; Cassiani et al., 2008) and RANS (Wilson and Flesch, 1999) studies, but also in wind

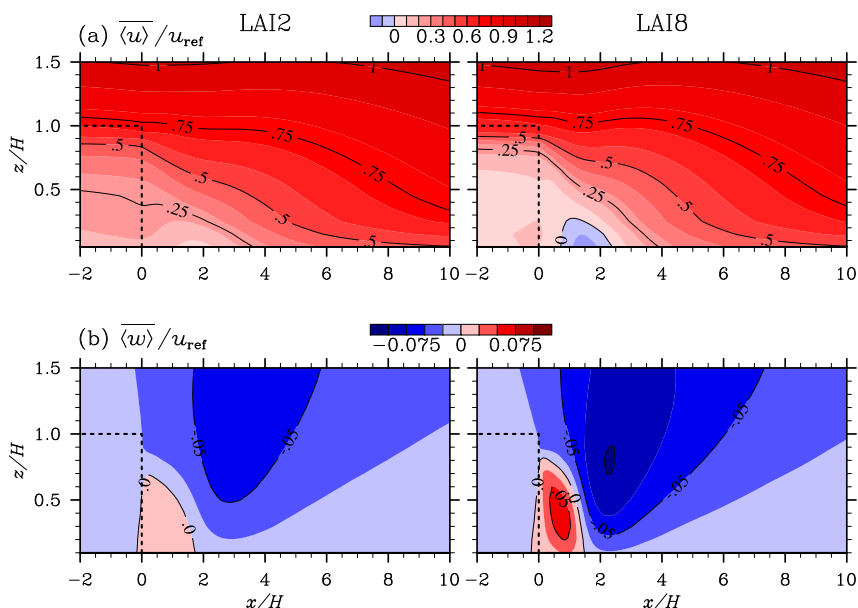


**Fig. 3** Streamwise vertical slices of: mean streamwise and vertical velocity components, **a**  $\langle \overline{u} \rangle$  and **b**  $\langle \overline{w} \rangle$ , respectively, from simulations LAI2 (left) and LAI8 (right). The mean corresponds to a spatial average in the spanwise (edge-parallel) direction and a 3-h time average, denoted by angled brackets and overbar, respectively. Reference velocity  $u_{\text{ref}}$  used for normalization is taken at reference position  $((x_{\text{ref}}, z_{\text{ref}}))$  above the clearing. The rear part of the forest patch is shown, with the edge at  $x/H = 0$  marked by the dashed black lines, followed by a part of the clearing patch.

**Table 2** Occurrence of lee recirculations in the mean streamwise flow for simulations LAI1-8 and UREF1-7. The respective maximum reversed  $u$ -velocity ( $\langle \overline{u} \rangle_{\text{min}}$ ) is listed, as well as the maximum streamwise extent  $\Delta x_r$  of the recirculation region. The former is normalized with  $U_H$ , being  $\langle \overline{u} \rangle(z = H)$  at the  $x$ -position of  $|\langle \overline{u} \rangle|_{\text{max}}$ .

LES run	$\langle \overline{u} \rangle_{\text{min}} / U_H$ (m s <sup>-1</sup> )	$\Delta x_r$ (H)	LES run	$\langle \overline{u} \rangle_{\text{min}} / U_H$ (m s <sup>-1</sup> )	$\Delta x_r$ (H)
LAI1	–	–	UREF1	-0.075	1.0
LAI2	–	–	UREF2	-0.077	1.0
LAI3	-0.006	0.3	UREF3	-0.078	1.0
LAI4	-0.075	1.0	UREF5	-0.077	1.0
LAI5	-0.125	1.2	UREF6	-0.076	1.0
LAI6	-0.159	1.4	UREF7	-0.073	1.0
LAI7	-0.186	1.5			
LAI8	-0.211	1.5			

tunnel (Markfort et al., 2014) and field experiments (Bergen, 1975; Flesch and Wilson, 1999; Detto et al., 2008). In the case of a sparse forest (LAI2), no lee recirculation is detected in the mean streamwise flow, in agreement with results of previous studies (e.g. Yang et al., 2006a; Cassiani et al., 2008). For the simulated range of  $LAI = 1$  to 8, we found lee recirculations in cases with  $LAI \geq 3$  (see Table 2), though for  $LAI = 3$ , the strength of the re-

versed flow is  $< 1\%$  of  $U_H$ . Cassiani et al. (2008) reported lee recirculations for  $LAI \geq 4$ , providing a good match with our results. As summarized in Table 2, the maximum streamwise extent  $\Delta x_r$  of the recirculation region slightly increases with  $LAI$ . Moreover, it should be noted that the maximum reversed velocity  $\overline{u}|_{\min}$ , normalized with  $U_H$  ( $= \overline{u}(z = H)$  at  $x$ -position of  $\overline{u}|_{\min}$ ), remarkably increases with  $LAI$  from roughly 1% of  $U_H$  (LAI3) to 21% of  $U_H$  (LAI8). This means the strongest recirculations can be found in the lee of the dense forests. Results of simulations UREF1-7 indicate no remarkable impact of wind speed on  $\overline{u}|_{\min}/U_H$  and  $\Delta x_r$ . Hence, the formation and the properties of a lee recirculation seem to depend mainly on forest morphology.

As mentioned earlier in Sect. 1, the occurrence of flow recirculations is typical for BFS flows. We know that such flow reversions are no permanent phenomenon in the lee of forests, though visible in the mean flow (LAI8) they rather expose an intermittent nature in time and along the forest edge, alternating with exit-flow events. Cassiani et al. (2008) found the relative occurrence of recirculation events (BFS-flow events) to depend on  $LAI$ . Following Cassiani et al. (2008), we analyzed the sample fraction  $Sf_{u < 0}$  of BFS-flow events as presented in Fig. 4, with  $Sf_{u < 0}$  being the number of measured samples with negative  $u$  divided by the total number of samples. Samples were taken at each timestep in a 3-h time interval, and at each grid point along the  $y$ -direction for selected  $x$ - $z$  positions, resulting in a total of  $\mathcal{O}(10^5)$  samples for each  $(x, z)$  coordinate. The streamwise evolution of  $Sf_u$  downstream of the lee edge is plotted here at two heights,  $z/H = 0.15$  (Fig. 4a) and  $z/H = 0.4$  (b), specifically chosen for comparability with other LES and field data. Solid lines represent three of our LES runs (LAI2, LAI4, LAI8), open symbols illustrate corresponding LES results of Cassiani et al. (2008) for the same  $LAI$  values, and solid circles visualize data of a field experiment by Flesch and Wilson (1999).

At both heights (Fig. 4a,b) and for all presented  $LAI$  and wind-speed values,  $Sf_u$  first increases with distance from the lee edge, forming a peak somewhere between  $1 < x/H < 2$ , which is the region where the lee recirculation is detected in  $\overline{u}(x, z)$  (not shown for all  $LAI$  values). Downstream of the peak,  $Sf_u$  decreases towards zero. The superposed solid and dashed lines for  $LAI = 4$ , marking the different simulated wind speeds, indicate that the wind speed has no effect on the distribution of  $Sf_u$ , which was not analyzed in previous studies so far. This means regardless of the wind speed, the relative occurrence of BFS-flow events remains the same. In contrast, the number of BFS-flow events significantly increases with  $LAI$ , which is in agreement with Cassiani et al. (2008). Based on the  $Sf_u$  data for the intermediate  $LAI$  values (not shown for reasons of clarity), we found the increase of  $Sf_u$  with  $LAI$  to converge for  $LAI \geq 6$ . A convergence of the recirculation properties towards the largest  $LAI$  was also reported by Cassiani et al. (2008). Overall, our  $Sf_u$  data are in good agreement with those in Cassiani et al. (2008) and Flesch and Wilson (1999), giving confidence to our results. Only for  $LAI = 2$  at  $z/H = 0.15$  (Fig. 4a), large deviations can be detected between  $Sf_u$  values of Cassiani et al. (2008) (triangles) and the present study (yellow line). These

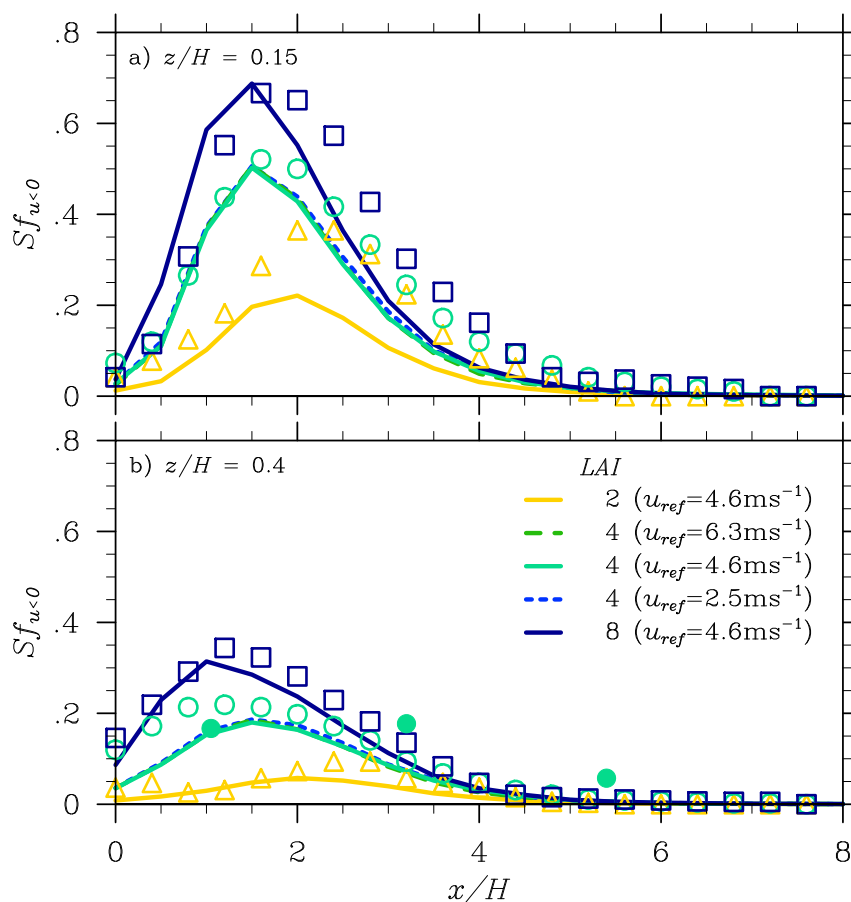


**Fig. 4** Sample fraction  $Sf_{u<0}$  of the relative occurrence of BFS-flow events as a function of  $x/H$ , at heights **a**  $z/H = 0.15$  and **b**  $z/H = 0.4$ : comparison of results of the present LES study (lines), the Cassiani et al. (2008) LES (open symbols) and the Flesch and Wilson (1999) field experiment (solid symbols).

might be attributed to the different vertical leaf distribution between our set-up and that of Cassiani et al. (2008), which has a more pronounced effect near the surface and for sparser forests. To summarize,  $Sf_u$  is a useful quantity for the dynamical characterization of the flow in the lee of forest patches, and it will be used once more in Sect. 3.4.

### 3.2 Scalar distribution in the lee of forests and the responsible transport mechanisms

As we know from previous studies, concentrations can be locally enhanced in regions with flow separation and recirculations, let it be in the lee of a hill (Katul et al., 2006; Poggi and Katul, 2007; Ross, 2011; Ross and Baker,



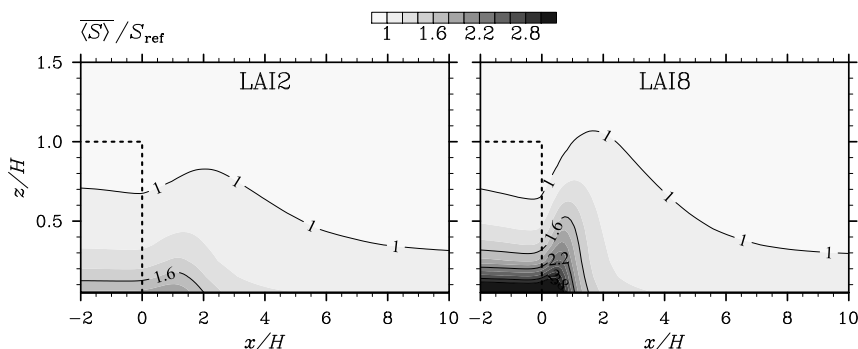


**Fig. 5** Streamwise vertical slices of mean concentration  $\overline{\langle S \rangle}$ , for simulations LAI2 and LAI8. Reference concentration  $S_{\text{ref}}$  used for normalization is taken at reference position  $((x_{\text{ref}}, z_{\text{ref}}))$  above the clearing. The forest is marked by the dashed black lines.

2013) or even deep inside a forest canopy (Sogachev et al., 2008; Kanani-Sühring and Raasch, 2014) where recirculations were also found to occur. Figure 5 shows  $x$ - $z$  slices of the mean scalar concentration  $\overline{\langle S \rangle}$  for simulations LAI2 and LAI8, normalized with reference concentration  $S_{\text{ref}}$ , being the mean concentration above the clearing surface at  $(x_{\text{ref}} = 33H, z_{\text{ref}} = 0.35H)$ .

For both LAI cases,  $\overline{\langle S \rangle}/S_{\text{ref}}$  is larger inside the forest than far downstream of the leeward edge above the clearing. In the immediate lee of the forest, the scalar is found to accumulate, forming a pronounced concentration peak with overshoots of  $\overline{\langle S \rangle}$  over  $S_{\text{ref}}$  of 20% (LAI2) and 100% (LAI8) at  $z_{\text{ref}}$ . Downstream of the respective peaks,  $\overline{\langle S \rangle}/S_{\text{ref}}$  values approach nearly constant levels. Numerical simulations by Ross (2011) and by Ross and Baker (2013) of the flow across fully forested hills revealed similar local scalar accumulation on the leeside of the hill, with similar peak strengths as detected in the present study. For the case of only partly forested hills, results of Ross and Baker (2013) further indicated that the peak strength can be further increased or decreased as compared to the fully-forested-hill case, depending on the location of the forest patch with respect to the hill summit.

Now the main question is which physical mechanisms steer the scalar transport in the lee of forests. To answer this question, we analyzed each term of the scalar balance equation (Eq. 1), regarding its relative importance. Figure 6 shows the streamwise evolution of each term,  $\overline{T} \in \{\overline{I}, \overline{II}, \overline{III}, \overline{IV}\}$  for simulations LAI2 (a,c) and LAI8 (b,d), at heights of  $z/H = 0.25$  (a, b) and  $z/H = 0.75$  (c, d), as representatives for the mechanisms in the lower and the upper half of the lee region, respectively. Each curve shows the time-averaged net transport of  $S$  at the given  $(x, z)$  positions by one of the transport terms  $\overline{T}$ , where positive values describe a concentration enhancement by that term and vice versa. Orange and blue colours illustrate the streamwise (#a) and vertical (#c) net transport of  $S$ , respectively, by the mean flow (II, solid lines), by resolved-scale turbulence (III, dashed) and by subgrid-scale turbulence (IV, dotted). Terms  $(\overline{II}-\overline{IV})_b$  (see Eq. 1) are not shown, since the flow field is statis-

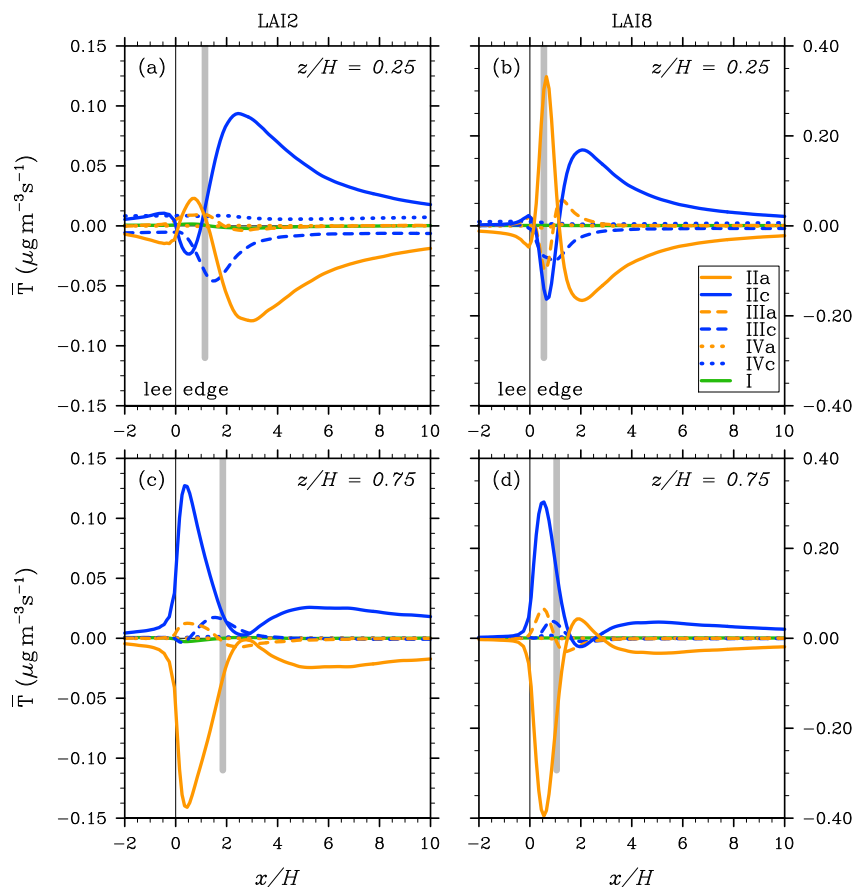


**Fig. 6** Scalar balance terms  $\bar{T} \in \{\bar{I}, \bar{II}, \bar{III}, \bar{IV}\}$ , time averaged over 3 h of simulated time, **a,b** at  $z/H = 0.25$  and **c,d** at  $z/H = 0.75$  for simulations LAI2 and LAI8, respectively. Term I: temporal change of  $S$ ; terms II, III, IV: net transport of  $S$  by mean flow, by resolved scale turbulence and by subgrid-scale turbulence in the streamwise (II-IVa) and vertical (II-IVc) direction. The lee edge is at  $x/H = 0$ . For comparison, the location of the scalar concentration peak at the respective height and  $LAI$  is marked by the vertical grey line.

tically homogeneous in the  $y$ -direction, hence, the time-averaged net transport by these terms is negligible. The vertical thick grey line marks the location of the concentration peak at the respective height and  $LAI$ , taken from the 3-h averaged concentration fields.

Overall, the streamwise evolution of a specific term is similar for simulation LAI2 and LAI8 at a specific height, beside the generally smaller magnitude of the values for LAI2 (note the different ordinates), since the disturbance of the flow and hence the scalar transport is less pronounced in a sparse-forest case. Except for the SGS terms (IVa,c), which are generally constant or small compared to the other terms, all terms are largest within  $3H$  distance from

the lee edge. This is where the largest impact of the flow can be found, e.g. with the occurrence of intermittent BFS-flow events (see Sect. 3.1). Further downstream above the clearing, values decrease towards zero (not shown), as the flow gradually adjusts to the new surface conditions. This is expected, since the adjusted flow above the clearing is nearly undisturbed, hence, it should not converge or diverge anywhere, except near the windward forest edge (c.f. Kanani-Sühring and Raasch, 2014, Fig. 5). Since the subgrid-scale net transport with its rather small streamwise-constant values exhibits no direct effect on the local scalar accumulation, it is not further treated. Hence, wherever we speak of turbulence or turbulent net-transport in the following, we refer to the resolved-scale part of turbulence.

We first discuss Fig. 6a, b, presenting the behaviour of the transport terms near the surface, where the scalar accumulation originates. In the case of LAI8 (Fig. 6b), where the mean streamwise flow recirculates near the surface in the immediate lee of the forest (see Fig. 3a), it is evident that the scalar peak (grey line) coincides with the positive peak of term IIa, i.e. the scalar peak falls in the region of strongest streamwise mean-flow convergence. Consequently, the mean streamwise net-transport (solid orange) leads to an accumulation of scalar, while the mean vertical (solid blue) as well as the turbulent streamwise and vertical (dashed orange and blue) net-transport are responsible for the depletion of scalar. The turbulent net transport is thereby in the same order of magnitude as that by the vertical mean flow, indicating that all these transport mechanisms are equally important in the immediate lee of the forest.

In the case of an absent lee recirculation as in simulation LAI2 (see Fig. 3a), the individual transport mechanisms in the scalar peak region (Fig. 6a) interact differently than in simulation LAI8 (Fig. 6b). In contrast to LAI8, the scalar peak (grey line) in LAI2 is not at the position of the IIa-peak, but rather at the intersection of terms IIa,c and IIIa. Hence, these three terms are in equal parts responsible for the scalar accumulation, and not solely term IIa as in simulation LAI8. The scalar depletion in case LAI2 is mainly achieved by the turbulent vertical net-transport (dashed blue).

Taking a look at the upper level (Fig. 6c, d) shows a different behaviour of the transport terms as compared to that at  $z/H = 0.25$ . At  $z/H = 0.75$ , the scalar enhancement in the scalar-peak region (grey line) is taken over by vertical net-transports with the mean and the turbulent flow (solid and dashed blue). These two transport terms are equally important for the scalar accumulation in the lee of a sparse forest. However, in the lee of a dense forest, the vertical net-transport by the mean flow (IIc) makes a 3-fold higher contribution than the turbulent counterpart (IIIc) in the grey-shaded region, attributed to the presence of the lee recirculation. The streamwise net-transport by turbulence (dashed orange) exposes an inflection point exactly at the scalar peak location, indicating that this term enhances the concentrations upstream and decreases the concentrations downstream of the scalar peak. Finally, the scalar depletion at this height results mainly from the divergence of the streamwise transport by the mean flow (solid orange).

This analysis of the important transport mechanisms in forest lee flows has demonstrated that advective transport processes are as important as the turbulent transport. The large streamwise net transport by the mean flow (IIa) implies that streamwise advection is not negligible for the scalar transport here, which must be considered for the interpretation of eddy-covariance measurements (Foken, 2008), since this flux-measurement technique disregards flux contributions from advective transports.

### 3.3 Behaviour of concentration and flux distributions under different atmospheric and plant-physical conditions

The analysis presented in Sect. 3.2 has demonstrated which physical mechanisms lead to the local scalar accumulation in the lee of forests. Now it shall be examined to what extent the scalar accumulation might depend on plant-physical and meteorological conditions. As mentioned in Sect. 2, we performed a series of LES with different forest densities and wind speeds for this purpose. Figure 7 presents the streamwise distribution of mean scalar concentration  $\overline{S}$  (a,b) and its flux  $\overline{w'S'}$  (c,d) for different  $LAI$  (a,c) and  $u_{\text{ref}}$  (b,d) values, exemplarily at  $z/H = 0.4$ . Both quantities  $\overline{S}$  and  $\overline{w'S'}$  are normalized with corresponding reference values  $S_{\text{ref}}$  and  $\overline{w'S'}_{\text{ref}}$ , taken at the same height above the clearing at the reference position  $x_{\text{ref}}$ .

For all  $LAI$  and  $u_{\text{ref}}$  cases,  $\overline{S}$  exposes a peak within the first few  $H$  downstream of the forest edge (Fig. 7a, b), as already seen in the concentration cross-sections for simulations LAI2 and LAI8 (Fig. 5). Further downstream of the peak region,  $\overline{S}/S_{\text{ref}}$  approaches unity in every case, i.e. concentrations decrease towards their respective  $S_{\text{ref}}$ , which is assumed to be the adjusted equilibrium value at that height above the clearing.

The location of the scalar peak is barely affected by  $LAI$  or wind speed, with deviations of less than  $0.5H$ . This is much different to what was found by Kanani-Sühring and Raasch (2014) for the behaviour of the scalar accumulation on the forest patch, where the distance between the windward forest edge and the peak location was largely dependent on  $LAI$  ( $\approx 10H$  variation between LAI1 and LAI8), due to the proportionality between  $LAI$  and the volume drag forces. However in the forest lee, the direct canopy drag is absent, consequently, the concentration-peak position is invariant of  $LAI$ . An equivalent conclusion was already drawn for the position of the flow-convergence region in Sect. 3.1, as found to be almost independent of  $LAI$  and wind speed.

Contrary to the behaviour of the peak location, the concentration-peak values do show large differences among the  $LAI$  and  $u_{\text{ref}}$  cases. For example at this specific height, peak concentrations are  $1.75 S_{\text{ref}}$  for LAI8 and  $1.2 S_{\text{ref}}$  for LAI2, speaking in percent, the peak value overshoots the equilibrium value  $S_{\text{ref}}$  by 75% for LAI8 and by 20% for LAI2, which is almost a factor 4 difference. A factor of 2 lies between the percental overshoot of cases UREF1 and UREF7. In comparison, the variability of the overshoots among the LAI and UREF

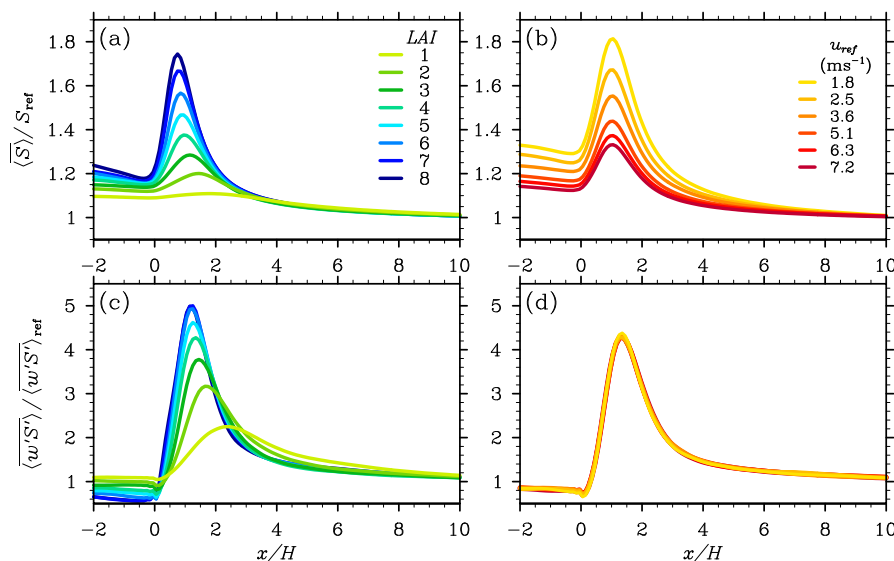


**Fig. 7** Streamwise evolution of mean **a,b** concentrations and **c,d** fluxes at  $z/H = 0.4$  for all simulated **a,c**  $LAI$  and **b,d**  $u_{\text{ref}}$ , normalized with reference values  $S_{\text{ref}}$  and  $\langle \overline{w'S'} \rangle_{\text{ref}}$ , respectively.  $\langle \overline{w'S'} \rangle_{\text{ref}}$  is taken from the same location as  $S_{\text{ref}}$ .

cases above the forest patch (see Kanani-Sühring and Raasch, 2014) was even more pronounced than in the lee region.

The adjustment of  $\langle \overline{S} \rangle$  towards  $S_{\text{ref}}$  is almost equal for the different  $LAI$  cases beyond  $x/H = 3$ , whereas the adjustment distance increases with decreasing wind speed. Nevertheless, concentrations are adjusted to  $1.05 S_{\text{ref}}$  (5% tolerance) in all cases downstream of  $x/H \approx 6$ . It should be noted that adjusted mean concentrations above the clearing are generally lower than above the forest patch at the same height, owing to the overall more efficient turbulent mixing of the scalar above the clearing. In general, the largest near-edge concentrations must be expected in the lee of dense forests under weak-wind conditions.

Scalar fluxes (Fig. 7c, d) expose a similar spatial evolution as the concentrations, with pronounced peaks in the near-edge region. Downstream of the respective peaks, fluxes decrease towards their equilibrium values  $\langle \overline{w'S'} \rangle_{\text{ref}}$ . Similar as found for the concentration distribution, scalar fluxes strongly depend on  $LAI$ , with peak values ranging roughly from  $2 \langle \overline{w'S'} \rangle_{\text{ref}}$  ( $LAI1$ ) to  $5 \langle \overline{w'S'} \rangle_{\text{ref}}$  ( $LAI8$ ). For  $LAI \geq 6$ , peak values converge, suggesting an upper limit is reached for the local flux enhancement in the lee of the densest forests. Inside the forest, fluxes are inversely proportional to  $LAI$ . Arising from Fig. 7d, the wind speed exposes to have almost no effect on the flux distribution, although scalar concentrations do show a wind-speed dependence. Same was detected and discussed in detail by Kanani-Sühring and Raasch (2014) for the fluxes above the forest patch. The invariance of the fluxes on wind

speed was attributed to the fact that larger  $w$  fluctuations, appearing under stronger winds due to the larger shear, are compensated by relatively small  $S$  fluctuations, and vice versa.

Overall, the appearance of locally enhanced scalar concentrations and fluxes, as well as their dependence on forest morphology, wind speed, and on landscape topography (as reported e.g. by Ross, 2011; Ross and Baker, 2013), altogether highlight that in situ concentration and flux measurements should be interpreted with special care.

### 3.4 Interpretation of micrometeorological measurements in the lee of forests

As shown above, the interpretation of the spatial representativeness of in situ micrometeorological measurements above forest clearings can be rather complicated. It has been demonstrated by means of Fig. 7 that concentrations and fluxes can be remarkably enhanced in the lee of forests, as compared to the respective adjusted values further downstream above the clearing. For the sake of completeness, Fig. 8 presents  $x$ - $z$  slices of the mean normalized scalar fluxes, for simulations LAI2 and LAI8. The total turbulent scalar fluxes are visualized here, i.e. the sum of resolved-scale and subgrid-scale fluxes, though, except for the near-surface levels, the contribution of the subgrid scales is negligible.

For both  $LAI$ , the background flux is almost the same, while peak fluxes are much higher for LAI8 than for LAI2 at every height, as already discussed for Fig. 7. The region with locally enhanced fluxes can reach up to  $z/H \approx 2$  (LAI8), and in the horizontal, it extends  $5H$  downstream of the forest edge in both cases. This means, if measuring sites are located within this region, large deviations of the measured fluxes from the clearing-representative flux must be expected, at least under the herein simulated conditions. In the dense-forest case, fluxes can even be negative in a small region near the surface at about  $x/H = 1$  (white shading), which is most likely to be connected to the presence of the lee recirculation.

Downstream of the respective peak region, fluxes decrease towards an equilibrium value at each height, representative for the actual surface conditions of the clearing. The near-surface ( $0.1 < z/H < 0.2$ ) fluxes are adjusted to the respective equilibrium values with 5% tolerance ( $1.05 \overline{w'S'}_{\text{ref}}$ ) about  $25H$  from the leeward forest edge (not shown), almost independently of  $LAI$  and wind speed. At larger heights, a distance of at least  $15H$  should be placed between the lee edge and the measuring position, in order to assure for the measurement of adjusted rather than of edge-disturbed fluxes.

If measurements are located closer to the leeward edge than  $15H$ , measured fluxes might significantly overestimate the equilibrium fluxes, as visible in Figs. 7 and 8. At such sensitive measurement sites, it is highly desirable to be able to estimate the magnitude of this flux enhancement, favourably with the help of along-the-way measured quantities. We hereby propose a new method for this purpose, utilizing the sample fraction  $Sf_{u < 0}$  of BFS-flow events, which can be easily extracted from the high-frequency velocity measurements

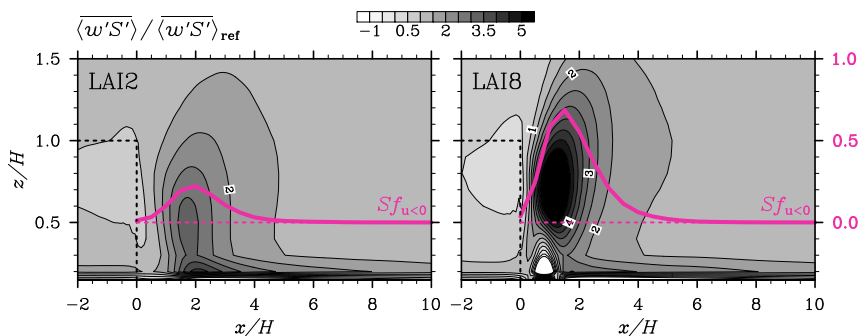


**Fig. 8**  $x$ - $z$  slices of mean scalar flux  $\overline{\langle w'S' \rangle}$ , normalized with  $\overline{\langle w'S' \rangle}_{\text{ref}}$ , for simulations LAI2 and LAI8. For comparison, the measure for the relative occurrence of BFS-flow events,  $Sf_{u<0}$  at  $z/H = 0.15$  (see Fig. 4), is plotted for both cases with the solid red line (see corresponding red labels on the right-hand-side ordinate).

captured by sonic anemometers. The red curves in Fig. 8 (see right-hand-side ordinate) show  $Sf_{u<0}$  at  $z/H = 0.15$ , as already presented in Fig. 4a for LAI2 and LAI8. Comparing the streamwise evolution of the fluxes to that of  $Sf_{u<0}$  indicates a very similar behaviour. The peak of  $Sf_{u<0}$  is located at the same position as the peak of  $\overline{\langle w'S' \rangle}$ , i.e. the most enhanced fluxes are located where the relative occurrence of BFS-flow events is largest. Outside of the flux-peak region bounded by the 1.5-isoline,  $Sf_{u<0}$  quickly approaches zero, while  $\overline{\langle w'S' \rangle}$  adjusts to its equilibrium value.

To summarize, a direct relation exists between the relative occurrence of BFS-flow events and the relative enhancement of scalar fluxes (and concentration) in the lee of forests. This qualitative relation can be used to locate regions with possibly enhanced fluxes, only by means of sampling high-frequency data of the edge-perpendicular velocity component (in this case the  $u$ -component) near the surface where the lee recirculation appears. Of course, a successful application of this method requires knowledge about the mean background flow, in order to identify the analyzed flow as a lee flow in the first place. Finally it should be noted that this method is suggested to be applicable under the herein simulated conditions, i.e. wherever surface sources of the considered scalar dominate over other sources or sinks.

## 4 Summary

By means of LES, we aimed at improving the yet scarce understanding of scalar transport processes in the lee of forest patches, with the greater goal to enable a better planning and interpretation of in situ micrometeorological measurements. We therefore simulated neutral flows across idealized forest-clearing transitions in flat terrain, in order to systematically examine the transport and distribution of surface-emitted scalars in the lee of forests for different forest densities and wind speeds. This is a follow-up study to the work pre-

sented by Kanani-Sühring and Raasch (2014), where locally enhanced scalar concentrations and fluxes were found above a forest patch downstream of a clearing-forest transition.

In the present study, we found locally enhanced scalar concentrations and fluxes in the lee of forest patches, for a wide range of forest densities and wind speeds. Similar accumulations of surface-emitted scalars were previously observed in the lee of hills (e.g. Katul et al., 2006; Ross and Baker, 2013), but so far, nothing similar has been reported in the context of forest-edge flows. As a first step, we investigated which physical mechanisms cause this accumulation, by means of separately analysing the terms of the scalar balance equation. The analysis exposed a different relative importance of individual transport terms in the lee of sparse forests than in the lee of dense forests. Behind dense forests, the accumulation of scalar is caused solely by the convergence of the mean streamwise transport of the scalar, due to the presence of a recirculation region in the mean flow near the forest edge. Behind sparse forests, where no mean recirculation is present, the convergence of the mean streamwise and vertical transport as well as the convergence of the turbulent streamwise transport are in equal parts responsible for the scalar build-up. To explain, lee recirculations are of intermittent nature, and their relative occurrence has been found, by means of LES (Cassiani et al., 2008) and field experiments (Flesch and Wilson, 1999; Detto et al., 2008), to increase with forest density. Our results agree with these findings, and they likewise implied that recirculations in the mean flow are only present in the lee of dense forests, which can be thought of as a backward-facing step (e.g. Armaly et al., 1983; Kostas et al., 2002; Markfort et al., 2014).

LES with different forest densities and wind speeds revealed that concentration levels increase with increasing forest density and with decreasing wind speed, conforming to the corresponding results above the forest patch (Kanani-Sühring and Raasch, 2014). However, scalar peak positions in the lee were nearly unaffected by wind speed and forest density, which is a different behaviour as found by Kanani-Sühring and Raasch (2014) for a clearing-forest transition, where peak positions strongly depended on forest density. Similar to the concentrations, scalar fluxes likewise increased with forest density, while they remained invariant of wind speed. Overall, the local enhancement of scalar concentrations and fluxes in the lee of forests can be of the same order of magnitude as detected in LES by Ross (2011) and by Ross and Baker (2013) in the lee of forested hills, where similar physical mechanisms lead to an accumulation of scalar.

The pronounced local enhancement of scalar concentrations and fluxes in the lee of forests (or hills) introduces a certain complexity to the interpretation of in situ micrometeorological measurements. In order to be able to identify regions of possibly enhanced scalar transport on-site, we proposed a new method, which is simply based on the analysis of high-frequency velocity data. We found that the relative frequency of intermittent lee-recirculation events correlates with the magnitude of the flux enhancement. Thus, regions with enhanced fluxes can be estimated by localizing and counting lee-recirculation



events, e.g. based on data recorded by sonic anemometers being a part of the basic equipment of micrometeorological sites.

It should be noted that our findings hold for (near) neutral conditions with weak to moderate winds, for the simulated forest-clearing configuration and for scalars that are predominantly emitted from surface sources. To what extent the above mentioned relations and suggestions might change under other meteorological conditions (e.g. stable or unstable stratification), more heterogeneous landscape configurations or other scalar source-sink distributions will be subject to further studies.

**Acknowledgements** This study was supported by the German Research Foundation (DFG) under grant RA 617/23-1. All simulations were performed on the SGI Altix ICE and CRAY XC30 at The North-German Supercomputing Alliance (HLRN) in Hannover and Berlin. NCL<sup>2</sup> has been used for data analysis and visualization.

## References

- Armaly BF, Dursts F, Pereira JCF, Schönung B (1983) Experimental and theoretical investigation of backward-facing step flow. *J Fluid Mech* 127: 473–496.
- Belcher SE, Harman IN, Finnigan JJ (2012) The wind in the willows: flows in forest canopies in complex terrain. *Annu Rev Fluid Mech* 44: 479–504.
- Belcher SE, Jerram N, Hunt JCR (2003) Adjustment of a turbulent boundary layer to a canopy of roughness elements. *J Fluid Mech* 488: 369–398.
- Bergen JD (1975) Air movement in a forest clearing as indicated by smoke drift. *Agric Meteorol* 15: 165–179.
- Cai XM, Barlow JF, Belcher SE (2008) Dispersion and transfer of passive scalars in and above street canyons. Large-eddy simulations. *Atmos Env* 42: 5885–5895.
- Cassiani M, Katul GG, Albertson JD (2008) The effects of canopy leaf area index on air-flow across forest edges: large-eddy simulation and analytical results. *Boundary-Layer Meteorol* 126: 433–460.
- Chan TL, Dong G, Leung CW, Cheung CS, Hung WT (2002) Validation of a two-dimensional pollutant dispersion model in an isolated street canyon. *Atmos Env* 36: 861–872.
- Deardorff JW (1980) Stratocumulus-capped mixed layers derived from a three-dimensional model. *Boundary-Layer Meteorol* 18: 495–527.
- Detto M, Katull GG, Siqueira M, Juang JY, Stoy P (2008) The structure of turbulence near a tall forest edge: the backward-facing step flow analogy revisited. *Ecol Appl* 18(6): 1420–1435.
- Dupont S, Brunet Y (2008) Edge flow and canopy structure: a large-eddy simulation study. *Boundary-Layer Meteorol* 126: 51–71.
- Finnigan JJ (2000) Turbulence in plant canopies. *Annu Rev Fluid Mech* 32: 519–571.
- Finnigan JJ (2008) An Introduction to Flux Measurements in Difficult Conditions. *Ecol Appl* 18(6): 1340–1350.
- Finnigan JJ, Belcher SE (2004) Flow over a hill covered with a plant canopy. *QJR Meteorol Soc* 130: 1–29.
- Flesch TK, Wilson JD (1999) Wind and remnant tree sway in forest cutblocks. I. Measured winds in experimental cutblocks. *Agric For Meteorol* 93: 229–242.
- Foken T (2008) *Micrometeorology*. Springer Berlin Heidelberg, 306 pp.

---

<sup>2</sup> The NCAR Command Language (Version 6.1.2) [Software]. (2013). Boulder, Colorado: UCAR/NCAR/CISL/VETS. <http://dx.doi.org/10.5065/D6WD3XH5>

- Fontan S, Katul GG, Poggi D, Manes C, Ridol L (2013) Flume Experiments on Turbulent Flows Across Gaps of Permeable and Impermeable Boundaries. *Boundary-Layer Meteorol* 147: 21–39.
- Frank C, Ruck B (2008) Numerical study of the airflow over forest clearings. *Forestry* 81(3): 259–277.
- Kanani-Sühring F, Raasch S (2014) Spatial variability of scalar concentrations and fluxes downstream of a clearing-to-forest transition: an LES study. *Boundary-Layer Meteorol*: DOI 10.1007/s10546-014-9986-3
- Kanani F, Träumner K, Ruck B, Raasch S (2014) What determines the differences found in forest edge flow between physical models and atmospheric measurements – An LES study. *Meteorol Z* 23(1): 33–49.
- Katul GG, Finnigan JJ, Poggi D, Leuning R, Belcher SE (2006) The influence of hilly terrain on canopy-atmosphere carbon dioxide exchange. *Boundary-Layer Meteorol* 118: 189–216.
- Klaassen W, Van Breugel PB, Moors EJ, Nieveen JP (2002) Increased heat fluxes near a forest edge. *Theor Appl Climatol* 72: 231–243.
- Kostas J, Soria J, Chong MS (2002) Particle image velocimetry measurements of a backward-facing step flow. *Exp Fluids* 33: 838–853.
- Letzel MO, Krane M, Raasch S (2008) High resolution urban large-eddy simulation studies from street canyon to neighbourhood scale. *Atmos Env* 42: 8770–8784.
- Letzel MO, Helmke C, Ng E, An X, Lai A, Raasch S (2012) LES case study on pedestrian level ventilation in two neighbourhoods in Hong Kong. *Meteorol Z* 21(6): 575–589.
- Markfort CD, Port-Agel F, Stefan HG (2014) Canopy-wake dynamics and wind sheltering effects on Earth surface fluxes. *Environ Fluid Mech* 14: 663–697.
- Maronga B, Gryschka M, Heinze R, Hoffmann F, Kanani-Sühring F, Keck M, Ketelsen K, Letzel MO, Sühring M, Raasch S (2015) The parallelized large-eddy simulation model (PALM) version 4.0 for atmospheric and oceanic flows: model formulation, recent developments, and future perspectives. *Geosci Model Dev Discuss*: DOI 10.5194/gmdd-8-1539-2015.
- Miller DR, Lin JD, Lu ZN (1991) Air flow across an alpine forest clearing: A model and field measurements. *Agric Forest Meteorol* 56: 209–225.
- Monin AS, Obukhov AM (1954) Osnovnye zakonomernosti turbulentnogo peremeshivaniya v prizemnom sloe atmosfery (Basic laws of turbulent mixing in the atmosphere near the ground). *Tr Akad Nauk SSSR Geophys Inst* 24: 163–187.
- Park SB, Baik JJ, Raasch S, Letzel MO (2012) A large-eddy simulation study of thermal effects on turbulent flow and dispersion in and above a street canyon. *J Appl Meteorol Climatol* 51: 829–841.
- Poggi D, Katul GG (2007) Turbulent flows on forested hilly region terrain: the recirculation. *QJR Meteorol Soc* 133: 1027–1039.
- Queck R, Bernhofer C, Bienert A, Eipper T, Goldberg V, Harmansa S, Hildebrand V, Maas HG, Schlegel F, Stiller J (2014) TurbEFA: an interdisciplinary effort to investigate the turbulent flow across a forest clearing. *Meteorol Z*, PrePub DOI 10.1127/metz/2014/0567
- Raasch S, Schröter M (2001) Palm - a large-eddy simulation model performing on massively parallel computers. *Meteorol Z* 10: 363–372.
- Raupach MR, Weng WS, Carruthers DJ, Hunt JCR (1992) Temperature and humidity fields and fluxes over low hills. *QJR Meteorol Soc* 118: 191–225.
- Ross AN (2008) Large-eddy simulations of flow over forested ridges. *Boundary-Layer Meteorol* 128: 59–76.
- Ross AN (2011) Scalar transport over forested hills. *Boundary-Layer Meteorol* 141: 179–199.
- Ross AN, Baker TP (2013) Flow over partially forested ridges. *Boundary-Layer Meteorol* 146: 375–392.
- Schumann U, Sweet RA (1988) Fast Fourier transforms for direct solution of Poissons equation with staggered boundary conditions. *J Comput Sci* 75: 123–137.
- Sogachev A, Leclerc MY, Zhang G, Rannik Ü, Vesala T (2008) CO<sub>2</sub> fluxes near a forest edge: a numerical study. *Ecol Appl* 18(6): 1454–1469.
- Wicker L, Skamarock W (2002) Time-splitting methods for elastic models using forward time schemes. *Mon Wea Rev* 130: 2088–2097.
- Williamson JH (1980) Low-storage Runge-Kutta schemes. *J Comput Phys* 35: 48–56.

### 3.3 Research article C: Enhanced scalar concentrations and fluxes in the lee of forest patches: A large-eddy simulation study

---

Enhanced scalar concentrations and fluxes in the lee of forest patches

21

- Wilson JD, Flesch TK (1999) Wind and remnant tree sway in forest cutblocks. III. A windflow model to diagnose spatial variation. *Agric For Meteorol* 93: 259–282.
- Yang B, Raupach MR, Shaw RH, Paw U KT, Morse AP (2006) Large-eddy simulation of turbulent flow across a forest edge. Part I: flow statistics. *Boundary-Layer Meteorol* 120: 377–412.

## 4 Summary and outlook

The scope of the present thesis was to improve the yet scarce understanding of scalar (e.g. temperature, humidity, CO<sub>2</sub>) transport in fragmented forested landscapes, and with this, to enable a better planning and interpretation of in-situ micrometeorological measurements in such landscapes. In order to contribute to a basic understanding of this matter, idealized forest-edge flows were studied by means of high-resolution large-eddy simulations (LES).

In today's weather and climate models, the soil-vegetation-atmosphere transfer (SVAT) of momentum and scalars is parametrized by embedded SVAT models under the assumption that the transfer is horizontally homogeneous across a classified surface or vegetation type (e.g. grassland, crop, forest). However, in heterogeneous landscapes with frequent discontinuities between surface types with different mechanic and thermodynamic surface characteristics, the flow frequently adjusts to the changing surface conditions, forming internal boundary layers (IBL). Within the IBL, the soil-vegetation-atmosphere exchange of momentum and scalars underlies an ongoing adjustment process, and is therefore spatially highly variable. Particularly at transitions between forested and unforested surface patches, the spatial variability of momentum and scalar transport is supposedly strongly pronounced. This spatial variability contradicts the general assumption of horizontal homogeneity, questioning the applicability of current SVAT parametrizations in weather and climate models for representing soil-vegetation-atmosphere exchange in highly fragmented landscapes. In order to improve SVAT parametrizations, micrometeorological measurements are performed near surface transitions, e.g. near forest edges. However, the high spatial variability of the exchange processes complicates the interpretation of these measurements, concerning their spatial representativity.

Especially the scalar transport near forest edges is to-date scarcely understood, however, since forests play a major role in the global ecosystem exchange, and thus greatly affect weather and climate, it is necessary to improve this understanding. Hence, the focus of this thesis was to investigate which physical mechanisms steer the scalar transport near windward and leeward forest edges, further, to what extent meteorological and plant-physical conditions modify the spatial variability of the scalar distribution and its transport, and finally, which implications result for the interpretation and planning of micrometeorological measurements.

Before the scalar transport near forest edges was treated, the overall applicability of the applied LES model together with its embedded canopy model for representing flows across forest canopies was verified against field and wind-tunnel data. As a first step, a neutrally-stratified flow across an infinite horizontally homogeneous vegetation canopy was simulated, and compared against corresponding canopy-flow profiles derived from tower measurements above different crop and forest types, as well as from wind-tunnel experiments, which have been summarized by Raupach et al. (1996) in the well-known "family portrait" of canopy turbulence. Different vertical canopy structures were simulated, which are in the range of the different vegetation types of the experiment canopies. An overall qualitative and quantitative agreement was found between the LES and the experiment data. Both, the shape of the vertical profiles as well as the range of values of mean wind speed, momentum fluxes, and several turbulence statistics within and above the canopies were well represented by the LES model. Especially the inflection of the wind profile near the canopy top, which is well-known to trigger the development of coherent turbulence structures (CTS), was properly

---

reproduced with the applied LES model, along with the characteristic length and separation scales of the CTS.

In a second step, in addition to this general validation of the applied LES model, forest-edge-flow LES were performed and compared to multi-dimensional field and wind-tunnel data, captured with Doppler lidar and laser Doppler anemometry, respectively, downstream of a clearing-to-forest transition (hereafter termed as windward forest edge). This data basis enabled a diverse comparison between the applied LES model, wind-tunnel and field experiments. Different LES set-ups of the flow across a windward forest edge were simulated, on the one hand representing neutrally-stratified wind-tunnel (open-channel) flows on an atmospheric scale, and on the other hand representing neutrally as well as unstably stratified ABL flows. Comparing the IBL properties, such as the IBL depth or turbulence statistics, demonstrated an overall quantitative agreement between the respective LES and the wind-tunnel/field experiments. Both, the gradual IBL development starting at the windward forest edge as well as the streamwise distribution of mean turbulence intensities within the IBL, as observed under wind-tunnel and atmospheric conditions, were well reproduced by the corresponding LES set-ups. Summarized, these two validation steps for homogeneous-canopy and forest-edge flows have indicated that the applied LES model is capable of adequately representing the characteristic features of canopy flows.

A further objective of this intercomparison was to analyze the impact of meteorological and plant-physical parameters on the IBL development downstream of a windward forest edge. The purpose behind this was to estimate the importance of appropriately representing the different physical site-conditions in numerical or wind-tunnel models, when comparing modelled and “real-world” flows, which is a matter of technical constraints or lacking knowledge of the “real-world” conditions. For example, wind tunnels can usually be operated only at neutral stratification, and they cannot represent geostrophic flow conditions. To study the possible effects of the mentioned physical parameters on the IBL features, several LES of forest-edge flows under a moderate wind speed were conducted, varying forest density, forest-gap (clearing) size, atmospheric stratification, and the dynamical flow forcing.

Changing the forest density in a wide range of different forest types showed only marginal effects on the IBL depth and turbulence intensity. In contrast, the streamwise length of forest gaps or clearings, i.e. the consideration of forest patches upstream of the windward forest edge, exposed significant effects on the IBL turbulence. Namely, with decreasing clearing length the IBL turbulence intensity was found to increase, and the IBL development proceeded at a higher rate. The reason for this is that for relatively short clearings, coherent canopy turbulence created above the upstream located forest patch is advected across the clearing towards the downstream located forest patch, noticeably affecting the development and the internal structure of the IBL above the downstream forest. These effects were more pronounced under neutral than under unstable stratification, since in the latter case convective motions promote the vertical mixing of the advected canopy turbulence above the clearing, so that the turbulence created above the upstream forest hardly reaches the downstream forest (please note that stable stratifications were not treated in the present thesis). Moreover, the effect of an Ekman-layer wind profile in the ABL versus a purely pressure-driven wind profile in laboratory flow was investigated. It was demonstrated that the additional directional shear of the horizontal wind in an Ekman layer overall increases the turbulence intensity of the approaching flow, which in turn enhances the IBL turbulence intensity, however, less effectively as compared to the gap-size effect. While the IBL turbulence was largely affected by the different meteorological and plant-physical parameters, the IBL depth was nearly unaffected. To summarize, these findings imply for the comparability of numerically-modelled and “real-world” forest-edge flow data that appropriately modelling forest-gap size, the atmospheric wind profile, and considering the atmospheric stability is

---

more important than to represent the forest density one-to-one, which should be considered in numerical modelling set-ups reproducing experiment site conditions. In wind-tunnel experiments, where atmospheric conditions cannot be reproduced properly, the attention should be put on the proper representation of the approaching flow concerning the effect of upstream located obstacles such as forests.

Another objective of this model-versus-measurement comparison was to identify the statistical requirements for capturing reliable flow fields above forests using Doppler lidar. In the “real world”, atmospheric conditions are never truly stationary, making it difficult to obtain sufficiently large lidar datasets for a specific atmospheric condition. By means of LES, it was identified that at least 2.5 hr of data should be available of one specific meteorological condition, in order to capture a statistically reliable picture of the IBL structure above a forest. For lidar measurements in the field, where atmospheric conditions are highly non-stationary, this implies that the necessary data amount has to be remarkably increased.

As an overall conclusion, it is emphasized that a combined application of LES and multi-dimensional field and wind-tunnel experiments is helpful for thoroughly investigating the flow field and the development of coherent canopy turbulence within the IBL above forests for various atmospheric regimes. While lidar is the only way of providing these multi-dimensional information in the field, LES can be used for systematic parameter studies under realistic atmospheric conditions in order to help interpret the captured lidar data and to test the suitability of the lidar measuring strategies. In turn, the availability of large datasets of multi-dimensional field and wind-tunnel data are a necessary prerequisite for reliably verifying LES models in canopy flows. With the present study, the first validation by Träumner et al. (2012) to introduce lidar as a state-of-art tool for multi-dimensionally capturing forest-edge flows, were largely extended, and recommendations for future model-to-experiment intercomparisons were given.

The overall goal of this thesis was to improve the understanding of the scalar transport near windward and leeward forest edges, and with this, to enable a better interpretation and design of in-situ micrometeorological measurements in such locations. As indicated by previous studies, locally enhanced scalar concentrations and fluxes might occur above forest patches downstream of windward edges (Klaassen et al., 2002; Klaassen and Sogachev, 2006; Sogachev et al., 2008; Ross and Baker, 2013), and likely also in the lee of forests, as suggested e.g. by the findings of Katul et al. (2006) and Ross (2011). In order to contribute to a firm knowledge base on this matter, idealized LES set-ups were simulated, treating neutral pressure-driven flows (without Coriolis force) across a periodic clearing-forest-clearing configuration in flat terrain, for a wide range of different forest densities at weak to moderate winds. Surface properties on the clearing and the forest patch were each horizontally homogeneous, while the vertical forest morphology was characterized by a dense crown and a sparse trunk layer. A passive scalar was considered, released at an equal source strength on the clearing and the forest floor, mimicking e.g. soil respiration of CO<sub>2</sub>. Different aspects were addressed, such as identifying the important physical mechanisms for the local enhancement of the scalar transport, and understanding the behaviour of the scalar enhancement under different meteorological and plant-physical conditions; finally, formulating implications for a better planning and interpretation of in-situ micrometeorological measurements near forest edges. All of these mentioned aspects were tackled for both, windward and leeward forest edges.

A pronounced local scalar enhancement was found inside the forest downstream of the windward forest edge, accompanied with locally enhanced scalar flux. This confirms the findings of Klaassen et al. (2002) and Sogachev et al. (2008), who attributed the local scalar accumulation to the mean streamwise advection of scalar-rich air from the clearing into the forest. However, by means of a term-by-term analysis of the scalar balance equation in the LES, it was found that the scalar accumulation is not only a result of mean streamwise

---

advection of the scalar, but it is in equal measures also steered by turbulent streamwise transports. This is attributed to the aerodynamic drag forces caused by the trees, leading to deceleration of the mean flow and suppression of turbulence, so that both, mean and turbulent streamwise transports converge, causing the scalar accumulation. The removal of scalar in this region can be mainly attributed to mean and turbulent vertical transports, whereby the relative contributions of these mechanisms was found to depend on forest density. In sparse forests, turbulent vertical transport dominated the scalar removal, whereas in dense forests, mean and turbulent vertical transports were similarly important. To summarize, this study has extended the understanding of the transport mechanisms near windward forest edges, based on the findings of the RANS study by Sogachev et al. (2008), where turbulent transports were not adequately represented. Moreover, the present findings imprint a high complexity to the interpretation of in-situ flux measurements within and above forests, since the local scalar transport near windward forest edges is steered not only by vertical turbulent fluxes of the scalar, but with remarkable contributions also by mean streamwise and vertical advective transports as well as by turbulent transports in the streamwise direction, which can hardly be measured.

It was further investigated how the local enhancement of scalar concentration and its flux depends on forest density and wind speed. The LES results demonstrated that the location of the peak in scalar concentration and flux is highly dependent on forest density. To be specific, with increasing forest density, peak locations were found to be closer to the windward forest edge, owing to the larger aerodynamic drag of denser forests so that the convergence of the scalar transport causing the scalar enhancement happens already at shorter distances from the windward edge. In contrast, the wind speed exposed to have nearly no effect on the peak locations. Moreover, the present LES results exhibited that peak concentrations strongly increase with increasing forest density and with decreasing wind speed, due to the decreasing efficiency of advective and turbulent transports. Also the peak fluxes increased with increasing forest density, however, they remained invariant of wind speed, in agreement with findings of Sogachev et al. (2008). Further, the simulated scalar-flux enhancement over a sparse forest was found to be similar as found in a field experiment by Klaassen et al. (2002) for the local enhancement of the turbulent flux of sensible and latent heat. To summarize, the largest local enhancement of scalar concentration and its flux should be expected for dense forests and under weak-wind conditions (the latter affects only scalar concentration), implying that under such conditions locally measured concentrations and fluxes can deviate most from their actual adjusted equilibrium values further downstream of the windward forest edge.

It was shown that scalar concentration and its flux is spatially highly variable in the edge region of a forest, while further downstream they gradually adjust to their equilibrium values. If the intention of a micrometeorological experiment is to measure the adjusted forest-atmosphere exchange of scalars, these measurements have to be performed at locations sufficiently downstream of the windward forest edge. In order to estimate the required distances (fetch) for optimum measuring positions, Belcher et al. (2012) proposed that the required fetch could be estimated as twice the flow-adjustment length  $X_A$ , which is an analytically derived function of forest drag, wind speed and Reynolds shear stress (Belcher et al., 2003), describing the distance from the forest edge where the in-canopy flow has adjusted. Within the present study, it was found that the formulation of  $X_A$  fails to quantify the flow adjustment region in dense forests, where an in-canopy flow recirculation occurs (e.g. Cassiani et al., 2008; Sogachev et al., 2008) which increases the actual length of the flow-adjustment region. Consequently, for dense forests, the fetch of  $2 X_A$  for the scalar flux adjustment, was found to be no longer a sufficient fetch estimate for the flux adjustment. In fact, the pre-factor of 2 as proposed by Belcher et al. (2012) was found to increase linearly with increasing

---

forest density, thus, a corrective function for the pre-factor was proposed.

In order to directly estimate the regions of enhanced forest-atmosphere scalar exchange, a new strategy was introduced, based on multi-dimensional flow-measuring techniques such as Doppler lidar. It is known that under conditions where surface sources of the scalar dominate over canopy sources/sinks (leaf-air interactions), the scalar flux adjustment takes place within the same distances as the momentum flux adjustment (see e.g. Belcher et al., 2012). This implies that regions of enhanced scalar fluxes can be estimated by locating regions of enhanced momentum fluxes above the forest by lidar. Of course, costly Doppler lidars are mostly not an option for short-term measuring campaigns, however, they can be useful for the preparation of long-term micrometeorological measurements.

Also in the lee of forests, locally enhanced scalar concentrations and fluxes were observed in the present LES study, so far not reported in the current literature. A term-by-term analysis of the scalar balance equation revealed that the scalar accumulation is caused by convergence of mean streamwise and vertical transports as well as of turbulent streamwise transports, while the relative importance of each transport mechanisms depends largely on forest density. In the lee of dense forests, the accumulation of scalar is caused solely by the convergence of the mean streamwise transport of the scalar, due to the presence of a lee rotor in the mean flow, which were already observed in previous experimental (Bergen, 1975; Detto et al., 2008) and numerical studies (Cassiani et al., 2008), in analogy to backward-facing-step flow (e.g. Markfort et al., 2014). In the lee of sparse forests, where no lee rotor appears in the mean flow, the convergence of the mean streamwise and vertical transport as well as the convergence of the turbulent streamwise transport are in equal parts responsible for the scalar accumulation. To explain, lee rotors are of intermittent nature, and their relative occurrence has been found, by means of LES (Cassiani et al., 2008) and field experiments (Detto et al., 2008), to increase with forest density, hence, a lee rotor in the mean flow appears only in the lee of dense forests, which is in agreement with results of the present study.

Moreover, it was found that concentration levels increase with increasing forest density and with decreasing wind speed, similar as observed near the windward forest edge (see above). However, in contrast to the windward forest edge, scalar peak positions in the lee of the forest were nearly unaffected by wind speed and forest density. Scalar fluxes in the lee of the forest likewise increased with forest density, while they remained invariant of wind speed. Overall, the local enhancement of scalar concentrations and fluxes in the lee of forests can be of the same order of magnitude as in the lee of a forested hill (Ross, 2011; Ross and Baker, 2013), where scalar accumulation was attributed to the presence of a rotor forming in the lee of the hill.

The pronounced local enhancement of scalar concentrations and fluxes in the lee of forests introduces a certain complexity to the interpretation of in-situ micrometeorological measurements. In order to be able to identify regions of possibly enhanced scalar transport on-site, a new method was proposed, which is based on the analysis of high-frequency flow data. It was found that the magnitude of local flux enhancement correlates with the relative occurrence of intermittent lee-rotor events. Thus, regions with enhanced fluxes can be estimated by localizing and counting lee-rotor events, e.g. based on flow data recorded by sonic anemometers, as being a part of the basic equipment of micrometeorological sites.

Despite the idealized form of the present LES study, its findings contribute to an improved understanding of scalar transport near forest edges, which enables an optimization of micrometeorological measuring strategies. These improvements are an essential prerequisite to advance SVAT parametrizations in weather and climate models for a better representation of the soil-vegetation-atmosphere exchange in fragmented landscapes. This becomes increasingly important, since the patchiness of the world's forests is continuously growing (FAO, 2010), mainly due to deforestation as e.g. highly practised in tropical rainforests.



---

## Outlook

Within the framework of this thesis, open questions concerning forest-atmosphere exchange in fragmented forested landscapes were treated, and recommendations for the optimization of micrometeorological measurement strategies were given. Since the current research of scalar transport in fragmented forested landscapes is still in its infancy, several open questions remain, which were not addressed in this thesis.

In order to contribute to a basic understanding of the scalar transport processes near forest edges, passive scalars were simply emitted at the surface. However in nature, the distribution of sources and sinks of scalars like temperature, humidity and trace gases (e.g. CO<sub>2</sub>) is much more complex. For example, the foliage layer of forests serves as a source for heat after being warmed by the solar radiation, or it serves as a sink for CO<sub>2</sub> by photosynthetic intake. The effects of the complex source-sink distributions on the adjustment of scalar transports downstream of forest edges, where first thoughts have been addressed by Sogachev et al. (2008) and Belcher et al. (2012), are so far not sufficiently understood.

Further complexity to the forest-atmosphere exchange is added when considering non-neutral atmospheric conditions. For example, during daytime when the solar radiation warms the foliage in the forest's crown layer, an unstably stratified layer forms above the forest top, while a stable stratification forms between the relatively cool trunk space and the heated crown layer, and at night, vice versa. These circumstances can result in complex coupling stages of the different forest layers, as well as between forest and the overlying atmosphere (e.g. Thomas and Foken, 2007). Here, a term-by-term analysis of the scalar transport equation by means of LES can help to quantify the importance of individual transport mechanisms under the different coupling regimes.

Moreover, it is yet not well understood how the thermal stratification of the atmosphere impacts the development of coherent canopy turbulence, which are known to effectively contribute to the forest-atmosphere exchange of momentum and scalars. This question might be addressed by lidar measurements of the flow field above forests (Träumner et al., 2012), combined with coherent-structure analysis as performed by Träumner et al. (2015) under the use of high-resolution LES data.

Landscape orography as well as forest-gap size are further influencing factors for the transport efficiency of coherent canopy turbulence as well as for the enhanced scalar transport near forest edges, where the relative effects of these factors on the scalar transport need to be quantified. Recent LES and field studies have revealed that complex flow structures can be induced by small to midsize forest gaps and local differences in forest inventory (Queck et al., 2014; Schlegel et al., 2015). It is yet unclear to what extent these internal heterogeneities within a forest patch, such as small gaps or horizontally variable tree heights and leaf area densities (mixed forests), affect the scalar transport and the occurrence of scalar-flux enhancement near forest edges.

LES has been proven useful to study scalar transport mechanisms systematically for various meteorological and plant-physical conditions, enabling to start with idealized flow scenarios and subsequently adding more complexity, in order to quantify different mechanisms separately, which in nature often superimpose each other. Despite this capability, more “real-world” data of scalar transport near forest edges would be desirable to verify LES results, e.g. by performing smoke-release experiments near forest edges as first done by Bergen (1975).

Even though several open questions remain to build a firm understanding of scalar transport in fragmented forested landscapes, the idealized studies of the present thesis have contributed to a basic understanding of the mechanisms responsible for the scalar transport near forest edges, and have enabled first implications for the interpretation of micrometeorological measurements in such regions.

## Acknowledgements

This PhD project was funded by the German Research Foundation DFG<sup>1</sup> under grant RA 617/23-1. Numerical simulations were performed on the SGI ALTIX of the North-German Supercomputing Alliance HLRN<sup>2</sup>. Results were analyzed and visualized by NCAR tools NCL<sup>3</sup> and VAPOR<sup>4</sup>.

I would like to address special acknowledgements to a number of individuals, who contributed in different ways to the realization and completion of this PhD project:

- My advisor Prof. Dr. Siegfried Raasch greatly supported my work by comprehensive mentoring and by providing financial support, even beyond the official funding period of the DFG project. I further received many chances to travel abroad, getting into contact with scientists all over the world.
- Prof. Dr. Günter Groß acted as the Co-reviewer of this PhD thesis.
- My colleagues within the joined DFG project EGER supported discussions about possible research questions, specially to mention Prof. Dr. Thomas Foken, Dr. Eva Falge and Linda Voß.
- Dr. Katja Träumner and Prof. Dr. Bodo Ruck at Karlsruhe Institute of Technology (Germany) provided data and ideas for one of the research articles in this PhD thesis. Further, they supported the article development by writing parts of the manuscript (Dr. Katja Träumner), and by contributing valuable discussions during the internal review process of our manuscript.
- Dr. Matthias Sühning proofread all articles as well as the remaining parts of this cumulative PhD thesis.
- My colleagues in the PALM group at IMUK joined scientific discussions on my study questions and helped to improve the quality of my conference contributions. Dr. Björn Maronga and Helge Knoop produced video animations of parts of my research results. Former PALM-group student Hannes Schulz contributed parts of his Bachelor thesis.
- Christiane Brünig, Berit Parbel, Gerda Stendel and Notker Fechner gave great support in burocratic and technical matters, and were always up for a chat.
- My very dear friends Linda Voß, Michael Schrempf, Jens Fricke and Viola Hilger, and my dear friends inside and outside of IMUK made the sometimes tough life as a researcher much happier. I will certainly miss those times. Cheers!
- My family always supported me on my way through education, from school up to this day. Now let's see what the real life brings.
- The best of all, my husband and very best friend Matthias gave continuous moral and scientific support. He always had faith in me, especially when I totally lost it, he was a superb motivator.

With you, life is just wonderful! Thank you for being my ring fellow ;-)

---

<sup>1</sup>Deutsche Forschungsgemeinschaft

<sup>2</sup>Norddeutscher Verbund für Hoch- und Höchstleistungsrechnen

<sup>3</sup>The NCAR Command Language (Version 6.0.0) [software]. (2011). Boulder, Colorado: UCAR/NCAR/-CISL/VETS. doi:10.5065/D6WD3XH5

<sup>4</sup>[www.vapor.ucar.edu](http://www.vapor.ucar.edu), a product of the Computational Information Systems Laboratory at the National Center for Atmospheric Research

## Bibliography

- Amiro, B.D., 1990:** Drag coefficients and turbulence spectra within three boreal forest canopies. *Boundary-Layer Meteorol.*, **52**, 227–246.
- Arakawa, A., V. R. Lamb, 1977:** Computational design of the basic dynamical processes of the UCLA general circulation model. *Methods Comput. Phys.*, **17**, 173–265.
- Baldocchi, D., E. Falge, L. Gu, R. Olson, D. Hollinger, S. Running, P. Anthoni, Ch. Bernhofer, K. Davis, R. Evans, J. Fuentes, A. Goldstein, G. Katul, B. Law, X. Lee, Y. Malhi, T. Meyers, W. Munger, W. Oechel, K.T. Paw U, K. Pilegaard, H.P. Schmid, R. Valentini, S. Verma, T. Vesala, K. Wilson, S. Wofsy, 2001:** FLUXNET: A new tool to study the temporal and spatial variability of ecosystem-scale carbon dioxide, water vapor, and energy flux densities. *Bull. Am. Meteorol. Soc.*, **82**, 2415–2434.
- Bergen, J.D., 1975:** Air movement in a forest clearing as indicated by smoke drift. *Agric. Meteorol.*, **15**, 165–179.
- Bergström, H., U. Högström, 1989:** Turbulent exchange above a pine forest II. Organized structures. *Boundary-Layer Meteorol.*, **49**, 231–263.
- Belcher S.E., I.N. Harman, J.J. Finnigan, 2012:** The wind in the willows: flows in forest canopies in complex terrain. *Annu. Rev. Fluid Mech.*, **44**, 479–504.
- Belcher S.E., N. Jerram, J.C. Hunt, 2003:** Adjustment of a turbulent boundary layer to a canopy of roughness elements. *J. Fluid Mech.*, **488**, 369–398.
- Blackadar, A., 1997:** *Turbulence and diffusion in the atmosphere*. Springer, Berlin, 185 pp.
- Bohrer, G., G.G. Katul, R.L. Walko, R. Avissar, 2009:** Exploring the effects of microscale structural heterogeneity of forest canopies using large-eddy simulations. *Boundary-Layer Meteorol.*, **132**, 351–382.
- Brown, K.W., W. Covey, 1966:** The energy-budget evaluation of the micro-meteorological transfer process within a cornfield. *Agric. Meteorol.*, **3**, 73–96.
- Breuer, M., 2002:** *Direkte Numerische Simulation und Large-Eddy Simulation turbulenter Strömungen auf Hochleistungsrechnern*. Shaker Verlag, Aachen, 433 pp.
- Businger, J. A., J. C. Wyngaard, Y. Izumi, E. F. Bradley, 1971:** Flux-profile relationships in the atmospheric surface. *J. Atmos. Sci.*, **28**, 181–189.
- Cassiani, M., G.G. Katul, J.D. Albertson, 2008:** The effects of canopy leaf area index on airflow across forest edges: large-eddy simulation and analytical results. *Boundary-Layer Meteorol.*, **126**, 433–460.
- Chan, T.L., G. Dong, C.W. Leung, C.S. Cheung, W.T. Hung, 2002:** Validation of a two-dimensional pollutant dispersion model in an isolated street canyon. *Atmos. Env.*, **36**, 861–872.
- Courant, R., K. Friedrichs, H. Lewy, 1928:** Über die partiellen Differentialgleichungen der mathematischen Physik. *Math. Ann.*, **100**, 32–74.
- Deardorff, J.W., 1980:** Stratocumulus-capped mixed layers derived from a three-dimensional model. *Boundary-Layer Meteorol.*, **18**, 495–527.

- Detto, M., G.G. Katull, M. Siqueira, J.Y. Juang, P. Stoy, 2008: The structure of turbulence near a tall forest edge: the backward-facing step flow analogy revisited. *Ecol. Appl.*, **18**(6), 1420–1435.
- Dyer, A. J., 1974: A review of flux-profile relationships. *Boundary-Layer Meteorol.*, **3**, 363–372.
- Dupont, S., Y. Brunet, 2008: Edge flow and canopy structure: a large-eddy simulation study. *Boundary-Layer Meteorol.*, **126**, 51–71.
- Dupont, S., Y. Brunet, 2009: Coherent structures in canopy edge flow: a large-eddy simulation study. *J. Fluid Mech.*, **630**, 93–128.
- Edburg, S.L., D. Stock, B.K. Lamb, E.G. Patton, 2012: The effect of the vertical source distribution on scalar statistics within and above a Forest Canopy. *Boundary-Layer Meteorol.*, **142**, 365–382.
- Etling, D., 2002: *Theoretische Meteorologie*. Springer Verlag, Berlin, Heidelberg, 354pp.
- Falkowski, P., R.J. Scholes, E. Boyle, J. Canadell, D. Canfield, J. Elser, N. Gruber, K. Hibbard, P. Höglberg, S. Linder, F. T. Mackenzie, B. Moore III, T. Pedersen, Y. Rosenthal, S. Seitzinger, V. Smetacek, W. Steffen, 2000: The global carbon cycle: a test of our knowledge of Earth as a system. *Science*, **290**(5490), 291–296.
- FAO – Food and Agriculture Organization of the United Nations, 2010: Global forest resources assessment 2010. *FAO Forestry Paper*, **163**.
- Finnigan, J.J., 2000: Turbulence in plant canopies. *Annu. Rev. Fluid Mech.*, **32**, 519–571.
- Finnigan, J.J., R.H. Shaw, 2000: A wind tunnel study of airflow in waving wheat: an Empirical Orthogonal Function analysis of the large-eddy motion. *Boundary-Layer Meteorol.*, **96**, 211–255.
- Foken, T. 2006: *Angewandte Meteorologie*. Springer Verlag, Berlin, Heidelberg, 325 pp.
- Foken, T., 2008: The energy balance closure problem: an overview. *Ecol. Appl.*, **18**(6), 1351–1367.
- Foken, T., F.X. Meixner, E. Falge, C. Zetzsch, A. Serafimovich, A. Bargsten, T. Behrendt, T. Biermann, C. Breuninger, S. Dix, T. Gerken, M. Hunner, L. Lehmann-Pape, K. Hens, G. Jocher, J. Kesselmeier, J. Lüers, J.C. Mayer, A. Moravek, D. Plake, M. Riederer, F. Rütz, M. Scheibe, L. Siebicke, M. Sörgel, K. Staudt, I. Trebs, A. Tsokankunku, M. Welling, V. Wolff, Z. Zhu, 2012: Coupling processes and exchange of energy and reactive and non-reactive trace gases at a forest site – results of the EGER experiment. *Atmos. Chem. Phys.*, **12**, 1923–1950.
- Fontan, S., G.G. Katul, D. Poggi, C. Manes, L. Ridolfi, 2013: Flume experiments on turbulent flows across gaps of permeable and impermeable boundaries. *Boundary-Layer Meteorol.*, **147**, 21–39.
- Gao, W., R.H. Shaw, K.T. Paw U, 1989: Observation of organized structure in turbulent flow within and above a forest canopy. *Boundary-Layer Meteorol.*, **47**, 349–377.
- Gardiner, B.A., 1994: Wind and wind forces in a plantation spruce forest. *Boundary-Layer Meteorol.*, **67**, 161–186.
- Garratt, J., 1990: The internal boundary layer – a review. *Boundary-Layer Meteorol.*, **50**, 171–203.
- Gryschka, M., 2010: *Untersuchungen zur Entwicklung von Rollenkonvektion in Kaltluftausbrüchen mittels Grobstruktursimulationen*. PhD thesis, Institute of Meteorology and Climatology, Leibniz Universität Hannover, 104 pp.

- Holmes, P., J.L. Lumley, G. Berkooz, 1996: *Turbulence, coherent structures, dynamical systems and symmetry*. Cambridge University Press, Cambridge, 420 pp.
- Huang, J., M. Cassiani, J.D. Albertson, 2009: The effects of vegetation density on coherent turbulent structures within the canopy sublayer: a large-eddy simulation study. *Boundary-Layer Meteorol.*, **133**, 253–275.
- Irvine, M.R., B.A. Gardiner, M.K. Hill, 1997: The evolution of turbulence across a forest edge. *Boundary-Layer Meteorol.*, **84**, 467–496.
- Kanani-Sühring, F., S. Raasch, 2015: Spatial variability of scalar concentrations and fluxes downstream of a clearing-to-forest transition: an LES study. *Boundary-Layer Meteorol.*, **155**, 1–27.
- Kanani, F., K. Träumner, B. Ruck, S. Raasch, 2014: What determines the differences found in forest edge flow between physical models and atmospheric measurements – an LES study. *Meteorol. Z.*, **23(1)**, 33–49.
- Kanda, M., M. Hino, 1994: Organized structures in developing turbulent flow within and above a plant canopy, using a large-eddy simulation. *Boundary-Layer Meteorol.*, **68**, 237–257.
- Katul, G.G., J.J. Finnigan, D. Poggi, R. Leuning, S.E. Belcher, 2006: The influence of hilly terrain on canopy-atmosphere carbon dioxide exchange. *Boundary-Layer Meteorol.*, **118**, 189–216.
- Klaassen, W., A. Sogachev, 2006: Flux footprint simulation downwind of a forest edge. *Boundary-Layer Meteorol.*, **121**, 459–473.
- Klaassen, W., P.B. van Breugel, E.J. Moors, J.P. Nieveen, 2002: Increased heat fluxes near a forest edge. *Theor. Appl. Climatol.*, **72**, 231–243.
- Kruijt, B., W. Klaassen, R.W.A. Hutjes, 1995: Edge effects on diffusivity in the roughness layer over a forest. – In: *Wind and Trees* (eds. M.P. Coutts and J.F. Grace), pp. 60–70, Cambridge University Press.
- Leclerc, M.Y., T. Foken, 2014: *Footprints in micrometeorology and ecology*. Springer Verlag, Berlin, Heidelberg, 1st Ed., 239 pp.
- Letzel, M.O., M. Krane, S. Raasch, 2008: High resolution urban large-eddy simulation studies from street canyon to neighbourhood scale. *Atmos. Env.*, **42**, 8770–8784.
- Markfort, C.D., F. Porté-Agel, H.G. Stefan, 2014: Canopy-wake dynamics and wind sheltering effects on Earth surface fluxes. *Environ. Fluid Mech.*, **14**, 663–697.
- Maronga, B., S. Raasch, 2013: Large-Eddy Simulations of Surface Heterogeneity Effects on the Convective Boundary Layer During the LITFASS-2003 Experiment. *Boundary-Layer Meteorol.*, **146**, 17–44.
- Maronga, B., M. Gryschka, R. Heinze, F. Hoffmann, F. Kanani-Sühring, M. Keck, K. Ketelsen, M.O. Letzel, M. Sühring, S. Raasch, 2015: The Parallelized Large-Eddy Simulation Model (PALM) version 4.0 for atmospheric and oceanic flows: model formulation, recent developments, and future perspectives. *Geosci. Model Dev. Discuss.*, doi: 10.5194/gmdd-8-1539-2015.
- Marshall, B.J., C.J. Wood, B.A. Gardiner, S.E. Belcher, 2002: Conditional sampling of forest canopy gusts. *Boundary-Layer Meteorol.*, **102**, 225–251.
- Monin, A. S., A. M. Obukhov, 1954: Basic laws of turbulent mixing in the atmosphere near the ground. *Trudy Academia Nauka SSR.*, **24**, 1963–1987.
- Monteith, J.L., 1973: *Principles of Environmental Physics*. Edward Arnold, London, 241 pp.

- Morse, A.P., B.A. Gardiner, B.J. Marshall, 2002: Mechanisms controlling turbulence development across a forest edge. *Boundary-Layer Meteorol.*, **103**, 227–251.
- Noh, Y., G. Goh, S. Raasch, 2010: Examination of the mixed layer deepening process during convection using LES. *J. Phys. Oceanogr.*, **40**, 2189–2195.
- Pan, Y., R.A. Birdsey, J. Fang, R. Houghton, P.E. Kauppi, W.A. Kurz, O.L. Phillips, A. Shvidenko, S.L. Lewis, J.G. Canadell, P. Ciais, R.B. Jackson, S.W. Pacala, A.D. McGuire, S. Piao, A. Rautiainen, S. Sitch, D. Hayes, 2011: A large and persistent Carbon sink in the World's forests. *Science*, **333(6045)**, 988–993.
- Patrinos A.N.A., A.L. Kistler, 1977: A Numerical Study of the Chicago Lake Breeze. *Boundary-Layer Meteorol.*, **12**, 93–123.
- Patton, E.G., T.W. Horst, P.P. Sullivan, D.H. Lenschow, S.P. Oncley, W.O.J. Brown, S.P. Burns, A.B. Guenther, A. Held, T. Karl, S.D. Mayor, L.V. Rizzo, S.M. Spuler, J. Sun, A.A. Turnipseed, E.J. Allwine, S.L. Edburg, B.K. Lamb, R. Avissar, R.J. Calhoun, J. Kleissl, W.J. Massman, K.T. Paw U, J.C. Weil, 2011: The canopy horizontal array turbulence study. *Bull. Amer. Meteor. Soc.*, **92**, 593–611.
- Pielke, R. A., 2002: *Mesoscale meteorological modeling*. Academic Press, San Diego, 2nd edition, 676 pp.
- Poggi, D., G.G. Katul, 2007: Turbulent flows on forested hilly region terrain: the recirculation. *Q.J.R. Meteorol. Soc.*, **133**, 1027–1039.
- Queck, R., C. Bernhofer, A. Bienert, T. Eipper, V. Goldberg, S. Harmansa, V. Hildebrand, H.G. Maas, F. Schlegel, J. Stiller, 2014: TurbEFA: an interdisciplinary effort to investigate the turbulent flow across a forest clearing. *Meteorol. Z.*, **23(6)**, 637–659.
- Raasch, S., D. Etling, 1998: Modeling deep ocean convection: Large eddy simulation in comparison with laboratory experiments. *J. Phys. Oceanogr.*, **28**, 1786–1802.
- Raasch, S., M. Schröter, 2001: PALM – A large-eddy simulation model performing on massively parallel computers. *Meteorol. Z.*, **10**, 363–372.
- Raupach, M.R., J.J. Finnigan, Y. Brunet, 1996: Coherent eddies and turbulence in vegetation canopies: the mixing-layer analogy. *Boundary-Layer Meteorol.*, **78**, 351–382.
- Roache, P.J., 1985: *Computational Fluid Dynamics*. Hermosa Publishers, Albuquerque, New Mexico, 6th edition, 446 pp.
- Ross, A.N., 2011: Scalar transport over forested hills. *Boundary-Layer Meteorol.*, **141**, 179–199.
- Ross, A.N., T.P. Baker, 2013: Flow over partially forested ridges. *Boundary-Layer Meteorol.*, **146**, 375–392.
- Ruck, B., E. Adams, 1991: Fluid mechanical aspects in the pollutants transport to coniferous trees. *Boundary-Layer Meteorol.*, **56**, 163–195.
- Schlegel, F., J. Stiller, A. Bienert, H.G. Maas, R. Queck, C. Bernhofer, 2012: Large-eddy simulation of inhomogeneous canopy flows using high resolution terrestrial laser scanning data. *Boundary-Layer Meteorol.*, **142**, 223–243.
- Schlegel, F., J. Stiller, A. Bienert, H.G. Maas, R. Queck, C. Bernhofer, 2015: Large-eddy simulation study of the effects on flow of a heterogeneous forest at sub-tree resolution. *Boundary-Layer Meteorol.*, **154**, 27–56.
- Schrötte, J., A. Dörnbrack, 2013: Turbulence structure in a diabatically heated forest canopy composed of fractal Pythagoras trees. *Theor. Comput. Fluid Dyn.*, **27**, 337–359.

- Schumann, U., 1975:** Subgrid scale model for finite difference simulations of turbulent flows in plane channels and annuli. *J. Comput. Sci.*, **18**, 376–404.
- Schumann, U., R.A. Sweet, 1988:** Fast Fourier transforms for direct solution of Poisson's equation with staggered boundary conditions. *J. Comput. Sci.*, **75**, 123–137.
- Shaw, R.H., 1977:** Secondary wind speed maxima inside plant canopies. *J. Appl. Meteorol.*, **16**, 514–521.
- Shaw, R.H., Y. Brunet, J.J. Finnigan, M.R. Raupach, 1995:** A wind tunnel study of air flow in waving wheat: two-point velocity statistics. *Boundary-Layer Meteorol.*, **76**, 349–376.
- Shaw, R.H., E.G. Patton, 2003:** Canopy element influences on resolved- and subgrid-scale energy within a large-eddy simulation. *Agric. For. Meteorol.*, **115**, 5–17.
- Shaw, R.H., U. Schumann, 1992:** Large-eddy simulation of turbulent flow above and within a forest. *Boundary-Layer Meteorol.*, **61**, 47–64.
- Shaw, R.H., I. Seginer, 1985:** The dissipation of turbulence in plant canopies. – In: *Proceedings of the 7th Symposium of the American Meteorological Society on Turbulence and Diffusion*, Boulder, Colorado, pp. 200–203.
- Shaw, R.H., J. Tavanger, D.P. Ward, 1983:** Structure of the Reynolds stress in a canopy layer. *J. Climate Appl. Meteorol.*, **22**, 1922–1931.
- Smagorinsky, J., 1963:** General circulation experiments with the primitive equation. Part 1: The basic experiment. *Mon. Wea. Rev.*, **91**, 99–164.
- Sogachev, A., M.Y. Leclerc, G. Zhang, Ü. Rannik, T. Vesala, 2008:** CO<sub>2</sub> fluxes near a forest edge: a numerical study. *Ecol. Appl.*, **18(6)**, 1454–1469.
- Stawiarski, C., K. Träumner, C. Knigge, R. Calhoun, 2013:** Scopes and challenges of dual-Doppler lidar wind measurements – an error analysis. *J. Atmos. Ocean. Tech.*, **30**, 2044–2061.
- Steinfeld, G., 2009:** *Die Beurteilung von Turbulenzmess- und Analyseverfahren der Mikrometeorologie durch virtuelle Messungen innerhalb von Grobstruktursimulationen*. PhD thesis, Institute of Meteorology and Climatology, Leibniz Universität Hannover, 96 pp.
- Su, H.B., R.H. Shaw, K.T. Paw U, 2000:** Two-point correlation analysis of neutrally stratified flow within and above a forest from large-eddy simulation. *Boundary-Layer Meteorol.*, **49**, 423–460.
- Su, H.B., R.H. Shaw, K.T. Paw U, C.H. Moeng, P.P. Sullivan, 1998:** Turbulent statistics of neutrally stratified flow within and above a sparse forest from large-eddy simulation and field observations. *Boundary-Layer Meteorol.*, **88**, 363–397.
- Sühring, M., B. Maronga, F. Herbort, S. Raasch, 2014:** On the effect of surface heat-flux heterogeneities on the mixed-layer-top entrainment. *Boundary-Layer Meteorol.*, **151**, 531–556.
- Thomas, C., T. Foken, 2007a:** Organised motion in a tall spruce canopy: temporal scales, structure spacing and terrain effects. *Boundary-Layer Meteorol.*, **122**, 123–147.
- Thomas, C., T. Foken, 2007b:** Flux contribution of coherent structures and its implications for the exchange of energy and matter in a tall spruce canopy. *Boundary-Layer Meteorol.*, **123**, 317–337.
- Träumner K., T. Damian, C. Stawiarski, A. Wieser, 2015:** Turbulent structures and coherence in the atmospheric surface layer. *Boundary-Layer Meteorol.*, **154**, 1–25.
- Träumner K., A. Wieser, B. Ruck, C. Frank, L. Röhner, C. Kottmeier, 2012:** The suitability of Doppler lidar for characterizing the wind field above forest edges. *Forestry*, **85**, 399–412.

- Watanabe, T., 2004:** Large-eddy simulation of coherent turbulence structures associated with scalar ramps over plant canopies. *Boundary-Layer Meteorol.*, **112**, 307–341.
- Wicker, L. J., W. C. Skamarock, 2002:** Time-splitting methods for elastic models using forward time schemes. *Mon. Wea. Rev.*, **130**, 2088–2097.
- Williamson, J. H., 1980:** Low-storage Runge-Kutta schemes. *J. Comput. Phys.*, **35**, 48–56.
- Yang, B., M.R. Raupach, R.H. Shaw, K.T. Paw U, A.P. Morse, 2006a:** Large-eddy simulation of turbulent flow across a forest edge. Part I: flow statistics. *Boundary-Layer Meteorol.*, **120**, 377–412.
- Yang, B., A.P. Morse, R.H. Shaw, K.T. Paw U, 2006b:** Large-eddy simulation of turbulent flow across a forest edge. Part II: momentum and turbulent kinetic energy budgets. *Boundary-Layer Meteorol.*, **121**, 433–457.
- Zhu, J., X. Li, Y. Gonda, T. Matsuzaki, 2004:** Wind profiles in and over trees. *J. Forestry Res.*, **15**, 305–312.



# Curriculum Vitae

## Personal Details

Family Name	Kanani-Sühring
First Name	Farah
Date of birth	19 May 1985
Place of birth	Hamm, Germany
Nationality	German

## Academic Career

Since 04/2014 **Research associate** at the Institute of Meteorology and Climatology, Leibniz Universität Hannover, Germany; Commissioned research for Deutsches Zentrum für Luft- und Raumfahrt (DLR; under grant D/224/67196260) within the framework of the BMWi research project SimBA – “Simulationswerkzeug für die hochgenaue und effiziente aerodynamische Berechnung und Auslegung von Windkraftanlagen”

04/2012 - 03/2014 **Representative of research associates** at the Institute of Meteorology and Climatology, Leibniz Universität Hannover, Germany.

12/2010 - 03/2014 **Research associate** at the Institute of Meteorology and Climatology, Leibniz Universität Hannover, Germany; DFG research project EGER on “Exchange processes in mountainous regions: Large-eddy simulations” (under grant RA 617/23-1).

## University Education

11/2010 **German “Diplom“ in meteorology.** Final grade: cum laude (1.6). Diploma thesis on “Footprintbestimmung mittels LES für das LITFASS-2003 Experiment“.

10/2005 - 11/2010 **Studies in meteorology,** Leibniz Universität Hannover, Germany.

---

Peer-Reviewed  
Publications

**Kanani-Sühring F, Raasch S, 2015:** Enhanced scalar concentrations and fluxes in the lee of forest patches: a large-eddy simulation study. Submitted to *Boundary-Layer Meteorol.*, under review.

**Hellsten A, Tu S, Steinfeld G, Kanani-Sühring F, Markkanen T, Järvi L, Lento J, Vesala T, Raasch S, 2015:** Footprint evaluation for flux and concentration measurements for an urban-like canopy with coupled Lagrangian stochastic and large-eddy simulation models. *Boundary-Layer Meteorol.*, online first, doi: 10.1007/s10546-015-0062-4

**Kanani-Sühring F, Raasch S, 2015:** Spatial variability of scalar concentrations and fluxes downstream of a clearing-to-forest transition: an LES study. *Boundary-Layer Meteorol.*, **155**, 1-27, doi: 10.1007/s10546-014-9986-3.

**Kanani F, Träumner K, Ruck B, Raasch S, 2014:** What determines the differences found in forest edge flow between physical models and atmospheric measurements? – An LES study. *Meteorol. Z.*, **23(1)**, 33-49, doi: 10.1127/0941-2948/2014/0542.

**Sühring M, Kanani-Sühring F, Charuchittipan D, Foken T, Raasch S, 2014:** Footprint estimation for elevated turbulence measurements – a comparison between large-eddy simulation and a Lagrangian stochastic backward model. *Boundary-Layer Meteorol.*, under revision.

Conference  
Contributions

**Tu S, Nordbo A, Kanani F, Rinne J, Vesala T, Hellsten A, Raasch S, 2014:** Large-Eddy Simulations for the Effects of Forest Canopy. *21st AMS Conference on Applied Climatology & 17th Symposium on Meteorological Observation and Instrumentation Personal, Westminster (CO), USA.*

**Tu S, Nordbo A, Kanani F, Rinne J, Raasch S, Vesala T, Hellsten A, 2014:** Fetch Effects of Forest Canopy on Flux Measurements. *EGU General Assembly 2014, Vienna, Austria.*

**Kanani F, Raasch S, 2013:** Difficulties in interpreting flux measurements near forest edges: a large-eddy simulation (LES) study. *DACH 2013, Innsbruck, Austria.*

**Kanani F, Raasch S, 2013:** Difficulties in interpreting CO<sub>2</sub> flux measurements near forest edges: an LES study (Awarded for best oral presentation ex aequo). *International Symposium on Patterns in Soil-Vegetation-Atmosphere Systems: Monitoring, Modeling and Data Assimilation, Bonn, Germany.*

---

**AV  
Media**

**Kanani F, Raasch S, 2012:** Interpretation of CO<sub>2</sub> flux measurements near a forest edge: an LES study (Awarded for best oral presentation ex aequo). *First International Education Forum on Energy and Environment, Hawaii's Big Island (HI), USA.*

**Foken T, Serafimovich A, Hübner J, Eigenmann R, Falge E, Meixner FX, Voß L, Raasch S, Kanani F, Held A, Sörgel M, Werle P, Eder F, Cieslik S, Liu H, Lamb BK, Leclerc MY, Duarte HF, 2012:** Turbulence Structures at a Forest Edge. *20th AMS Symposium on Boundary Layers and Turbulence, Boston (MA), USA.*

**Kanani F, Maronga B, Knoop H, Raasch S, 2014:** Large-eddy simulation of a forest-edge flow – Adjustment of a turbulent flow to the changing surface conditions at a clearing-to-forest transition. *TIB/AV-Portal*, doi: 10.5446/14297

**Kanani F, Maronga B, Knoop H, Raasch S, 2014:** Large-eddy simulation of the scalar transport in a forest-edge flow – Spatial variability of the scalar distribution and the scalar transport downstream of a clearing-to-forest transition. *TIB/AV-Portal*, doi: 10.5446/14311